Lower Passaic River
Sediment Transport Model

LOWER EIGHT MILES OF THE LOWER PASSAIC RIVER
LOWER PASSAIC RIVER SEDIMENT TRANSPORT MODEL

TABLE OF CONTENTS

LIST OF TABLES

LIST OF FIGURES

LOWER EIGHT MILES OF THE LOWER PASSAIC RIVER
LOWER PASSAIC RIVER SEDIMENT TRANSPORT MODEL

LIST OF ATTACHMENTS

1 INTRODUCTION

1.1 BACKGROUND

The Lower Passaic River (LPR) is a partially-stratified estuary that is connected to the New York/ New Jersey (NY/NJ) Harbor Estuary through Newark Bay (Figure 1-1). The LPR has a federally authorized navigation channel from River Mile (RM) 0-15.4, which was constructed at the end of the 19th century, then sporadically maintained through the 1950s above RM2 and through 1983 below RM2. When maintenance dredging stopped, sediment infilling rates in the artificially deep channel were relatively high (approximately 4 inches /year from historical bathymetry data). However, as the deep channel has filled in, the river has begun to reach a quasi-steady state, with overall patterns of infilling slowing considerably and alternating with some scouring during high flow events (Sea Engineering, et.al. 2011). Note that there are also navigation channels in Newark Bay, which continue to be maintained by the U.S. Army Corps of Engineers (USACE), and continue to be deepened periodically to accommodate larger ships. The most recent Harbor Deepening Project, which increases channel depths up to 50 feet, began in 2005 and is expected to be finished in 2014 when deepening of channels in the Arthur Kill is completed.

In the LPR, as maintenance dredging was declining, industrial activities along the river were growing, and industries and municipalities disposed of wastewaters in the LPR. The coincidence of chemical disposal in the river, along with the filling-in of the navigation channel, created conditions which promoted an accumulation of contaminated sediments in the LPR. LPR sediments are contaminated with a number of contaminants of potential concern (COPCs) and contaminants of potential ecological concern (COPECs) that pose risks to human and ecological health.

The LPR cross-sectional area declines steadily from RM0 to RM17.4, with a pronounced constriction at RM8.3. At that location, a change in sediment texture is observed. The

river bed below RM8.3 is dominated by silt material with pockets of silt and sand mixtures, while above RM8.3, the bed is characterized by coarser sediments with pockets of silt, often outside the channel. About 85 percent of the silt surface area in the LPR is located below RM8.3, and by volume, about 90 percent of silts in the LPR are located below RM8.3.

The lower 8-mile reach of the LPR has been identified as the major source of contamination to the rest of the river and Newark Bay. Through a Focused Feasibility Study (FFS), the U.S. Environmental Protection Agency (USEPA) is evaluating taking an action on the sediments of the lower 8 miles (FFS Study Area), while a larger study of the 17-mile Lower Passaic River Study Area (LPRSA) is on-going. The FFS evaluates the following alternatives:

1. No Action

2. Deep Dredging with Backfill involves dredging all contaminated fine-grained sediments throughout the FFS Study Area bank to bank (9.7 million cubic yards) and placing two feet of sand backfill. It results in the restoration of the authorized navigation channel in RM0-8.3.

3. Capping with Dredging for Flooding and Navigation (also called "Full Capping" in the modeling reports) includes dredging of enough fine-grained sediment (4.3 million cubic yards) so that an engineered sand cap can be placed over the FFS Study Area bank to bank without causing additional flooding and to accommodate the continued and reasonably-anticipated future use of the federally-authorized navigation channel between RM0.0 and RM2.2.

4. Focused Capping with Dredging for Flooding includes dredging of fine-grained sediments (1.0 million cubic yards) in selected portions of the FFS Study Area (adding up to about one third of the FFS Study Area surface) with the highest gross and net fluxes of COPCs and COPECs to a depth of 2.5 feet so that an

engineered sand cap can be placed over those portions dredged without causing additional flooding. It does not include dredging in the federally-authorized navigation channel to accommodate continued and reasonably-anticipated future use.

The FFS Study Area is an operable unit of the Diamond Alkali Superfund Site, which includes the former Diamond Alkali facility located at 80-120 Lister Avenue in Newark. The Diamond Alkali Superfund Site also encompasses the following work:

- A group of companies named the Cooperating Parties Group (CPG) is implementing an on-going remedial investigation and feasibility study (RI/FS) of the 17-mile LPRSA under USEPA oversight.

- Occidental Chemical Corporation (OCC) is implementing (with Tierra Solutions [Tierra] performing the work), under USEPA oversight, a non-time critical removal of 200,000 cubic yards (cy) of highly contaminated sediments from the LPR adjacent to the former Diamond Alkali facility in Newark (Tierra Removal). Dredging, dewatering and transport off-site of the first 40,000 cy of sediment (known as Phase 1 of the Tierra Removal) were completed in 2012. Phase 2 (160,000 cy) is undergoing a separate engineering study and proposal that will be submitted to the public for review and comment at a later date.

- The CPG is implementing, under USEPA oversight, a time-critical removal action to address the risks posed by elevated concentrations of dioxins and polychlorinated biphenyls (PCBs) (and other contaminants) found at the surface of a mudflat on the east bank of the LPR at RM10.9 in Lyndhurst (RM10.9 Removal). Implementation started in 2013 and will be on-going in 2014.

- Tierra is implementing an on-going RI/FS of the Newark Bay Study Area under USEPA oversight.

1.2 PURPOSE AND OBJECTIVE

A sediment transport and contaminant fate and transport modeling analysis of the LPR was performed as one component in the FFS' analysis of the above remedial alternatives. Sediment transport results provided input to a contaminant fate and transport model, which in turn provided contaminant exposure concentrations to human health and ecological risk assessments. The objective of the sediment transport modeling was to develop a mathematical representation of the processes affecting sediment transport behavior, so that simulated sediment transport results could be used to assess the transport of sorbed contaminants in the fate and transport modeling. The objective of the contaminant fate and transport modeling was to develop a mathematical representation of the processes affecting contaminant fate and transport behavior of dissolved and sorbed contaminants based on the associated sediment transport results. The simulated contaminant exposure results could then be used in assessments of human health and ecological risk associated with exposure to COPCs and COPECs in the FFS Study Area under the remedial alternatives listed above.

1.3 DATA SETS

The sediment transport and contaminant fate and transport model development relied on several data sets collected during the course of the FFS, 17-mile LPRSA RI/FS, Newark Bay Study Area RI/FS and university studies. This section briefly summarizes how those data sets were collected. More detail on each data set is included in Chapter 2 of the Remedial Investigation Report for the FFS (RI).

- Bathymetry: Multiple bathymetric surveys have been conducted on the LPR by Tierra and the CPG, both under USEPA oversight, and by USACE. In 1995 to 2001, Tierra conducted five single-beam surveys between RM0.9 and RM7 along common transects to facilitate direct comparison. The other bathymetric surveys characterize RM0 to RM8 or RM0 to RM17.4. The 2007, 2008, 2010 and 2011 surveys conducted by CPG were multi-beam surveys.

- 1995 Remedial Investigation Program: OCC/Tierra Solutions conducted a remedial investigation of the LPR, between approximately RM1 – RM6, under USEPA oversight. Sediment physical parameters, including grainsize distributions and contaminant concentration in the river sediments, were measured and used to develop model initial conditions.

- 2005 Geophysical and side scan sonar survey: A side scan sonar survey sponsored by USACE was conducted in 2005 between RM0 and RM14 to characterize the sediment surface in the LPR. This survey involved the use of a geophysical acoustic surveying technique capable of discerning sediment classes by acoustic reflectivity. The interpretation of the acoustic reflectivity was then calibrated by the collection of discrete surface samples throughout the LPR. Grain-size distribution was also analyzed, and used to describe the bed composition.

- 2005 and 2007 Newark Bay Phase I and Phase II Studies: Tierra Solutions conducted sampling in Newark Bay as part of the Newark Bay Study Area RI, under USEPA oversight. Grainsize, organic carbon content and contaminant concentrations were measured and used for the sediment transport, organic carbon, and contaminant fate and transport modeling.

- 2005 Sedflume and Gust microcosm study: As part of the 17-mile LPRSA RI/FS, Sedflume erosion testing was conducted by USACE personnel from the Engineer Research and Development Center (ERDC). Erosion measurements were made on 28 cores collected from 14 locations in the LPR. The Gust microcosm was used by Chesapeake Biogeochemical Associates to measure erosion rates of very near surface sediment. Both data sets were used in the evaluation of erosion properties specified in the sediment transport model.

- 2008 Consolidation testing: As part of the 17-mile LPRSA RI/FS, Sea Engineering performed Sedflume erosion measurements on four cores created

with sediment from a depositional area at RM2.2, which were allowed to consolidate for 1, 7, 17, and 28 days. This testing was conducted to obtain site-specific information of the effect of consolidation on erosion properties.

- Water Column Monitoring:
  - 2000-2002 Rutgers University: Acoustic-Doppler current profiler (ADCP) and acoustic backscatter (ABS) measurements were obtained by Dr. Robert Chant during six deployments in the Kill van Kull (KVK) and two deployments in the Arthur Kill (AK). These data were used to develop boundary conditions for the sediment transport model.

  - 2004-2005 Rutgers University: Dr. Chant conducted a field program involving moored instrumentation and shipboard surveys. The moored instrumentation consisted of one ADCP, with surface and bottom conductivity and temperature (CT) recorders in the Harrison Reach and surface and bottom CT units at four additional stations. The moored instrumentation deployments covered approximately 8 months during the period from September 2004 through October 2005. Twelve shipboard surveys included vertical casts recording CT, density and optical backscattering (OBS) along a transect from Newark Bay to the upstream end of the salt intrusion.

  - 2008-2009 Rutgers and U. Delaware (UDEL): Dr. Chant deployed moored ADCPs, surface and bottom CT units and near-bottom OBS sensors at five locations (Kill van Kull, Arthur Kill, Newark Bay and near the mouths of the LPR and Hackensack Rivers). Data were recorded for 10 months during a 12 month period. These data were used for model calibration. The study included a single beam bathymetry survey of Newark Bay conducted by Dr. Christopher Sommerfield's group at UDEL, which was used for describing bathymetry during the harbor deepening project. The study also included sediment grab samples and coring, but those data were not available at the time of model setup for the FFS project.

- 2009 Tierra Solutions hydrographic program: As part of the planning for Phase 1 of the Tierra Removal, Tierra Solutions retained Ocean Surveys, Inc. to conduct a hydrographic survey. The purpose of this survey was to obtain data to support a modeling evaluation of the effect of construction of a sheetpile enclosure around the sediment removal area. The survey was conducted over roughly a five-week period and included deployment of ADCP, temperature, conductivity, salinity, and turbidity data recorders at three locations. The program also included vessel-mounted ADCPs and vertical casts recording conductivity, salinity, temperature, pH, and turbidity at three locations across the river at each mooring location.

- 2009 and 2010 CPG Physical Water Column Monitoring (PWCM) program: Between mid-October and mid-December 2009, the CPG's program included moored instrumentation at five locations in the LPR (RM13.5, 10.2, 6.7, 4.3, and 1.4) including ADCPs, and surface and bottom sensors to record conductivity, temperature, depth, and OBS. In addition, an OBS sensor was deployed upstream of Dundee Dam. In the spring of 2010, the program included the same plan for the LPR, and was expanded to include two sampling locations in Newark Bay, one each in the Kill van Kull and Arthur Kill, and one near the mouth of the Hackensack River. A wave gauge was also installed in Newark Bay. The fall 2009 and spring 2010 PWCM data were used extensively in the sediment transport model calibration.

- March 2010 high flow sampling: Following an intense rain storm in March 2010 flows over Dundee Dam exceeded 450 cms (~15,900 cfs), a flow with a recurrence interval of more than 25 years. Dr. Chant mobilized to measure vertical profiles of salinity, temperature and OBS data on three transects between Newark Bay and approximately RM5.5 of the LPR. These measurements provide an indication of conditions in the lower portion of the

LPR under high flow conditions, and were an important data set used in the sediment transport model calibration.

- 2008 CPG Low Resolution Coring: In 2008, a comprehensive low resolution sediment coring program was conducted (AECOM, 2010a), which included the collection of 109 sediment cores along the LPR from RM0 to RM17.4 (Dundee Dam), with additional sampling locations in the tributaries and above Dundee Dam. Cores were advanced to refusal or presence of the red sand/clay layer. A co-located sediment grab sample was also collected at each coring location for the analysis of Be-7 in the top 1-inch of sediments. Sediment samples were analyzed for a suite of chemical parameters, including PCDD/F[1] congeners, PCB Aroclors and congeners, PAH[2] compounds, pesticides, SVOC[3], VOC[4], herbicides, metals including mercury, methylmercury, TPH[5], TOC[6], grainsize, and other general chemistry parameters. The grainsize data were used in developing initial conditions for the sediment transport bed, because these data filled spatial gaps in coverage, especially upstream of RM7, which was the limit of the 1995 Tierra RI data. Sediment carbon and contaminant concentrations from this data set were used in the carbon and contaminant fate modeling.

1.4 MODELING APPROACH

The sediment transport model ECOMSED, with the bed model, SEDZLJS (HydroQual, 2007a) was used for .the modeling analyses. This model is not a morphological model (e.g. planform migration is not represented); however, the feedback from changes in bed elevations on hydrodynamic transport was accounted for by modifying the model

[1] PCDD/F is an acronym for Polychlorinated Dibenzodioxins and Polychlorinated Dibenzofurans

[2] PAH is an acronym for Polycyclic Aromatic Hydrocarbon

[3] SVOC is an acronym for semi-volatile organic compounds

[4] VOC is an acronym for volatile organic compounds

[5] TPH is an acronym for total petroleum hydrocarbons

[6] TOC is an acronym for total organic carbon

bathymetry each integration time step. The spatial domain extends from the upstream freshwater inputs at Dundee Dam and Oradell Dam on the Passaic and Hackensack Rivers, respectively, to the downstream tidal boundaries at the eastern end of the Kill Van Kull and the southern end of the Arthur Kill (Figure 1-1).

The spatial resolution of the model grid was developed to balance the ability to resolve sediment transport processes, and still perform long simulations to drive the contaminant fate and transport models and support the evaluation of risk reduction. The grid resolution was evaluated with a grid convergence test (HydroQual, 2008), in which comparisons were made for salinity, velocity, bottom shear stress, and flushing time computed with the final grid and a grid with resolution increased by a factor of four. Comparisons to data showed only minor improvements in performance (and equivalent performance in some cases) at a cost of a factor of eight increase in computational time associated with the higher resolution grid.

The model was used to simulate the period of water years[7] 1996 through 2012. Model results were compared to estimates of water column suspended-solids data (derived from acoustic backscattering) and changes in bathymetry noted between single-beam and multibeam bathymetry surveys. Hydrodynamic boundary conditions (freshwater flow and tidal elevations) for the period 1995 through 2012 were based on results obtained from a larger-domain hydrodynamic model (HydroQual, 2008). Those results were mapped onto the Newark Bay grid that extends to the ends of the Kills. Upstream boundary conditions were developed following an approach used in the Contamination Assessment and Reduction Project (CARP[8]) (HydroQual, 2007b). Downstream boundary conditions for

[7] "Water year" is a term used by the U.S.Geological Survey and is defined as a 12-month period from October 1 through September 30, of the following year. The water year is designated by the calendar year in which it ends (e.g. water year 2010 begins October 1, 2009 and ends September 30, 2010)

[8] CARP was a comprehensive sampling and modeling program sponsored by the Port Authority of New York-New Jersey (and other federal, state and local agencies, as well as non-governmental groups) to better understand the nature and extent of sediment contamination in the New York-New Jersey Harbor Estuary.

solids at the eastern end of the Kill Van Kull and the southern end of the Arthur Kill were developed from data collected in multiple deployments by Dr. Robert Chant and Dr. Christopher Sommerfield (Sommerfield and Chant, 2010).

Sediment data were analyzed to develop an understanding of the spatial distribution of bed properties and to assign representative sediment size classes throughout the model domain. Sedflume data were used to describe erosion properties of the sediment bed (see Section 3.2.3). (See Table 1-1 for information about these various data collection programs.)

Model calibration focused on two different time scales: short-term variations in water column suspended solids and long-term (i.e. annual or multi-year) net sediment accumulation/loss. The short-term comparisons of model results to water column suspended solids rely on data collected in the CPG's PWCM program and data collected during a particularly high river-flow condition (AECOM, 2010b). Longer-term net sediment-transport behavior was evaluated by comparing simulated long-term net sediment accumulation/loss to patterns derived from a series of single-beam and multibeam bathymetric surveys.

In February 2013, five peer reviewers, chosen as experts in their fields, were charged with determining whether the LPR-specific modifications to the CARP model have produced a tool that is adequate for USEPA to use in the FFS to compare the relative effects that implementation of each of the four remedial alternatives would have on future surface sediment concentrations. The peer reviewers were tasked with reviewing a draft of this report (Appendix BII) and Appendix BIII. The review was structured as a "letter peer review" in accordance with the 2006 USEPA Peer Review Handbook (EPA/100/B-06/002), which means that the panel members performed their reviews and provided their written comments separately, without physically convening. The key issues raised by the peer reviewers that resulted in changes to the sediment transport model included the model's ability to compute sediment accumulation (infilling), the need to simulate a 100-year flow event and adding sensitivity analyses for the magnitude of the upstream

suspended solids (among others). More information about the peer review process, the comments received and how those comments were addressed is provided in a peer review report dated September 2013 (HDR|HQI, 2013).

Table 1-1. Data Sets used in Sediment Transport Modeling

Investigation	Year	Study Name	Surveying Agency	Surveying Company	Survey Extent (RM)	Governing Work Plan
Sediment	1995	Passaic 1995 RI Sampling Program	USEPA	Tierra	RM1 to RM7	Tierra Solutions, Inc. (Tierra). January 1995.
	2005	Aqua Survey Inc. (ASI) Geophysical and Side Scan Sonar Survey	NJDOT-USACE	Aqua Survey Inc.	RM0 to RM17	Malcolm Pirnie, Inc. August 2005 and January 2006
	2005	2005 Sedflume Testing	USEPA	USACE	RM0 to RM15	Malcolm Pirnie, Inc. August 2005 and January 2006
	2005	2005 Gust Microcosm Testing	USEPA	Chesapeake Biogeochemical Associates	RM0 to RM15	Malcolm Pirnie, Inc. August 2005 and January 2006
	2005	Tierra Newark Bay Study Phase I	USEPA	Tierra	Newark Bay	Tierra, 2005
	2007	Tierra Newark Bay Study Phase II	USEPA	Tierra	Newark Bay	Tierra, 2007
	2008	Sedflume Consolidation Testing	USEPA	Sea Engineering	RM2.2	Malcolm Pirnie, Inc. August 2005 and January 2006
	2008	2008 CPG Low Resolution Sediment Coring	USEPA	CPG	RM0 to RM17	ENSR, 2008

Table 1-1. Data Sets used in Sediment Transport Modeling (Continued)

Investigation	Year	Study Name	Surveying Agency	Surveying Company	Survey Extent (RM)	Governing Work Plan
Water Column	2000 - 2002	December 2000 – May 2002 Rutgers University Kill van Kull and Arthur Kill Deployments	Port Authority of NY & NJ	Rutgers University	Kill van Kull and Arthur Kill	Not Available
	Aug - Oct 2004	August to October 2004 Rutgers University Survey First Deployment	NJDOT-USACE	Rutgers University	RM0 to RM6	Malcolm Pirnie, Inc., 2005
	Nov - 2004 to Jan – 2005	November 2004 to January 2005 Rutgers University Survey Second Deployment	NJDOT-USACE	Rutgers University	RM0 to RM6	
	Jul - Sep 2005	July to September 2005 Rutgers University Survey Third Deployment	NJDOT-USACE	Rutgers University	RM0 to RM6	
	2008-2009	Rutgers University and University of Delaware ADCPs Study	Rutgers University	Rutgers University and University of Delaware	Unknown	Not Available
	2009	Tierra ADCP Moorings Study	USEPA	Tierra	RMs 2.1, 3.2 and 4.1	Not Available
	2009-2010	CPG Physical Water Column Monitoring Program	USEPA	CPG	RMs 1.4, 4.2, 6.7, 10.2 and 13.5	AECOM, 2010b
	2010	2009-2010 CPG Physical Water Column Monitoring	USEPA	CPG	Newark Bay, Kill van Kull, Arthur Kill, Hackensack River Mouth	AECOM, 2010b
	2010	CPG High-Flow Water Column Suspended Solids Sampling	USEPA	CPG	LPR	AECOM, 2010b

Table 1-1. Data Sets used in Sediment Transport Modeling (Continued)

Investigation	Year	Study Name	Surveying Agency	Surveying Company	Survey Extent (RM)	Governing Work Plan
Bathymetry	Mar-1995	March/April 1995 Ocean Surveys, Inc. for Tierra	USEPA	Tierra	RM0.87 to RM6.97	Not Applicable
	Nov-2004	November 2004 Rogers Surveying, Inc. for USACE	USACE	Rogers Surveying, Inc.	RM-0.54 to RM17.42	Not Applicable
	Sep-2007	CPG - Multi-Beam (MB) and Single-Beam (SB) Bathymetry	USEPA	CPG	RM-0.50 to RM14.45 (MB) RM0.5 to RM8.21 and RM14.38 to RM16.54 (SB)	Not Applicable
	Jun-2010	CPG - Multi-Beam Bathymetry	USEPA	CPG	RM-0.5 to RM14.27	Not Applicable
	Oct-2011	CPG – Multi-Beam Bathymetry	USEPA	CPG	RM-0.5 to RM14.27	Not Applicable

[a]: The original vertical datum for surveys was MLW as defined by the USACE. The transect density for the surveys was approximately 52 transects per mile.

2 MODELING FRAMEWORK

2.1 ECOMSED – HYDRODYNAMIC AND SEDIMENT TRANSPORT MODEL

The ECOM module of ECOMSED is a three-dimensional, time-dependent hydrodynamic model based on the work of Blumberg and Mellor (1980, 1987), and has a long history of successful applications to oceanic, coastal and estuarine waters. The model (HydroQual, 2007a) incorporates the second order turbulence closure model of Mellor and Yamada (1982) with the stability functions of Galperin et al. (1988) to provide a realistic parameterization of vertical mixing processes in density-stratified waters. The model accommodates realistic coastline geometry and bottom topography through use of an orthogonal curvilinear horizontal coordinate system and bottom-following sigma layers in the vertical. Prognostic variables include free surface elevation, the three components of velocity, temperature, salinity, turbulence kinetic energy, and turbulence macroscale. The momentum equations are nonlinear and incorporate a variable Coriolis parameter. Prognostic equations governing the thermodynamic quantities, temperature, and salinity account for water mass variations brought about by highly time-dependent coastal upwelling/downwelling processes as well as horizontal advective processes. Barotropic and internal motions are calculated efficiently by use of a mode splitting technique whereby the volume transport and vertical velocity shear are solved separately. Other computed quantities include density, vertical eddy viscosity, vertical eddy diffusivity, and bottom stress.

The ECOMSED model system allows for calculation of additional bottom stresses due to wind-waves, but this capability is not invoked for the LPR because the system is highly fetch-limited in the domain of interest. The Newark Bay section of the model domain can be wave-impacted at times; however, based on a sensitivity analysis it was concluded that the added complication of specifying wave regimes and scenarios and calculating wave-current boundary shear stresses was not deemed warranted. The sensitivity simulation with wind-waves showed a change in the gross solids flux from Newark Bay

to the LPR of approximately 5% and no change in the net solids flux compared to a simulation without wind-waves generated shear stresses.

Newark Bay sediments can also be affected by ship-driven resuspension, which is a process not explicitly included in ECOM-SED. Ship traffic information from Newark Bay clearly documents that a substantial amount of traffic enters from New York-New Jersey Harbor and travels northward in the Bay. Only a fraction sail north to Port Newark Channel and a much smaller fraction sails north of Port Newark Channel. Based on this information, it was concluded that ship-driven resuspension is a process that may need to be represented for Newark Bay. Given the added complexity of incorporating ship effects on resuspension into the model, and the limited ship traffic in Northern Newark Bay and the LPR, it was concluded that ship-driven resuspension was not was not necessary for the FFS.

2.2 SEDZLJS – SEDIMENT BED SUBMODEL

The SED module of ECOMSED is HydroQual's state-of-the-art three-dimensional sediment transport model. It realistically simulates cohesive and non-cohesive sediments in a variety of aquatic systems (e.g., lakes, rivers, estuaries, bays and coastal waters). The SED module is configured to run in conjunction with the hydrodynamic model and a wave model (if waves are included). SED uses the same numerical grid, structure and computational framework as the hydrodynamic model. Sediment dynamics inherent in the model include sediment resuspension, transport, settling, deposition, and consolidation of multiple classes of cohesive and non-cohesive sediments.

There are two different sediment transport modeling frameworks incorporated in ECOMSED. In the mid-1990s, concepts of cohesive sediment resuspension, settling and consolidation (Lick et al., 1994) were incorporated within the ECOM modeling framework to create ECOMSED (SEDZL). Over a period of several years, significant modifications were made to ECOMSED (HydroQual, 2007a) to include generalized open boundary conditions, tracers, better bottom shear stresses through a submodel for bottom

boundary layer physics, surface wind-wave models, non-cohesive sediment transport, and dissolved and sediment-bound tracer capabilities. ECOMSED has been used in a number of sediment transport studies, including: Pawtuxet River in Rhode Island (Ziegler and Nisbet, 1994), Watts Bar Reservoir in Tennessee (Ziegler and Nisbet, 1995), Lavaca Bay in Texas (HydroQual, 1998), Tannery Bay in Michigan (Cannelton Industries, 1998), and Green Bay in Wisconsin (Shrestha et al., 2000). In 2007, the peer-reviewed sediment bed model SEDZLJ (Jones and Lick, 2001) was incorporated into HydroQual's hydrodynamic model framework, ECOMSED. SEDZLJ provides the option of using gross erosion rates measured from a Sedflume study (McNeil et al., 1996; Jepsen et al., 1997; Roberts et al., 1998) performed in the water body of interest to estimate erosion rates of fine-grained sediment beds, in combination with erosion rates for non-cohesive sand-sized sediments obtained from the literature (Roberts et al., 1998), as the basis to compute sediment transport. The incorporation of SEDZLJ into ECOMSED was performed by Dr. Craig Jones (developer of the SEDZLJ computer code) of Sea Engineering, Inc. (SEI). Dr. Jones also added Sanford's (2008) consolidation routine for deposited sediment layers, which is described in more detail below. The resulting computer code was peer-reviewed by Dr. Earl Hayter of the USEPA (at the time of the review, now with USACE-ERDC) and was applied for the capping/armoring analysis of the LPR (Appendix B, Section I).

The integration of the SEDZLJ bed model and Sanford's consolidation model into ECOMSED and other related code modifications provided six primary benefits in the upgraded model referred to as ECOM-SEDZLJS:

1. Computation of erosion fluxes as a function of measured erosion rates;
2. Division of total erosion fluxes into bedload and suspended load components;
3. Simulation of bedload transport;
4. Computation of deposition fluxes as a function of defined or calculated critical values for each particle class size
5. Simulation of a user-defined number of particle size classes; and
6. Flexible simulation of consolidation effects in deposited cohesive sediment layers.

These code modifications substantially improve the ability of ECOMSED to simulate the expected differential transport of sediments comprised of particles with a continuum of grainsizes and subject to significant bedload transport. The presence of sand fractions in sediments throughout the LPR, which are especially significant above RM8.3, made this particularly important in the present case.

2.3 EROSION

The governing equations for erosion in SEDZLJ (Jones and Lick, 2001) are expressions that interpolate between measured/tabulated erosion rates (cm/s) as functions of applied boundary stress (dy/cm^2) and depth (cm) in the sediment bed:

$$E(\tau_b) = \left(\frac{\tau_{m+1} - \tau_b}{\tau_{m+1} - \tau_m}\right) E_m + \left(\frac{\tau_b - \tau_m}{\tau_{m+1} - \tau_m}\right) E_{m+1} \qquad (2\text{-}1)$$

$$In[E(Th)] = \left(\frac{Th_0 - Th}{Th_0}\right) In[E^{L+1}] + \left(\frac{Th}{Th_0}\right) In[E^{L}] \qquad (2\text{-}2)$$

where: $E(\tau_b)$ = erosion rate as a function of shear stress; τ_b = bottom skin-friction shear stress (see below); τ_m = tabulated erosive shear stress less than τ_b, and E_m = tabulated erosion rate at that shear stress; τ_{m+1} = tabulated erosive shear stress greater than τ_b, and E_{m+1} = tabulated erosion rate at that shear stress; $E(Th)$ = erosion rate as a function of depth in the sediment bed; Th = sediment layer thickness; Th_0 = initial sediment layer thickness; and the superscripts L and $L+1$ denote depths in the sediment profile at the upper and low limits of the eroding sediment layer. Equations (2-1) and (2-2) can be combined to express the erosion rate as a function of both shear stress and depth in the sediment. The onset of erosion occurs at the critical shear stress for erosion, τ_{ce}, which is

defined as the shear stress at which erosion is initiated at a rate of 10^{-4} cm/s ($3.28E^{-6}$ ft/s) (operational definition from Sedflume).

2.4 NON-COHESIVE BEDLOAD VS. SUSPENDED LOAD FRACTIONATION

When the shear stress acting on grains comprising a non-cohesive bed exceeds the critical shear stress for a given grainsize, particles may be transported as bedload (in a thin layer in contact with the bed) or as suspended load (fully entrained in the water column away from the bed). The governing equations used to fractionate eroded sediments into bedload and suspended load are:

$$f_{SL} = \begin{cases} 0 & for\ \tau_b \le \tau_{cs} \\ \dfrac{\ln(u_* / w_s) - \ln(\sqrt{\tau_{cs} / \rho_w} / w_s)}{\ln(4) - 1n(\sqrt{\tau_{cs} / \rho_w} / w_s)} & for\ \tau_b > \tau_{cs}\ and\ \dfrac{u_*}{w_s} < 4 \\ 1 & for\ \tau_b > \tau_{cs}\ and\ \dfrac{u_*}{w_s} \ge 4 \end{cases} \qquad (2\text{-}3)$$

$$\tau_{cs} = \begin{cases} \rho_w \left(\dfrac{4w_s}{d_*} \right)^2 & for\ d \le 400\,\mu m \\ \rho_w \left(0.4 w_s \right)^2 & for\ d > 400\,\mu m \end{cases} \qquad (2\text{-}4)$$

where: τ_{cs} = critical shear stress for transport as suspended load; w_s = particle fall velocity; d_* = particle dimensionless diameter = $d\left[(\rho_s - 1)g / \nu^2\right]^{1/3}$; d = particle diameter; ρ_s = particle density; ρ_w is the water density; f_{SL} = fraction of the total amount eroded that is transported as suspended load; and $u_* = \sqrt{\tau_b / \rho_w}$ is the shear velocity. The fraction transported as bedload = (1-f_{SL}). Equations (2-3) and (2-4) can be used, in conjunction with the particle grainsize distribution and critical shear stress for erosion, to evaluate the erosion fluxes of sediment by grainsize that are transported by bedload and suspended load as a function of the bottom shear stress.

All cohesive sediments are assumed to be transported as suspended load.

2.5 CALCULATION OF THE SKIN FRICTION SHEAR STRESS

The bottom shear stress acting on the bed (i.e. the total bed shear stress) is a function of the total hydrodynamic roughness and can be expressed in terms of two separate components: (1) form drag and (2) grain stress (i.e. skin friction). Individual grains on the surface of the sediment bed are subjected only to the skin friction component of the total bed shear stress. The total bed shear stress is computed from the near-bed hydrodynamic velocities according to the "log law" velocity profile:

$$u(z_b) = \frac{u_{*T}}{\kappa} \ln\left(\frac{z_b}{z_{0T}}\right) \tag{2-5}$$

Where $u(z_b)$ is the horizontal velocity in the first sigma level above the bottom, with height z_b at the mid-point of that sigma level, u_{*T} is the total shear (friction) velocity, $\kappa = 0.4$ is von Karman's constant, and z_{0T} is the total bottom roughness parameter. Equation (2-5) leads to

$$\tau_T = \rho_w {u_{*T}}^2 = \rho_w C_{dT} u(z_b)^2 \tag{2-6}$$

Where the total drag coefficient C_{dT} is given by

$$C_{dT} = \left(\frac{\kappa}{\ln\frac{z_b}{z_{0T}}}\right)^2 \tag{2-7}$$

ECOM-SEDZLJS hydrodynamic calculations use spatially and temporally constant total bottom roughness parameter to generate time and space varying total stress distributions based on changing water depth and bottom layer velocity[9]. The fraction of the total stress responsible for sediment mobilization (the "grain stress" or "skin friction" fraction) must then be calculated in the sediment transport model at each cell and time step. This is done in several steps. An initial estimate of the grain stress shear velocity u_{*S}' is calculated from (e.g., Grant and Madsen, 1982; Glenn and Grant, 1987):

$$u_{*S}' = u_{*T}\left(\frac{\ln\frac{z_b}{z_{0T}}}{\ln\frac{z_b}{z_{0S}'}}\right) \tag{2-8}$$

Where Z_{0S} = D_{50}/15 is the grain roughness parameter based on the median sediment particle diameter. Equation (2-8) is valid for fully rough turbulent boundary layers, which is a very good approximation for large grainsizes and high values of u_{*S}. In some cases, especially over cohesive sediments and for moderate flows, Equation (2-8) underestimates the true skin friction shear velocity because the boundary layer is actually smoothed turbulent or transitional. The model accounts for this possibility by re-estimating a new grain roughness parameter z_{0S} using the transitional boundary layer formula of Winterwerp and van Kesteren (2004), Table 2.2:

$$z_{0S} = \frac{0.11\upsilon}{u_{*S}'} + z_{0S}' \tag{2-9}$$

[9] In the LPR model, a spatially and temporally constant value of Z_{0T}= 1 mm was set during calibration of the hydrodynamic model. This value, which corresponds to a physical bottom roughness of k_{bT} = 30 Z_{0T} = 30 mm = ~1.2 in. and C_{dT} = 0.0034 referenced to Z_b = 1 m above the bottom, was found to give good agreement between observed and predicted surface elevations and currents.

Equation (2-9) is used to estimate the corrected equivalent grain roughness parameter over the entire range of boundary layer turbulence conditions, taking its initial estimate of u_{*S}' from Equation (2-8). A new estimate of u_{*S} is then calculated from

$$u_{*S} = u_{*T}\left(\frac{\ln\frac{z_b}{z_{0T}}}{\ln\frac{z_b}{z_{0S}}}\right) \tag{2-10}$$

The final step in estimating the grain stress fraction is to account for the formation and decay of bedforms in non-cohesive model cells. In the real world, the formation and decay of bedforms results in dynamically changing total bottom roughness z_{0T}, which can vary both spatially and temporally. The hydrodynamic feedback from dynamically changing total bottom roughness can be accounted for directly in model systems where the sediment transport and hydrodynamic calculations are two-way coupled (e.g., Warner et al., 2008). The one-way coupling (from hydrodynamics to sediment transport) of ECOM-SEDZLJS does not allow for hydrodynamic feedback on the total bed roughness, instead keeping the total roughness constant everywhere and at all times. However, the model can account for the changing grain stress fraction that accompanies changing bedform scales, even if it cannot account for the changing bedform scales. In other words, increasing bedform roughness results in a greater proportion of the total stress going into the form drag of the bedforms and a smaller proportion into the grain roughness. Conversely, decreasing bedform roughness will result in a smaller proportion of the total stress going into the form drag of the bedforms and a larger proportion into the grain roughness.

The revised grain stress fraction is calculated by reference to Table 5.1 of van Rijn (1993), reproduced in Figure 2-1. This table classifies bedforms according to a nondimensional transport parameter *T* and nondimensional particle size d_{*50} (defined above). The nondimensional transport parameter is given by

$$T = \frac{\tau_s - \tau_{ce}}{\tau_{ce}} \tag{2-11}$$

where $\tau_S = \rho_w u_{*S}{}^2$ is the skin friction calculated using Equation (2-10) and τ_{ce} was defined above. The model implements an estimate of bedform roughness z_{0B} as defined by Warner et al. (2008)

$$z_{0B} = \frac{8}{30}\frac{\Delta^2}{\lambda} \tag{2-12}$$

The bedform height Δ and bedform length λ are given in van Rijn (1993) for each of the bedform types listed in Figure 2-1, assuming that all of the bedforms in the LPR remain in the Lower Transport Regime (i.e., sub-critical flow). Substituting van Rijn's expressions for bedform dimensions into Equation (2-12) yields

$$z_{0B} = 3.81 d_{50} \text{ for mini-ripples} \tag{2-13}$$

$$z_{0B} = 2.13\times10^{-4} h\left[(1-e^{-0.1T})(10-T)\right]^2 \text{ for mega-ripples} \tag{2-14}$$

$$z_{0B} = 4.25\times10^{-4} h\left[\left(\frac{d_{50}}{h}\right)^{0.3}(1-e^{-0.5T})(25-T)\right]^2 \text{ for dunes} \tag{2-15}$$

where h is the water depth. In the "mega-ripples and dunes" regime, the roughness used is a weighted combination of mega-ripples and dunes ranging from all mega-ripples at T=3 to all dunes at T=10. Transitions between regimes are smoothed to prevent sudden jumps across regime boundaries. An example calculation of the expected physical roughness height $k_b = 30\ Z_{0B}$ covering a range of non-cohesive grainsizes and grain stresses typical of the LPR sediment transport model, with h = 5 m (16.4 ft), is shown in

Figure 2-2. The primary purpose of this exercise is to prevent unrealistically large grain stress estimates under conditions in which large bedforms would be expected. Thus, if k_b < 30 mm, k_b =30 mm (1.2 inch), which corresponds to keeping the original z_{0T} from the hydrodynamic model. In other words, if the predicted bedform scales result in a bottom roughness that is less than that input from the hydrodynamic model, then that input value is kept and the grain stress correction stops at Equation (2-10).

Finally, under large bedform conditions a revised estimate of the grain stress fraction is calculated as

$$f_g = \left(\frac{u_{*SB}}{u_{*T}} \right)^2 = \left(\frac{\ln \frac{z_b}{z_{0B}}}{\ln \frac{z_b}{z_{0S}}} \right)^2 \qquad (2\text{-}16)$$

where u_{*SB} is the skin friction shear velocity in the presence of bedforms. The net result of all of these calculations is a significant decrease (up to a factor of 3) in grain stress compared to the square of Equation (2-8) for many active sand transport conditions encountered in the LPR, as shown in Figure 2-3 for the same conditions as in Figure 2-2. Implementing this formulation significantly reduced excess erosion of the sandy regions of the upper LPR during storms, while predicting bedforms of approximately the same size as those observed in a multibeam survey of the upper LPR following a flood.

The Little and Mayer (1972) data set provides a record of bed coarsening in a flume experiment, and was used as a validation data set for SEDZLJ (James et al., 2010). As part of the incorporation of SEDZLJ into ECOMSED, SEI and HydroQual applied the ECOMSED implementation of SEDZLJ to the Little and Mayer (1972) experimental data set. This test reproduced the behavior of the original validated SEDZLJ (Appendix BI).

2.6 BED CONSOLIDATION

Sanford (2008) outlines in detail the overall theory behind the consolidation model implemented here. As cohesive sediments deposit or erode the density of the sediment bed changes in response to the addition or reduction of overlying sediment. The consolidation model reproduces the measured effects of changes in sediment bed properties at any point in the sediments as a function of overlying bed mass. Sanford (2008) also generally included the effects of bioturbation, which are not implemented in this version of ECOMSED.

The basic premise of Sanford's model was to reproduce changes in solids volume concentration ϕ_s and critical shear stress for erosion (τ_{ce}) with depth due to changes in sediment bed structure. The consolidation model implemented in ECOM-SEDZLJS computes the equilibrium profile of bulk density ρ_b (g/cm^3) instead of ϕ_s. Since ρ_b varies as a linear function of ϕ_s the overall mechanistic description remains unchanged from that described in Sanford (2008). The parameter of interest, ρ_b, is defined by an equilibrium profile which is generally described by the equation:

$$\rho_{beq} = \rho_{b\infty} - \left(\rho_{b\infty} - \rho_{b0}\right)\exp(-cm) \tag{2-17}$$

where $\rho_{b\infty}$ is the ultimate equilibrium value at depth, ρ_{b0} is the equilibrium value at the sediment-water interface, *m* is the mass of the overlying sediment bed (can be converted to *z* with a density profile), and *c* scales the consolidation depth. All three of these parameters are determined empirically from LPR-specific data (see subsection 3.2.7.2 for LPR data analysis), based on laboratory consolidation experiments. The equilibrium profile is defined relative to the instantaneous sediment-water interface, so it moves with changes in the sediment bed height.

Once a sediment specific equilibrium profile has been determined, it is applied to deposited layers of the sediment bed. At any point in time (*t*) and bed mass position (*m*), the instantaneous value of the bulk density is assumed to approach equilibrium in a first order manner.

$$\frac{\partial \rho_b}{\partial t} = r_c \left(\rho_{beq} - \rho_b\right) H\left(\rho_{beq} - \rho_b\right) - r_s \left(\rho_b - \rho_{beq}\right) H\left(\rho_b - \rho_{beq}\right) \qquad (2\text{-}18)$$

where *H* is the Heaviside step function $\left[H\left(\arg\right) = 1\right.$ when the argument is >0 and $\left.H\left(\arg\right) = 0 \text{ otherwise}\right]$, r_c (1/day) is the empirically determined first-order consolidation rate and r_s (1/day) is the empirically determined first-order swelling rate.

The model structure above is applied in ECOM-SEDZLJS to deposited sediments. Sediments below deposited layers are called the parent bed, and are assumed to retain field measured properties. The parent bed erosion rates are based on Sedflume measured erosion rates, which do not vary with time, even if a layer becomes closer to or farther from the surface due to net erosion or deposition. On the other hand, Sedflume measured erosion rates (E) in consolidation experiments (Roberts et al., 1998) have been most accurately described with a power law formulation that is a function of applied skin friction shear stress (τ_S) and bulk density:

$$E = A\tau_S{}^n \rho_b{}^m \qquad (2\text{-}19)$$

where *A*, *n*, and *m* are empirically determined coefficients. Because an erosion rate threshold of 0.0001 cm/s (3.28E-6 ft/s) is used in Sedflume to define the critical shear stress, it is a simple exercise to calculate critical shear stress for erosion (τ_{ce}) using the above equation with these empirically determined coefficients.

$$\tau_{ce} = \sqrt[n]{\frac{0.0001}{A\rho_b{}^m}} \qquad (2\text{-}20)$$

Equations (2-17) to (2-20) allow the critical shear stress and erosion rate for any layer in the deposited sediments to be readily calculated.

The above description is used for deposited beds in the cohesive size ranges. Sandy beds may also deposit. The bulk density of sands is assumed constant in the model at 1.92 g/cm^3 (62.43 lb/ft^3). The masses of sandy layers are still used mechanistically in Equation (2-17) to determine the equilibrium density of layers below the sand, since the weight of the sandy layers will result in a higher degree of consolidation. The erosion properties of deposited sandy layers are determined using the same formulation as that used for the sandy active layer in the SEDZLJ model (i.e. values are determined from Roberts et al. (1998) quartz data).

2.7 FLUFF AND TRANSITIONAL LAYERS

A new bed layering approach was added for the near-surface sediment to improve the representation of sediment that is resuspended and re-deposited on typical tidal cycles. This approach was introduced in the CPG's modeling effort (Moffat & Nichol, et. al., 2013) for the 17-mile LPRSA RI/FS and is referred to as the "fluff layer". The bed can now have an active layer at the surface, a fluff layer below the active layer, and a transitional layer below the fluff layer. Below the transitional layer are either depositional layers (containing sediment that deposited during the simulation) or the layers of the parent bed (the bed present at the start of the simulation). In this application, the fluff layer and transitional layers are assigned a thickness of 1 mm (0.04 inch) each. Sediment in the fluff layer is more easily eroded than sediment in the transitional layer, which is more easily eroded that the sediment in the deeper layers. Erosion from the fluff and transitional layers is calculated as a function of shear stress, without a density dependence.

Fluff and transitional layers are formed by deposition of solids from the water column, with the fluff layer filling first. If the thickness of each layer increases to its maximum thickness, additional deposition results in a transfer of sediment from the fluff layer through the transitional layer and into the depositional layers. The source of solids resuspended to the water column begins with the fluff layer, followed by the transitional layer, then the depositional layers, and finally the parent bed. If the applied grain-shear stress is high enough to erode some, but not all size classes present in the layer from which erosion is occurring (fluff, transitional, depositional or parent) sediment is moved to the active layer and erosion is limited to only size classes with a critical shear stress less than the applied grain-shear stress. This process results in coarsening of the surface sediment.

2.8 PARTICLE SETTLING

Settling of cohesive sediments in the water column is modeled as a function of suspended sediment concentration, approximating the effects of a combination of a background (or washload) concentration combined with tidally resuspended and deposited aggregates. Non-cohesive sediments, on the other hand, are assumed to settle discretely, without interaction with other particles.

Cohesive sediment settling is modeled by assuming (based on site-specific observations) that the single cohesive class used in the LPR version of ECOM-SEDZLJS actually consists of a combination of a very slowly settling background population of particles and a relatively rapidly settling population of bed aggregates or flocs that are resuspended and deposited on a tidal cycle basis. Time varying flocculation and floc break-up are not modeled explicitly in ECOM-SEDZLJS, although an empirical dependence on suspended sediment concentration is used. In the absence of direct measurements of suspended-particle settling characteristics for the LPR, a semi-empirical approach was adopted. A reasonable concentration-dependent functional form was developed and parameterized to optimize agreement with observed suspended-sediment profiles derived from acoustic backscatter data (see subsection 4.2).

Because the observations show a low background concentration that never seems to completely settle, as well as a slowly settling, well-mixed washload during periods of high river flow, a slowly settling particle population is assumed representing both disaggregated small flocs and river-borne new fine particles that have not yet flocculated. This population is assumed to settle with a weak dependence on concentration c that allows for the effects of hindered settling at very large concentrations (e.g., Winterwerp and van Kesteren 2004, p 135), according to:

$$w_f = \max\left[0.001, 0.2*(1-0.00004c)\right] \tag{2-21}$$

where w_f is settling velocity in mm/s and c is in mg/L. This settling velocity is essentially constant at 0.2 mm/s (7.87E-3 inch/s) over almost all of the relevant range of observed suspended sediment concentrations.

Observations during periods of tidal resuspension, on the other hand, show a population of cohesive particles (in addition to the above fine fraction) that are rapidly resuspended and deposited over just fractions of a tidal cycle. A functional form that gives good agreement with observed vertical profiles of suspended sediment under these conditions (assuming a quasi-steady Rouse profile of suspended solids at maximum tidal flow) for a variety of flows and total suspended loads is

$$w_a = \min\left[\frac{3c}{200}, 3\right] \tag{2-22}$$

where again w_a is in mm/s and c is in mg/L. This form and its parameters were obtained after much experimentation by fitting to site-specific data (estimates of suspended solids derived from acoustic backscatter data).

For the LPR model, the fraction of slowly settling particles *f* is assumed to vary in such a way that it dominates at very low concentrations, becomes very small in the range of tidal resuspension, and again dominates at storm event concentrations.

$$f = 0.99\exp(-0.2c) + \frac{0.01}{0.01 + 0.99\exp(-.003c)} \tag{2-23}$$

Equations (2-21), (2-22) and (2-23) are shown in the upper three panels of Figure 2-4. Parameter values were all based on analysis of LPR suspended sediment concentrations derived from acoustic backscatter data (Section 4.2).

The behavior described by Equation (2-23) is required because there is only one cohesive sediment class in the LPR implementation of SEDZLJS. The total cohesive sediment settling velocity, w_s, in mm/s is a concentration-weighted function given by

$$w_s = (1 - f)w_a + fw_f \tag{2-24}$$

which is shown in the bottom panel of Figure 2-4. Equation (2-24) is shown to give reasonable agreement to observations under a broad range of conditions (Section 3).

The settling velocity of the non-cohesive sand fractions (w_s) is specified as input to the model and is computed from particle diameter (d) using the formulation of Cheng (1997):

$$w_{s,i} = \frac{\nu}{d_i}\left[\left(25 + 1.2d_{*,i}^2\right)^{0.5} - 5\right]^{1.5} \tag{2-25}$$

where the subscript *i* refers to one of the sand fractions and ν is the kinematic viscosity. The dimensionless particle diameter, d_* is defined as

$$d_* = d\left[g\left(\gamma_s - 1\right)/\nu^2 \right]^{1/3} \tag{2-26}$$

Where g is gravitational acceleration and γ_s is sediment specific gravity (≈ 2.65 for quartz sand).

2.9 DEPOSITION

In this implementation of ECOM-SEDZLJS, sediment in active transport deposits to the sediment bed differently depending on whether it is cohesive or non-cohesive.

Cohesive sediments in suspension deposit to the sediment bed following the formulation of Krone (1962):

$$D = w_s c_b p_d, \text{ where}$$
$$p_d = \begin{cases} 1 - \dfrac{\tau_S}{\tau_d} & \text{for } \tau_S \le \tau_d \\ 0 & \text{for } \tau_S > \tau_d \end{cases} \tag{2-27}$$

Where p_d is the probability of deposition and τ_d is the critical shear stress for deposition. In this implementation, p_d is set to 1 for the cohesive solids class, which allows cohesive solids to deposit at all shear stress conditions.

For non-cohesive sediments, Gessler's (1967) formulation is used, in which the probability of deposition is described as a Gaussian distribution centered at a grain-size dependent critical shear stress:

$$D = w_s c_b p_d, \text{ where}$$
$$p_d = \frac{1}{\sqrt{2\pi}} \int_{-\infty}^{Y} e^{-0.5x^2} dx \tag{2-28}$$
$$Y = \frac{1}{\sigma}\left(\frac{\tau_d}{\tau_S} - 1 \right)$$

where σ (= 0.57) is Gessler's standard deviation for shear stress variation and x is a dummy variable. The critical shear stresses for deposition, τ_d, are equal to 2.8, 19.9, and 122.0 dy/cm^2 for particle diameters of 250, 1000, and 4100 μm, respectively (van Rijn, 1993).

3 MODEL INPUTS

The following sections describe inputs for the sediment transport component of the model. These include boundary conditions at the upstream freshwater boundaries, open-water tidal boundaries, loadings from stormwater and combined-sewer overflows, and sediment bed properties. Model inputs and setup for the hydrodynamic component are described separately (HydroQual, 2008).

3.1 BOUNDARY CONDITIONS

3.1.1 Freshwater Boundaries

Freshwater solids boundary conditions used in this modeling effort are based on relationships between suspended sediment loading and river flow developed as part of the CARP project (HydroQual, 2007b). Relationships for the Upper Passaic and the Saddle Rivers were reevaluated using mean flows that include flow records for the period after completion of the CARP analysis. The methodology used to develop relationships between suspended sediment loadings and river flow is based on the Normalized Sediment Loading analysis (HydroQual, 2007b), in which suspended sediment data are segregated into two subsets based on river flow conditions at the time of data collection. The boundary between the two flow regimes is defined by a flow equal to two times the annual average flow. The suspended sediment loading relationships were derived from log-log regressions of loading vs. flow corrected to eliminate the low-bias introduced by performing the regression of log-transformed values (Ferguson, 1986). The loading function for the Saddle River was used for the Second and Third Rivers and MacDonald Brook.

Suspended sediment data collected by the USGS from the Upper Passaic River at Little Falls and the Saddle River at Lodi are plotted vs. river flow on Figure 3-1. The two regression equations (higher and lower flow regimes) for the Upper Passaic River are forced to have a common value at a flow equal to two times the annual average flow. In

the case of the Saddle River, suspended-solids data were available for the lower flow conditions; however no data were available for the higher flow region. For the higher flow regime, the relationship used in CARP was used in this work. It is based on an empirical loading equation parameterized based on the annual average flow and the size of the drainage area.

Temporal plots of the flow, suspended-solids concentration and solids mass loading are presented on Figures 3-2 through 3-6 for the Passaic River, Saddle River, Third River, Second River, and Hackensack River, respectively. For water years 1996-2007, river flow inputs were specified as daily averages. In October 2007 flow boundary conditions were changed to hourly values because of the availability of hourly records from the USGS gage at Dundee Dam (gage #01389890).

3.1.2 Open-water Tidal Boundaries

Time varying concentrations for total suspended solids (TSS) at the Kill van Kull and Arthur Kill open boundaries were derived from analyses of data collected in two monitoring programs conducted by Dr. Robert Chant from Rutgers University. Both programs included ADCP and ABS measurements. The first program was conducted in 2000–2002 (Chant, 2005), and the second was conducted in 2008-2009 in collaboration with Dr. Christopher Sommerfield from the University of Delaware (Sommerfield and Chant, 2010). A finding of the research of Sommerfield and Chant (2010) was that deepening of the navigation channels in the Kills to accommodate larger draft vessels changed the magnitude of solids loading from the harbor to the Newark Bay system. Between 1885 and 2000, the shipping channels connecting Newark Bay, the Kull van Kull, and Arthur Kill were deepened from natural depths of approximately 12–20 ft to depths of 35–40 ft. The Kill van Kull and Newark Bay Channels were deepened further to depths of 40–45 ft by November 2004 as part of the NY-NJ Harbor Deepening Projects which is managed by the USACE New York District with a target depth of 45 ft in the Kills and Newark Bay area. Additional Harbor Deepening Projects started again around 2005, with a target depth of 50 ft; some parts of the Kills and Newark Bay areas

were deepened to 50 ft as of 2008. Deepening of the Kill van Kull and Newark Bay channels was completed in 2012. Therefore, data from the 2000-2002 and 2008-2009 programs were analyzed separately, and boundary condition relationships derived from the two data sets were applied to different time periods. TSS boundary conditions derived from the earlier data set were applied to the simulation of 1995 through 2004 and boundary conditions from 2005 through 2010 were based on the 2008-2009 data set.

3.1.2.1 2000-2002 Monitoring Data

Deployment locations are shown in Figures 3-7 and 3-8. TSS concentrations (mg/L) were estimated from ABS (dB) measurements, using the calibration relationship developed from site-specific TSS data (Chant, 2005).

$$\text{TSS(mg/L)} = \exp\left(-4.7 + 0.10252 \cdot ABS\right) \tag{3-1}$$

Particle size information was not available to describe the distribution of particle sizes for the TSS estimates. In the absence of additional information, it was assumed that all suspended solids entering the model domain through the open boundary were silt-sized particles.

It was anticipated *a priori* that measured TSS concentrations crossing the open boundary during portions of the tidal cycle with inflow to Newark Bay might differ fundamentally from measured TSS concentrations crossing the open boundary during outflow conditions, because the former will be influenced more strongly by processes occurring in the Hudson River and New York-New Jersey Harbor (for the Kill van Kull) or the Raritan River and Raritan Bay (for the Arthur Kill), while the latter will be influenced more strongly by processes occurring in the Lower Passaic and Hackensack Rivers and Newark Bay. Therefore, a protocol was developed to extract ADCP/ABS data for inflow conditions only to avoid potential data confounding with fundamentally different outflow conditions.

Current directions at the ADCP/ABS deployments sites were strongly rectified by the narrow channels of the Kill van Kull (KVK) and Arthur Kill (AK). Histograms of current direction (at 2º increments) were distinctly bimodal in individual ADCP vertical bins (e.g., Figure 3-9) for each ADCP deployment, making it possible to define a limiting range of current directions that encompassed approximately 95% of the ADCP/ABS data collected during inflow conditions only. Through this protocol, it was discovered that the bimodal histogram for current direction from the KVK3 ADCP deployment was shifted distinctly to the right by approximately 45º as compared to the other five KVK deployments. The reason for this shift could not be determined, but the KVK3 data was sufficiently anomalous that it was omitted from further analysis.

Current speed, current direction, and TSS estimates for the remaining five KVK deployments were all similar, despite the fact that two of the deployments were on the opposite side of the Kill van Kull channel from the other three deployments (Figure 3-7). Data from these five KVK deployments were pooled into a single data set for the Kill van Kull open boundary, and data from the two AK deployments were likewise pooled into a single data set for the Arthur Kill open boundary. Inflow current velocity and ABS/TSS measurements were recorded every 30 minutes at 0.5-m (1.64 ft) vertical intervals starting at the seabed. For each vertical interval, paired velocity-TSS measurements were extracted from the data record (Chant, 2005) aggregated into 5 cm/s (0.164 ft/s) bins (to eliminate effects of uneven numbers of data points in different velocity ranges), and the average TSS concentration of each bin was assigned to the median velocity of that bin. For example, at the 0.5-m vertical increment above the seabed for the pooled KVK data, there were 150 data records with inflow current speeds in the range of 0 cm/s to 5 cm/s. The corresponding 150 ABS measurements were converted to TSS estimates with Equation (3-1), and the average of those TSS estimates was paired with the median velocity of the bin (i.e. 2.5 cm/s or 0.082 ft/s) to provide a representative velocity-TSS data point. At the same 0.5-m vertical increment above the seabed for the pooled KVK data, there were 276 data records with inflow current speeds in the range of 5 cm/s to 10 cm/s (0.328 ft/s). The corresponding 276 ABS measurements were converted to TSS estimates, and the average of those TSS estimates was assigned to the median velocity of

the bin (i.e., 7.5 cm/s or 0.246 ft/s) to provide a second representative velocity-TSS data point. This procedure was repeated until all KVK data records at the 0.5-m vertical increment above the seabed were processed. The resulting paired velocity-TSS data points describe a representative relationship between current speed and TSS for the Kill van Kull open boundary at a height above the seabed of 0.5 m. A power function of the form

$$TSS(z) = a(z) + b(z)U(z)^C \quad (3\text{-}2)$$

was fit to the velocity-TSS pairs (e.g., Figure 3-10) to derive a parametric relationship for TSS concentration (mg/L) based on inflowing current velocity (U in cm/s), where a, b, and c are regression coefficients, and z is the height of the ABS bins above the seabed. Inflowing current velocities in the Kill van Kull were considerably faster than in the Arthur Kill, and regressions of estimated TSS concentration vs. current speed were reasonably robust throughout the water column. Regression coefficients and coefficients of determination for Equation (3-2) are listed in Table 3-1 for ABS vertical intervals at the Kill van Kull open boundary.

Table 3-1. Coefficients and Goodness of Fit Measures for TSS Regression Equation (3-2) for the Kill van Kull Open Boundary.

ABS BIN	Distance from Bottom (m)	Regression Coefficients			Coefficient of Determination (R^2)
		a	***b***	***c***	
1	0.5	14.8	2.45 E-04	2.74	0.91
2	1.0	15.1	6.16 E-06	3.32	0.85
3	1.5	12.0	4.05 E-02	1.32	0.90
4	2.0	9.53	2.51 E-01	0.952	0.98
5	2.5	10.5	5.29 E-02	1.29	0.93
6	3.0	10.5	1.68 E-02	1.53	0.91
7	3.5	10.9	3.21 E-03	1.85	0.89
8	4.0	9.46	1.20 E-02	1.55	0.82
9	4.5	8.86	1.42 E-02	1.49	0.94
10	5.0	9.08	2.81 E-03	1.81	0.84
11	5.5	7.50	1.99 E-02	1.38	0.92
12	6.0	7.15	1.54 E-02	1.42	0.93

Table 3-1. Coefficients and Goodness of Fit Measures for TSS Regression Equation (3-2) for the Kill van Kull Open Boundary.

ABS BIN	Distance from Bottom (m)	Regression Coefficients			Coefficient of Determination (R^2)
		a	***b***	***c***	
13	6.5	6.25	3.48 E-02	1.23	0.88
14	7.0	6.07	2.45 E-02	1.28	0.93
15	7.5	5.37	4.73 E-02	1.13	0.82
16	8.0	5.50	2.89 E-02	1.20	0.85
17	8.5	5.13	3.05 E-02	1.17	0.81
18	9.0	4.77	3.38 E-02	1.14	0.80
19	9.5	4.87	1.76 E-02	1.25	0.77
20	10.0	4.70	2.96 E-02	1.11	0.80
21	10.5	4.61	3.00 E-02	1.08	0.70
22	11.0	4.67	9.08 E-03	1.31	0.64
23	11.5	4.63	4.28 E-03	1.50	0.60

A related procedure was used to determine vertically variable relationships between TSS concentration and inflowing current speed at the Arthur Kill open boundary. For the Arthur Kill, regression correlations for Equation (3-2) were reasonably strong near the bottom, but estimated TSS concentrations were uncorrelated with inflowing current speed at and beyond about 7 m (~23 ft) above the bottom. To maintain a similar procedure over the entire water column, paired velocity-TSS measurements were extracted from the data record for each ABS sensor vertical interval, aggregated into 5 cm/s bins, and the average TSS concentration of each bin was assigned to the median velocity of that bin. For ABS sensor intervals less than 7 m above bottom, the resulting velocity-TSS pairs were fit to Equation (3-2), as was done for the Kill van Kull. However, for ABS sensor intervals greater than or equal to 7 m above bottom, the velocity-TSS pairs at each sensor interval were simply averaged for TSS concentration, since they were only weakly correlated or uncorrelated with inflowing current speed. At the Arthur Kill open boundary, regression coefficients and coefficients of determination for Equation (3-2) are listed in Table 3-2 for ABS sensor vertical intervals less than 7 m above the seabed. For ABS sensor vertical intervals greater than or equal to 7 m above bottom, Table 3-2 lists average inflowing TSS concentrations and standard deviations at each sensor height. Only data recorded during inflowing periods were used to develop boundary conditions.

For modeling purposes, estimated inflowing TSS concentrations at the open boundaries were determined using Equation (3-2) where applicable, with the velocity-TSS relationships from Tables 3-1 and 3-2 and inflowing current speeds extracted from the calibrated hydrodynamic model of the LPR/NB. The average values from Table 3-2 were used for the upper portion of the water column at the Arthur Kill boundary. The LPR/NB hydrodynamic model is comprised of ten vertical sigma layers, with each sigma layer representing ten percent of the water column depth. Water depth and, hence, sigma-layer thickness changes spatially with bathymetry and temporally due to tides and wind stress. Each sigma layer has an associated current speed representing the model-calculated current at the vertical midpoint of the layer. For each sigma layer, a TSS boundary condition was assigned based on model inflowing current speed and the velocity-TSS relationship from the closest matching ABS vertical interval. For example, if at time t the depth of the water column at the Kill van Kull open boundary was 16 m (52.5 ft), then the thickness of the lowermost sigma layer would be 1.6 m (5.25 ft), and the midpoint of the layer would be 0.8 m (2.625 ft) above the bottom. The inflowing current speed for that sigma layer would be extracted from the hydrodynamic model and would be applied to the velocity-TSS relationship for KVK ABS vertical bin 2 located at 1.0 m (3.28 ft) above bottom (Table 3-1). The process would be repeated for the remaining nine sigma layers to give a vertical distribution of inflowing TSS at the open boundary. The open boundary was treated as uniform for TSS in the lateral (cross-channel) direction.

Table 3-2. Coefficients and Goodness of Fit Measures for TSS Regression Equation (3-2) for ABS Bins 1-13 and Mean Binned TSS and Standard Deviations for ABS Bins 14-23 at the Arthur Kill Open Boundary

ABS BIN	Distance from Bottom (m)	Regression Coefficients			Coefficient of Determination (R^2)
		a	***b***	***c***	
1	0.5	5.92	3.73 E-04	2.68	0.97
2	1.0	6.49	8.27 E-03	1.51	0.99
3	1.5	6.32	2.78 E-02	1.27	0.98
4	2.0	6.47	1.08 E-02	1.49	0.91

Table 3-2. Coefficients and Goodness of Fit Measures for TSS Regression Equation (3-2) for ABS Bins 1-13 and Mean Binned TSS and Standard Deviations for ABS Bins 14-23 at the Arthur Kill Open Boundary

ABS BIN	Distance from Bottom (m)	Regression Coefficients			Coefficient of Determination (R^2)
		a	***b***	***c***	
5	2.5	6.25	2.05 E-03	1.88	0.97
6	3.0	6.20	7.00 E-04	2.09	0.97
7	3.5	5.80	4.10 E-03	1.61	0.80
8	4.0	5.67	2.97 E-03	1.59	0.81
9	4.5	5.46	2.50 E-03	1.60	0.64
10	5.0	5.11	1.32 E-03	1.74	0.75
11	5.5	4.81	1.21 E-04	2.29	0.84
12	6.0	4.56	3.72 E-06	3.06	0.87
13	6.5	4.27	4.35 E-08	4.08	0.86
		Mean TSS Concentration (mg/L)			**Standard Deviation**
14	7.0	4.19			± 0.32
15	7.5	3.84			± 0.21
16	8.0	3.65			± 0.14
17	8.5	3.45			± 0.15
18	9.0	3.39			± 0.22
19	9.5	3.30			± 0.16
20	10.0	3.25			± 0.24
21	10.5	3.23			± 0.26
22	11.0	3.17			± 0.12
23	11.5	3.02			± 0.34

3.1.2.2 2008-2009 Monitoring Data

The Hudson River Foundation funded studies of Newark Bay that included instrument platforms in the Kill van Kull and Arthur Kill (Summerfield and Chant, 2010). As part of this program, monitoring platforms were deployed for two periods: the first from April 11, 2008 to August 15, 2008 and the second from September 16, 2008 to March 10, 2009. Each monitoring deployment included measurements of temperature, water depth current velocities and acoustic backscattering. Vertical profiles of velocities and acoustic backscattering were recorded at 0.25-m (0.82 ft) intervals in the Arthur Kill and 0.5 m (1.64 ft) intervals in the Kill van Kull, at a frequency of once every 10 minutes. Two different ADCP instruments were used and separate regression equations were used to estimate TSS concentrations from ABS measurements from each instrument (Summerfield and Chant, 2010):

For the 1200 kHz ADCP:

$$TSS(i) = 10^{(0.0387 \times abs(i) - 2.083)} \quad (3\text{-}3)$$

and for the 600 kHz ADCP:

$$TSS(i) = 10^{\left(0.0387 \times \left\{\frac{[abs(i) - 9.47]}{0.9}\right\} - 2.083\right)} \quad (3\text{-}4)$$

where *i* is bin number and *abs(i)* is backscatter value (dB) in bin *i*.

ADCP current data from the Kill van Kull were analyzed to develop histograms of currents direction for individual vertical bins (Figure 3-11) and composited through the water column (Figure 3-12). Corresponding plots were developed for ADCP data from the Arthur Kill (Figures 3-13 and 3-14, respectively). These analyses were used to segregate the data for in-flowing and out-flowing periods, and only data recorded during in-flowing periods were used to develop boundary conditions.

Vertical distributions (Figure 3-15) of velocity (top panels) and TSS estimates (bottom panels) were plotted for each 10 minute interval within each hour and used to identify periods with suspect data. Elevated TSS concentrations in the upper portion of the water column (e.g. Figure 3-15, middle panel of bottom row; white triangles) were suspected to be caused by boat wake interference and screened out of the analysis if the concentration was more than two times greater than the next deeper vertical bin.

Data retained through the screening mentioned above were used to compute solids loads (per unit width) as the product of velocities and TSS concentrations and bin heights. Solids loads for each ADCP vertical bin were associated with one of the 10 sigma layers (each 10% of the total depth) used in ECOMSED. Data analyses revealed different relationships between solids loads and velocity during periods of accelerating and decelerating in-flowing velocities, as well as an effect of the spring-neap tidal cycle. Solids loads at the Kill van Kull and Arthur Kill for individual sigma layers (with sigma layer one at the surface and ten at the bottom) were evaluated by the following regression equation (Equation 3-5), applied separately to data obtained during periods of accelerating and decelerating in-flowing velocity at each location:

$$Load = a(V^b)(R^c) \quad (3\text{-}5)$$

where *Load* is total 10-minute TSS mass per time per unit width for ADCP bins within a specific sigma level; V is average sigma-level velocity; R is daily tidal range; and a, b, and c are regression coefficients. The regression results are summarized in Table 3-3 and Figures 3-16 and 3-17 for the Kill van Kull and Table 3-4 and Figures 3-18 and 3-19 for the Arthur Kill. Results from the second sigma level were used for the surface sigma level, where surface interference limits data reliability.

The calibrated hydrodynamic model of the Lower Passaic-Hackensack-Newark Bay system (HydroQual, 2008) includes the same model grid as the sediment transport model used in this effort, but also extends up the Hudson River, through Long Island Sound, and

out to the New York Bight. Time series of Kill van Kull and Arthur Kill currents and tidal ranges were extracted from the larger-domain hydrodynamic model and used to calculate solids loads, which were then converted to concentrations by dividing by the current velocity. In the absence of additional data, the open boundary for TSS was treated as uniform in the lateral (cross-channel) direction. During periods of the model simulation for which TSS data are available, the data were used rather than relying on the regression results.

Table 3-3. Regression Coefficients for Kill van Kull Solids Loads

KVK	Accelerating Velocity			Decelerating Velocity		
Sigma	***a***	***b***	***c***	***a***	***b***	***c***
2	18.0	1.19	0.253	17.7	1.18	0.771
3	18.5	1.28	0.479	19.0	1.20	1.04
4	17.2	1.24	0.729	18.2	1.18	1.30
5	16.6	1.19	0.939	19.4	1.16	1.44
6	20.8	1.28	0.930	21.9	1.12	1.52
7	23.3	1.14	1.14	27.9	1.00	1.34
8	56.9	1.55	0.407	48.5	1.00	0.840
9	116	1.71	0.261	64.0	1.00	0.783
10	143	1.75	0.139	101	1.29	0.544

Table 3-4. Regression Coefficients for Arthur Kill Solids Loads

AK	Accelerating Velocity			Decelerating Velocity		
Sigma	**A**	**b**	**c**	**a**	**b**	**c**
2	11.0	1.48	0.254	12.2	1.51	0.291
3	10.8	1.39	0.400	10.7	1.34	0.475
4	10.8	1.37	0.482	7.44	1.00	0.549
5	12.3	1.39	0.484	8.43	1.00	0.509
6	15.3	1.44	0.430	14.8	1.36	0.522

Table 3-4. Regression Coefficients for Arthur Kill Solids Loads

AK	Accelerating Velocity			Decelerating Velocity		
Sigma	A	b	c	a	b	c
7	18.8	1.50	0.433	10.2	1.00	0.486
8	28.4	1.66	0.502	11.4	1.00	0.650
9	47.2	1.77	0.525	14.6	1.00	0.684
10	49.2	1.52	0.455	50.0	1.46	0.440

3.2 SEDIMENT BED PARAMETER DEVELOPMENT

Sediment-transport modeling with ECOM-SEDZLJS requires definition of sediment bed and grainsize properties. At the outset of the sediment transport modeling, a sediment bed parameterization was developed to represent the sediments in the LPR as accurately as possible. Available data were analyzed and compiled into a description of particles size classes, distributions of the size classes, critical shear stresses, erosion rates, and bulk densities of the sediment bed. This section outlines the development of the sediment bed parameters utilized.

Various programs collected data that describe particle size distributions, densities, side scan sonar texture characterization, and bathymetry in the LPR and Newark Bay. These programs include the Tierra's 1995 remedial investigation, ASI's 2005 geophysical investigation (Aqua Survey, 2006) and the CPG 2008 Low Resolution Coring Program (AECOM, 2010a) for the LPR; and for Newark Bay, Tierra's Phase I and Phase II sediment investigation programs. Additionally, Sedflume sediment erosion rate measurements (USACE, 2006) and Gust Microcosm resuspension measurements (Chesapeake Biogeochemical Associates, 2006) were made to characterize bed erosion properties. Physical features noted in multibeam bathymetry data were used as a basis for distributing bed physical properties.

3.2.1 Morphologic Features

2008 high resolution multibeam survey data were used to characterize the finer scale features of morphologic regions of the river. Using the 2008 bathymetry data, seven different morphologic features were used to describe the commonly observed features in the LPR. The regions are:

1. Abutment – Hard structures such as bridge piers or scour protection in the vicinity of bridges that can alter flow and scour patterns.
2. Abutment Scour – Readily identifiable scour due to abutment features.
3. Broad Shoal –Broad mudflats and/or point bars typically located on the inside of river bends.
4. Island – In the upstream portions of the river, above water island features are present.
5. Margins – Broad channel margins near the shoreline that are often similar to the broad shoals but can also be anthropogenic shoreline features.
6. Smooth Channel – Broad relatively flat central channel present through much of the river. Although there are perturbations, the overall feature is considered smooth.
7. Deep Scoured Channel – Channel regions that typically occur on the outside of river bends where there is enhancement of velocity and shear stress, resulting in the maintenance of a deeper scoured feature at these locations. The delineation is not meant to suggest that these are long-term net scour features.

These qualitative morphologic definitions are intended to help understand the general lateral and longitudinal features in the river. Figures 3-20 through 3-22 illustrate the multibeam survey data and the identified morphologic regions of the river in the vicinity of RM2, RM4 and RM6. The point bar deposit/mudflat regions on the inside bends, where the current velocity is lower, are consistent with expectations for a typical curving channel flow. This behavior can be observed nearly uniformly throughout the river with corresponding deep channels on the outer bends where the current velocity is higher. The

presence of these features suggest that during high river flow events, the highest shear stresses and higher probability for erosion can be expected in the deeper channels and the lowest shear stresses and higher probability for deposition can be expected on the shoals. Additionally, the long-term presence of these features shows that the tidal currents maintain the channel morphology, such as the presence of deeper channels, during periods of net sediment influx from the direction of Newark Bay.

Both typical and atypical bedforms exist in the channels of the LPR. Figure 3-23 illustrates bed features near RM2.7 and RM8.3. Near RM2.7, where the sediment bed is predominantly fine material, typical sand waves and ripples do not form; although, there are perturbation features (i.e. lumps) at the river bed (possibly large detritus mounds or clumps of stiff material of unknown origin) that show a shallower slope on the upstream lee of the feature. This feature suggests a net upstream direction to near-bed sediment transport at the time of the survey. The RM8.3 bedforms are typical of uniform sand waves moving downstream with the smooth slope facing upstream. The shape of the feature has a dominant downstream directionality. The bedforms suggest that the bidirectional flow in this region was not significantly affecting the bed in this region at the time of the survey (low flow).

3.2.2 Sediment Bed Particle Size

Looking at and into the sediment bed can provide information on the long- and short-term behavior of sediments in various regions of the river. One of the most basic sediment bed properties is the particle size. In addition to a large number of surface grabs of approximately 15 cm (0.5 ft) deep that were collected as part of the 2005 field effort (Aqua Survey, 2006), a side scan survey was conducted. The particle size measurements were used to calibrate a bottom textural classification based on the side scan reflectivity. The side scan data provide a broad delineation of surface rock, gravel, sand, and silt. The data are limited in that they often do not distinguish between more detailed classifications such as sandy silt or silty sand, and represent only the surface of the sediment and not the 15 cm sample depth of the grab. Figure 3-24 shows an overlay of the bottom type on the

river. The lower eight miles of the river are dominated by silt material (light blue) with pockets of silt and sand (green). RM8.3 shows a dramatic shift to sand and gravel sediment (brown) with pockets of silt (light blue). Figure 3-25 shows a close up of this fairly sharp transition. Although the side scan data provide a continuous delineation, it is based on surface conditions which can vary rapidly with flow. Some level of variation can be expected. The transition at RM8.3 is associated with morphological features, the typical extent of the salt front, and estuarine circulation propagation which deliver and trap fine sediment at the bed. The reasons for the coarser sediment size upstream of RM8.3 are likely a combination of winnowing due to high river flows and the proximity of bedrock and potential sand and gravel sources to the bed of the river in the upstream regions.

3.2.2.1 Size Class Definition

The 1995 Tierra, 2005 ASI, and the 2008 CPG grainsize data were combined to develop a more comprehensive picture of the surface sediment. The data were used to define four size classes—representative of the silt, fine sand, coarse sand, and gravel fractions—to approximate the behavior of both fine- and coarse-sediment transport and the interaction of these particles (e.g. armoring). Table 3-5 presents the properties of the four size classes. It is noted that critical shear stresses listed in Table 3-5 are size-class-specific values used to determine whether or not an individual size class will erode when the boundary shear stress exceeds the critical shear stress for the bulk sediments. The critical shear stress for erosion for the bulk sediments (i.e., mixtures of size classes) were derived from Sedflume data.

For the cohesive size-class, the critical shear stress for erosion was determined through model calibration against TSS calculated from ABS measurements, as described above. The critical shear stress for deposition was assumed to be equivalent to that for erosion. The properties of the sand and gravel classes are determined according to van Rijn's (1993) recommendations. The settling speeds are determined based on Cheng's (1997) formulation for the settling of natural particles. The settling speed for the silt size class is

variable based on a weighting of washload and suspended sediment, as described in section 2.7.

Table 3-5. Particle Size Class Properties

Effective Diameter (µm)	Settling Speed (cm/s)	Critical Shear for Erosion (Pa)	Critical Shear for Suspension (Pa)
34	Variable	0.05	0.05
250	2.67	0.17	0.28
1000	11.13	0.54	1.99
4100	27.63	3.3	12.2

3.2.2.2 Spatial Distribution of Sediment Size Classes

The sediment grainsize data and morphological regions were imported into Arc-Map to compute average fractions of each grainsize within each contiguous morphological region. The decision to compute averages, rather than perform spatial interpolation was made because of the high degree of small-scale spatial variability observed in Sedflume cores collected at the same sampling station. An example of the grainsize averages within contiguous morphological regions is shown on Figures 3-26 through 3-29 for four sections of the river.

The particle sizes correlate strongly to morphologic regions in the river. The highest fine content is located on lower energy inner bends of the river identified as broad shoals in the morphology maps. The higher velocity channel regions and deeper scoured channels generally have higher sand content. The strong correlation suggests that using morphology to guide the distribution of sediment properties in modeling work can provide an accurate method to extrapolate limited data sets.

After computing grainsize distributions for each morphologic region, the model grid was overlaid on the grainsize results and an area weighted average grainsize distribution was

calculated for cases where more than one morphological region fell in a single grid cell. A morphologic delineation was not available for Newark Bay, and therefore, grainsize data in Newark Bay were distributed through spatial interpolation, which was performed separately within and outside of the navigation channels.

3.2.3 Sediment Erosion Measurements

Erosion measurements were made on both field and lab cores using the Sedflume device to measure down-core profiles of erosion rates and from field samples using the Gust Microcosm to measure very-near surface erosion rates. The erosion data from these efforts highlight the variability in sediment behavior in the LPR, which represented a significant challenge for model parameterization and calibration. As described below, sufficient data are not available to describe or explain small-scale variability in erosion properties and, as a result, the model parameterization attempts to describe the average characteristics of the erosion data for fine-grained sediment areas. The overall result of this is that the model is expected to generate results with less variability than the data, but approximate the central tendency of the data.

3.2.3.1 Sedflume Core Measurements

Sediment cores were collected from 14 sites along the LPR by Chesapeake Biogeochemical Associates and analyzed in the USACE Sedflume mobile laboratory by USACE-ERDC. Two cores were collected as replicates at each location for a total of 28 cores. The results of the bulk property analysis and erosion rate experiments have been presented and discussed in the report "Erodibility Study of Passaic River Sediments Using USACE Sedflume" (USACE, 2006).

Figure 3-30 shows the sites along the river selected for core collection. Analysis notes from Borrowman et al. (2005) documented that sediment cores from sites P01 through P05 were nominally 30 to 40 percent fines. Sediment cores at P07 were influenced by organic content, and percent fines influenced cores at sites P06, P08, and P09, although for Core P09B erosion rates appeared to be related to bulk density. Additionally,

sediment cores from sites P06 through P09 contained leaves and pockets of trapped gas that influenced several of the erosion rates. Sediment cores from sites P11, P14, and P15 were very susceptible to erosion at low shear stresses, while cores from site P12 showed resistance to erosion that was similar to that of the Site P01 through P05 cores.

Replicate coring at each of the 14 sites varied in separation from about 1 (3.28 ft) to 10 m (32.8 ft). Noteworthy heterogeneity was often observed between replicate cores from the same sampling site. Figures 3-31 and 3-32 illustrate the measured erosion rates, particle size, and bulk density from replicate locations P05A and P05B. These sites were within 10 m of each other and although the sites have comparable median particle size with depth, the measured erosion rate profiles are quite different. Comparing erosion rates for 1.6 Pa (2.32E-4 psi) (solid red line and circles) one can readily see over an order of magnitude difference in erosion rate between the two replicates.

3.2.3.2 Gust Microcosm Measurements

Chesapeake Biogeochemical Associates collected cores for additional erosion experiments during the same field data collection program conducted to obtain cores for field Sedflume analyses. Cores for Gust microcosm experiment were collected at stations 1, 3, 5, 6, 9, and 13 (Figure 3-30). The major emphasis of this program was the determination of very near surface critical stresses and erosion rates using the approach outlined in Sanford and Maa (2001). All field work was carried out from May 16-20, 2005. The results are summarized in "Passaic River Erosion Testing and Core Collection: Field Report and Data Summary" (Chesapeake Biogeochemical Associates, 2006).

3.2.3.3 Sedflume Consolidation Measurements

Sea Engineering, Inc. (SEI) conducted a Sedflume analysis on four consolidation cores created from a single surficial sediment sample from the LPR. The primary goal of this work was to characterize the consolidation characteristics of sediment. Surface sediment was collected at the location of Malcolm Pirnie's high resolution core at RM2.2, which

has been identified as a depositional area for fine material. The material was mixed together (i.e. composited), slurried into a fluid mud, and poured into four laboratory Sedflume cores. The four reconstructed cores were used to evaluate the effects of consolidation on erosion rates and sediment density over time. Cores were tested in the Sedflume at 1-day, 7-days, 17-days, and 28-days to determine the effects of time since deposition and consolidation on sediment erosion rates. In addition, each core was sub-sampled at vertical intervals to determine sediment bulk density and particle size distribution. The final results are outlined in the report "Sedflume Consolidation Analysis, Passaic River, New Jersey" (SEI, 2008).

3.2.4 Sediment Erosion Rates

The Sedflume erosion experiments provide basic data for determination of erosion rates and critical shear stresses for cohesive sediments in the river. The emphasis of the data analysis here will be for cohesive sediments, as non-cohesive sediment erosion rates and critical shear stress can more generally be defined as a function of particle size and particle density. The Sedflume data for cohesive sites must be analyzed in a manner that allows for definition of the initial model bed based on a discrete number of cores.

Following the methods of Roberts et al. (1998) and others, where density is the primary factor affecting the down-core profile of erodibility, the erosion rate for each interval can be approximated by

$$E = A\tau^n\rho^m \qquad (3\text{-}5)$$

where E is the erosion rate (cm/s), τ is the shear stress exerted by the moving fluid on the sediment surface (dy/cm2), and ρ is the sediment bulk density (g/cm3). A, n and m are constants that depend on the sediment characteristics. However, the variation of erosion rate with density cannot always be determined in the field due to natural variation in other sediment properties (e.g. mineralogy, organic content, and particle size). Therefore, the density effects and other factors affecting erodibility were subsumed into the constant

A, which varies vertically in the sediment, thereby incorporating the effect of vertical density variations. The equation used in the Sedflume analysis was an abbreviated variation of Equation (3-5):

$$E = A\tau^n \tag{3-6}$$

Erosion of the sediment from the initial bed (also referred to as "parent bed") is described in the model by Equation (3-6). Solids that deposit on top of the parent bed are stored in compartments in the model referred to as "depositional layers", and in the case of cohesive layers, this is where consolidation effects are represented. Erosion from these layers is described by Equation (3.5).

3.2.5 Data Analysis for Cohesive Areas

The definition of the sediment bed in the sediment transport model requires an initial distribution of sediment properties (e.g. particle size, bulk density, erosion properties). The behavior of the sediment bed as any model simulation progresses will be constrained by these initial definitions; therefore, it is important to utilize the field measured data in a rigorous manner that most accurately bounds real-world conditions. A detailed description of the analyses of data obtained in the three types of erosion experiments (Sedflume field cores, Gust microcosm, and consolidation experiments) is presented in Attachment A. In the following section, the portion of the analysis retained to develop model inputs is summarized, with a brief description of the conflicting results obtained in the three experiments.

3.2.5.1 Variability in Erosion Rates from Sedflume Field Cores

A useful way to illustrate variability of sediment characteristics (which is described in more detail in Attachment A) is to 1) compute A and n values (Eq. 3-6) from erosion rates from a sequence of increasing applied shear stress, 2) use the derived A and n values to compute erosion rates for a fixed set of shear stresses consistent across all depth intervals and cores, 3) compute log-average erosion rates for each depth interval and core, and 4) normalize layer-specific erosion rates to the core-average erosion rates.

Figure 3-33 presents the intra-core erosion rate ratios for four cores as an example (similar plots for all cores are included in Attachment A. This procedure highlights the depth intervals that will erode most rapidly and those that will tend to resist erosion, relative to other depth intervals within the core. Normalizing by the depth-averaged erosion rate of a core provides an erosion-rate ratio that is a measure of the relative susceptibility to erosion (i.e., erodibility) of each depth interval, relative to the average erodibility of the core. Inspection of the results indicates that near-surface depth intervals tend to have the highest erosion rate ratios, indicating that this material is relatively erodible. The erosion rate ratios generally decrease with depth, as would be expected for a normally consolidated cohesive sediment, although there is some variability associated with this downward trend due to sediment heterogeneity.

A similar procedure was followed to compare the relative magnitudes of erosion rates among cores from different locations within the LPR. The depth averaged geometric mean erosion rates for each core were normalized by the site-wide geometric mean erosion rates for N = 22 cores (including 2 duplicate cores at each of 11 cohesive sediment sample locations). These site-wide erosion rate ratios are compared on Figure 3-34. The resulting erosion rate ratios for duplicate cores collected at the same sampling location (compare cores A and B) vary by nearly an order of magnitude for 4 of the 11 pairs of cohesive sediment cores collected (sample locations P03, P05, P06 and P07). This high degree of small-scale variability indicates that spatial interpolation of erosion parameters from the analysis of the field cores is not appropriate.

3.2.5.2 Erosion Rates from Sedflume Field Cores and Consolidation Experiments

Erosion rates derived from the Sedflume tests performed with relatively undisturbed, well-consolidated field cores tended to be higher than erosion rates from the consolidation experiment for consolidation times greater than seven day, and critical shear stresses derived from the field cores were lower than those derived from consolidation times longer than seven days. Previous modeling efforts attempted to use the field-core derived erosion rates as the basis for parameterizing the erosion properties

in fine-grained sediment areas. A cumulative frequency distribution approach was adopted to address variability in erosion rate measurements within fine-grained sediment areas of the LPR, as described in detail in Attachment A. Effectively, this involved using the higher erosion rate data in areas with lower shear stresses and low erosion rate data in areas with high shear stresses. In that same effort, the inconsistency between the erosion properties of the field cores and the consolidation data was addressed by re-analyzing the down-core profiles of erosion rates from the field cores to develop the parameters for erosion rates from the depositional layers. Using that set of parameters, the amount of infilling computed for the Deep Dredging Alternative was less than expected. In the present analysis, the consolidation data set was used as the primary basis for developing the erosion properties for both the depositional layers and the parent bed.

3.2.5.3 Parameterization of Erosion Properties of Depositional Layers

The consolidation experiments generated descriptions of the downcore variations in bulk density, critical shear stress and erosion rates after 1-day, 7-days, 17-days, and 28-days, of consolidation. The data were organized in an Excel spreadsheet and the consolidation algorithm (Sanford, 2008) was entered in the spreadsheet to calculate vertical profiles of critical shear stress and erosion rates as a function of the applied shear stress and consolidation time. The vertical profiles of critical shear stress and erosion rates as a function of shear stress were calculated for each of the four consolidation times. The consolidation model parameters were developed using Excel's solver add-on to minimize the sum of the squares of the residuals of both the erosion rates (in $g/cm^2/s$) and critical shear stresses for the combined data set of the four consolidation periods. The fits of the time varying vertical structure of critical shear stress and erosion rates are presented on Figure 3-35. The parameters derived from the analysis are listed in Table 3-6.

Table 3-6 Consolidation Parameters

Parameter	Group 1
d_{bsur}	1.24
d_{binf}	1.34
d_{bexc}	0.50
d_{conr}	0.15
A	20.0
m	-60
n	1.9

3.2.5.4 Erosion Properties of Parent Bed

The erosion properties derived from the consolidation experiment were used to calculate erosion rates for the parent bed in cohesive areas of the model domain, based on the erosion rates for the depositional layers (in $g/cm^2/s$) vertical density profile for the parent bed. The consolidation parameters used to develop the parent bed erosion rates were modified slightly during testing to balance behavior of water column TSS and amounts of infilling with the post-dredging bathymetry. The parameter d_{bexc}, which controls the vertical gradient of the critical shear stress, was changed from 0.5 to 0.3 and the exponent n, which relates erosion rate to shear stress, was reduced from 1.9 to 1.8. The resulting erosion rates as a function of shear stress and depth in the bed are presented in Table 3-7 and shown graphically on Figure 3-36.

Table 3-7. Parent Bed Erosion Rates for Cohesive Areas

top (cm)	0	2	5	10	15	20	45	70
bottom (cm)	2	5	10	15	20	45	70	320
thickness (cm)	2	3	5	5	5	25	25	250
tau (dyn/cm2)	**Erosion Rate (cm/s)**							
2	8.27E-05	1.00E-09	1.00E-09	1.00E-09	1.00E-09	1.00E-09	1.00E-09	1.00E-09
4	5.79E-04	8.38E-09	1.00E-09	1.00E-09	1.00E-09	1.00E-09	1.00E-09	1.00E-09
8	2.63E-03	7.67E-05	1.00E-09	1.00E-09	1.00E-09	1.00E-09	1.00E-09	1.00E-09
16	1.03E-02	5.50E-04	3.37E-05	3.91E-06	2.28E-06	2.10E-06	2.07E-06	2.07E-06
32	3.82E-02	2.52E-03	3.31E-04	1.35E-04	1.18E-04	1.16E-04	1.16E-04	1.16E-04
64	1.37E-01	9.94E-03	1.65E-03	8.20E-04	7.43E-04	7.33E-04	7.32E-04	7.32E-04
128	4.83E-01	3.67E-02	6.70E-03	3.57E-03	3.27E-03	3.24E-03	3.23E-03	3.23E-03
tau crit	1.0	4.0	9.7	13.4	14.0	14.1	14.1	2000.0

3.2.6 Erosion from the Fluff and Transitional Layers

Erosion from the fluff and transitional layers is calculated as:

$$E = A\tau^n$$

Where E is erosion rate in cm/s, *A* is a coefficient equal to 1.0E-4, which developed through calibration to water column TSS data, τ is the grain-shear stress (dynes/cm^2)and n is a constant, assigned as one in this case. The critical shear stress for the fluff layer and transitional layers, which were also developed through calibration to the water column TSS data are .5 and 4.0 (dynes/cm^2), respectively.

3.2.7 Assignment of Erosion Parameters to Model Grid

ECOM-SEDZLJS provides the flexibility to assign separate erosion rates and grainsize distributions to each cell, or to specify a more limited number of sets of model inputs and assign the same set of inputs to multiple grid cells. The latter option was adopted for the LPR. Grid cells were classified as either cohesive or non-cohesive based on median grainsize, D_{50}, and composition. Different approaches were used for assigning erosion parameters in non-cohesive versus cohesive areas, as summarized in the following subsections and described in more detail in Attachment B.

3.2.7.1 Non-cohesive Regions

As mentioned previously, cells with a sand percentage greater than 60% were defined as non-cohesive. Six representative particle size distributions were developed to represent the cells in sand regions. These distributions were based on the statistical distribution of sediments and the percentage of fines in the sand cells. Table 3-8 shows the size range and average particle size of the six non-cohesive regions.

Table 3-8. Non-Cohesive Region Properties

Region	Range of D_{50} (μm)	Average Particle Size of Cells in Range (μm)
1	130 - 155	141
2	151 - 242	203
3	176 - 417	281
4	224 - 523	336
5	228 - 600	374
6	293 - 594	394

The erosion rates and critical shear stresses were determined for each sand region based on the Roberts et al. (1998) Sedflume data set. The average particle size from each cell was used to determine the appropriate initial erosion rate values from the laboratory quartz values. It has been shown in the Roberts et al. (1998) work that these values are consistent with the summary of previous work on sands presented in van Rijn (1993). These values yield a complete description of initial bed critical shear stresses for erosion and erosion rates for non-cohesive sediments as a function of shear stress.

3.2.7.2 Cohesive Regions

The analysis of the grainsize data resulted in a total of 94 sets of grainsize inputs, 51 of which are in cohesive areas. Twenty-six of the cohesive grainsize distributions are assigned to LPR grid cells, 20 to Newark Bay and the Kills, and 5 to the Hackensack River. Erosion rates, discussed in section 3.2.5.4, as a function of applied shear stress and depth in the sediment are assigned based on the values in Table 3-7. Spatial variations in grainsize distributions will result in spatial variations in erosion rates due to differences in bed coarsening. The spatial distribution of core assignments is shown in Figure 3-37.

4 MODEL CALIBRATION

4.1 INTRODUCTION

The model simulation period used for calibration includes water years 1996 through 2010 (October 1, 1995 – September 30, 2010). Model calibration involved comparisons of model results with estimates of suspended solids collected in several different periods, and comparisons with changes in bed surface elevations derived from single and multibeam bathymetry surveys. The CPG executed a Physical Water-Column Monitoring (PWCM) program (AECOM, 2010b) in the fall of 2009 and spring and early summer of 2010. The program included acoustic backscattering measurements at 12-minute intervals, which provided a basis for evaluation of sediment transport behavior on intratidal time scales.

Following a period of intense rainfall in March 2010, the CPG contracted Dr. Robert Chant from Rutgers University to perform vertical casts of OBS along transects from Newark Bay to approximately RM5 in the LPR. Flow conditions during the sampling corresponded to approximately a 1 in 20-year recurrence interval. Suspended solids estimated from the OBS provided a basis for testing the sediment transport model under fairly extreme flow conditions.

Single-beam bathymetry surveys conducted between 1995 and 2004 provided estimates of net solids transport behavior over longer time scales. Multibeam surveys conducted between 2007 and 2010 provide a highly spatially detailed data set for evaluation of sediment transport of a period that included significant flow events. Comparison of model simulation results to each of these data sets are presented in the following sections.

4.2 MODEL COMPARISON TO PWCM DATA

Moored ADCP current velocity and turbidity data were collected by Ocean Surveys, Inc. (OSI) for the CPG at five stations between October and December 2009 and again between March and July 2010. The five stations were located at RMs 1.4, 4.2, 6.7, 10.2, and 13.5. Water column profiles of TSS were computed from ADCP acoustic backscatter (ABS) data. This measurement program is referred to as the Physical Water-Column Monitoring (PWCM) program, and it yielded long time series of estimated TSS for comparison to model predictions.

Except for brief periods of elevated flow in late October 2009, early December 2009, late March-early April 2010, and late April 2010, most river flows during the PWCM program were low to moderate. The highest flows occurred during a 2-week period from late March to early April 2010, when average flows were approximately 200 m^3/s (~7100 cfs) (approximately a 2 year recurrence interval for the Passaic) and the peak flow reached 300 m^3/s (~10500 cfs) (approximately a 5 year recurrence interval). The lowest flows occurred in June and July 2010, when flows were frequently well below the long-term median flow of 17 m^3/s (600 cfs) for the Passaic River.

A typical model-data time series comparison is shown in Figure 4-1, which covers the week from Oct 29 to Nov 4, 2009 (days 28-35 since Oct 1, 2009 on the horizontal time axis) at RM1.4. The figure shows model output (blue lines) from all 10 model sigma levels (each 10 percent of the water column; five upper panels on left and right). The averages of TSS data as estimated from ABS data reported within each sigma level are plotted as a red line, with shading around the line to show the 90 percentile prediction interval. The prediction interval reflects both the scatter in the regression of TSS to ABS and the extrapolation of the regression outside the range of ABS readings included in the regression for each mooring location. The figure also shows river flow and predicted bed elevation change (two lower left panels), as well as predicted and observed total water depth and predicted applied skin friction shear stress for comparison to predicted sediment surface layer critical shear stress for erosion (two lower right panels). The TSS

versus ABS regressions and a full set of model comparisons to ADCP-derived TSS data are included in Attachment C.

During the week shown in Figure 4-1, river flow was moderately high, at about 50 cms (1765 cfs). Tides increased from neap towards spring, with generally good agreement between predicted and observed water level. In the upper water column, modeled and TSS computed from ABS data agree well, with typical maximum tidal TSS of about 30 mg/L decreasing to < 10 mg/L at slack high tide. The model predictions agree with observations. The phase of tidal fluctuations in TSS is generally very well predicted. This phase behavior is especially illuminating of sediment transport dynamics. Predicted tidal resuspension occurs only once per tidal cycle, on the accelerating flood tide as applied shear stress exceeds sediment critical stress. The flood dominance at this location is due to the addition of the flood tide and the flood-directed estuarine circulation. This semi-diurnal, flood-dominated resuspension tends to pump near-bottom suspended sediment upstream over repeated tidal cycles. The fact that both predicted and observed increases in TSS sometimes happen before local resuspension indicates advection of higher suspended solids from upstream at the end of the ebb tide, which are then carried back upstream on the flooding tide and added to by local resuspension.

The model-data comparison from the next station upstream, at RM 4.2, is shown in Figure 4-2 for the same time period. At this location simulated TSS concentrations are generally less than TSS concentrations estimated from ABS measurements, although the simulated values fall within the lower range of the TSS-ABS prediction interval. Both the upper and lower water column concentrations are well-predicted with respect to the tidal phase. TSS concentrations at RM4.2 are higher than either downstream at RM 1.4 or upstream at RM 6.7 (Figure 4-3) , most notably in the ABS measurements but also in the model predictions. Tidal fluctuations are dominantly quarter-diurnal, corresponding to local resuspension during the accelerating phases of both flood and ebb tide. Resuspended TSS increases in magnitude as tidal range increases towards spring tides. Taken all together, these behaviors indicate that RM 4.2 was in the vicinity of both the actual and predicted turbidity maximum zone, with regular resuspension and deposition

of bottom sediments on each phase of the tide. Nevertheless, predicted bed elevation changes were small.

The model-data comparison from the next station upstream, at RM 6.7, is shown in Figure 4-3. As in Figure 4-1, there is generally good agreement between predicted and observed TSS, both in magnitude and phase. The model tends to under-predict peak TSS values in the lower part of the water column, but not as much as at RM 4.2. In general, tidal fluctuations are a dominantly quarter-diurnal, with magnitudes that increase as tidal range increases but remain slightly lower than at RM 4.2. It appears that this station is slightly on the upstream side of the turbidity maximum at this time, with significant local resuspension and deposition still occurring during the accelerating phases of both flood and ebb. Bed elevation changes are negligible.

The model-data comparisons from the next two stations upstream at RM 10.2 and RM 13.5 are shown in Figures 4-4 and Figure 4-5, respectively. In both the model predictions and the data, the general levels of TSS are greatly reduced compared to those at RM 4.2 and RM 6.7. Within this context, the model again agrees well in the predicted phase of TSS, and with the magnitude of the concentrations at RM10.2, but over-predicts tidal peaks in TSS at RM 13.5. Both model and data indicate a predominantly semi-diurnal pattern at these stations, with maxima occurring during or at the end of ebb. At RM10.2, the applied bottom stress exceeds the critical stress only during ebb at neap tide, and much more strongly during ebb at spring tide. The applied bottom shear stress only exceeds the critical stress for erosion very briefly during peak ebb at RM13.5. The strong ebb-dominance of the bottom shear stress pattern also indicates that sediment transport dynamics have switched to those of a tidal river at these locations.

The interpretations of Figures 4-1 to 4-5 are corroborated by the axial slices of predicted TSS presented in Figures 4-6 and 4-7. These slices show axial-depth distributions of TSS at 1700 and 2300 on day 31 in Figures 4-1 to 4-5, during maximum flood and maximum ebb respectively. At maximum flood, the turbidity maximum is centered at approximately RM 5, with associated elevated TSS extending from approximately RM 1

to RM 9. TSS at RM 13.5 is quite low. Salt (and presumably the innermost extent of the estuarine circulation) intrudes up to RM 4.5, and the lower layer is well mixed. At maximum ebb, the turbidity maximum is less pronounced and centered at RM 4. The salinity intrusion is at approximately the same bottom location, but much more strongly sheared seaward. TSS at both upstream stations is higher than during flood, but generally lower than in the stations under the direct influence of the turbidity maximum. It seems likely that the intensity of the turbidity maximum at this time is due to reworking of relatively new sediment delivered during the high river flow events on days 24 and 28, since TSS concentrations this high are unusual during periods of lower river flow.

The highest river flow during the PWCM program occurred on April 1, 2010, when flow reached 300 cms (~10500 cfs), approximately a 5-year event. This flow followed an even larger flood on March 16, 2010, which took place before the moorings were in place for the spring monitoring period. Figures 4-8, trough 4-12 show time series of predicted and observed TSS from RM 1.4, 4.2, 6.7 10.2, and 13.5, respectively, from March 29 to April 4, 2010. There are several important points to be made from these figures. First, the model clearly over-predicts the magnitude of peak TSS throughout the river during this event, but again the phase is well-predicted. The magnitude is most likely over-predicted because the procedure used to estimate sediment loads over Dundee Dam does not account for flow history, assigning the same representative sediment load to each flow regardless of antecedent conditions. In reality, it is likely that the March 16 flood scoured much of the sediment available for erosion in the watershed upstream of Dundee Dam, leading to much lower actual loads during the April 1 flood than those estimated by the model and thus to the lower observed TSS magnitudes in Figure 4-8 through 4-12. However, the correctly predicted phase of TSS shows that the model captured the correct sediment transport dynamics. In the upper and mid-water column at RM 1.4, for example, tidal maxima in TSS occur semi-diurnally at the end of ebb tide. Bottom stress is dominated by the ebb tide as well, with virtually no flood tide towards the end of the week. This indicates a situation in which the estuary has been pushed downstream of RM 1.4 and the entire LPR is acting as an ebb-dominated tidal river, with associated sediment transport patterns. TSS patterns in the bottom two sigma levels are much more complex

due to short-lived disequilibria between applied stress and critical stress, resulting in sporadic resuspension episodes, but there are no data available for comparison to these predictions. The pattern of ebb dominance is even more apparent further up-river, where it is accompanied by complex patterns of predicted erosion and deposition during the flow event. Interestingly, bed elevations are predicted to return almost to normal by the end of the week.

As a final example of model-data time series comparisons during the PWCM program, Figure 4-13 and 4-14 show the week from June 14-21 at RM 4.2 and 6.7, respectively. This period was characterized by flows at or below long-term median levels, with typical spring tides. Figure 4-13 shows relatively low TSS concentrations in the upper water column, with both the magnitude and phase of predictions agreeing well with the data. Near the bottom, the model under-predicts the observed large semi-diurnal TSS fluctuations, but again there is relatively good phase agreement. The data in particular indicate strongly flood-biased sediment transport, resulting in upstream pumping of sediment in the lower layer. The model shear stress pattern favors the same behavior, with muted predicted TSS response. This behavior corresponds to that expected for lower layer estuarine transport downstream of the turbidity maximum, where both flow and sediment transport are directed upstream. Figure 4-14 shows the expected behavior for the center of the turbidity maximum, similar to Figure 4-2. Large quarter-diurnal stress and TSS fluctuations are present in both the model predictions and the data, though the model under-predicts TSS maxima more so in the bottom half of the water column.

4.2.1 PWCM Fluxes

The USEPA and CPG modeling teams worked together to calculate vertically integrated solids fluxes from ADCP derived velocities and ABS derived suspended solids. Daily net solids fluxes from data and model results are plotted versus daily freshwater flow on Figure 4-15. The data represent the vertically integrated flux calculated as the product of ADCP bin velocity, ABS-estimated solids concentration and bin height, with the dimensions of mass per time per unit width (e.g. metric tons per day per meter). The data

values quantify the flux at the exact location of the ADCP platform, with extrapolations made to the near surface and the portion of the water column from the bottom up to the blanking distance above the ADCP. The model fluxes represent the daily net vertically integrated mass load (M/T) divided by the width of the model grid cell, to generate a dimensionally consistent unit for comparison to the data.

The fluxes computed by the model are in general agreement with the fluxes derived from data in terms of the magnitude of the fluxes and the flow condition that typically represents the reversal in the direction of the flux. Fluxes in the downstream direction are shown as positive values on Figure 4-15. At RM13.5 the daily net flux is in the downstream direction throughout the Fall 2009 PWCM period, and the model and data agree reasonably well. At RM6.7, fluxes in the upstream direction (negative fluxes) are primarily limited to flow conditions less than 20 to 25 cms (706 to 882 cfs), although on some days with flows in this range, downstream fluxes of a limited magnitude (< 0.5 MT/d/m) are noted in both the data and model results. Both model and data show increasing downstream solids fluxes with increasing freshwater river flow, although the slope of the data is steeper than the model results.

At RM4.2 the model and data agree well in terms of transition in the flux direction (at ~30 cms or 1060 cfs), and slope of flux versus flow up to approximately 90 cms (3178 cfs), although the scatter in the values derived from the data at a given flow are more pronounced than the variability in the model results. For the seven days with flows greater than 90 cms, the range of the model results is fairly small, between 3.5 and 5.5 MT/m/d, while the data vary between 0.5 and 13 MT/m/d. At RM1.4, the model and data agree quite well over the range of flow conditions that occurred during the Fall 2009 PWCM period.

It is noted that the comparisons shown on Figure 4-15 include only model results for the grid cell containing the ADCP. In the calibration summary (section 4.6) cross-sectional total loads (M/T) are presented for a wider range of flow conditions, and these show consistent relationships between the flow at which solids transport generally shifts from

net downstream transport to net upstream transport. As expected, the simulated net transport versus flow, presented in section 4.6, shows more variability than the model results for the limited period of the Fall 2009 PWCM program (Figure 4-15). It is also noted that solids fluxes can be affected by cross-sectional variations in velocity and solids concentrations, for which little data are available to rigorously assess the potential effect on comparison of fluxes computed from data at a single point in a cross section with model results averaged over a model grid cell.

4.2.2 PWCM Summary

Summarizing the results of the PWCM model-data comparison exercise:

1. The PWCM observations covered a broad range of flow conditions. Moderate and low-flow conditions were likely typical of the response of the LPR. However, the highest observed flows in late March to early April 2010 closely followed an even stronger flood in mid-March that occurred before the observational program began, so it may not have represented typical high-flow conditions because of scour during the preceding high-flow event.

2. In the examples presented, the model often over-predicted peak tidal TSS levels near the bottom, though there were times when the predictions were very similar to the data and times when observed TSS levels were higher than the predictions. In general, however, the overall range of the predicted tidal fluctuations was similar to the range of the observations and observed spatial patterns of high and low tidal TSS were well predicted. More importantly, the phase of the predictions usually agreed well with the phase of the observations. This indicates that the model captured the fundamental sediment dynamics of the LPR well. In particular, changes in tidal sediment periodicity as the turbidity maximum migrated up and down the LPR were well reproduced.

3. It seems likely that the differences between predicted and observed TSS magnitude were related to differences in modeled and actual sediment source strength. There are two basic sources of TSS that are important from this perspective, direct loading that accompanies high river flows and resuspension of previously deposited sediments. Close to the mouth of the river, solids inputs from Newark Bay can also be an important component of the intratidal solids transport, although this source is less important during high flow conditions. The model over-prediction during the high river flow event of late March – early April 2010 likely reflected the fact that the model loading function does not account for scour history in the watershed above Dundee Dam. Differences between predicted tidal TSS magnitude and observations likely reflect difficulties with predicting the delicate balance between erosion and deposition of the thin floc layer at the sediment surface. However, the fact that the model correctly predicted turbidity maximum spatial and temporal dynamics indicates that it transported the pool of mobile particles that is the source of the turbidity maximum correctly, though it may have over-estimated the size of that pool.

4. Daily net solids fluxes computed from the Fall 2009 PWCM data and model results for the same period show consistent features, with generally net upstream solids transport (except for RM13.5) at flow conditions less than 30 cms (1060 cfs). Data-derived solids fluxes and model results are of similar magnitude and show similar trends with river flow up to approximately 70 cms (2472 cfs). The limited data above 80 cms (2825 cfs) tend to indicate higher fluxes than those computed by the model for RM6.7 and RM4.2, and fluxes consistent with the model at RM13.5 and RM1.4. Given the variability in the relationship between acoustic backscattering and suspended solids, and the limited range of suspended solids data available to develop the relationship, the comparisons between the PWCM derived fluxes and model results are considered acceptable.

4.3 MODEL SIMULATION RESULTS DURING MARCH 2010 HIGH-FLOW

In an effort to test the sediment transport model over a wider range of flow conditions, the model results were compared to suspended-solids estimates derived from OBS data collected by Dr. Robert Chant, Rutgers University during a high flow condition on March 16, 2010.

4.3.1 Data Description

On March 16, 2010 after a major storm event, peak flows over Dundee Dam exceeded 450 cms (~16000 cfs) for more than a day. Based on USGS flow records at Little Falls (USGS, 2013), this flow has a recurrence interval of more than 20 years, so this event represented a rare opportunity to sample an extreme flow. No moorings were in place at the time of the event, but Dr. Chant mobilized to measure vertical profiles of salinity, temperature and OBS from a small vessel on three transects between Newark Bay and approximately RM5.5 of the LPR. These measurements took place centered on mid-day on March 16, very close to peak flow. Figure 4-16 is a map of individual locations of data collection points during those transects. Transect 1 commenced approximately one hour following high tide and was conducted on the ebbing tide. Sampling started from the west side of Newark Bay and continued up the LPR to approximately RM5.5. Transect 2 started from the ending position of Transect 1 (RM5.5) and proceeded downriver and approximately 5 miles into Newark Bay. Transect 2 began at roughly mid-tide and ended approximately 90 minutes before low tide. Transect 3 began in Newark Bay about one hour before low tide and proceeded upstream in the LPR to RM5, finishing near low tide.

For each trip and sampling location salinity, temperature and OBS data were collected at various depths. Solids concentrations were estimated from OBS values using Chant's previous TSS vs. OBS calibration. The highest solids concentrations were measured in Transect 3. In general, concentrations were lowest in Newark Bay (around 50 mg/L) and highest near the mouth of the LPR (RM0–3, TSS concentration around 500 mg/L). At the upstream extent of the sampling (LPR RM5 to5.5) concentrations were around 100 mg/L during Transect 1 and Transect 2 while Transect 3 concentrations were around 150 to 200

mg/L. Comparing nearby stations, it is apparent that total suspended solids in Transect 3 were substantially higher than in Transect 1.

4.3.2 Suspended Solids Comparison

Figures 4-17 through 4-19 show the longitudinal section of the LPR sampled on March 16, 2010 for transects 1 through 3, respectively. Color coded circles (top panels) represent concentrations of TSS estimated from OBS data. The continuous profile on the bottom panels were developed by interpolating these discrete data points, although it is noted that this is a composite profile, using data for each transect that were collected over periods of 45 minutes to almost two hours.

Simulated TSS concentrations for March 16, 2010 were extracted from the 1995-2012 model simulation and compared with TSS estimates derived from the OBS data (Figure 4-20. The field TSS estimated from OBS data are plotted on the horizontal axis and model results matched by location and time are plotted on the vertical axis. The solid line connecting the two opposite ends of the panel is the 1:1 line of agreement and the dotted lines represent factor of 2 variations around that line. The three columns display results for the three transects and within each column, the three rows present comparisons for the top 30%, middle 30% and bottom 40% of the water column. As can be seen from the Figure 4-20, the model results tend to be lower than the data; however, the majority of the points lie within the factor of 2 variation line indicating that the model in general doesn't over represent or under represent the data by more than a factor of 2 in most cases. In those cases where the model results fall outside the factor of two lines, generally at the lower observed solids concentrations, the model tends to be lower than the data. There are a few instances where the model over predicts the data by more than a factor of 2 in the lower two thirds of the water column for Transect 2.

There are a few possible explanations for the discrepancies in the preceding model-data comparisons. To begin, the model response to this high flow event is necessarily affected by LPR in-stream bed conditions that evolved over the course of approximately 14.5

years of model simulation. Further, and of considerable importance, is that this event did not include solids loading from the watershed during the period of the rising hydrograph, and it may be that an under estimation of upstream solids loading is the source of the discrepancy between model and data. Finally, the comparison was made without the benefit of event-specific calibration of the TSS-OBS relationship. In view of these considerations, these results are considered encouraging.

4.3.2.1 Sediment Bed Erosion

Figure 4-21 and 4-22 show the net bed elevation change and maximum erosion predicted by the model between March 11, 2010 and March 20, 2010. As can be seen from these figures, the maximum erosion during that period is not very large; most of the areas in the river erode less than 5 cm (~2 inch), with a very limited number of cells eroding between 10cm (~4 inch) and 20 cm (~8 inch). Given the 1 in 20-year flow conditions, sediment bed erosion of 5 cm is not very large and is near the limit of the resolution of any direct measurements, even if such measurements were available (they are not). Additional erosion of only a few millimeters of sediment would result in sufficient water column solids to explain the difference between simulated TSS and the data derived from the OBS measurements.

4.3.2.2 Upstream Boundary Loading

The upstream boundary loading in the model is based on very limited data set and is generalized. Under high flows, there is no provision for differing loads during the rising or falling limb of the flow, nor is there any provision for different sediment loads during different storms. The uncertainty in the amount of upstream loadings as well as composition can be a contributing factor to the differences between simulated TSS and the OBS data. It is not clear how fine sands in the flow over Dundee Dam on the rising limb of this flood compare with the fraction of non-cohesive solids (<15%) in the model's upstream boundary inputs during high flows. Non-cohesive solids in suspension could alter the TSS vs. OBS relationship derived at lower-flow conditions.

Given the uncertainty in bed initializations, upstream loadings and the data measurements themselves, the model seems to be performing adequately in predicting TSS concentrations in the water column during the March 2010 high-flow event.

4.4 EVALUATION OF SIMULATED BED ELEVATION CHANGES

Single-beam bathymetric surveys were conducted in 1989, 1995, 1996, 1997, 1999, 2001, and 2004, and provide data to estimate bed elevation changes during the calibration period. The 1989 and 2004 surveys extend upstream to Dundee Dam. The 1995 survey extends to approximately RM8 and the remainder of the surveys extend upstream to the vicinity of RM7. The portion of the river for which single-beam bathymetry data can be compared during the calibration period is limited to the section downstream of RM8.3, where the bed is dominated by fine-grained sediments. Bathymetric changes in this area are not influenced by sand waves as they could be in the predominantly non-cohesive reach upstream of RM8.3. Bathymetric comparisons upstream of RM8.3 are limited to data sets obtained with multibeam surveys. Multibeam bathymetric surveys were conducted in September 2007, December 2008, June 2010 and October 2011 (AECOM, 2010c). The multibeam surveys extend longitudinally from RM0 to approximately RM14, although the lateral extent does not cover as much of the shallower areas as the single-beam surveys, due to limitations of the instruments.

The expectation is that the bed elevation changes computed by the model should be less variable than actual bed elevation changes, because of factors related to scale, sediment heterogeneity, and factors not represented in the model. In many cases bed elevation changes estimated from the bathymetry data show spatial variations of erosion or deposition on spatial scales smaller than a model grid cell. Because sediment transport processes are non-linear, grid-wide average shear stresses do not necessarily produce the same erosion and deposition patterns as the average of the sub-grid scale erosion and deposition resulting from sub-grid scale variations in bathymetry, velocity and shear stress. Sediment heterogeneity on a sub-grid scale can not be represented, nor is this type of information available to populate a finer-grid model of the system. In this application,

the variability of the Sedflume experimental results led to specification of average bed properties and erosion characteristics across large regions of the river, further reducing spatial variability of computed erosion and deposition. It is important to recognize that there are some additional factors that influence erosion and deposition that are not included in the model. These factors include gas ebullition resulting from decomposition of organic matter in the sediment, propeller-induced turbulence, and barge or boats running aground.

4.4.1 Model-Data Comparisons Using 2010 and 2011 Multibeam Bathymetry Data

Multibeam bathymetric survey data provide a fine-scale picture of bathymetry variations across the swath covered by the survey. At the scale of the multibeam data, changes such as formation, migration, or disappearance of bedform features appear as net erosion or deposition, however in subsequent model-data comparisons, these fine-scale bathymetric changes are averaged out over the spatial scale of model grid cells.

Surveys conducted in June 2010 and October 2011 bounded a time period with an extreme flow following Hurricane Irene (peak flows of 20,800 and 24,700 cfs at Little Falls and Dundee Dam, respectively), and two other elevated flow conditions (based on Dundee Dam records) of over 16,000 cfs in March 2011 and over 14,000 cfs in September 2011, less than two weeks after Hurricane Irene. Based on records at Little Falls (USGS, 2013), the peak flow of 20,800 cfs (daily average of 20,500 cfs) represented a 90-year flood.

Figures 4-23 to 4-28 show the changes in surface sediment bed elevations between 2010 and 2011, calculated by subtracting the 2010 sediment surface elevation from the 2011 sediment surface elevation (negative values represent erosion). The maps also show the spatial extent of the overlap between the two bathymetric surveys. Particularly in the lower river (Figures 4-26 and 4-27) it is clear that the surveys didn't extend to the banks because of water depth limitations. The maps clearly show erosion extending over a larger portion of the area than areas where net deposition is observed. Even with a 90-

year recurrence-interval flow during this period, areas of erosion of several feet or more are fairly limited.

The 2010 to 2011 bathymetry changes were aggregated onto the model grid and compared to changes simulated by the model (Figures 4-29 and 4-30). In the section of the river upstream of RM8.3 (Figure 4-29) both the data and model results show net erosion over the majority of the river, interspersed with smaller pockets of net deposition. Although not always in exactly the same location, the general trends are consistent. Upstream of RM14, both data and model show a mix of erosion depth of about 30 cm (~1 ft) and areas with little change or small net deposition. Between RM14 and 12.5, both show smaller depths of erosion, and an increase in the depths of erosion downstream of RM12.5. Between RM12.5 and RM8.3, the data show less erosion in the middle of the river than in the grid cells along the riverbanks. The model results also show variations in the depth of erosion in rows of grid cells across the river, but with more variation from one side to another than the data.

Downstream of RM8.3 (Figure 4-30) more deposition is seen in both the model results and data than in the section of the river upstream of RM8.3. In the area where the river widens near RM7.5, the model results indicate a greater area and depth of deposition than the data and this, in part, is attributed to the grid features in this location. Both the model and data show less erosion in the reach between RM7 and 5 than in the remainder of reach downstream to RM2. The model results show net deposition along the northern riverbank between RM5 and 3.5 in an area where the multibeam surveys did not cover completely. Between RM3.5 and 2 the model and data agree quite well, with deposition on the south side of the river and net erosion on the north side.

The areas and volumes of deposition (positive values) and erosion (negative values) are summarized by 1-mile reaches on Figures 4-31 and 4-32. The areas of erosion and deposition simulated by the model agree with the data in the majority of the reaches in both spatial patterns and magnitude. The most notable exceptions are in RM7-8 and 0-2 where the model results show larger areas of deposition and smaller areas of erosion

compared to the data. The comparison of erosion and deposition volumes simulated by the model and derived from the data (Figure 4-32) shows more reach to reach variation in deposition volumes simulated by the model than indicated by the data. In approximately half of the reaches, the simulated deposition volumes agree reasonably well with the low levels of deposition indicated by the data. In the remaining reaches the simulated deposition volumes are larger than the data. Much of the inconsistency is due to fairly localized simulated sediment accumulation, such as near RM7.5, 4.3, and 2, which are areas with incomplete coverage by the multibeam bathymetry surveys. The volumes of erosion are reproduced reasonably well by the model, with the most notable differences between RM1 and 3. Between RM1 and the upstream limit of the surveys, near RM14.5, the erosion volumes simulated by the model and derived from the data agree to within approximately 12 percent.

4.4.2 Model-Data Comparisons Using 2007 and 2010 Multibeam Bathymetry Data

Surveys conducted in September 2007 and June 2010 bounded a time period with several elevated flow conditions in the Passaic River. Based on daily records at Little Falls, this period included a maximum flow of 15,600 cfs, five days with flows over 10,000 cfs, and 38 days with flows over 5,000 cfs (425, 283, 142 cms, respectively). Figures 4-33 to 4-38 show the changes in surface sediment bed elevations between 2007 and 2010, calculated by subtracting the 2007 sediment surface elevation from the 2010 sediment surface elevation (negative values represent erosion). The maps also show the spatial extent of the overlap between these two bathymetric surveys, and similar to the 2010 – 2011 comparisons, these surveys also do not extend to the riverbanks, particularly in the lower river (Figures 4-37 and 4-38).

Overall the comparison of the 2007 and 2010 bathymetry surveys shows relatively small net changes in bathymetry over this period, with most changes occurring in longitudinal strips more narrow that the width of the model grid cells. It is interesting to note that on several bends in the upper portion of the river, (i.e. RM9.6, 10.9, and 11.4 on Figure 4-34) the bathymetry comparisons show net erosion on the inside of the bends, which is

contrary to expected long-term patterns, and likely related to the magnitude of the flows during this period and the fact that the 2010 survey was conducted approximately three months following the March 2010 high flow (15,600 cfs at Little Falls).

The bathymetry changes determined from the 2007 and 2010 multibeam surveys were averaged onto the model grid for comparison to bed elevation changes simulated by the model (Figures 4-39 and 4-40). In cases where only a portion of a model grid cell was covered by the bathymetry survey data, the average of the data is shown over the entire model grid cell; however subsequent area and volume comparisons are based on applying the model results to only the area of the grid cell covered by the multibeam surveys.

The section of the river upstream of RM8.3 (Figure 4-39) shows widespread areas with small amounts of net erosion in both the model and data. In the 6-mile stretch covered by the multibeam surveys upstream of RM8.3, there are four localized areas with sediment accumulation in several grid cells that is not reflected in the data: RM10, 10.6, 11.7, and 14. These are areas with fairly limited coverage by the multibeam surveys. The same applies to two areas of above-average erosion near RM9.7 and 11.3.

Between RM9 and RM7.8 (Figure 4-40), both the model results and data indicate a transition from net erosion to net deposition. Between RM7.8 and RM7, the data indicate net erosion, which varies from less than 1 inch in several grid cells to 1 to 4 inches in the middle of the river and as much as 7 inches in one cell on the east side of the river. The model results show small changes of less than 2 inches (5 cm) in several of these cells and deposition of 6 to 18 inches (15-45 cm)in the cells near RM7.5 where the river widens. Between RM7 and RM5 both the model and data show only small changes in bathymetry in the majority of grid cells. The model results included a limited number of cells with bathymetry changes of 6 to 9 inches. Between RM5 and 2 the data show changes of between 1 and 4 inches (2.5 – 10 cm) over most of the river. The model results show changes of l inch (2.5 cm) or less in this reach, with limited areas showing larger amounts of deposition between RM4.5 and RM4, and between RM2 and RM3, which are areas not covered fully by the multibeam surveys.

In the reach of the river from RM2 to RM0 (Figure 4-40), both the model and data show a transition from erosion to deposition moving downstream towards Newark Bay, although with more pronounced deposition seen in the data, with accumulations of 3 to 12 inches of sediment in a number of grid cells. At the upper end of this section, the data show more of a mix of erosion and deposition, with many grid cells showing erosion or depositional changes of less than 4 inches. The model results in this section also show a mix of erosion and deposition, but of smaller magnitude than the data.

The areas of net erosion and deposition between 2007 and 2010 are presented on Figure 4-41, with the same y-axis scale used for the 2010-2011 period (Figure 4-31). The comparison of simulated areas of erosion and that derived from the data are in reasonable agreement for the vast majority of the 1-mile reaches. The data indicate the area of erosion is greater than the area of deposition for all but the most-downstream reach of the river. This pattern is reflected in the model results, with the exception of a few reaches (RM10-RM9 and RM8-RM6) where localized deposition shifts the balance. The volumes of deposition and erosion (Figure 4-42) within each 1-mile reach are substantially smaller than those for the 2010-2011 period shown on Figure 4-32. Upstream of RM11, the simulated volumes of deposition, although small, are greater than the deposition volumes indicated by the data. The effect of the localized deposition near RM7.5 and RM4.3 can be seen in the reach-total deposition volumes. Both the model and data show an increase in the deposition volumes downstream of RM4, with the model results showing less deposition than the data downstream of RM1, as seen previously in Figure 4-40. The model results indicate more variation in the reach total erosion volumes compared to the data, but the magnitude of the observed and simulated erosion volumes are reasonably consistent. The reach exhibiting the largest total erosion volume, based on both the data and model results, is the RM2-RM1 reach.

4.4.3 Model-Data Comparisons Using Single-beam Bathymetry Data

Figure 4-43 shows the alignment of the single-beam survey transects near RM2.5. Because the 1995-2001 surveys (Tierra, 1995) were designed to follow the same transect lines, the alignment among these surveys is more consistent than it is for the remaining surveys. Comparison of the single-beam bathymetric data sets generally show increasingly larger bed elevation changes over longer time periods. Attempts were made to quantify the magnitude of bed elevation change that could be determined accurately from comparison of two single-beam data sets. Although many of the factors affecting the accuracy of the comparisons were quantified, questions about the unquantified errors led to the decision to limit the use of the single-beam data to the longest time period within the calibration period, the period between the 1996 and 2004 surveys.

The single-beam bathymetry data sets were analyzed with a probabilistic technique known as conditional simulation to estimate bed elevations on a six foot-by-nine foot grid. At each six foot-by-nine foot grid point, a mean bed elevation was calculated from the probabilistic simulations. These mean estimates were aggregated onto the sediment transport model grid and used to calculate a grid-cell mean bed elevation change, and 95% confidence limits (based on with-in cell variability) of the bed elevation change between two bathymetric surveys. Because of the additional step of estimating bed elevations between the single beam bathymetry data points, the changes in bed elevation derived from the single beam survey data are considered more uncertain then the changes calculated from the multibeam data sets.

Bathymetry changes computed over the period between the 1996 and 2004 single-beam bathymetric surveys are compared to the mean elevation changes generated with the probabilistic analysis (conditional simulations) of the data on Figure 4-44. For simplicity, the mean elevation changes generated from the conditional simulations are labeled as “data” in right hand panel of Figure 4-44. The hydrograph for the period 1996 through 2004 is shown on the top panel of Figure 4-44 with vertical green lines indicating

the times of the bathymetric surveys between which bed elevations are shown on the lower portion of the page.

The bathymetric surveys span approximately 8 years and the model results and the data have points of qualitative agreement and points of contrast over this timeframe. Between RM7 and 6, both the model results and data indicate a split between erosion and deposition, although immediately below RM7, the data show sediment accumulation in several grid cells where the model results indicate a fairly neutral condition with, small amounts of erosion. The data indicate a mix of depositional and erosional areas, both laterally and longitudinally, while the model results show the upstream half of this reach as erosional and the lower half as depositional. Between RM5 and 4 the model results show a transition from erosion on the outside of the bend on the south side of the river to deposition on the north side. The data indicate more deposition on the outside of the bend and a mix of erosion and deposition on the inside of the bend on the north side of the river. Between RM3.5 and 2.5, the model results show net erosion (of less than 1 cm/yr or 0.4 inch/yr) over much of the northern half of the river, with deposition confined to the southern half, and predominately in the grid cells along the southern river bank. The data in this reach generally indicate deposition across the entire width of the river, with the higher rates to the north of the centerline of the river.

At the bend at RM2.2 both the model and data show erosion on the outside of the bend and deposition on the inside of the bend, with the exception of the row of grid cells closest to the inside river bank, where the data indicate small amounts of erosion. On the inside of the bend, the model tends to predict greater deposition rates than the data and on the outside of the bend, the model tends to predict lower erosion rates than the data. The substantial deposition predicted by the model on the inside bend near RM2.2 is affected by the grid configuration in this area. Downstream of RM2, the data show more accumulation than the model results, which is contributed to by the amount of solids accumulated on the inside of the bend at RM2.2.

Area and volume of erosion and deposition simulated by the model and derived from the data are summarized by river-mile on Figures 4-45 and 4-46, respectively for the period between the 1996 and 2004 single beam bathymetric surveys. (The negative values on the y-axis of Figures 4-45 and 4-46 indicate area or volume of erosion.) With the exception of the reach between RM1 and 2, from upstream to downstream, both the model and data generally show an increasing trend in area with net deposition (Figure 4-45). In this same section, between RM2 and 7 the data show less variability in area of net erosion among the one-mile reaches, while the model results show an increasing trend with distance moving downstream, which is due to areas with very small (< 1cm or 0.4 inch) depths of erosion. Downstream of RM2 the model results include some areas of net erosion, whereas the data do not. In each one-mile reach, the model computes net deposition in approximately 50 percent of the area indicated by the data as depositional, and net erosion over a larger area than indicated by the data. The volume of net erosion, however, is less than that indicated by the data, as seen in Figure 4-46. The smaller erosion volume over a larger area equates to a simulated average erosion depth of 1.7 cm (0.7 inch) compared to 12.6 (5 inch) derived from the data. The net deposition volume simulated by the model is less than the data in each reach except between RM2 and 3. The simulated depositional volume is approximately 75% of the volume derived from the data.

4.5 SEDIMENT FLUX SUMMARIES

Sediment movement within the LPR is summarized in several forms in this section. These include cumulative fluxes (mass loads, Section 4.5.1) and time averaged fluxes for selected time periods (Sections 4.5.2 & 4.5.3). The cumulative sediment fluxes (Section 4.5.1) include fluxes of solids advected in the water column, and net and gross exchange with the bed. Summaries for selected periods include averages for the entire 17-year simulation (Section 4.5.2) and for shorter periods spanning a single year (section 4.5.3.1), and periods of high and low flow (Sections 4.5.3.2 and 4.5.3.3, respectively).

4.5.1 Cumulative Sediment Fluxes

Modeled sediment fluxes in the LPR were examined for the 17-year simulation interval from September 1995 through September 2012. The river was divided into seven reaches of between 2.2 mi and 2.4 mi in length:

- *Reach 7*: RM 16.7 to 14.4 (Figure 4-47)
- *Reach 6*: RM 14.4 to 12.2 (Figure 4-48)
- *Reach 5*: RM 12.2 to 9.8 (Figure 4-49)
- *Reach 4*: RM 9.8 to 7.6 (Figure 4-50)
- *Reach 3*: RM 7.6 to 5.3 (Figure 4-51)
- *Reach 2*: RM 5.3 to 3.0 (Figure 4-52)
- *Reach 1*: RM 3.0 to 0.7 (Figure 4-53)

Cumulative sediment flux (both suspended load and bedload) was calculated along cross-channel transects at the upstream and downstream end of each reach (Figures 4-47 to 4-53, middle panels). During periods of low flow, most notably between mid 2001 and 2002, the cumulative water column sediment flux decreases, signaling a net upstream transport during those times due to estuarine circulation. Those periods also show a net deposition of solids transported upstream due to estuarine circulation. Also calculated were cumulative gross sediment erosion/deposition (bottom panels, red and blue lines, left axis) and cumulative net sediment erosion/deposition (bottom panels, green lines, right axis). The magnitude of cumulative gross sediment erosion/deposition for each reach was much larger than the net erosion/deposition, so it is difficult to discern a difference between the two curves (bottom panels). Note also the different vertical scales and 1000-fold difference in units between gross sediment erosion/deposition (left -axis, bottom panels) and net sediment erosion/deposition (right axis bottom panels).

The most noticeable features of the cumulative plots of modeled sediment flux and gross/net erosion and deposition are the sharp steps that occurred during particularly high flow events. Response to these events varied from reach to reach. For *Reach 7* (RM16.7

– 14.4), the high-flow events generally resulted in net erosion (Figure 4-47, bottom panel); whereas, the reach was net depositional between events. From March 2005 onward, the increased frequency of high-flow erosive events resulted in an overall net erosion for the reach. Prior to the April 2007 and March 2010 high flow events, the net accumulation approached the March 2005 condition, but net erosion during these storms and subsequent high flows in 2011 result in a small net accumulation over the 17-year period, but a net loss between March 2005 and October 2012. For *Reach 6* (RM14.4-12.2), model results suggested that this reach is net depositional (Figure 4-48, bottom panel), although much of the sediment accumulation from the first 15 years was remobilized with the high flows in 2011, particularly Hurricane Irene, near the end of August 2011. From 1995 through 2006, the high-flow events marked by step responses in the middle and bottom panels, resulted in small step increases in net deposition (bottom panel). However, high-flow events in April 2007, March 2010, and 2011 resulted in decreases in net deposition.

For *Reach 5* (RM12.2-9.8), simulated net deposition increased gradually over most of the first 15-years of simulation, with noticeable increases in net deposition at the times of the high flow events in April 2005 and March 2010 (Figure 4-49, bottom panel). Net erosion resulted from the high flow conditions following Hurricane Irene in 2011. Model results (Figure 4-50) indicate that *Reach 4* (RM9.8-7.6) was fairly unchanged in net accumulation from 1995 through March 2005. Gradual accumulation after that point, modified by both net accumulation and losses during storms resulted in a small net accumulation over the 17-year simulation. *Reach 3* (RM7.6-5.3) showed a response (Figure 4-51) similar to *Reach 4* up to the April 2007 high flow period, which resulted in net accumulation of sediment. Net erosion following Hurricane Irene resulted in essentially no net accumulation in this reach during the 17- year simulation.

For *Reach 2* (RM5.3-3.0), simulated cumulative net erosion/deposition show a more-gradual increase in net deposition, with small increases at the time of high flow events in 2007 and 2010. Unlike the reaches upstream of this location, the high flow conditions following Hurricane Irene resulted in a net accumulation of solids in *Reach 2* in 2011.

For *Reach 1* (RM3.0-0.7), the model results show net accumulation of sediment through the 17-year simulation (Figure 4-53, bottom panel). The apparent rate of net deposition increased near the start of calendar year 2003, as evidenced by the increased slope of the cumulative net deposition curve. Model results show a substantial rise in net deposition, in response to the high flow following Hurricane Irene in 2011.

4.5.2 17-Year Average Sediment Fluxes

Figure 4-54 summarizes the water year 1995-2012 average total solids loading (suspended and bedload) through the LPR for both the cohesive and non-cohesive fractions. The only reaches showing net increases in solids loading are between RM16.7 and RM14.4, which is due to the contribution of the Saddle River, and CSO inputs between RM7.6 and RM5.3, which more than offset solids deposition in these reaches. A net decrease in solids transport is calculated in each subsequent reach moving downstream. Between RM14.4 and RM9.8 the reduction in total solids transport is affected more by the reduction in non-cohesive solids than cohesive solids. This is also true in the reach between RM5.3 and RM3. Downstream of RM9.8 the reduction in cohesive solids transport represents the larger component of the reduction in totals solids transport. The largest reduction in solids transport occurs over the reach from RM2.9 to RM0.8. The negative non-cohesive load at RM0.8 represents a small net upstream transport of fine sand due to estuarine circulation.

4.5.3 Sediment Fluxes for FFS StudyArea for Selected Time Periods

The 17-year average fluxes presented on Figure 4-54 are the result of sediment inputs from the Upper Passaic River at Dundee Dam, tributaries, CSOs, Newark Bay, and a great deal water column-bed exchanges. The next series of flux summaries will focus-in spatially on a section of the lower river between the upstream boundary of the FFS Study Area at RM8.3 and near the downstream extent of the FFS Study Area at RM0.8, at the point where the FFS Study Area widens in the approach to Newark Bay. The following summaries will also focus-in temporally, beginning with model results from a one-year

period (water year 1998 – an average flow year), and then narrowing the time periods to separate high-flow and low-flow periods.

4.5.3.1 Water Year 1998 Fluxes

The annual average flow during water year 1998 of approximately 33 cms (1180 cfs) was near the long term average of approximately 32 cms (~1150 cfs). The hydrograph shows low-flow periods at the beginning and end of the year, with higher flows in between, including a peak flow of 250 cms (~8800 cfs). Annual average, high flow and low flow sediment fluxes are summarized on Figures 4-55 through 4-57, respectively. Sediment fluxes for the entire water year are presented on Figure 4-55 (in metric tons per day) with both gross and net fluxes for total solids (black arrows), the cohesive fraction (maroon arrows) and the non-cohesive fraction (green arrows). Gross fluxes are shown for both upstream and downstream transport of each solids group, with bedload and water column transport shown separately for non-cohesive transport. Inputs from stormwater (CSOs) are labeled as "Lateral Loads" and shown at the top of the figure. The overall solids balance for this section of the river is dominated by cohesive solids transport. Cohesive solids transport includes a significant component in the upstream direction at both the upstream boundary (105 MT per day) and downstream boundary (114 MT per day) of this reach. As expected, net transport at each interface is in the downstream direction. The annual average net deposition to the bed for both the cohesive (42 MT per day) and non-cohesive components (2 MT per day) represents a small difference between much larger gross resuspension and deposition. The gross exchanges of non-cohesive solids are dominated by erosion into bedload and deposition from bedload. Inputs of non-cohesive solids from CSOs are a bigger source in this reach than either bedload or suspended transport from outside this reach. The gross deposition represents approximately 55% of the solids load transported from upstream. When the additional loads from lateral inflow (CSOs and SWOs) and inflow from Newark Bay are added to the upstream source, the net deposition represents approximately 22% of the solids inputs to the FFS Study Area. For comparison to the subsequent summaries for low- and high-flows periods within water year 1998, note that for the full year, the net transport from

upstream is approximately 77 MT per day and transport out at the downstream end of the reach is approximately 38 MT per day.

4.5.3.2 Water Year 1998, High-flow Fluxes

During the period between February 1st and June 22nd, 1998, river flow averaged approximately 63 cms (2230 cfs), which was approximately two times higher than the annual average and included a maximum flow of 250 cms (~8800 cfs). Simulated sediment fluxes in the downstream direction for this period (Figure 4-56) are considerably greater than the annual averages (by factors of 2 to 2.5). Upstream solids transport at the northern limit of the FFS Study Area was less than annual average rate by approximately 40%. The gross erosion and deposition terms increased by roughly 30 to 40%, but with more of an increase in gross deposition compared to gross resuspension, resulting in a doubling of the net non-cohesive deposition (from 2 to 4 MT per day) and an increase in the net cohesive solids by more than a factor of 2.5 (from 42 to 111 MT per day).

4.5.3.3 Water Year 1998, Low-flow Fluxes

In the first month of water year 1998, river flow averaged less than 4 cms (~120 cfs) with a maximum flow of less than 12 cms (~410 cfs). Sediment fluxes for October 1997 (Figure 4-57) are considerably lower than the annual averages shown on Figure 4-55. Most noticeable is the net upstream solids transport at RM8.3 and nearly zero net transport at RM0.8 during this period. At both of these locations, the net solids fluxes are a difference between gross upstream and downstream fluxes that are larger in magnitude than the net fluxes. Net resuspension of cohesive solids from the bed adds to the upstream cohesive flux at RM0.8 to produce the net upstream cohesive flux at RM8.3. Interestingly, the low flow period turns out to be a period of net resuspension (46 and 1 MT per day for non-cohesive and cohesive solids respectively). This is in contrast to the high flow period during which net deposition occurred (46 and 1 MT per day for non-cohesive and cohesive solids respectively). This somewhat counter-intuitive result is largely a reflection of the nearly 4-fold higher upstream loading rate that occurs during

the higher flow conditions (185 MT per day) in comparison to low flow conditions (47 MT/day), and trapping within the lower river reach of a high percentage of this increased solids input to the system.

4.6 DISCUSSION

The LPR has been described as an estuary that has been dredged historically, filled-in following cessation of dredging, and is approaching a quasi-equilibrium bathymetry (Chant et.al., 2010). The observation is supported by the analysis of bathymetric data discussed in Section 4.5 and with model results for the 2007-2010 period that showed solids accumulation as only a small fraction of solids input over Dundee Dam. The concept of a quasi-equilibrium comes from the observations (from the physical water column monitoring program mooring data) and model results, which show net upstream transport of solids under low flow conditions and net downstream transport during higher flow conditions. The bathymetric surveys completed in the last several years (i.e. 2007, 2008, 2010, and 2011) show locations switching between erosional and depositional, depending on the flow regime between surveys.

The net direction of solids transport varies as a function of river flow and tidal conditions and location in the river. Figures 4-58 - 4-61 summarize solids loading passing cross-channel transects as a function of river flow, with each page presenting model results for a different tidal range (<1.5, 1.5-2, 2-2.5, and >2.5 m, respectively or 5, 5-6.5, 6.5-8, and >8 ft, respectively). Within any of the tidal ranges shown on Figures 4-58 – 4-61, the flow range that marks the transition from net downstream to net upstream transport increases from upstream to downstream.

Solids fluxes in the LPR are controlled by both the gravitational circulation and tidal pumping. Gravitational circulation is dominated by river flow in the upper estuary and estuarine circulation in the lower estuary. River flow dominated sediment flux is mostly due to downstream advection of river-borne solids. River flow control dominates in the upper estuary, since increases in river flow increase both downstream net volume

transport and sediment delivery. The direction of net solids transport due to estuarine circulation is dependent on the location in the river relative to the estuarine turbidity maximum (ETM). Upstream of the ETM estuarine circulation-dominated net fluxes are in the downstream direction (same as river flow) and in the upstream direction downstream of the ETM. It is the convergence of net sediment flux that produces the ETM. The trade-off between upstream and downstream net fluxes is complicated by changes in the estuarine circulation and salt structure due the changing dynamical balance between river flow and tidal mixing. Tidal pumping refers to net solids transport, independent of river flow, which is caused by asymmetries in tidal velocities. In the LPR tidal pumping generally results in net upstream solids transport, although the magnitude is variable in space and time.

The interaction of these processes creates complex and potentially confusing patterns, as shown in Figures 4-58-4-61. These figures present the daily net solids load versus daily average freshwater flow for the 15-year simulation, for eight cross-channel transects spaced slightly more than 2 miles apart, from RM16.7 to RM0.7. Net downstream and net upstream solids transport is distinguished in each panel by the grey and yellow shading, respectively. The daily solids loading vs. flow pairs are segregated by the tidal range, and presented for tidal range <1.5m (5 ft) (Figure 4-58), 1.5-2.0m (5–6.5 ft) (Fig. 4-59), 2.0-2.5m (6.5–8 ft) (Fig. 4-60) and >2.5 m (8 ft) (Fig. 4-61). The variability in solids transport at any given flow suggests that the solids loadings and related salinity intrusion, respond more gradually than the daily river flow. It is noted that the model results, even in the river-dominated upstream transects, do not exhibit the typical hysteresis in solids loading versus river flow, because the boundary conditions do not include such a feature. The typical hysteresis of higher solids concentrations on the rising limb and lower concentrations on the falling limb of a hydrograph could be a characteristic of the boundary input at Dundee Dam, but the boundary data were not detailed enough to identify that feature. Therefore, the boundary conditions are based on the same solids concentration for a given river flow, regardless of whether the flow is on a rising, falling or steady portion of the hydrograph.

The tradeoff between river dominance and tidal pumping, is most apparent at the furthest upstream station (RM16.7). At low tidal range, river flow dominates and sediment flux is downstream almost all the time, with a power dependence of approximately 1.5. As tidal range increases, the basic pattern remains the same except that fluxes switch to being upstream at low river flow. This shows the influence of tidal pumping in the upstream direction that becomes apparent at low river flow. The greater the tidal range, the higher the river flow at which this transition occurs, and the sharper the transition becomes.

The influence of the estuarine circulation is most apparent at the lower river mile stations. Below RM10, there is a mode of transport with increasing upstream flux as river flow increases. This behavior is most apparent at low tidal range and river flows between 1-50 cms (35–1765 cfs). Interestingly, much of this river flow range (flows > 10 cms or 350 cfs) also has a mode of transport with increasing river flow resulting in increasing downstream transport, which may signify the influence of the estuarine circulation in the lower estuary. There is a broad range where increases in river flow increase the strength of the estuarine circulation, but for which the ETM convergence is still upstream of these locations. This explains increasing upstream flux with increasing river flow. However, there are also times when the same river flow results in downstream transport, perhaps when the ETM convergence is nearby or slightly downstream. This means that the estuarine circulation reacts slower than the daily averaging periods used to produce these plots. For example, if it takes the estuarine circulation 5 days to adjust to a change in river flow, then the first half of that period will still behave as though dominated by the previous river flow. In other words, the transport behavior of the LPR lags behind its riverine forcing by several days. The fortnightly cycle of tidal forcing also comes into play here, since changes in tidal mixing also change the estuarine circulation. The system is complex and dynamic, so an instantaneous response should not be expected, and apparent bi-modality is likely just a reflection of this fact.

At low river flows and high tidal range, upstream net flux becomes almost independent of river flow in the lower estuary. This indicates the importance of tidal pumping when the

water column is relatively well-mixed. Once the water column is well-mixed at a given location, the strength of the river flow doesn't matter as much.

The sediment transport model has been tested over a wide range of conditions in a continuous 17-year simulation. The parameterization of the bed allows the model, after 14 years of simulation, to reproduce the estuarine circulation and phasing behavior noted in the detailed TSS data obtained by the CPG in the Physical Water-Column Monitoring program (Figures 4-1 to 4-14). The model also produced results for the March 2010 high-flow condition that generally reproduce the estimates of TSS derived from OBS measurements (Figure4-20). Lack of boundary condition data through the storm and preceding the day of data collection contribute to uncertainty in representing the solids loading to the system and likely contribute to lower simulated concentrations compared to a portion of the data, although cross-plots of model vs. data show the model results to be within a factor of two for the majority of the data (Figure 4-20).

The general agreement between the multibeam bathymetric data sets provides a degree of confidence that the model is producing results consistent with a system that is reaching or has reached a quasi-equilibrium bathymetric condition (Figures 4-29 to 4-32 and 4-39 to 4-42). This is encouraging for application of the model to evaluate potential remedies that maintain the bathymetry closer to current conditions. Evaluations of scenarios involving more substantial changes in bathymetry include more uncertainty. Extrapolations of historical conditions and infilling rates under a deeper bathymetry configuration in the LPR involve uncertainty because of changes in hydrodynamic conditions in Newark Bay resulting from the deepening of the navigation channels in the bay and through the Kills. Application of the model to potential remedial scenarios (Section 6) shows an increase in the rate of infilling in alternatives involving deepening of portions of the LPR, which is consistent with expectations.

5 SENSITIVITY ANALYSES

5.1 SENSITIVITY INTRODUCTION

The calibrated sediment transport model was used for a series of sensitivity analyses to assess the relative significance of different inputs and parameters. Performing the sensitivity analysis to key parameters/inputs is an integral part of the model development process for a variety of reasons. One reason is that sensitivity analysis provides a way to answer several key questions such as:

1. How would the overall results change if a certain parameter/input was changed?
2. How reliable are the results, given the uncertainty in some inputs?
3. Does the model reproduce expected patterns related to the change in parameter values?

Answering the first and second questions is a way to determine if the model has been calibrated with reasonable parameters and inputs given the range of uncertainty of the inputs. The answer to the third question is helpful in assessing whether the model responds appropriately, both qualitatively and quantitatively, to the change in the model input or the parameter.

5.2 SENSITIVITY ANALYSIS SET UP

The importance of choosing critical parameters/inputs and a representative model simulation period cannot be overstated. The parameters/inputs for the sensitivity analysis were chosen from the broad list of parameters based on the purpose of the overall study and the uncertainty associated with the parameters. Careful consideration must be given in choosing the parameters for sensitivity analyses. For example, a parameter that is known with a very high degree of certainty might not be an appropriate choice unless the intention is to answer question 3 stated above. The following parameters/inputs were identified for the sensitivity analysis:

1. Upstream boundary conditions.
2. Downstream boundary conditions.
3. Critical shear stress of cohesive solids.
4. Settling velocity of cohesive particles.
5. Erosion rate of cohesive particles.
6. Effective Grainsize of model size classes.

In total, twelve sensitivity simulations were performed and in each of those simulations, only one of the above parameters was changed at once. Following USEPA guidance (2009) parameter values were either increased or decreased by a fixed amount of their base values. In this case a value was changed by 20% of its base value, although it is noted that USEPA, 2009 cites 10% as the common value for parameter variation. Based on computational resource considerations, it was decided to run the sensitivity analysis simulations for one representative year. The water year 1998 was chosen as the model simulation period because the average flow in this year is very close to the long-term average of the flow in the river.

5.3 SENSITIVITY ANALYSIS RESULTS

Based on the objectives of the sensitivity analysis, the output matrix for the sensitivity analysis was identified. The following model outputs were included in the output matrix:

1. Solids mass flux across eight transects along the length of the river.
2. Gross mass erosion in the seven reaches between the eight transects.
3. Gross mass deposition in the seven reaches between the eight transects.
4. Net mass erosion/deposition in the seven reaches between the eight transects.

Figures 5-1 through 5-4 demonstrate the results of the sensitivity analysis. Figures 5-1 and 5-2 show the gross erosion and deposition in the seven reaches bounded by the eight transects and Figure 5-3 shows the net deposition in those reaches. The Figure 5-4 shows

the change in transport across the eight transects in response to the change in the parameter/input. Each of the plots show the percent change relative to the base case, which is the run with the original, unperturbed parameter/input.

5.3.1 UPSTREAM BOUNDARY CONDITIONS

The response of the water column solids flux passing eight transects to increases or decreases in the solids load crossing the upstream boundary is shown in Figure 5-4. The change in the solids flux at RM16.6 is directly proportional to the change in the boundary solids load. At each successive downstream transect, the percent change in the flux decreases from the 20% change seen at RM16.6. This is expected since other sources of solids (e.g. resuspension) increasingly contribute to solids fluxes at downstream transects. The change in the upstream boundary solids load changes both the settling velocity of the cohesive solids as well as armoring due to increased/decreased amount of coarser particles. These factors contribute to inconsistent responses in gross deposition and gross erosion, with some reaches showing an increase in gross deposition and erosion in response to a decrease in the boundary solids inputs, and the opposite response to an increase in the solids inputs. In each reach, however, both the gross erosion and gross deposition respond in the same way to the changes in the upstream boundary solids inputs, resulting in a consistent response in the net deposition. Decreases in upstream boundary solids inputs result in a decrease in net deposition and increases in the loading result in an increase in net deposition. The response of net deposition in several reaches is more than the percent change in the boundary solids loading; this is because the net deposition is a small difference between the gross deposition and gross erosion. Overall, the results of this sensitivity run make qualitative and quantitative sense. The relationship relating upstream boundary conditions to river flow, used to develop model inputs, was based on historical data, which is characterized by typical variability (Figure 3-1). Consistency between the assigned upstream boundary TSS-flow relationship and TSS estimated from OBS measurements recorded in the PWCM program indicate that the assigned TSS boundary conditions provide a reasonable characterization of TSS loading at Dundee Dam.

5.3.2 DOWNSTREAM BOUNDARY CONDITIONS

The 20% increase or decrease in the downstream boundary condition generates only a small response in gross deposition, gross erosion, and advective fluxes between reaches (Figures 5-1, 5-2, and 5-4). The most substantial response is in the net deposition in the reach between RM9.7 and RM7.4 (Figure 5-3). This is due to the small differences in the gross deposition and gross erosion, which translate into a pronounced response in net deposition. In general, the responses to the 20% changes in the downstream boundary concentrations make sense, given the spatial distance between the downstream boundaries and the locations where the responses were evaluated. The TSS boundary conditions assigned at the downstream tidal boundaries are based on an analysis of a substantial amount of data collected over a period of years before and during period when navigation depths were increased in the navigation channels to and in Newark Bay. These sensitivity analyses indicate that uncertainty associated with the downstream tisal boundaries is quite tolerable because of the minimal impact of these inputs on the FFS study area.

5.3.3 CRITICAL SHEAR STRESS FOR COHESIVE SOLIDS

The sediment transport model uses the critical shear stress for cohesive solids for erosion of cohesive particles. Changes of +/- 20% in critical shear stress produced changes of less than 5% in the solids fluxes across the transects summarized on Figure 5-4. Changes in gross deposition and gross erosion were also less than ~5% in response to the 20% change in four of the seven reaches, with the exceptions being in adjacent reaches between RM12.1 and 7.4 and downstream between RM2.8 and 0.5. The responses in the adjacent reaches upstream and downstream of RM9.7 are in opposite directions in the two reaches, but in each reach the gross erosion and gross deposition changed in response to the increase and decrease in the critical shear stress in the same direction (decrease in deposition and erosion for both cases in RM12.1 - RM9.7, and increase in deposition and erosion for both cases in RM9.7- RM7.4). Although the change in the solids flux between these reaches in the critical shear stress sensitivity simulations is small, the response in the flux between these two reaches is the largest of the sensitivity results. With smaller

amounts of cohesive areas in these upstream reaches, the response to changes in cohesive solids transport can be magnified in terms of percent change in the gross deposition and erosion. The change in critical shear stress produced a small response in the net deposition between RM12.1 and RM9.7, but a much bigger response between RM9.7 and RM7.4. The response of the model to changes in the critical shear stress for cohesive solids indicate that the model results are consistent with expectations. The assignment of the value used in the calibration is constrained by the comparisons between simulated water column TSS and concentrations estimated from the PWCM ABS data, particularly the phasing of intratidal concentration variations.

5.3.4 COHESIVE SOLIDS SETTLING VELOCITY

The change in cohesive settling velocity by 20% produced an increasing response in the water column solids fluxes from upstream to downstream. The response at each transect was as expected; increasing the settling velocity decreased the solids flux and decreasing the settling velocity increased the solids flux. Water column solids fluxes at RM16.6 were not affected by the 20% change in the cohesive solids settling velocity. At RM2.8, the response had increased to near 10%. At RM0.5, the response is more than the 20% change in the settling velocity, with approximately a 22% decrease in the solids flux in response to a 20% increase in the settling velocity and approximately a 30% increase in response to the 20% decrease in the settling velocity.

The gross deposition responded in the same direction as gross erosion to changes in the cohesive solids settling velocity, but the magnitude and direction of the response varied from reach to reach. The responses in the net deposition within each reach were more consistent, with increases in the settling velocity resulting in increases in net deposition, and the opposite for decreases in the settling velocity. The most sensitive reach, again, was RM9.7 – RM7.4, where the 20% changes in settling velocity produced 100% changes in net deposition. The differences in gross erosion and deposition among reaches in response to changes in settling velocities are affected by the concentration dependent settling function used in the model. An increase in the settling velocity

function can cause increased deposition in one reach that reduces concentrations transported to another reach, which could generate a lower settling velocity than the original, because of the dependence on concentration. Vertical gradients in TSS, estimated from ABS data, provide an important constraint on the cohesive solids settling velocity because calculated vertical gradients in water column solids are sensitive to changes in settling velocity, but in a more systematic manner than erosion and deposition fluxes. The comparisons between simulated TSS and concentrations estimated from the PWCM ABS data indicate that the assigned settling velocity for cohesive solids is reasonable.

5.3.5 EROSION RATE OF COHESIVE PARTICLES

The 20% increase or decrease in the erosion rate of the cohesive particles results in a much smaller response (<3%) in the water column solids fluxes. The responses of both gross erosion (Figure 5-1) and gross deposition (Figure 5-2) are consistent with each other in each reach. The only reach with a response in gross erosion and deposition rates greater than 20% is between RM12.1 and RM9.7, where a 20% decrease in the erosion rate results in approximately a 27% reduction in both gross erosion and deposition. In this reach, an increase of ~38% in both the gross erosion and deposition rates results from a 20% increase in the cohesive solids erosion rates. With the exception of the most upstream reach, where there is little sensitivity, the other reaches show a response in gross erosion and gross deposition of between 8 and 18% to the 20% changes in erosion rates, with the response in the same direction as the change in erosion rate. The changes in cohesive solids erosion rates of $\pm$ 20% have a relatively small effect (<~5%) on the net fluxes at each transect, which is consistent with the responses in gross erosion and gross deposition, indicating that changes in the assigned cohesive sediment erosion rates influence solids cycling within each reach more than the net transport through the LPR.

5.3.6 EFFECTIVE GRAINSIZE OF MODEL SIZE CLASSES

To evaluate the sensitivity of the results of the sediment transport model to change in effective grainsize of the model size classes, two sensitivity simulations were performed by increasing and decreasing the representative grainsizes by 20%. Along with the grainsizes, critical shear stresses and erosion rates of the bulk sediment were changed to reflect the change in those inputs due to the change in average D_{50}. The critical shear stresses of the model grainsizes were also changed to reflect the change in the grainsize. It is noted that the fractions of the sediment in each size class specified in the initial conditions were not recomputed, so this sensitivity does not evaluate how the model would have behaved if different boundaries were used to divide the sediment into size classes. This sensitivity addresses the question of whether the model would behave differently if the sediment grainsize data were biased high or low.

The water column solids fluxes (Figure 5-4) show very low sensitivity to the representative grainsizes assigned to the non-cohesive solids classes. This suggests that contaminant transport between reaches and exported to Newark Bay is not highly sensitive to potential bias in the grainsize data used to develop initial conditions for sediment composition and size. Within each reach there is a consistent direction to the response of both the gross erosion and gross deposition. Between RM14.3 and 5.2, the response of both gross erosion and deposition within each reach was an increase in the gross rates with a decrease in the effective grainsize. The opposite response is seen in the most upstream reach. Downstream of RM5.2 both an increase and decrease in the effective diameter resulted in lower gross erosion and lower gross deposition fluxes, although the increase in the grainsize had more of an effect than the reduction. The response of the net deposition is quite varied.

These complicated responses arise because many factors are tied to the effective grainsize of non-cohesive solids. Additional factors that complicate interpretation of these results are the dependence of the application of cohesive versus non-cohesive erosion parameters on the D_{50}, and the effect of the D_{50} on grain stress partitioning. The conclusion, that the

overall solids transport between reaches and export to Newark Bay are not substantially affected by as much as a 20% bias in the effective grainsize, suggests that it is not essential to resolve the interconnections of grainsize (and D_{50}) on grain-stress partitioning, cohesive versus non-cohesive classification, critical shear stress, bed armoring, etc. to be able to address the primary factors affecting contaminant transport and fate. Based on the extensive data used to develop the grainsize initial conditions, and the results of these sensitivity analyses, it is concluded that the assigned representative grainsizes are reasonable.

5.4 SENSITIVITY ANALYSIS CONCLUSIONS

The sensitivity analysis results indicate that the transport of solids between reaches and export from the LPR to Newark Bay (Figure 5-4) is much less sensitive to variations in these selected parameters than the gross and net deposition and erosion behavior within sub-reaches of the river. The solids fluxes between sub-reaches and export to Newark Bay were most sensitive to upstream solids boundary conditions and the cohesive solids settling velocity function. Continued sampling of solids boundary inputs, including both concentration and composition, will continue to improve estimates of model boundary conditions. Comparisons of model results to the vertical gradient in suspended solids estimated from ABS data (see section 4 figures, starting at Figure 4-1) provides a good test that the assigned settling function appropriately characterizes the behavior of the mix of solids types transported into and through the LPR.

5.5 UNCERTAINTY

Model uncertainty can be evaluated using quantitative approaches such as Monte Carlo Analyses for models requiring limited computational resources and short simulation times. Addressing model uncertainty for computationally intensive models is much more of a challenge. Uncertainty analyses were performed for the Lower Duwamish Waterway's sediment transport model (Quantitative Environmental Analysis, 2008). These, involved developing upper and lower bound estimates for selected model inputs and running 6-year with permutations of the upper and lower bound values for the

selected parameters, requiring 2n simulations, where n is the number of parameters included in the analysis (i.e. 2n = 32 simulations for n = 5 parameters). Results from the simulations were compared to the calibration results to identify upper and lower bound sets of parameters which were then used in long-term simulations (21 years). This approach was considered for the FFS modeling, which includes hydrodynamics and sediment transport, a eutrophication model, and a contaminant fate and transport model. The time required to implement a similar approach and include each of these components was estimated 6 to 9 months, even with a dedicated bank of computers.

As an alternative, an approach discussed in USEPA's 2005 Contaminated Sediment Remediation Guidance for Hazardous Waste Sites, which relies on consideration of residuals between model results and data (Connolly and Tonelli, 1985) was adopted. The uncertainty propagated through the models is being evaluated using this approach with the exposure concentrations generated by the fate and transport model and passed to the risk assessment.

Although not propagated through the model components, residuals for the sediment transport model-data comparisons were analyzed. These include comparisons between computed TSS concentrations and estimates derived from ABS data collected as part of the CPG's 2009 PWCM program (Table 5-1) and bed elevation changes compared to differences computed from bathymetric survey data (Table 5-2). While the median relative errors for these comparisons might seem high, they represent a very strict test. Both data sets contain uncertainty, so the comparisons to the model results are not based on precise data values. Uncertainty in PWCM data is characterized on the time series plots (e.g. Figures 4-1 – 4-5) by prediction limits that account for variability in the TSS vs. ABS data used to develop the regressions and in the extrapolation of the regressions to higher and lower ABS values. In addition, small variations in timing of the TSS data can introduce substantial residuals because the data are changing rapidly in time.

Median relative errors for the bathymetric comparisons are based on grid-cell by grid cell comparisons, which is a strict test because patterns of erosion and deposition vary at

scales smaller than a grid cell, and the data available to develop model inputs are not available at the same fine-scale. Figure 5-5 summarizes the cumulative frequency distributions of bed elevation changes for three time periods. The agreement between the model and data is more consistent on this basis, with better agreement for the multibeam data sets than for the single beam data.

Table 5-1. Median Relative Errors for 2009 PWCM Estimate TSS Concentrations

Station at RM	Median Relative Error
1.4	-43.53%
4.2	-44.45%
6.7	-29.42%
10.2	-20.04%
13.5	3.06%

Table 5-2. Median Relative for Bed Elevation Changes for Single and Multibeam Data sets

Bathymetric Survey Period	Median Relative Error
2010 – 2011	-58.03%
2007 – 2010	-97.83%
1996 – 2004	-101.11%

6 SEDIMENT TRACER AND CAP STABILITY SIMULATIONS

The sediment transport model was used to evaluate solids transport behavior for existing bed conditions and several remedial scenarios involving dredging and capping. An evaluation of cap stability is described in Appendix BI.

6.1 SOLIDS TRACER SIMULATIONS – EXISTING SEDIMENT CONDITIONS

The model was used to perform simulations to contribute to the understanding of how sediment from various parts of the model domain is transported throughout the study area. The model was used to track solids from different sources (e.g. Dundee Dam, Newark Bay, tributaries) to evaluate how their relative proportions in sediment accumulations vary along the length of the river. The numerical tracking was accomplished by using separate state variables to represent silt-sized solids from different sources and calculating the fraction of the total deposition contributed by each state variable. Separate state variables were used to track the following sources

1. Upper Passaic River at Dundee Dam
2. Newark Bay
3. In-place Lower Passaic River sediments,
4. Tributaries, Stormwater and CSOs,
5. Hackensack River
6. Other (in-place sediments in the Kills), and
7. Open Boundaries

The hydrograph from water year 1998 was used for these simulations because the average flow at Little Falls for water year 1998 (1180 cfs) most closely matches the long-term average of 1140 cfs.

The relative contributions of the seven source categories to net cohesive sediment accumulation in each grid box at the end of the simulation of water year 1998 are

presented on Figures 6-1 through 6-7, and summarized in one mile increments in Figure 6-8. Deposition of the silt-sized particles passing over Dundee Dam accounts for the majority of the total cohesive sediment deposition upstream of RM12 ranging from nearly 100% at RM17 to approximately 70% at RM12 (Figures 6-1 and 6-8). The cells in this area with smaller fractions of Dundee Dam solids tend to have very small amounts of net deposition. From RM12 to RM10 the contribution to total deposition from Dundee Dam solids is roughly 25%, although in the year used for this tracer simulation, there was not much total accumulation in this reach. In the reach of the river between RM10 and RM6 accumulated silt-sized sediment originating from Dundee Dam accounts for approximately 60% of silt-sized solids accumulation. From RM6 to RM1 the Dundee Dam fraction drops to approximately 40%. From RM1 and out into Newark Bay, the fraction of deposition from solids that passes over Dundee Dam within the single year accounts for a rapidly declining fraction of the total deposition.

Resuspended LPR silt-sized sediment was tracked by transferring in-place bed sediment to a new state variable as it erodes into the water column. The resuspended LPR cohesive sediments account for a very small fraction of the total accumulation near RM17 and increase to about 10% between RM14 and RM12, with some high and low points in between (Figures 6-2 and 6-8). Between RM12 and RM10 resuspended LPR silts accounts for approximately 40% of the deposition, mainly because of two areas of localized deposition on the inside of bends in a reach that otherwise has fairly little deposition in this particular year. Between RM10 and RM6, resuspended LPR silt accounts for approximately 20% of the sediment accumulation, and this fraction increases to approximately 30% between RM6 and RM1. Downstream of RM1 and out into Newark Bay, the fraction from resuspended LPR sediment drops off as deposition shifts to tidal boundary (at the ends of the Kills) and resuspended Newark Bay silt becomes a dominant fraction of the fine-grained sediment deposition.

The open boundary, Newark Bay, and Hackensack River, and combined tributaries plus CSOs/Stormwater behave similarly, representing a diminishing fraction of the deposition with distance upstream of Newark Bay (Figures 6-3, 6-4, 6-5, and 6-8).

Contributions to total deposition from cohesive solids originating in Tributaries and CSO/stormwater (Figures 6-6 and 6-8) are fairly small because of the relatively small loading from these sources. The largest contribution from the tributaries is in the vicinity of the Saddle River where there are individual cells where the cohesive solids deposition is as much as 80% tributary solids, and the 1-mile average is about 10%. Over the rest of the river these two components generally make up about 3 - 5% of the cohesive solids deposition. Contribution of silt originating from in-place sediment in the Kills is fairly negligible in the LPR (Figure 6-7).

The contributions of the various solids sources to deposition averaged over one-mile reaches of the river are summarized on Figure 6-8. The empirical mass balance (EMB) analysis (Appendix C) produces one average estimate of the contribution of these various sources, while the sediment transport model shows spatial variations. The EMB estimates 48% of the deposition from resuspended LPR sediment, 32% from solids passing over Dundee Dam, almost 14% from Newark Bay, slightly less than 6% from tributaries and less than 0.5% from CSOs. These tracer simulation results averaged over RM2-12 (the appropriate spatial extent to compare to the EMB) indicate a higher proportion (39%) of the total mass accumulation from silts input at Dundee Dam and a lower fraction (33%) of the accumulation from resuspended LPR sediment. The 1-mile averages and maps of the relative contributions from each category do show variability around the average values, and it is important to note that the model results would vary some, depending on the hydrograph selected for the analysis. Considering that these tracer simulation results are for only a one-year simulation, agreement with the EMB results is quite reasonable.

6.2 SOLIDS TRACER SIMULATIONS – WITH REMEDIATION COMPONENTS

Additional numerical tracking simulations were performed as part of an evaluation of potential active remedial alternatives. These simulations were used to evaluate how solids from one section of the river would be transported to a remediated section, and

deposited on top of the post-remediation clean surface. These simulations were performed to address questions of recontamination of potential active remedial alternatives and where to begin remediating the LPR. Bank-to-bank remedial alternatives for different reaches were simulated as representative of active remedial alternatives for this particular evaluation. Two of three simulations use existing bathymetry and one uses a deeper bathymetry in the FFS Study Area.

6.2.1 River Mile 0-8.3 Cap Simulation

The FFS includes consideration of a bank-to-bank cap over the FFS Study Area. A simulation was performed to assess the degree to which fine grained sediments from the reach between RM8.3 and RM12, or from Newark Bay, could erode and deposit on top of a cap in the FFS Study Area. For this simulation, the model inputs describing the top two feet of sediment in the FFS Study Area were changed to reflect the characteristics of upland borrow sand, which has only 1% in the cohesive size class and is much courser than the native sediment. As in the tracer simulations for native sediment, this simulation used different state variables in the sediment transport model to track the movement of solids from two potentially contaminated areas: RM8.3 - RM12 of the LPR and Northern Newark Bay/Hackensack River.

The spatial distribution of the total deposition contributed by sediment from RM8.3 to RM12 of the LPR (Figure 6-9) and Northern Newark Bay and the Hackensack River (Figure 6-10) are presented in a format consistent with the previous tracer simulation results. The results of this simulation indicate that solids eroded from the RM8.3 - RM12 reach represent between 5 and 10 percent (average ~7%) of the solids deposited on top of the RM0 - RM8.3 cap, at the end of this one-year simulation. Sediment transported into the LPR from Northern Newark Bay and the Hackensack River contributes over 40% of the total deposition in a number of LPR grid cells as far upstream as RM5, with more accumulation of Newark Bay/Hackensack River Silt on the outsides of the bends between RM2 and RM 4. Newark Bay and Hackensack River silt accounts for 31% of all of the silt accumulation on top of the RM0 - RM8.3 cap.

The preceding results are summarized by one-mile reaches of the LPR on Figure 6-11. Approximately seven percent of the solids calculated to accumulation on top of the cap come from the RM8.3 - RM12 reach of the LPR. In the upstream half of the 8-mile cap, 15 to 28% of the net accumulation is from solids transported in from Newark Bay and the Hackensack. In the lower four miles, this contribution varied from 17% to 31% over these one-mile reaches.

6.2.2 River Mile 0-8.3 Remediated with Deepened Bathymetry Simulation

A second sediment tracer simulation was performed to evaluate the contributions of unremediated silt from LPR RM8.3 to RM 12 and Newark Bay/Hackensack River to silt accumulation in the FFS Study Area if the bathymetry in the FFS Study Area were deepened, consistent with a potential remedial alternative. The summary of the results for the deepened bathymetry (Figure 6-12) show a similar average contribution (~7%) of RM8.3 - RM12 silt to accumulation in the RM0-8.3 reach, although with more of a spatial gradient from upstream to downstream. Between RM4 and RM8.3, approximately 10% of the silt accumulation originates from the RM8.3-12 reach, and this fraction drops to approximately 7% between RM2 and RM4, and to less than 2% in the lower two miles, where accumulation of silt from Northern Newark Bay and the Hackensack increases to between 35 and 40% of the total silt accumulation. With the deepened bathymetry, the overall silt accumulation in the FFS Study Area increases by almost a factor of two, but the fraction from RM8.3-12 silt remains relatively constant.

6.2.3 River Mile 8.3-12 Cap Simulation

A third sediment tracer simulation was performed to evaluate the progression of a remedy from upstream to downstream. In this case the inputs to the model for the reach of the river between RM8.3 and RM12 were modified to represent a two-foot thick cap, constructed to original grade. As in the previous simulations, fine-grained sediments from different areas were assigned to different state variable. Silt from northern Newark Bay and the Hackensack River were represented by one state variable, the unremediated

fine-grained sediments of the FFS Study Area were represented by another, and all other fine grained sediments were represented by a third cohesive size class (in addition to the non-cohesive size classes). The summary of the results of the RM8.3 - RM12 cap, shown on Figure 6-13, indicate that over one third of the solids accumulating on top of the RM8.3 - RM12 cap came from the unremediated area between RM0 and RM83. More fine-grained sediments from an unremediated FFS Study Area accumulated on top of the RM8.3-12 cap than accumulated on top of the FFS Study Area cap from an unremediated RM8.3-12 area.

6.3 REMEDIAL ALTERNATIVE SIMULATIONS

The sediment transport model was used to simulate future conditions for four alternatives being evaluated for the FFS Study Area:

Alternative 1 – No Action
Alternative 2 – Deep Dredging with Backfill (Deep Dredging)
Alternative 3 – Capping with Dredging for Flooding and Navigation (Full Capping)
Alternative 4 – Focused Capping with Dredging for Flooding – (Focused Capping, addresses about 33% of the FFS Study Area)

The hydrographs (and other tidal forcing) for the period October 1995 – October 2010 (water years 1996-2010) were repeated in 15-year cycles to simulate conditions into the future to October 2059, which is 30 years after remedy-related construction would be completed. Bathymetry associated with completion of the HDP was assigned at the start of each of the future condition 15-year cycles. Model simulation inputs and results for the period October 1995-March 2018 are common to all alternatives. Boundary conditions for TSS were developed as a function of river flow, and not changed over time into the future. Contaminant conditions specific to each particular alternative are described below. All alternatives include completion of the Phase 1 and Phase 2 Tierra Removals and the RM10.9 removal.

Releases of solids from dredging operations are simulated for each alternative when dredging is represented without the construction of a coffer dam or sheet-pile enclosure. The total mass of sediment to be dredged divided by the dredging duration for an individual grid cell was multiplied by a dredging-loss rate to determine a solids source rate to the water column. A dredging-loss rate of 3% was specified, based on data from the 2005 Environmental Dredging and Decontamination Pilot Study (LBG 2012) and data from other sediment sites. Losses during dredging were simulated in the model split equally between the surface and bottom water column layers. These are the two points in the dredging operation where the greatest losses are expected.

6.3.1 Description of Alternatives

Alternative 1 – No Action – This alternative does not include any additional remediation beyond the Phase 1 and Phase 2 Tierra Removals and the RM10.9 removal.

Alternative 2 – Deep Dredging with Backfill – Dredging of the FFS Study Area begins in March 2018 and is completed in 2029 progressing from upstream at RM8.3 downstream to RM0. The simulation includes completion of the Tierra Removal, Phases 1 and 2, and the RM10.9 Removal with the same schedule and assumptions as used in Alternative 1. Substantial changes in bathymetry result from the removal of 9.7 million cubic yards (cy) of sediment as part of Alternative 2.

The bathymetry used in the hydrodynamic model was adjusted each timestep during the dredging period to account for the depth changes in the individual grid cell where dredging was being simulated at an average production rate. The bed composition was modified at the completion of dredging and backfilling in each grid cell.

Alternative 3 – Capping with Dredging for Flooding and Navigation – For the Alternative 3 scenario, dredging of the FFS Study Area begins in March 2018 and is completed in 2022. Dredging of the federally authorized navigation channel progresses upstream from RM0 to RM2.2. Then dredging for flooding progresses from RM8.3 downstream to

RM2.2, followed by restoration of the Kearny flats near RM0. Alternative 3 includes completion of the Tierra Removal, Phases 1 and 2, and the RM10.9 Removal with the same schedule and assumptions as used in Alternative 1.

The volume dredged in the Alternative 3 simulation, 4.3 million cy, is approximately 44% of the volume dredged in the Alternative 2.

Because sediment removal and cap placement are designed to bring the river bed back to original grade, bathymetric changes were not included in the hydrodynamic model, except in the areas deepened for navigation. Changes in bathymetry are included in the hydrodynamic model each timestep as dredging progresses in grid cells deepened for navigation. The composition of the bed was changed to represent the new cap material (sand) when removal and capping was completed in each individual grid cell.

Alternative 4 – Focused Capping with Dredging for Flooding – For the simulation of Alternative 4, dredging of the FFS Study Area begins in March 2018 and is completed in 2019. Dredging progresses from upstream near RM8.3 to downstream near RM0, addressing selected cells targeted for remediation. Alternative 4 includes completion of the Tierra Removal, Phases 1 and 2, and the RM10.9 Removal with the same schedule and assumptions as used in Alternative 1.

Model grid cells were selected for Focused Capping based on the gross and net contaminant resuspension per unit area from each grid cell computed by the contaminant model in a No Action simulation based on a knee of the curve analysis. The selected cells represent approximately 33 % of the RM0-8 surface area. The volume dredged in the Alternative 4 simulation, one million cy, is approximately 10% of the volume dredged in Alternative 2.

6.3.2 Sediment Bed Changes in Alternatives

Maps showing the spatial patterns of bed elevation changes in each grid cell for the four alternatives are presented on Figures 6-14 through 6-17. Results for the period after completion of the active remediation are presented on these maps to facilitate comparisons among the alternatives. Because the duration of the construction for each of the active remediation alternatives is different, comparisons among the alternatives are complicated by both the timing and location of remediation. Note that the No Action simulation covers a 17-year period, while the remediation scenarios are each 15 yeas long, and therefore, the bed elevation changes on Figures 6-14 through 6-17 are presented in terms of cm/yr rather than simply centimeters of change.

The similarities between the No Action (Figure 6-14) and Alternative 4 - Focused Capping (Figure 6-17) are not unexpected because Alternative 4 doesn't involve any changes in bathymetry. The increase rate of infilling in the results from Alternative 2 – Deep Dredging, compared to the No Action simulation is apparent in many locations across the FFS Study Area, particularly upstream of RM7, which is near the upstream limit of the deepening. Increased sediment accumulation rates in the results for Alternative 3 - Full Capping are most noticeable downstream of RM2.2, where the deepening for the navigation channel is included. In this reach, sediment accumulation for the Full Capping Alternative exceeds the accumulation rate for the Deep Dredging Alternative, suggesting that the accumulation may be supply limited, and that more widespread accumulation in the Deep Dredging Alternative limits sediment available for deposition in the reach downstream of RM2.2.

The rates of sediment accumulation for the four alternatives are summarized by 1-mile reaches on Figures 6-18 through 6-21. The results for the No Action (Figure 6-18 and Focused Capping Alternative (Figure 6-21) are very similar, with the differences attributed to the slightly different hydrograph in the 17-year No Action simulation compared to the 15-year period for the alternatives. Figures 6-18 and 6-20 highlight the increase in sediment accumulation in the portion of the river downstream of RM2.2

where the deepening for the navigation channel creates a zone of preferential deposition in the Full Capping Alternative. An increase within the FFS Study area of the sediment accumulation rate in the Deep Dredging alternative (Figure 6-21) is more than double the accumulation rate in the No Action simulation. The sediment mass accumulated in the FFS Study Area of approximately 52,000 MT per year is approximately 115% the total average solids loads from the combined inputs over Dundee Dam and from tributaries and CSOs. This suggests that the rate of infilling is limited by the supply of solids from freshwater inputs and Newark Bay.

7 REFERENCES

AECOM. 2010a. Low Resolution Coring Characterization Summary, Lower Passaic River Study Area RI/FS, March 2010.

AECOM. 2010b. Quality Assurance Project Plan/Field Sampling Plan Addendum, Remedial Investigation Water Column Monitoring/Physical Data Collection for the Lower Passaic River, Newark Bay and Wet Weather Monitoring. Prepared for Lower Passaic River Cooperating Parties Group. Lower Passaic River Restoration Project, Newark, NJ. Revision 4. March 2010.

AECOM, 2010c. Quality Assurance Project Plan for Lower Passaic River Restoration Project: Periodic Bathymetry Surveys, Revision 2.

Aqua Survey, Inc., 2006. Technical Report, Geophysical Survey, Lower Passaic River Restoration Project, June 2006.

Blumberg, A.F. and G.L. Mellor. 1980. A coastal ocean numerical model. In: Mathematical Modeling of Estuarine Physics, Proceedings of an International Symposium, Hamburg, August 24–26, 1978. J. Sundermann and K.P. Holz, Eds., Springer-Verlag, Berlin.

Blumberg, A. F. and G.L. Mellor. 1987. A description of a three-dimensional coastal ocean circulation model. In: Three-Dimensional Coastal Ocean Models, N.S. Heaps, Ed. American Geophysical Union, pp. 1–16.

Borrowman, T.D., 2005. Passaic River Sedflume Experiment Log. U.S. Army Engineer Research and Development Center, Vicksburg, MS. June 2005.

Cannelton Industries, Inc. 1998. Stability of Tannery Sea Sediments: Revision 1, Report, submitted to USEPA Region V, Cannelton Industries, with Technical Support by Conestoga-Rovers and Associated and HydroQual.

Chant, R.J. 2005. Hydrodynamics of the Newark Bay/Kills system, New Jersey. Report prepared for New Jersey Department of Environmental Protection, Toxics Reduction Workplan for New York-New Jersey Harbor, Study I-E.

Chant, R.J., D. Fugate, and E. Garvey, 2010. The Shaping of An Estuarine Superfund Site: Estuaries and Coasts. Published online, 10 September, 2010.

Cheng, N.-S. 1997. Simplified settling velocity formula for sediment particle. Journal of Hydraulic Engineering, 123: 149–152.

Chesapeake Biogeochemical Associates, 2006. Passaic River Erosion Testing and Core Collection: Field Report and Data Summary. Prepared for Malcolm Pirnie, Inc. under Subcontract No. KC-ACE2002-31, March 2006.

Connolly, J.P., and R. Tonelli, 1985. Modeling Kepone in the Striped Bass Food Chain of the James River Estuary. Estuarine Coastal and Shelf Science (20), pp. 349-366, 1988.
Galperin, B., L.H. Kantha, S. Hassid, and A. Rosati. 1988. A quasi-equilibrium turbulent energy model for geophysical flows. Journal of the Atmospheric Sciences, 45: 55–62.

ENSR. 2008. Quality Assurance Project Plan RI Low Resolution Coring/Sediment Sampling Lower Passaic River Restoration Project Newark, New Jersey. May 2, 2008. Revision 1 July 18, 2008; 2 July 24, 2008; 3, July 29, 2008; and 4 October 20, 2008.

Ferguson, R.I. 1986. River loads underestimated by rating curves. Water Resources Research 22(1):74-76

Gessler, J. (1967). The beginning of bedload movement of mixtures investigated as natural armoring in channels. Translation T-5. California Institute of Technology, Pasadena CA.

Glenn, S.M. and W.D. Grant. 1987. A suspended sediment stratification correction for combined wave and current flows. Journal of Geophysical Research, 92: 8244–8264.

Grant, W.D. and O.S. Madsen. 1982. Movable bed roughness in unsteady oscillatory flow. Journal of Geophysical Research, 87: 469–481.

HDR|HydroQual, 2013. "Report of the Peer Review of Sediment Transport, Organic Carbon and Contaminant Fate and Transport Model." Project Number: 337-193191, HDR|HydroQual, September 2013.

HydroQual, Inc. 1998. Development and Application of a Modeling Framework to Evaluate Hurricane Impacts on Surficial Mercury Concentrations in Lavaca Bay.

HydroQual, Inc. 2007a. A Primer for ECOMSED, Version 1.4. December 2007.

HydroQual, Inc. 2007b. A model for the evaluation and management of contaminants of concern in water, sediment, and biota in the NY/NJ Harbor Estuary. Sediment Transport/Organic Carbon Production Sub-model. Report prepared for the Hudson River Foundation on behalf of the Contamination Assessment and Reduction Project (CARP).

HydroQual, Inc. 2008. Final Hydrodynamic Modeling Report of the Lower Passaic River Restoration Project and Newark Bay Study, January 2008.

James, S.C., C.A. Jones, M.D. Grace, and J.D. Roberts. 2010. Advances in sediment transport modeling. Journal of Hydraulic Research, 48(6): 754–763

Jepsen, R.A., J.D. Roberts, and W. Lick. 1997. Effects of bulk density on sediment erosion rates. Water, Air, & Soil Pollution, 99(1–4): 21–31.

Jones, C. and W. Lick. 2001. Contaminant flux due to sediment erosion. Proceedings of the 7th International Conference: Estuarine and Coastal Modeling, pp. 280–293.

Krone, R.B. 1962. Flume Studies of the Transport of Sediment in Estuarial Processes, Final Report, Hydraulic Engineering Laboratory and Sanitary Engineering Research Laboratory, University of California, Berkeley.

Lick, W., J. Lick, and C.K. Ziegler. 1994. The resuspension and transport of fine-grained sediments in Lake Erie. Journal of Great Lakes Research, 20(4):599–612.

Little, W.C. and P.G. Mayer. 1972. The role of sediment gradation on channel armoring. ERC-0672. Georgia Institute of Technology, Atlanta GA.

Louis Berger Group, Inc. (LBG), 2012. "Environmental Dredging Pilot Study Report." Prepared by LBG for USACE New York District. July 2012.

Malcolm Pirnie, Inc. 2006. "Lower Passaic River Restoration Project Field Sampling Plan Volume 1." January 2006.

Malcolm Pirnie, Inc., 2005. Quality Assurance Project Plan Lower Passaic River Restoration Project. Prepared in conjunction with Battelle and HydroQual, Inc. August 2005.

McNeil, J., C. Taylor, and W. Lick. 1996. Measurement of erosion of undisturbed bottom sediments with depth. Journal of Hydraulic Engineering, 122(6): 316–324.

Mellor, G.L. and T. Yamada. 1982. Development of a turbulence closure model for geophysical fluid problems. Reviews of Geophysics and Space Physics, 20: 851–875.

Moffat & Nichol and Deltares, 2013. LPR/NB RI/FS Modeling Program - Status of the CPG's Sediment Transport Model. Prepared for the Cooperating Parties Group, January 2013.

Quantitative Environmental Analysis, 2008. Lower Duwamish Waterway Sediment Transport Modeling Report –Final. Prepared for U.S. Environmental Protection Agency Region 10 Seattle, WA and Washington State Department of Ecology Northwest Regional Office Bellevue, WA. October 2008.

Roberts, J., R. Jepsen, D. Gotthard, and W. Lick. 1998. Effects of particle size and bulk density on erosion of quartz particles. Journal of Hydraulic Engineering, 124(12): 1261–1267.

Sanford, L.P. 2008. Modeling a dynamically varying mixed sediment bed with erosion, deposition, bioturbation, consolidation, and armoring. Computers & Geosciences, 34: 1263–1283.

Sanford, L.P. and Maa, J.P.-Y. 2001. A unified erosion formulation for fine sediments. Marine Geology, 179(1-2): 9-23.

Sea Engineering, Inc., 2008 Sedflume Consolidation Analysis, Passaic River, New Jersey. Prepared for HydroQual, Inc. and USEPA. December, 2008.

Sea Engineering, Inc., and HDR|HydroQual, 2011. Lower Passaic River System Understanding of Sediment Transport May 2011.

Shrestha, P.L., A.F. Blumberg, D.M. Di Toro, and F. Hellweger. 2000. A three-dimensional model for cohesive sediment transport in shallow bays, Invited Paper, ASCE Joint Conference on Water Resources Engineering and Water Resources Planning and Management, July 30-August 2, 2000, Minneapolis, MN.

Sommerfield, C.K. and R.J. Chant. 2010. Mechanisms of Sediment Trapping and Accumulation in Newark Bay, New Jersey: An Engineered Estuarine Basin (HRF 008/07A). Final Report to Hudson River Foundation, New York, NY, July 2010.

Tierra Solutions, Inc. 2007. Newark Bay Study Area Remedial Investigation Work Plan, Phase II [Rev.2, Amendment 1]. November 2007.

Tierra, Solutions, Inc. 2005. Newark Bay Study Area Remedial Investigation Work Plan [Rev.1]. September 2005.

Tierra Solutions, Inc. (Tierra). 1995. Passaic River Study Area Remedial Investigation and Feasibility Study Work Plans, Volume 3 of 5: Field Sampling Plan and Feasibility Study Work Plan. January 1995.

USACE, 2006. Erodibility Study Of Passaic River Sediments Using USACE Sedflume. U.S. Army Engineer Research and Development Center, Vicksburg, MS. June 2006.

USEPA, 2006. "Peer Review Handbook 3rd Edition." EPA/100/B-06/002. Prepared for the USEPA by Members of the Peer Review Advisory Group, for EPA's Science Policy Council.

USEPA, 2009. Understanding the Use of Models in Predicting the Effectiveness of Proposed Remedial Actions at Superfund Sediment Sites. OSWER Directive 9200.1-96FS, November 2009.

USGS, 2013. Personal communication. Emails from A. McHugh to E. Garland regarding updated flood frequency for USGS Passaic River at Little Falls, NJ gage(01389500) August 13 and December 3, 2013.

van Rijn, L.C. 1993. Principles of Sediment Transport in Rivers, Estuaries and Coastal Seas, Aqua Publications, Amsterdam, The Netherlands.

Warner, J.C., C.R. Sherwood, R.P. Signell, C.K. Harris, and H.G. Arango. 2008. Development of a three-dimensional, regional, coupled wave, current, and sediment-transport model. Computers & Geosciences, 34(10): 1284–1306.

Winterwerp, J.C. and W.G.M. van Kesteren. 2004. Introduction to the Physics of Cohesive Sediment in the Marine Environment. Amsterdam, The Netherlands, Elsevier B.V.

Ziegler, C.K. and B.S. Nisbet. 1994. Fine-grained sediment transport in Pawtuxet River, Rhode Island. Journal of Hydraulic Engineering, 120(5): 561–576.

Ziegler, C.K. and B.S. Nisbet. 1995. Long-Term Simulation of Fine-Grained Sediment Transport in Large Reservoir. Journal of Hydraulic Engineering 121(11): 773-781.

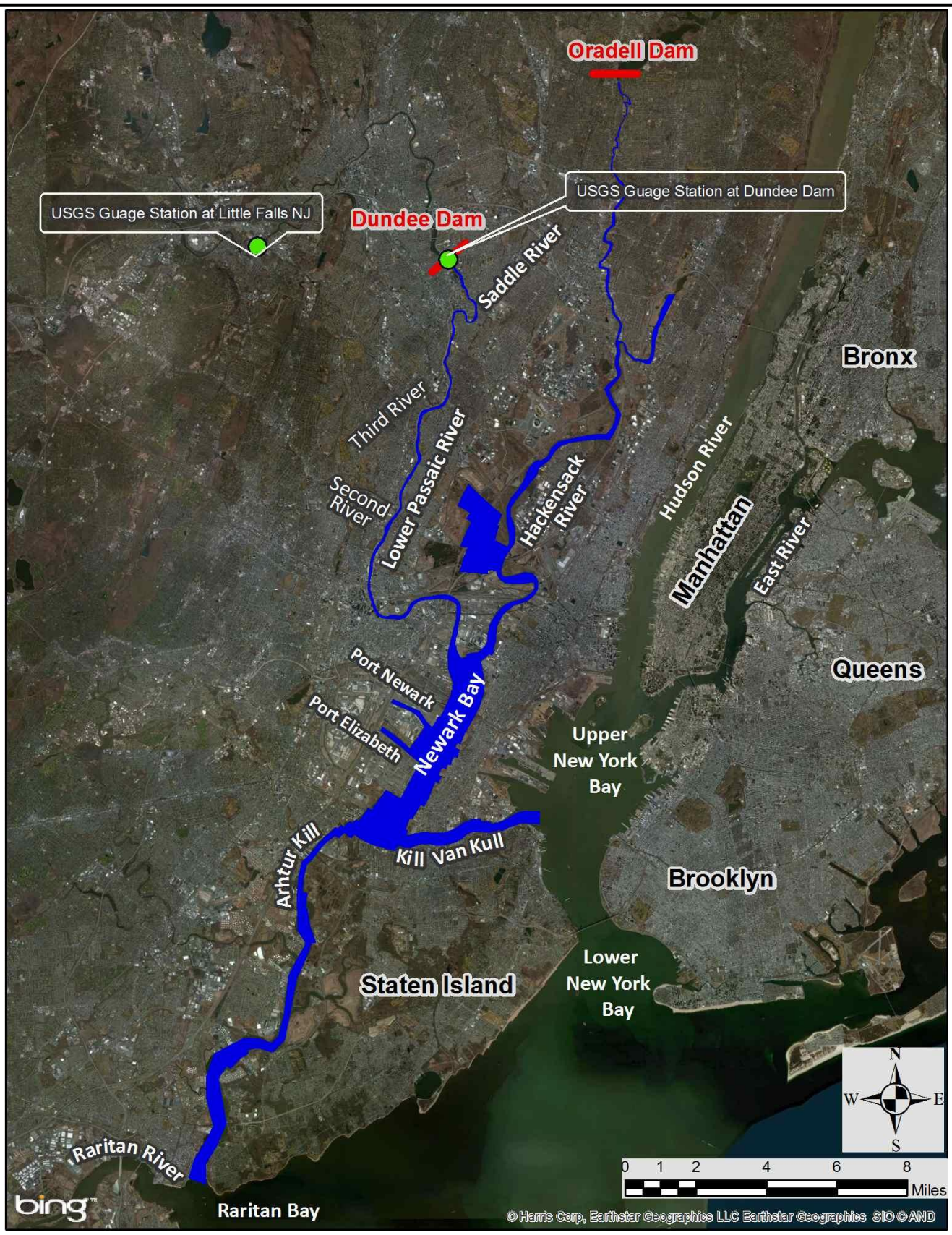

Location Map	Figure 1-1
Lower Eight Miles of the Lower Passaic River	2014

Summarizing the following classification is proposed by Van Rijn:

Transport regime		Particle size	
		$1 \leq D_* \leq 10$	$D_* > 10$
Lower	$0 \leq T \leq 3$	mini-ripples	dunes
	$3 < T \leq 10$	mega-ripples and dunes	dunes
	$10 < T \leq 15$	dunes	dunes
Transition	$15 < T < 25$	washed-out dunes, sand waves	
Upper	$T \geq 25$, $Fr < 0.8$	(symmetrical) sand waves	
	$T \geq 25$, $Fr \geq 0.8$	plane bed and/or anti-dunes	

Table 5.1 *Classification of bed forms according to Van Rijn*

Quantitative classification of bedform regimes for unidirectional flow from Van Rijn (1993), where T is non-dimensional excess stress and D* is non-dimensional grainsize as defined in the text

Figure 2-1

2014

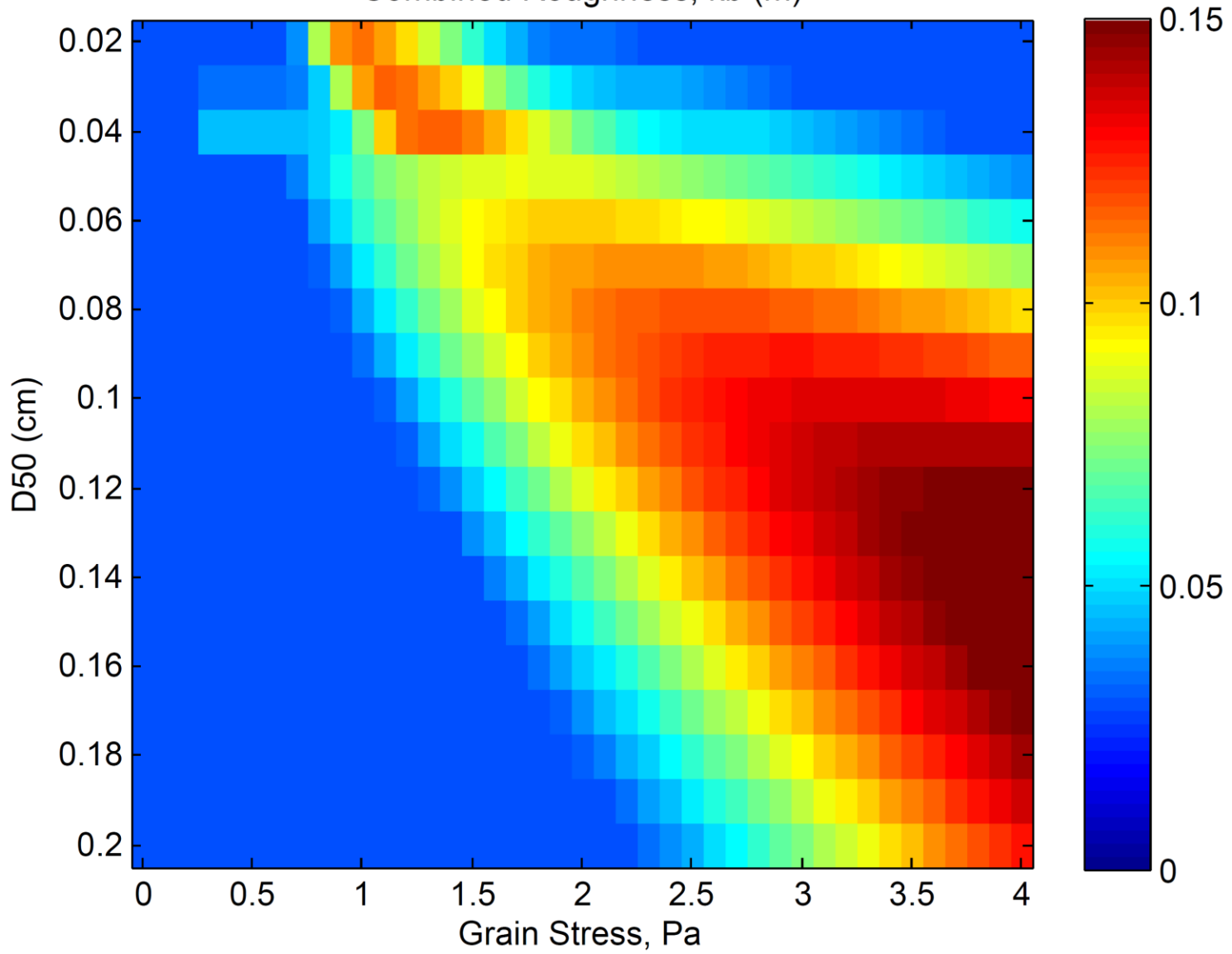

Example calculation of the physical roughness height, kb = 30 Z0B, (Eqs. 2-13 to 2-15) with h = 5m

Lower Eight Miles of the Lower Passaic River

Figure 2-2

2014

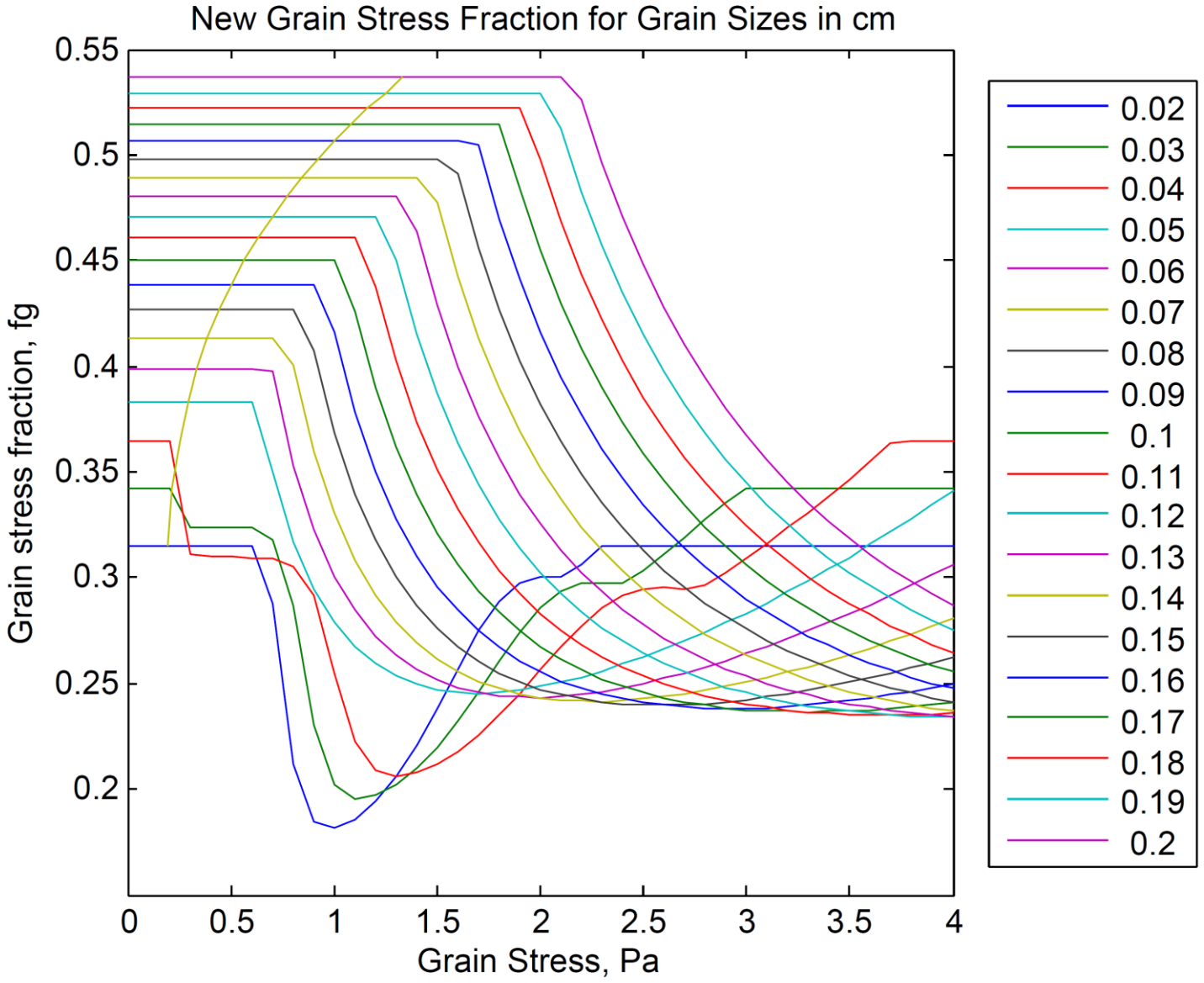

Change in grain stress fraction as a function of grain stress and grainsize (Eq. 2-16)

Lower Eight Miles of the Lower Passaic River

Figure 2-3

2014

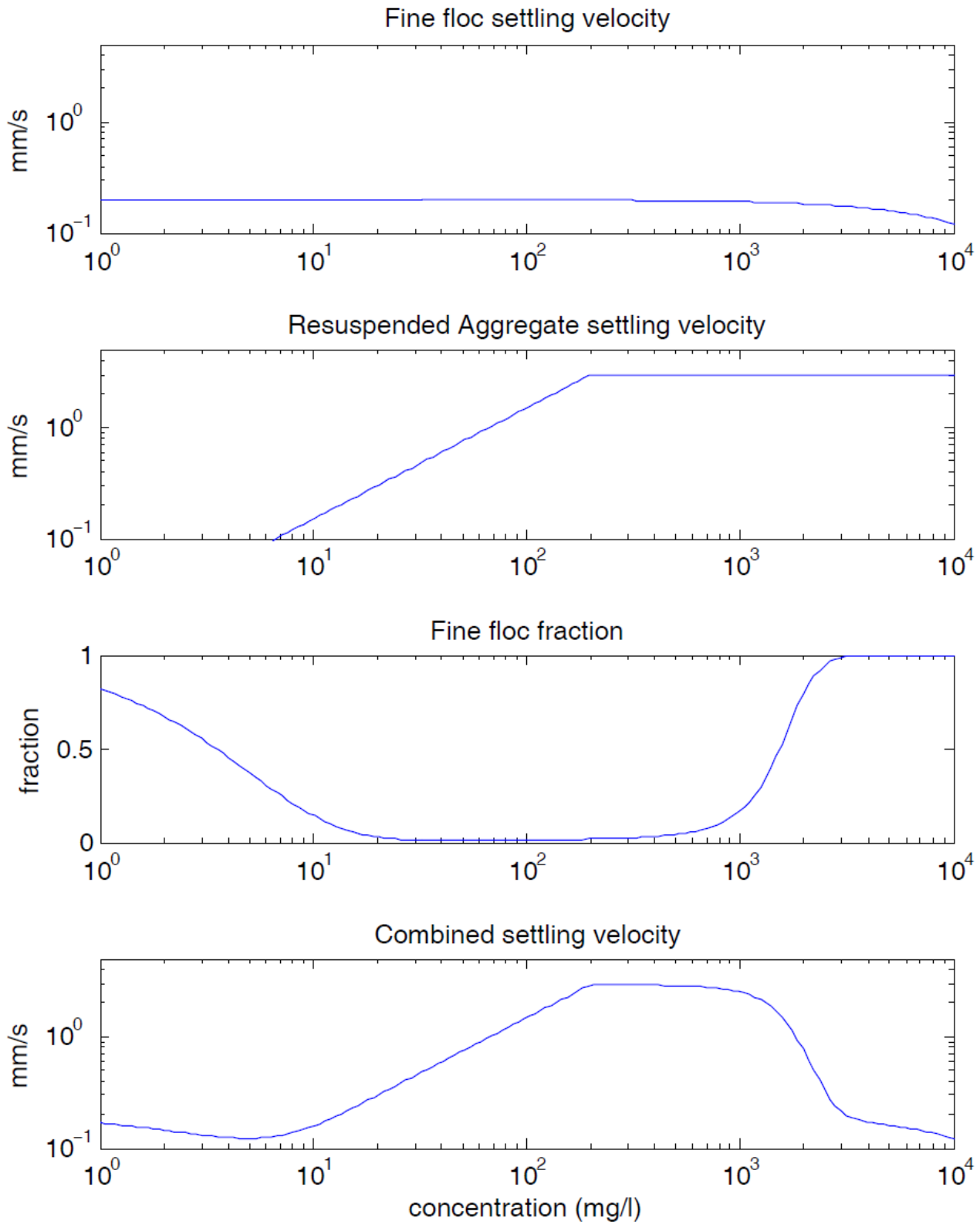

Representations of the concentration dependence of the components of the cohesive settling velocity formulation

Lower Eight Miles of the Lower Passaic River

Figure 2-4

2014

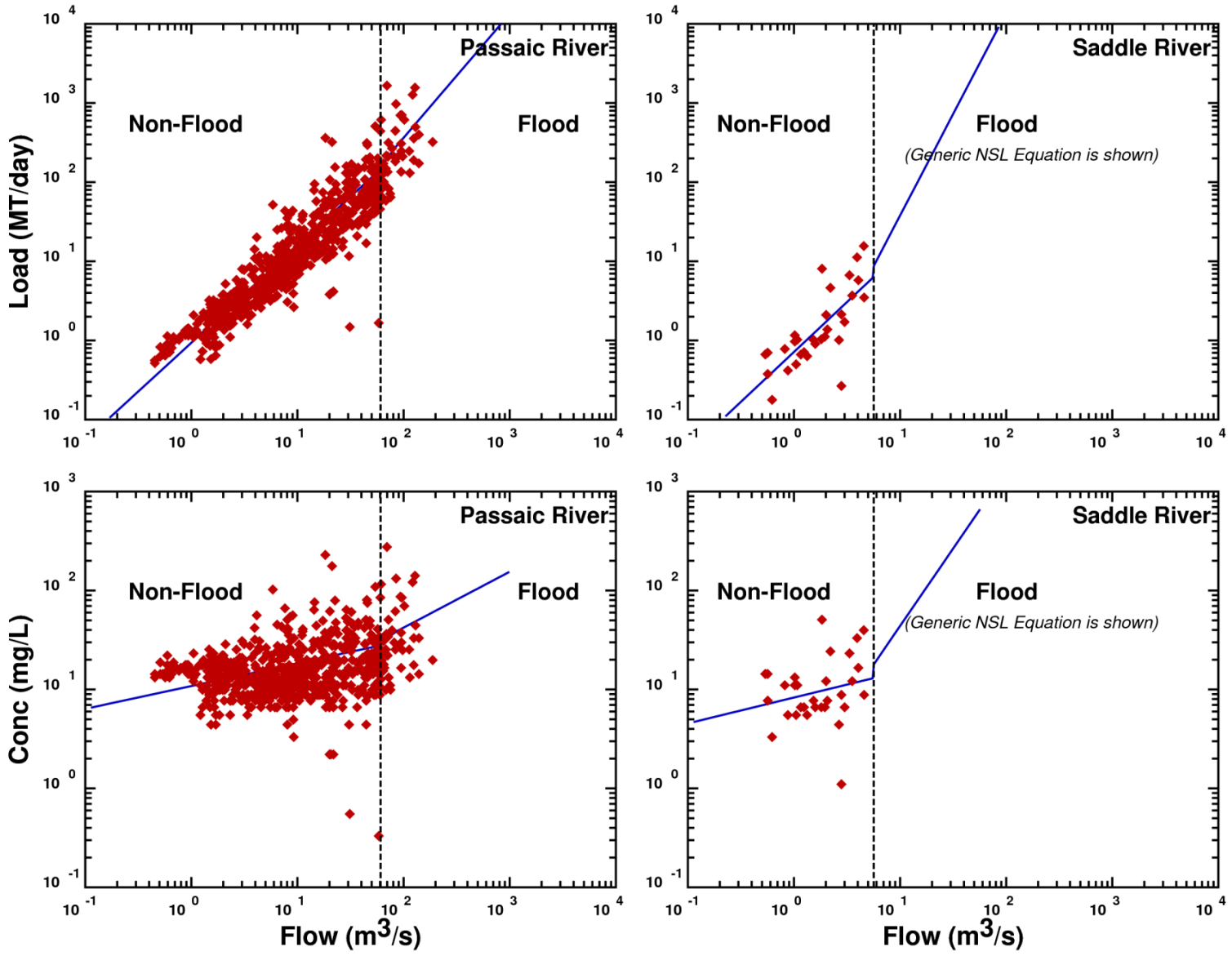

Suspended sediment data from the Upper Passaic River and the Saddle River versus river flow

Figure 3-1

Lower Eight Miles of the Lower Passaic River

2014

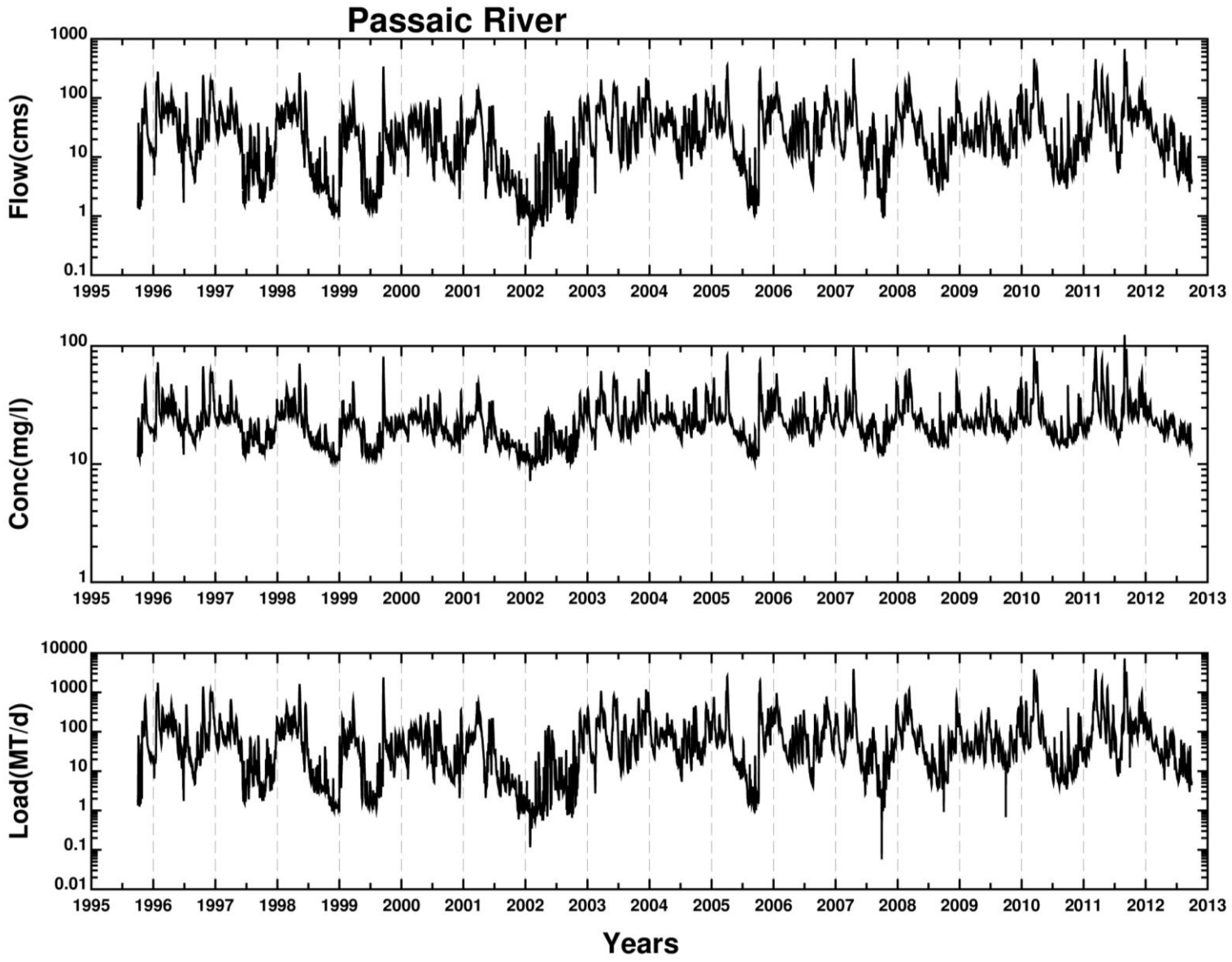

Flow, suspended solids concentration and solids mass loading in Upper Passaic River

Lower Eight Miles of the Lower Passaic River

Figure 3-2

2014

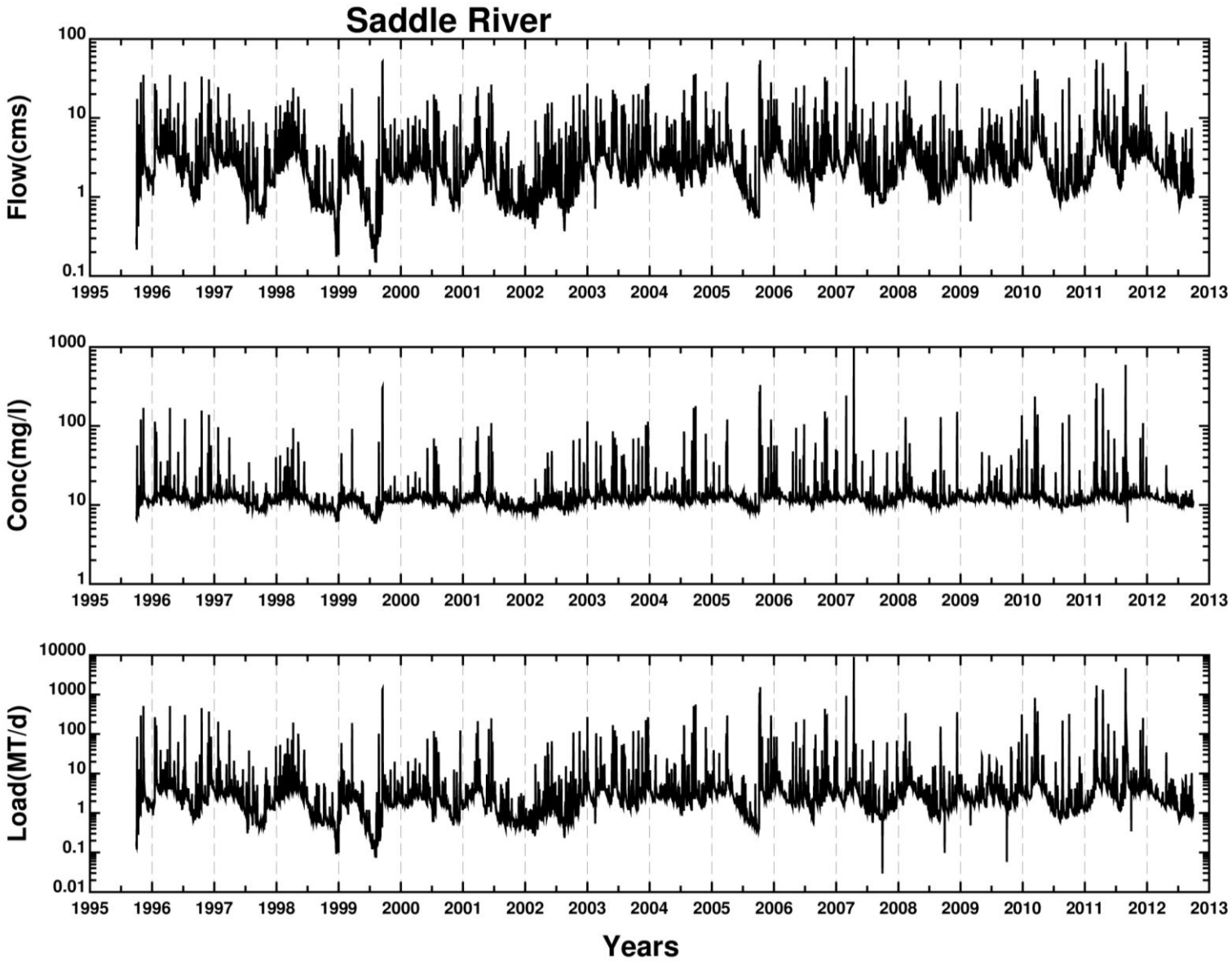

Flow, suspended solids concentration and solids mass loading in Saddle River

Figure 3-3

Lower Eight Miles of the Lower Passaic River

2014

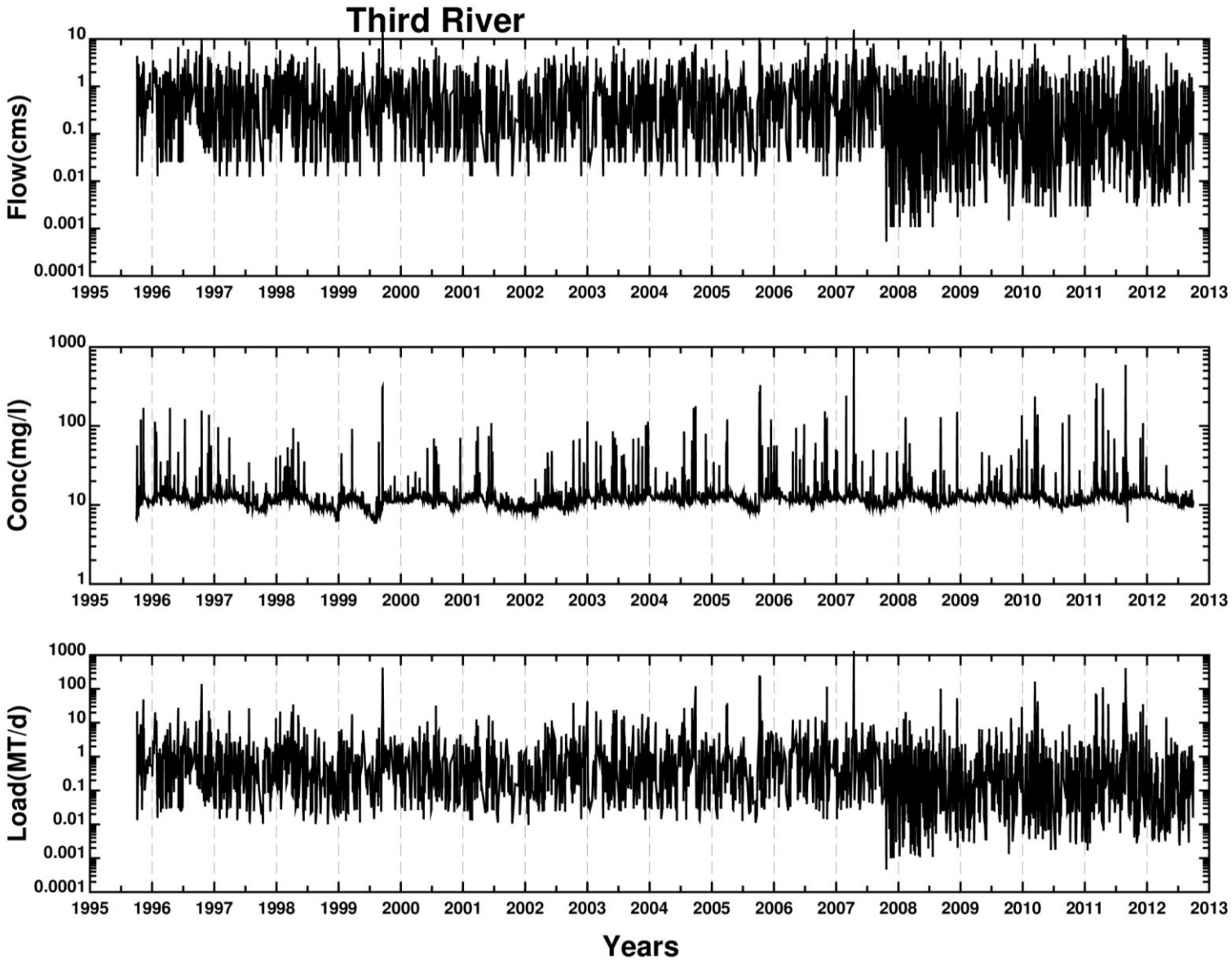

Flow, suspended solids concentration and solids mass loading in Third River

Figure 3-4

Lower Eight Miles of the Lower Passaic River

2014

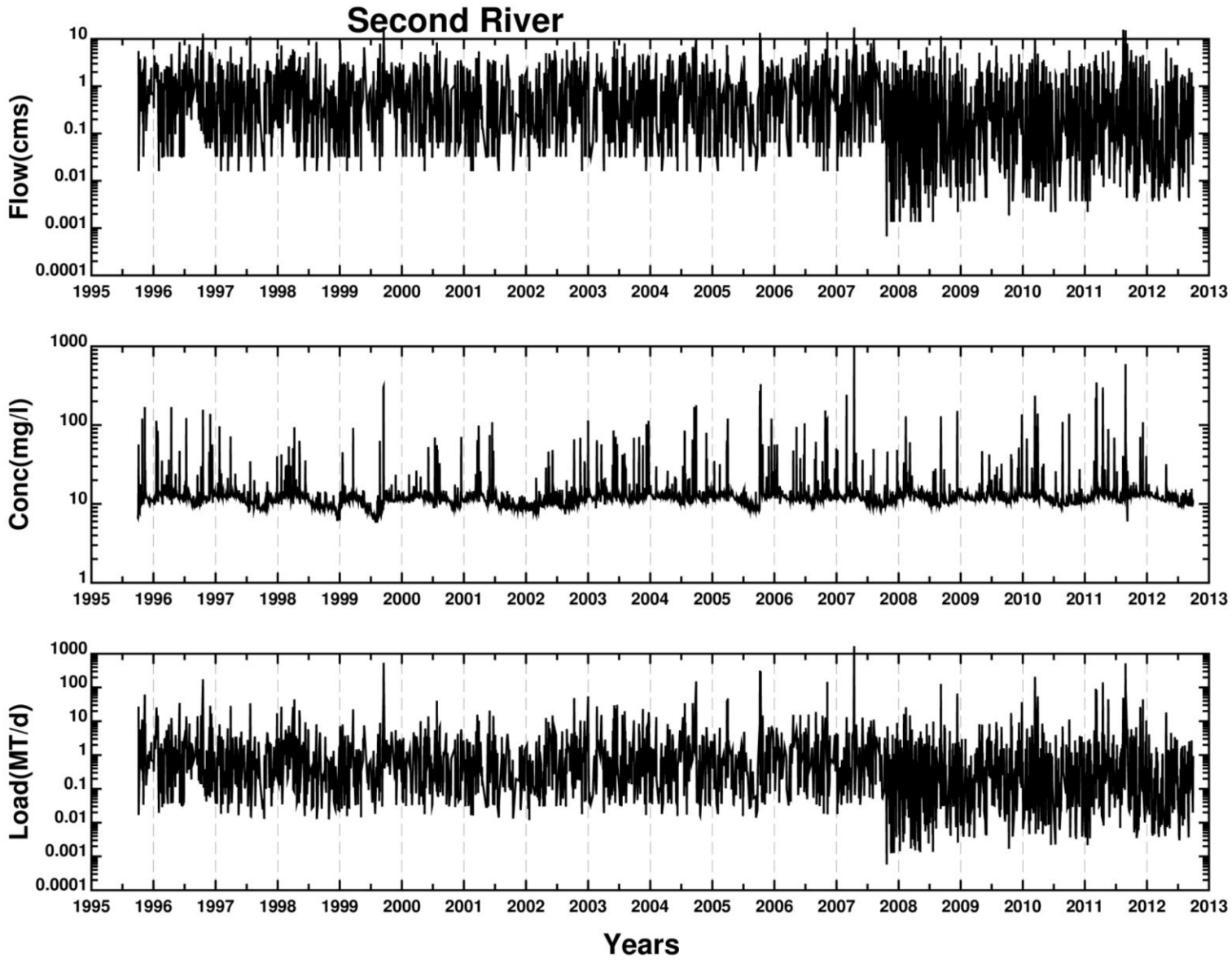

Flow, suspended solids concentration and solids mass loading in Second River

Figure 3-5

Lower Eight Miles of the Lower Passaic River

2014

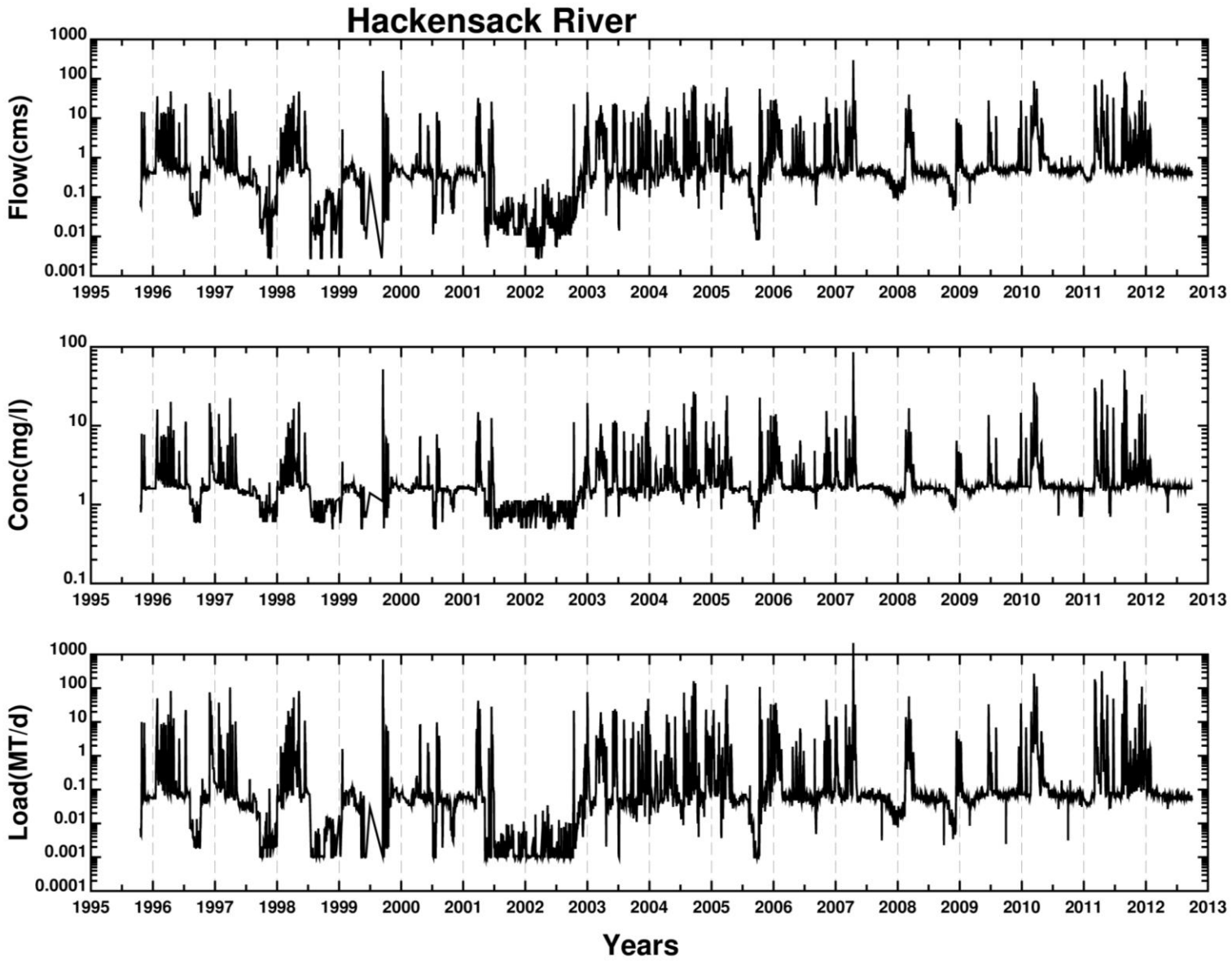

Flow, suspended solids concentration and solids mass loading in Hackensack River

Lower Eight Miles of the Lower Passaic River

Figure 3-6

2014

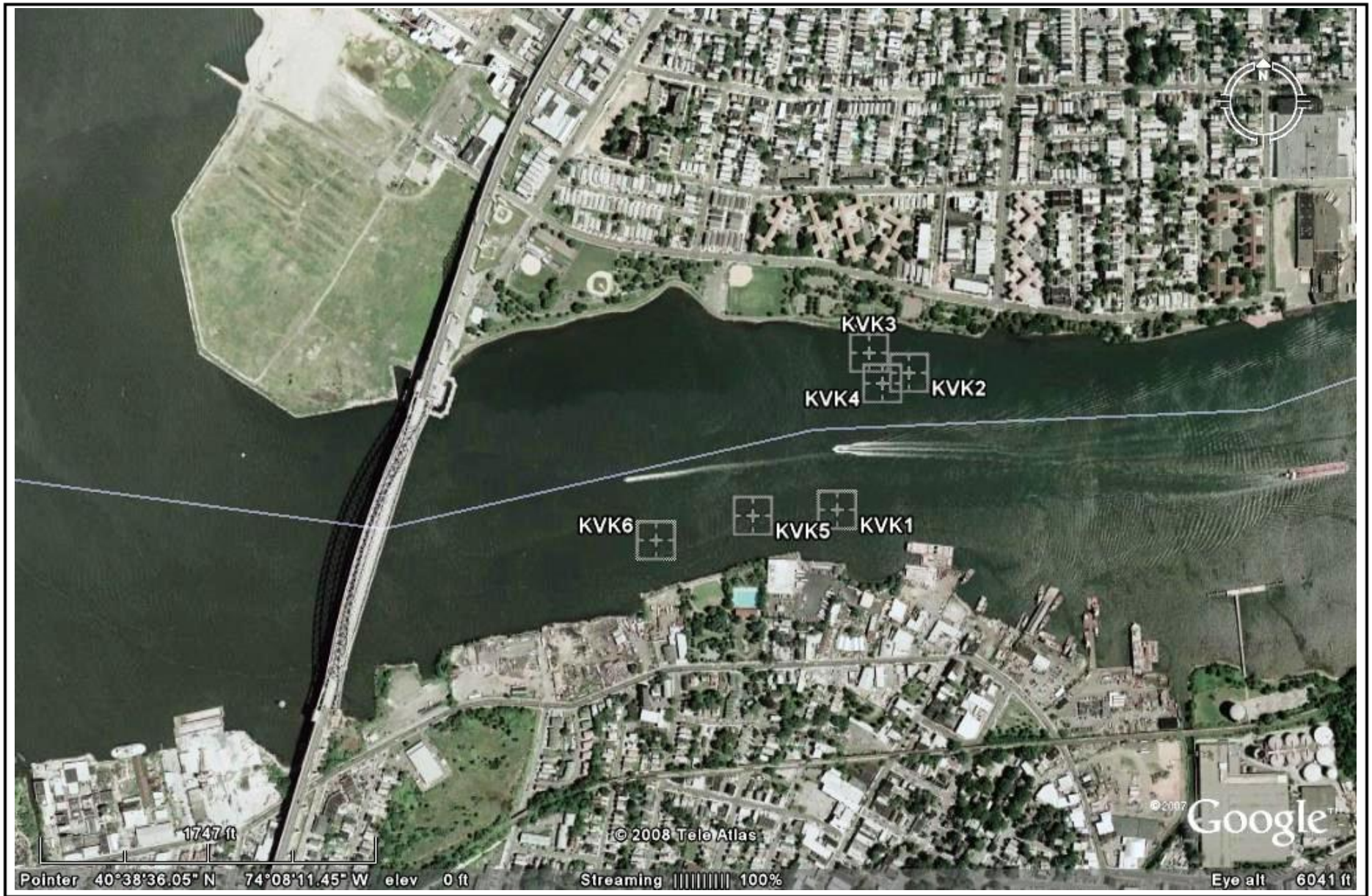

Location of ADCP deployments at the western end of the Kill Van Kull

Figure 3-7

Lower Eight Miles of the Lower Passaic River

2014

Location of ADCP deployments at the southern end of the Arthur Kill

Lower Eight Miles of the Lower Passaic River

Figure 3-8

2014

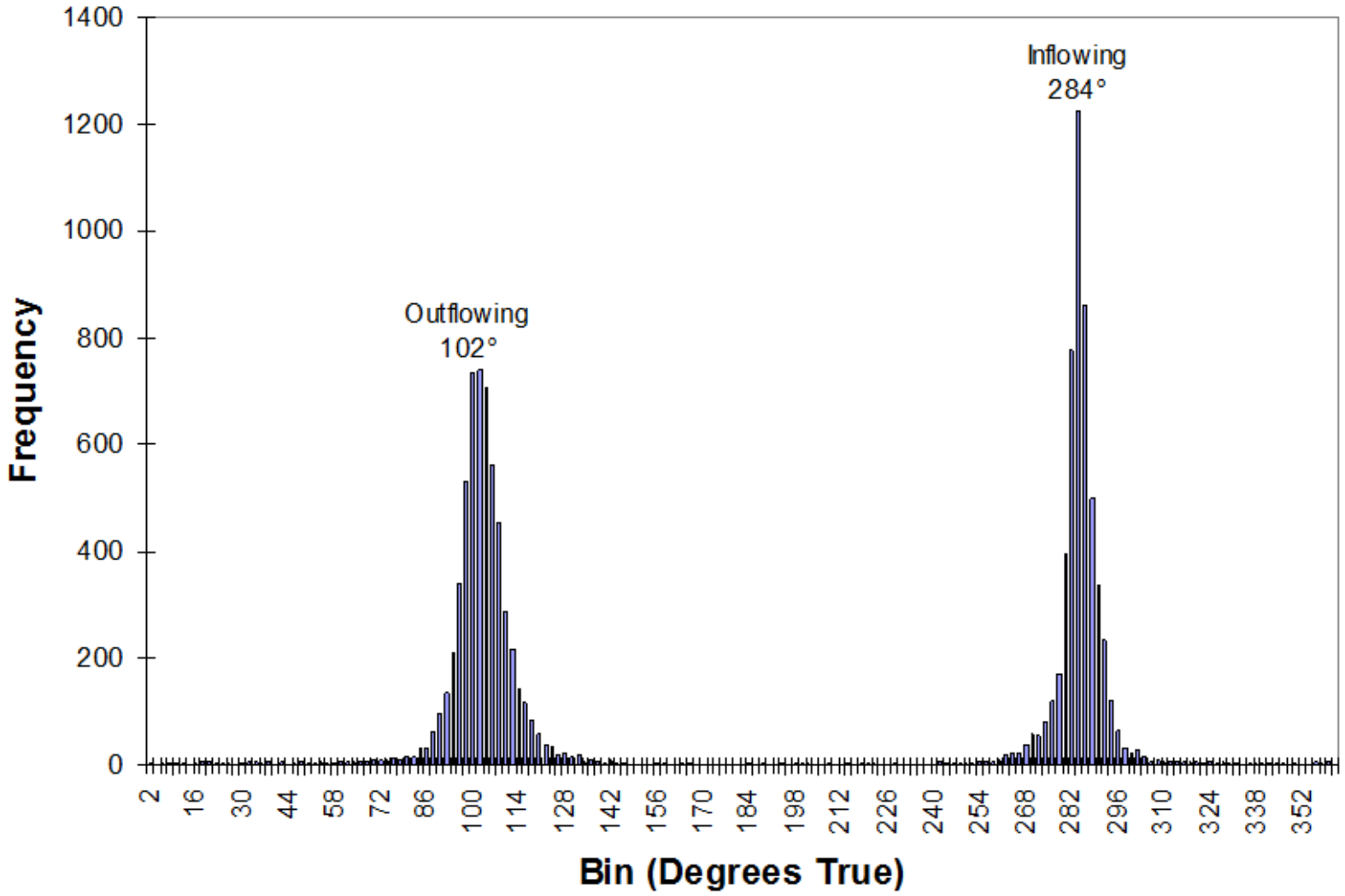

Histograms of current direction recorded by ADCP

Lower Eight Miles of the Lower Passaic River

Figure 3-9

2014

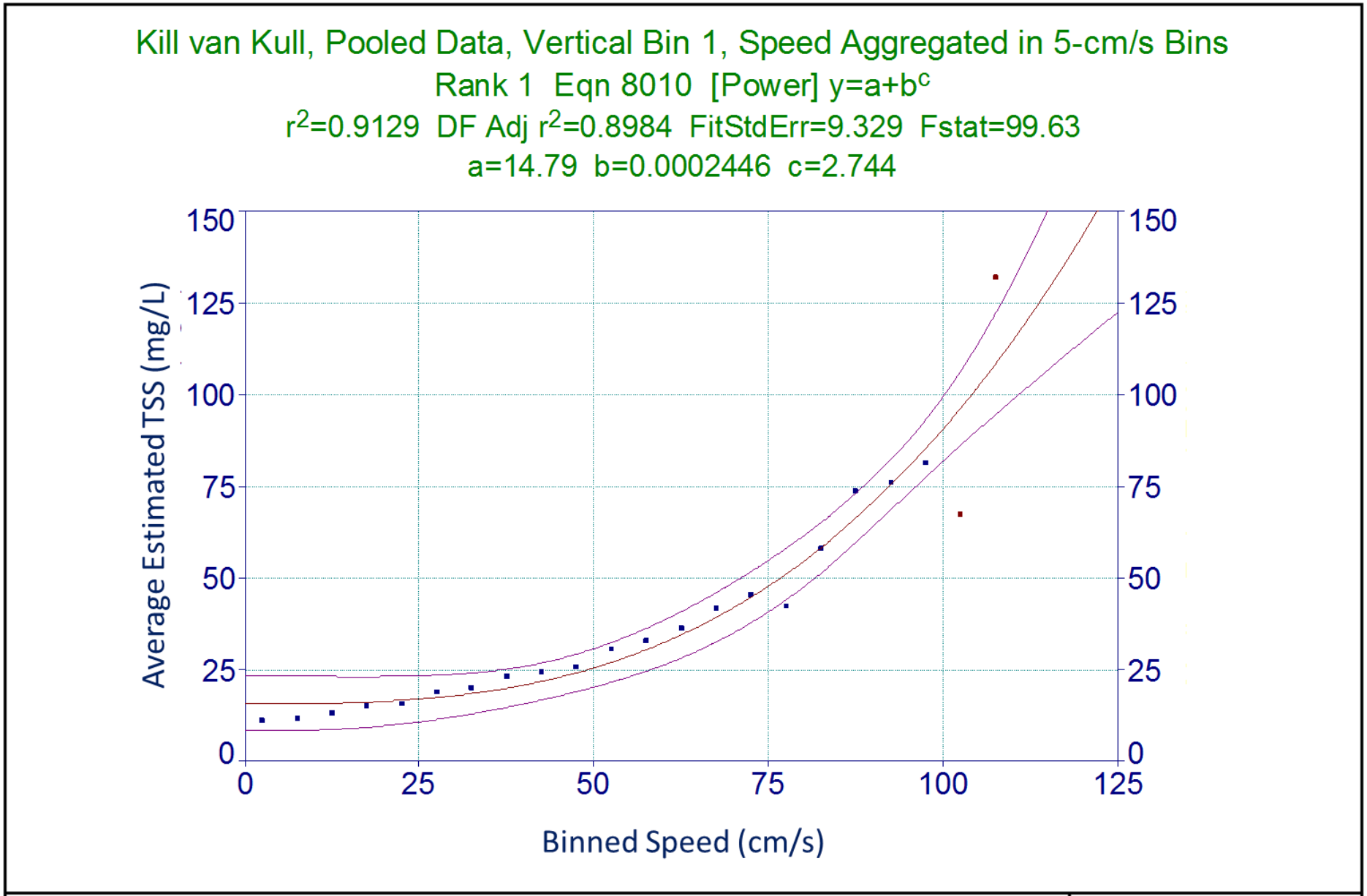

ADCP TSS versus current speed

Lower Eight Miles of the Lower Passaic River

Figure 3-10

2014

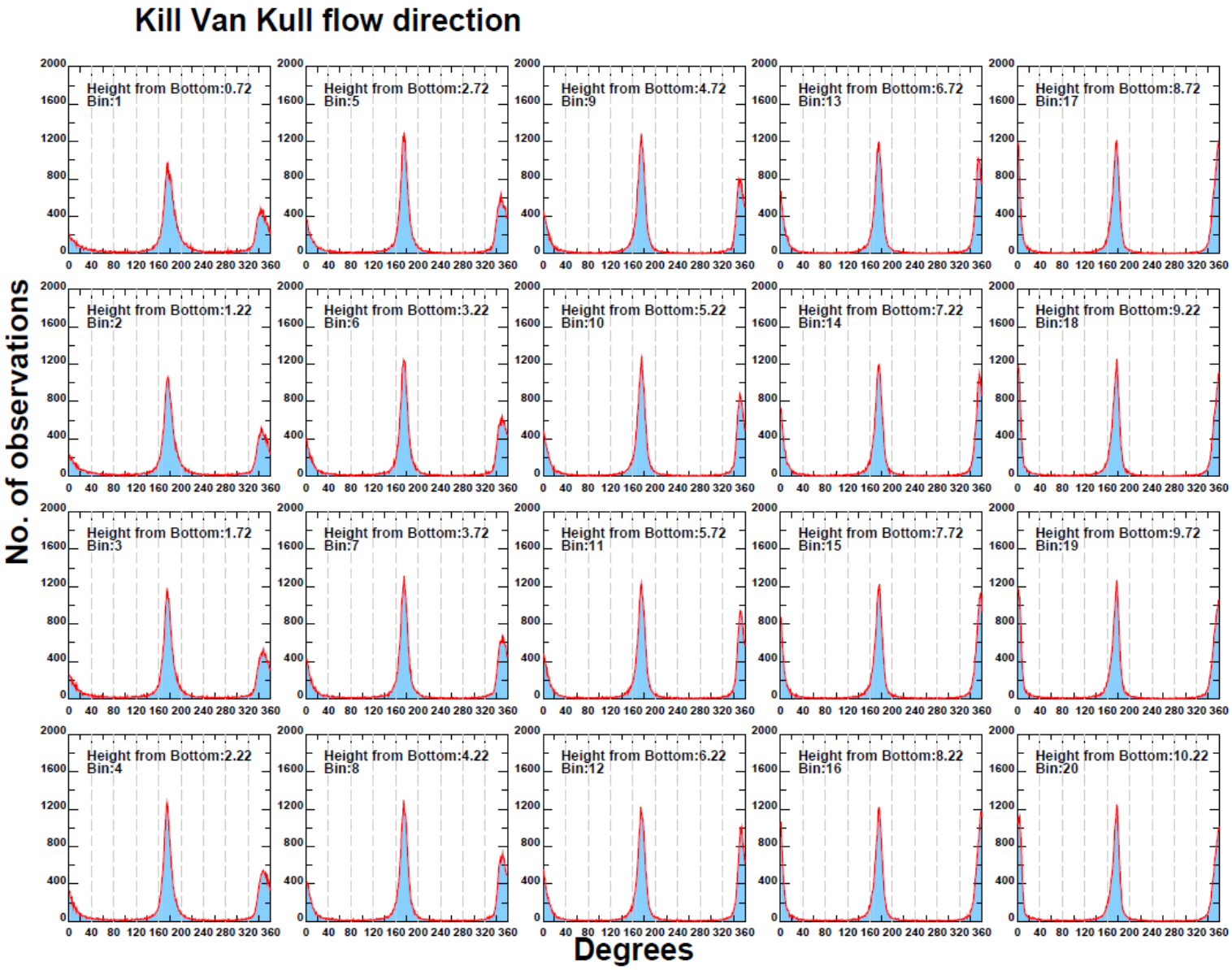

Kill Van Kull histograms of current direction for individual vertical bins

Figure 3-11

Lower Eight Miles of the Lower Passaic River

2014

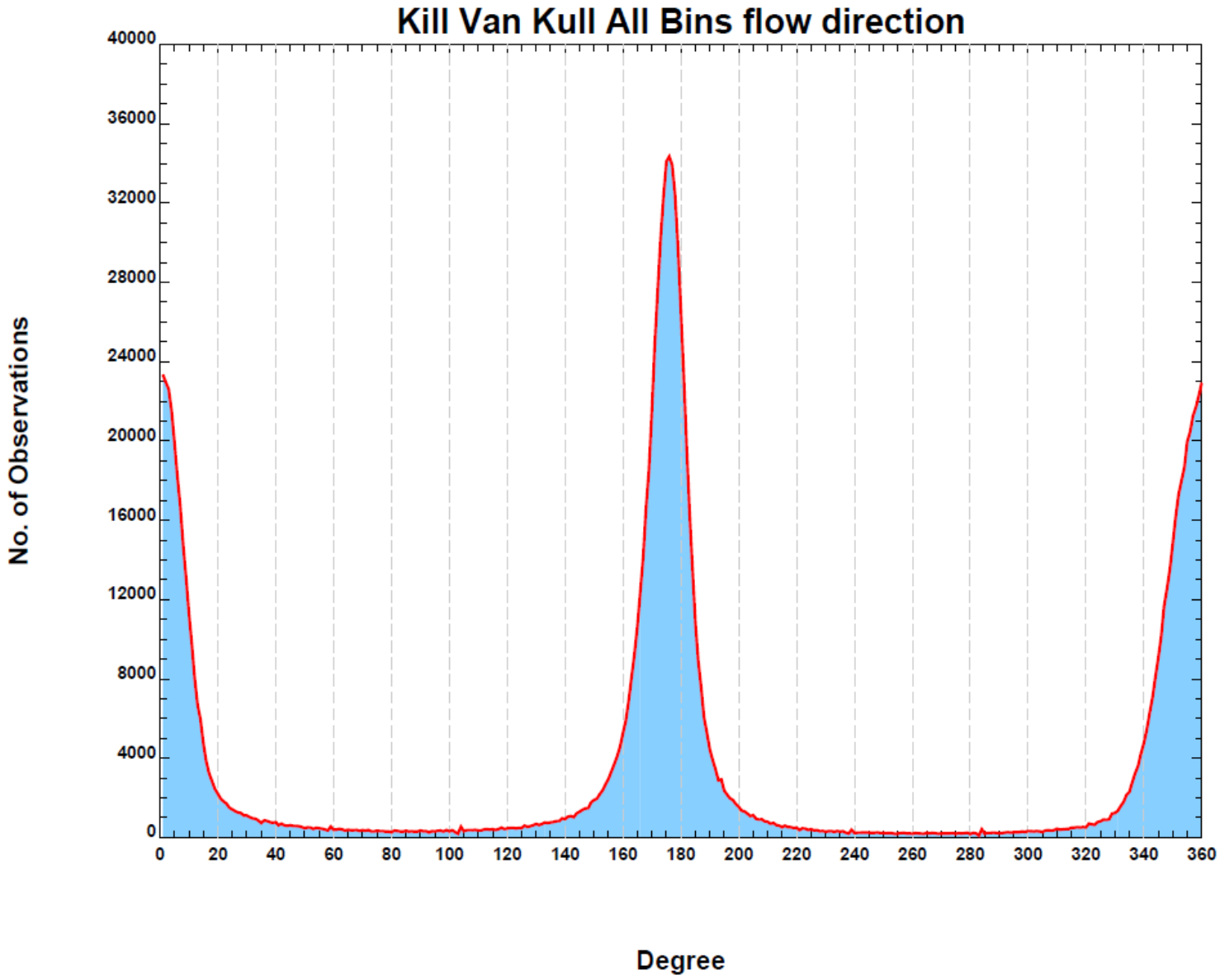

Kill Van Kull histograms of current direction in all bins

Lower Eight Miles of the Lower Passaic River

Figure 3-12

2014

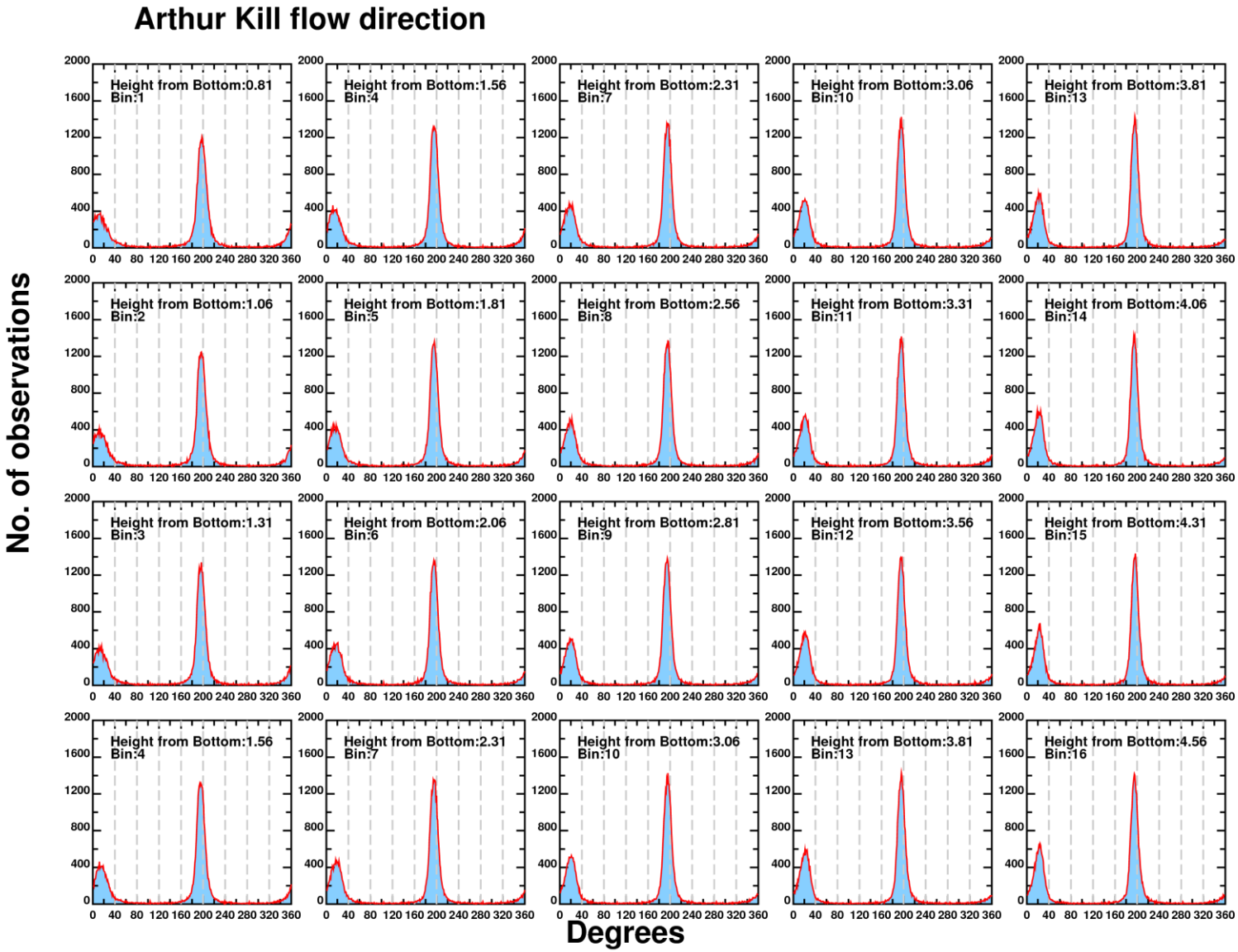

Arthur Kill histograms of current direction for individual vertical bins

Figure 3-13

Lower Eight Miles of the Lower Passaic River

2014

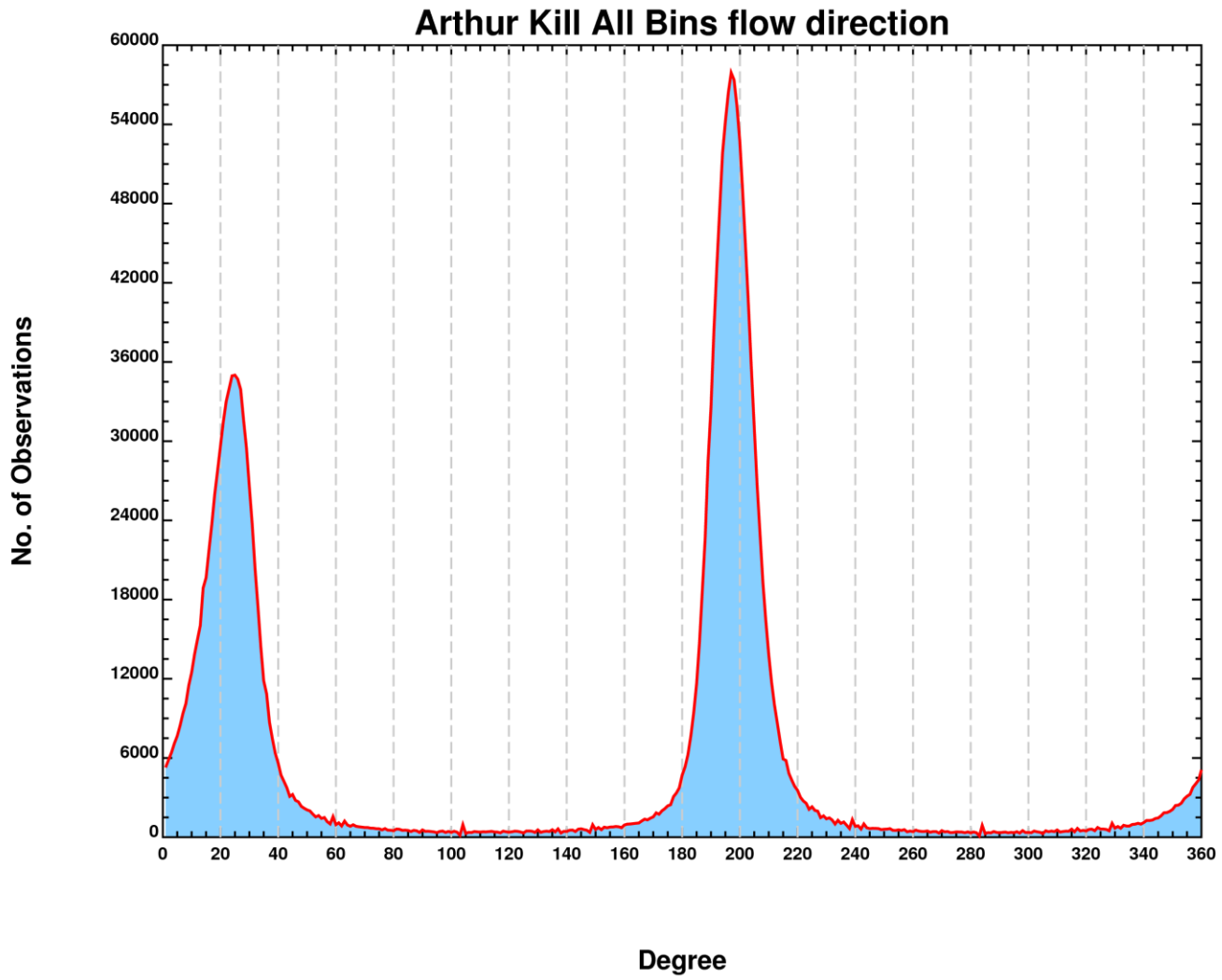

Arthur Kill histograms of current direction in all bins

Lower Eight Miles of the Lower Passaic River

Figure 3-14

2014

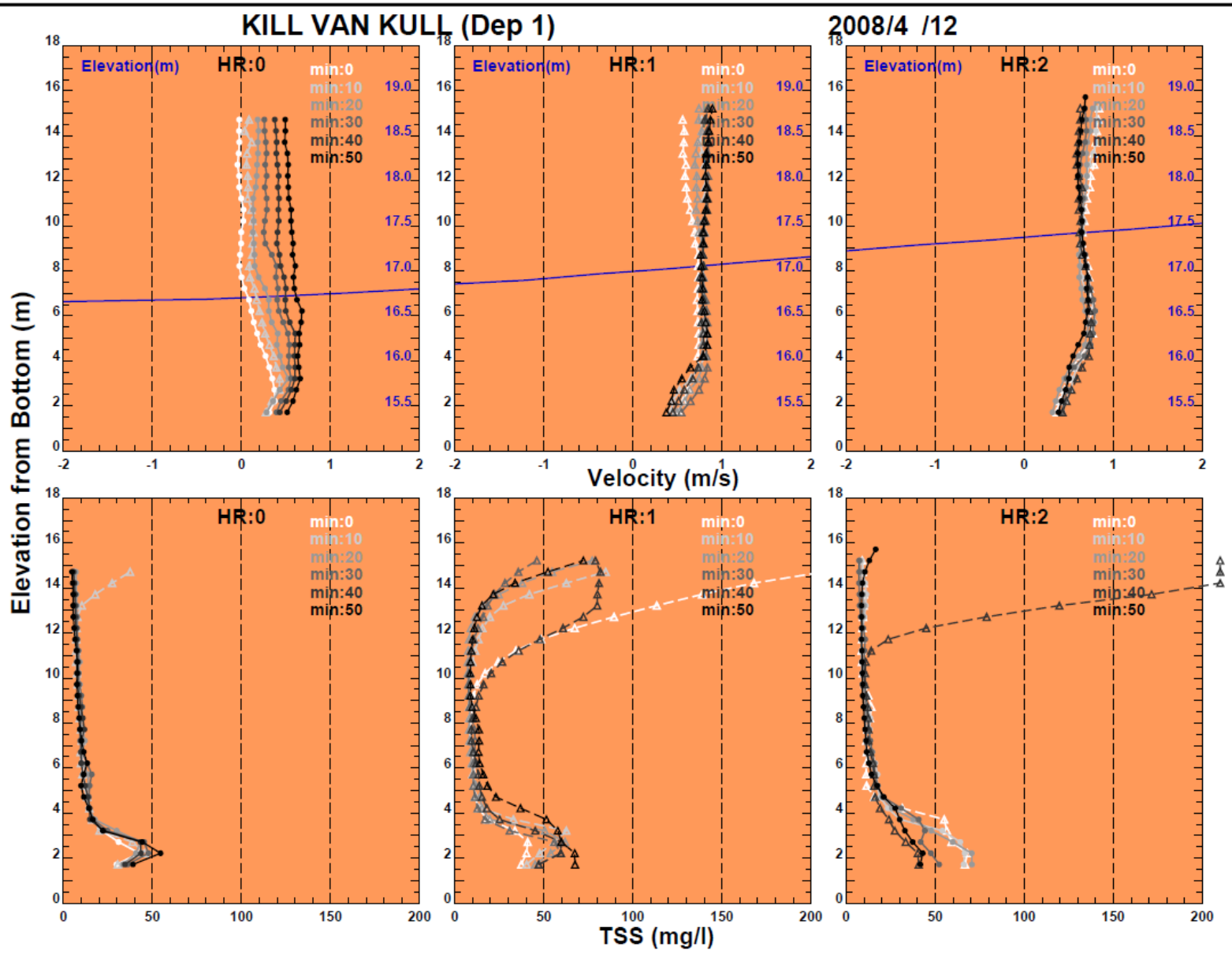

Kill Van Kull examples of vertical profile of currents and TSS with bad surface data

Figure 3-15

2014

Lower Eight Miles of the Lower Passaic River

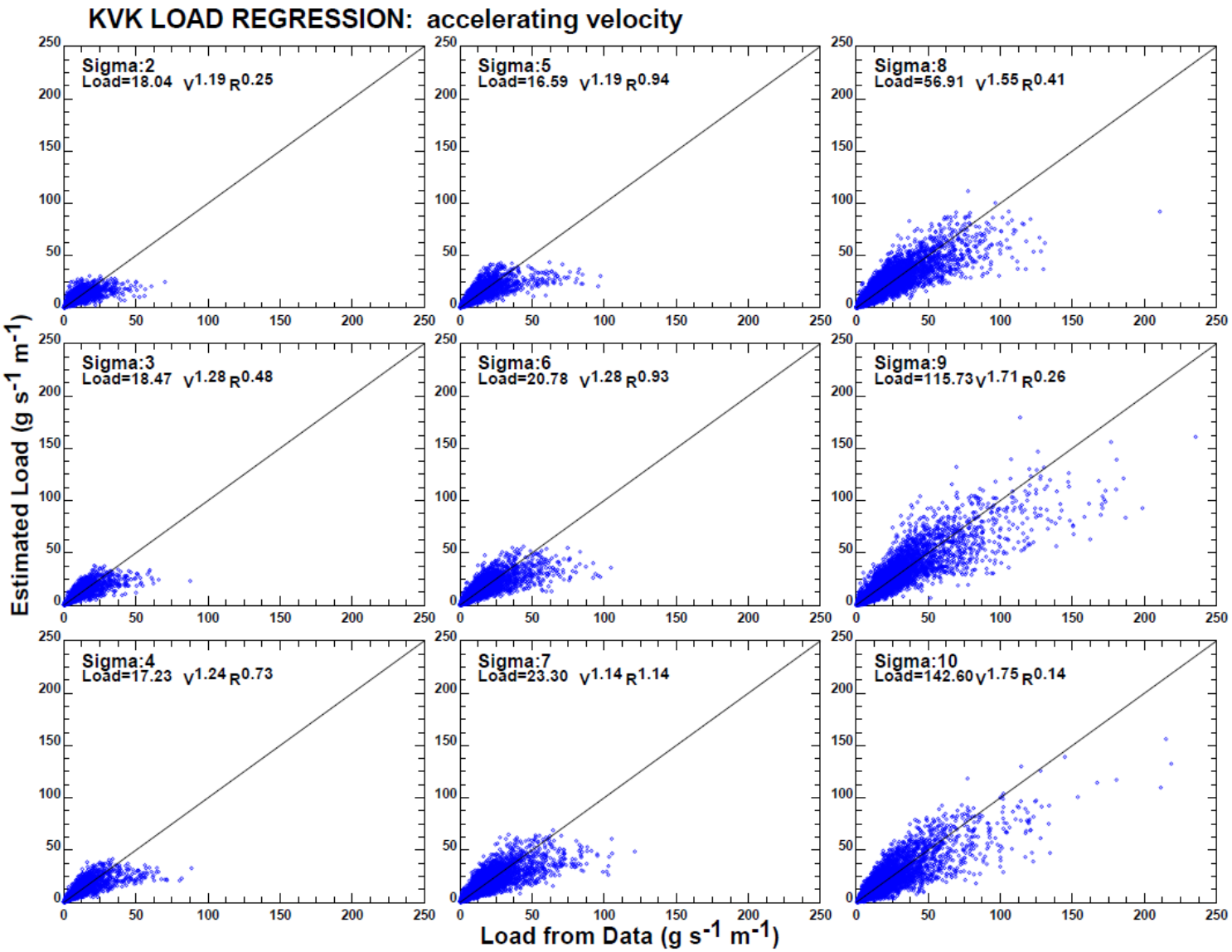

Kill Van Kull calculated vs. measured load - accelerating velocity

Lower Eight Miles of the Lower Passaic River

Figure 3-16

2014

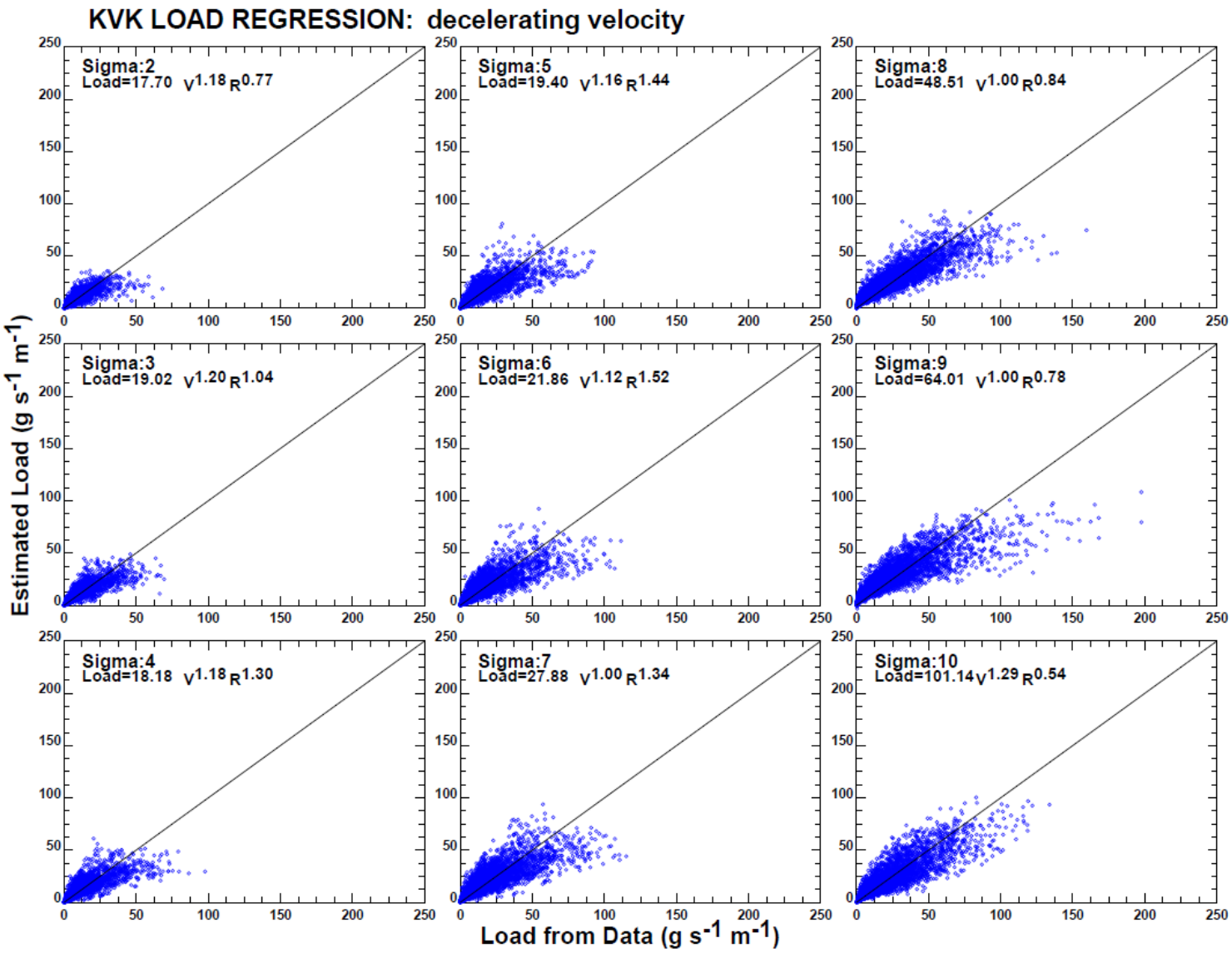

Kill Van Kull calculated vs. measured load - decelerating velocity

Lower Eight Miles of the Lower Passaic River

Figure 3-17

2014

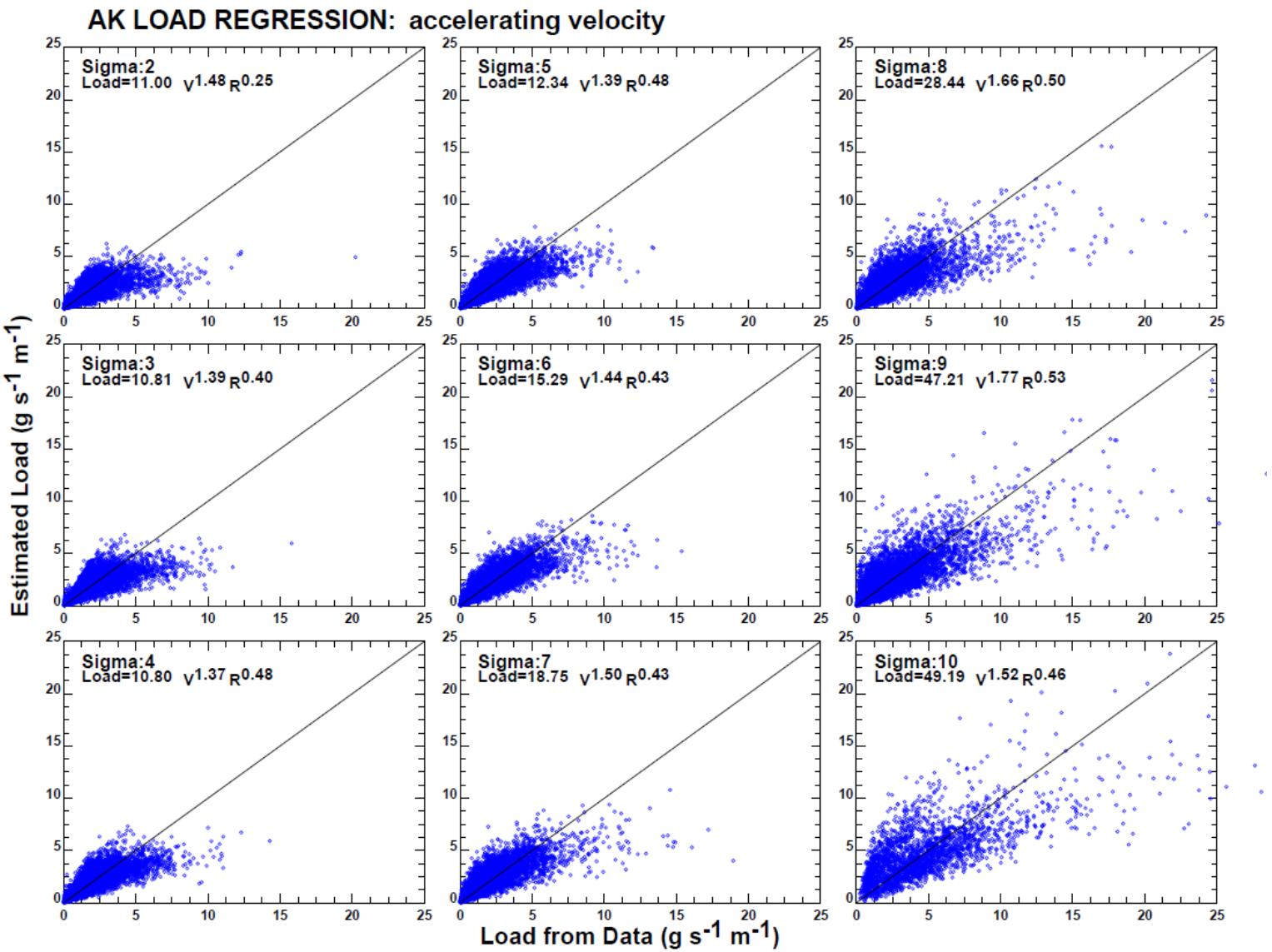

Arthur Kill calculated vs. measured load - accelerating velocity

Figure 3-18

Lower Eight Miles of the Lower Passaic River

2014

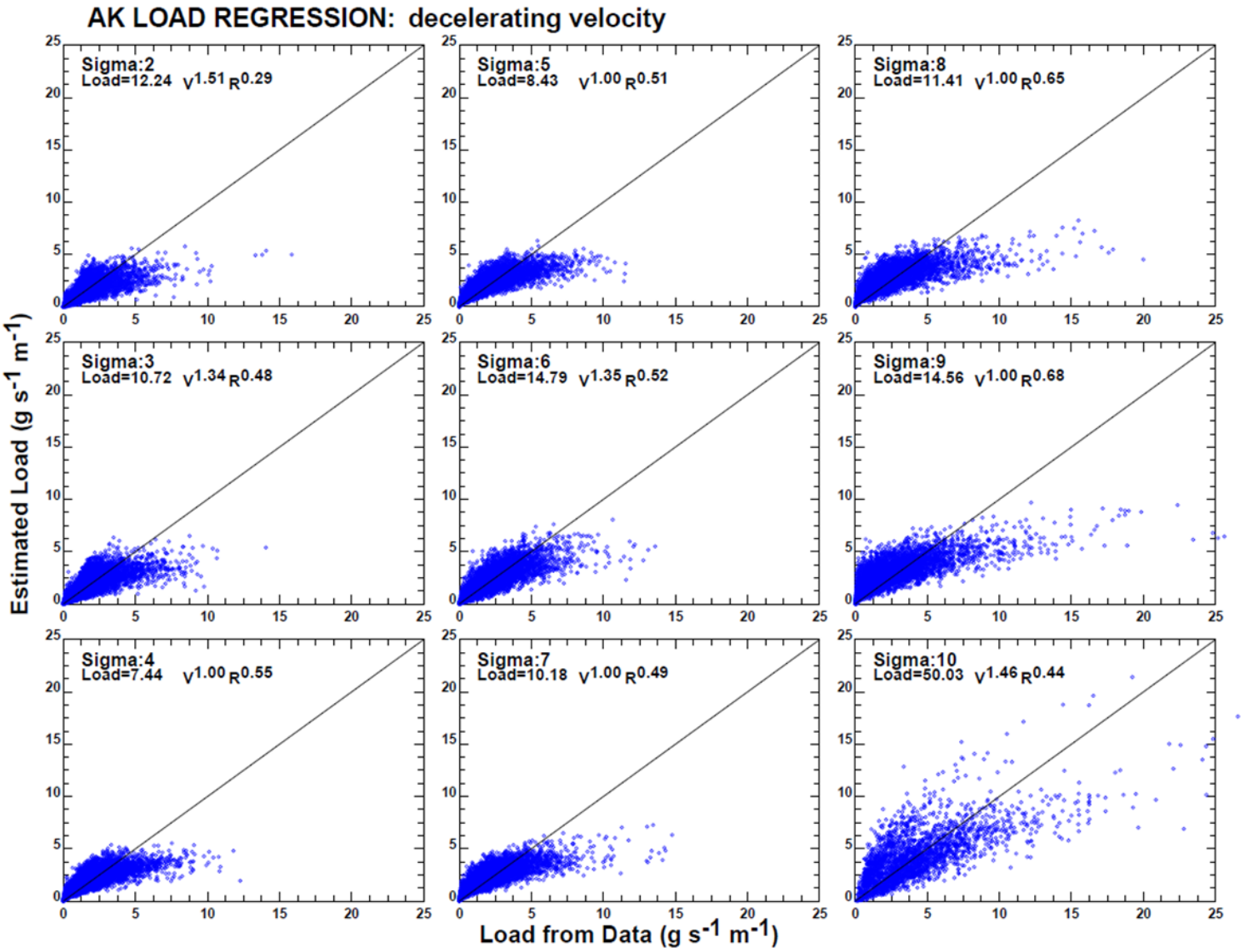

Arthur Kill calculated vs. measured load - decelerating velocity

Figure 3-19

Lower Eight Miles of the Lower Passaic River

2014

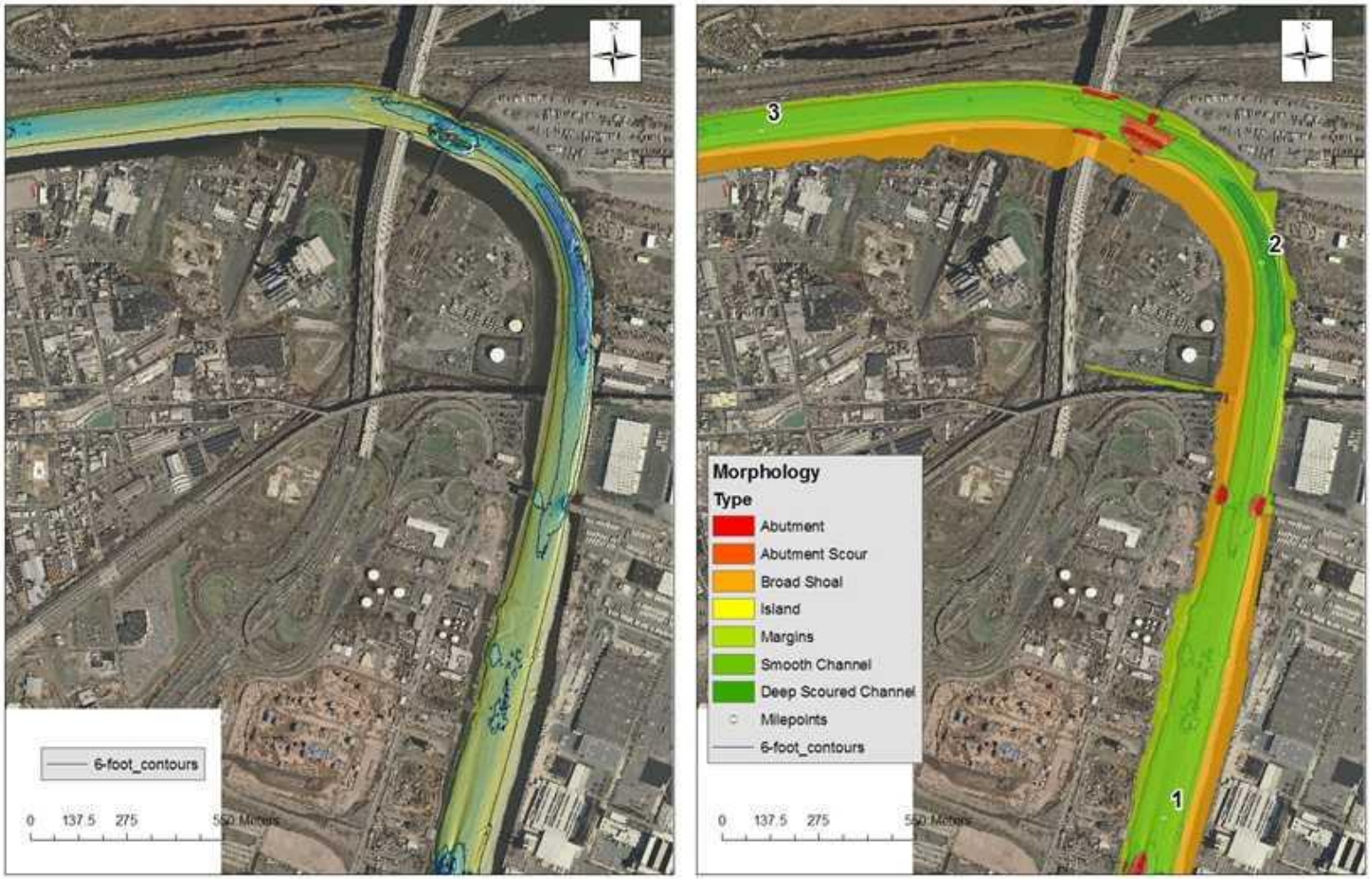

Shaded multibeam data and contours from the 2008 survey and an overlay of qualitatively identified morphologic regions near RM2

Lower Eight Miles of the Lower Passaic River

Figure 3-20

2014

Shaded multibeam data and contours from the 2008 survey and an overlay of qualitatively identified morphologic regions near RM4

Lower Eight Miles of the Lower Passaic River

Figure 3-21

2014

Shaded multibeam data and contours from the 2008 survey and an overlay of qualitatively identified morphologic regions near RM6

Lower Eight Miles of the Lower Passaic River

Figure 3-22

2014

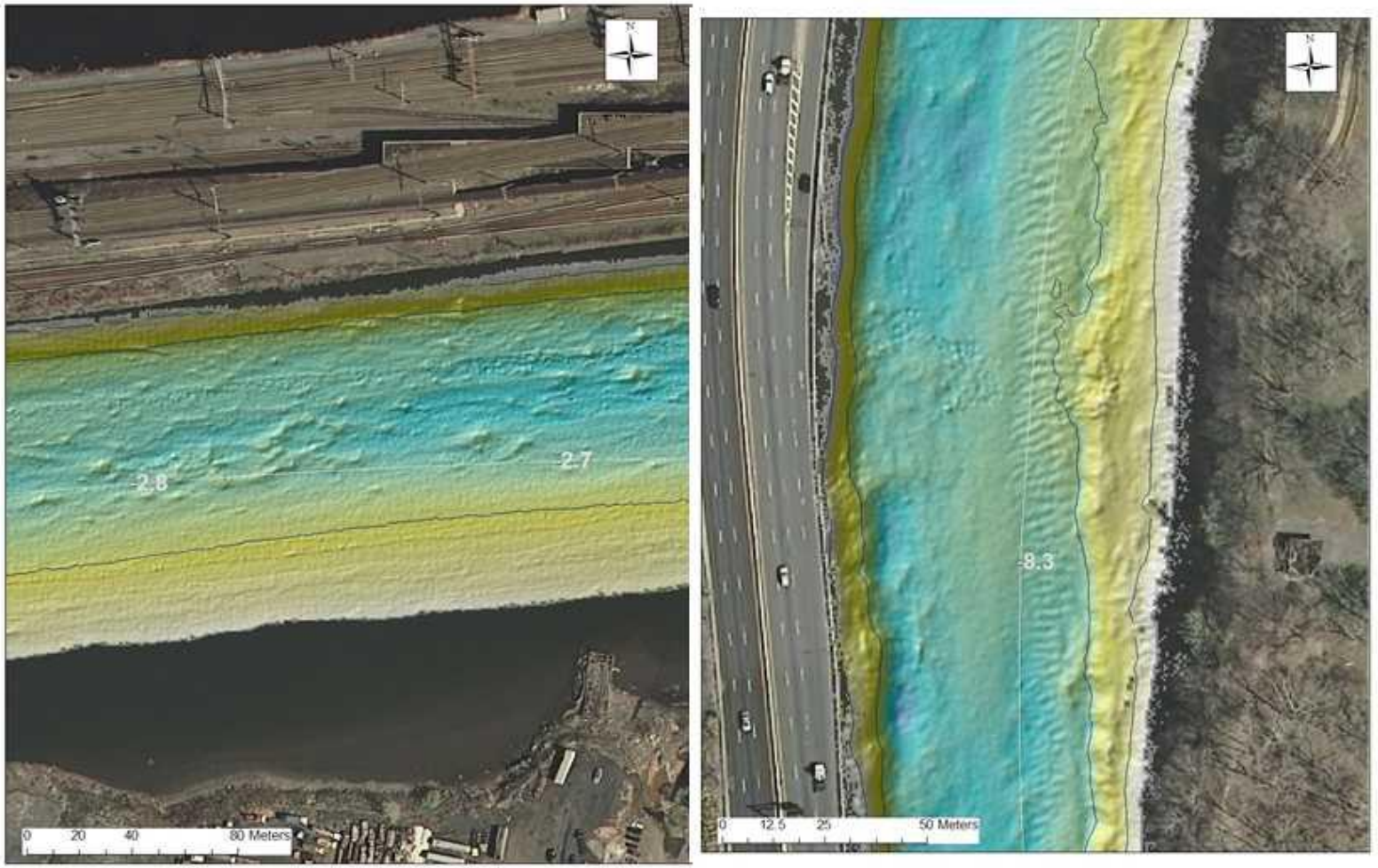

Shaded multibeam data from the 2008 survey highlighting bed features near RM2.7 (left) and RM8.3 (right)

Lower Eight Miles of the Lower Passaic River

Figure 3-23

2014

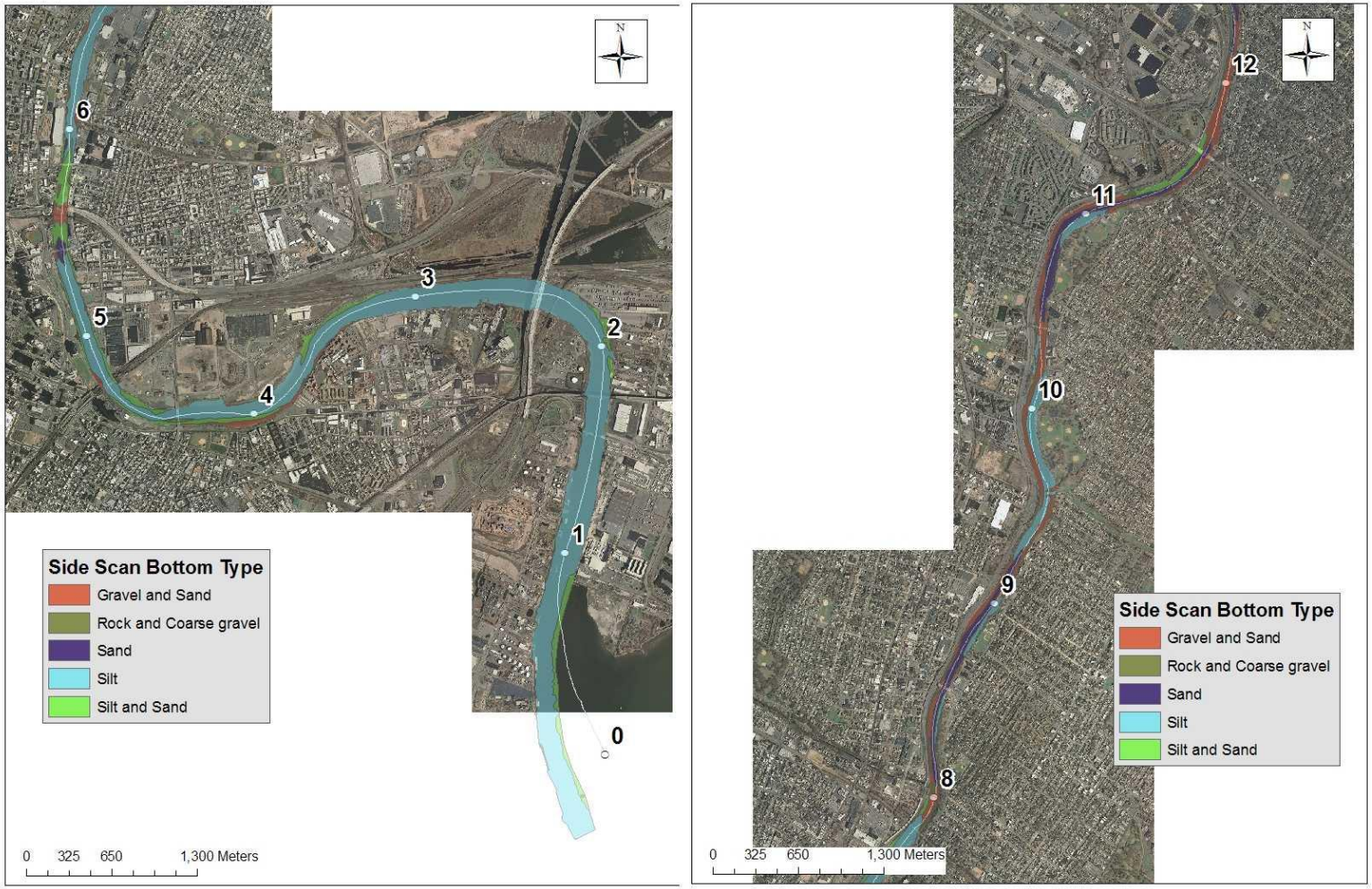

Side scan bottom texture identification from RM0-6 and 8-12

Lower Eight Miles of the Lower Passaic River

Figure 3-24

2014

Side scan bottom texture identification from near RM8

Figure 3-25

Lower Eight Miles of the Lower Passaic River

2014

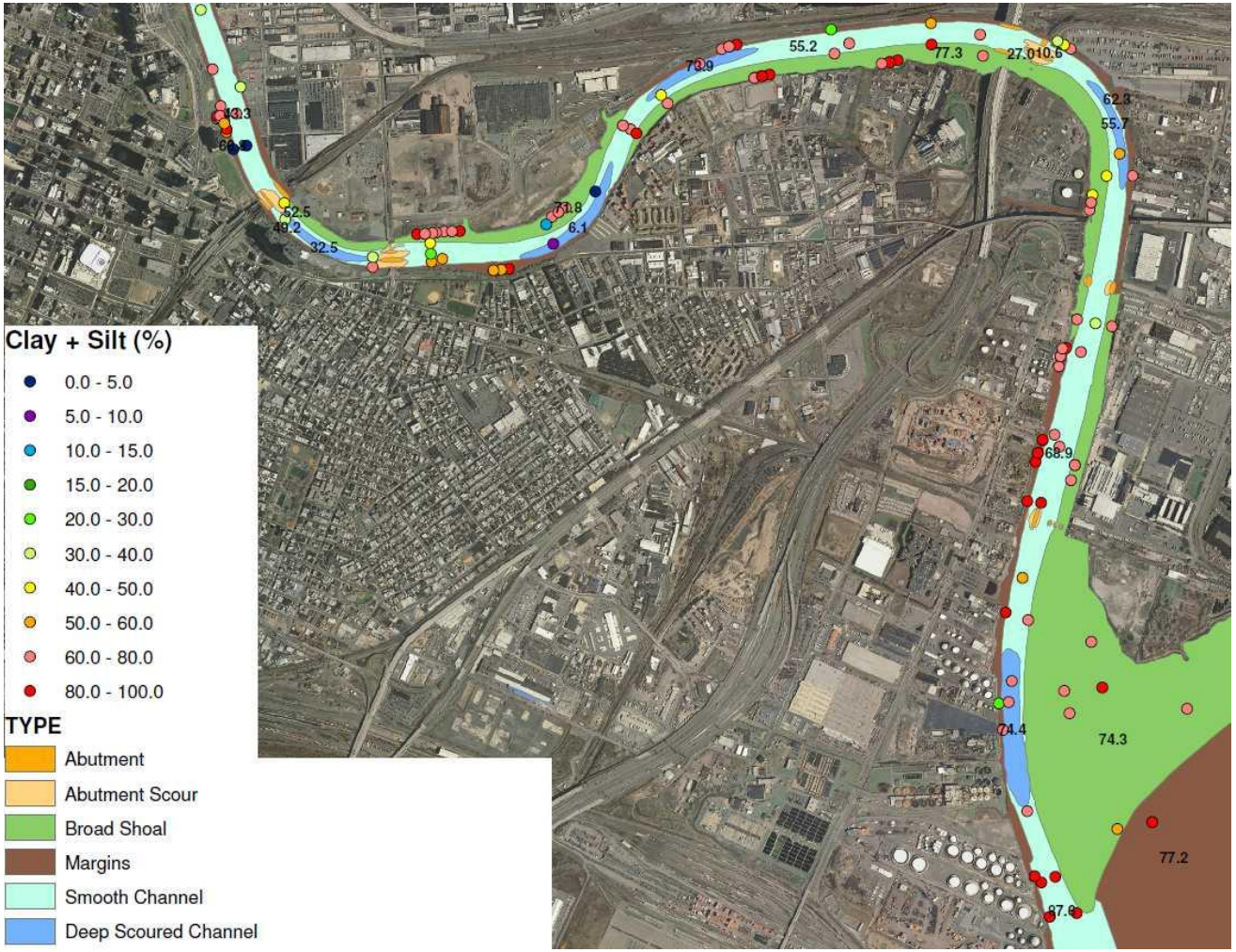

Grainsize averages within geomorphic areas - view 1

Lower Eight Miles of the Lower Passaic River

Figure 3-26

2014

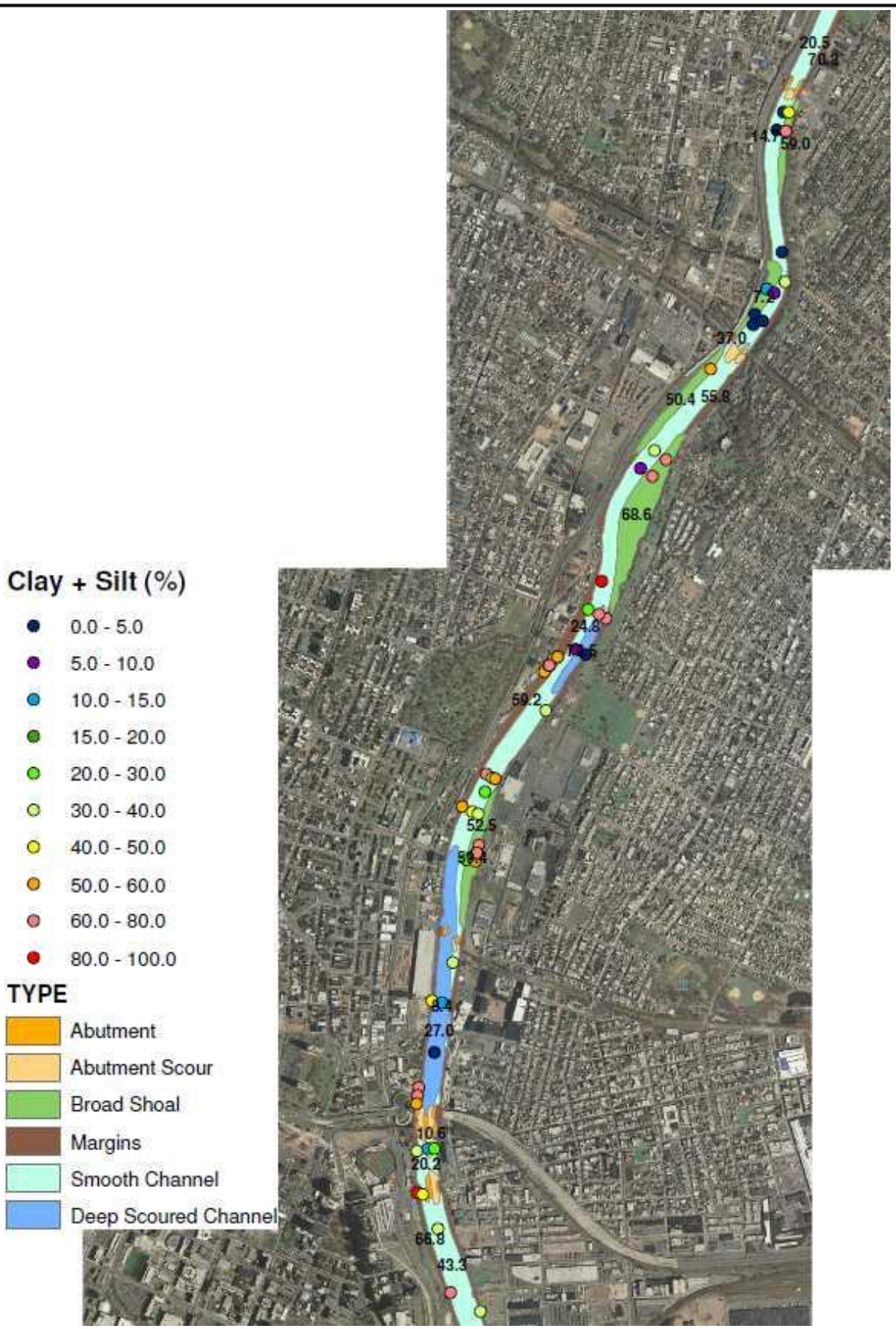

Grainsize averages within geomorphic areas - view 2

Figure 3-27

Lower Eight Miles of the Lower Passaic River

2014

Grainsize averages within geomorphic areas - view 3

Figure 3-28

Lower Eight Miles of the Lower Passaic River

2014

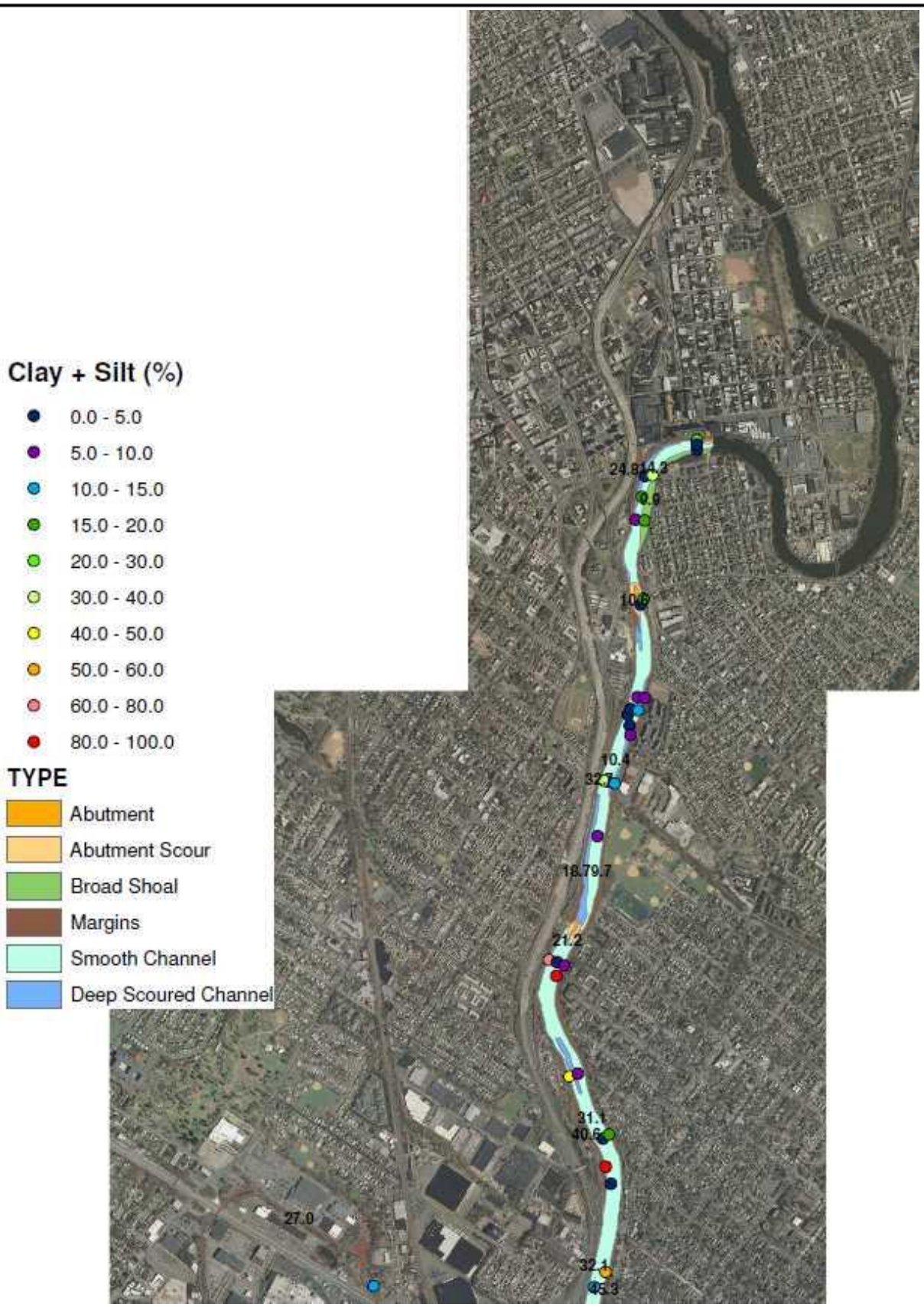

Grainsize averages within geomorphic areas - view 4

Figure 3-29

Lower Eight Miles of the Lower Passaic River

2014

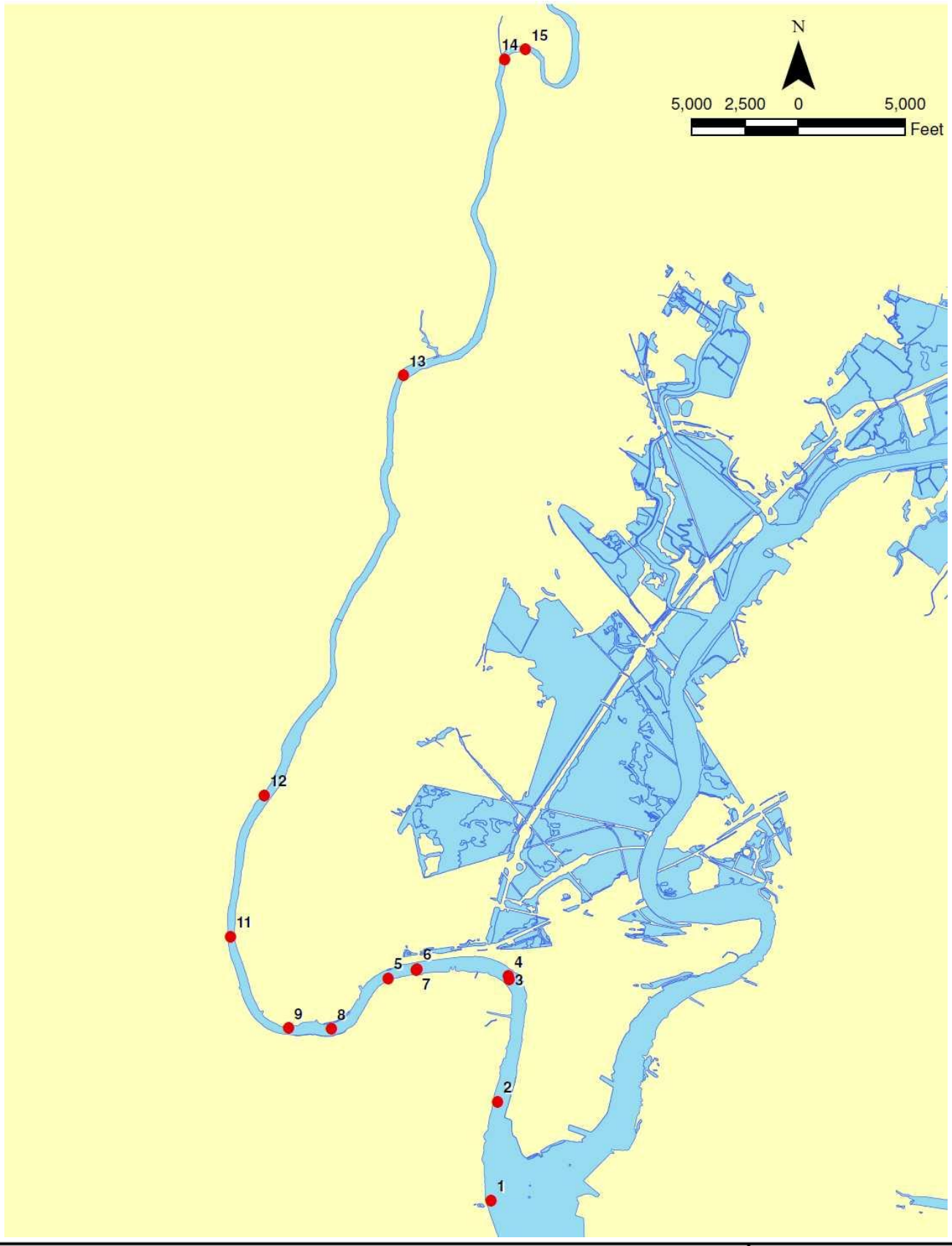

Locations of Sedflume core collection

Figure 3-30

Lower Eight Miles of the Lower Passaic River

2014

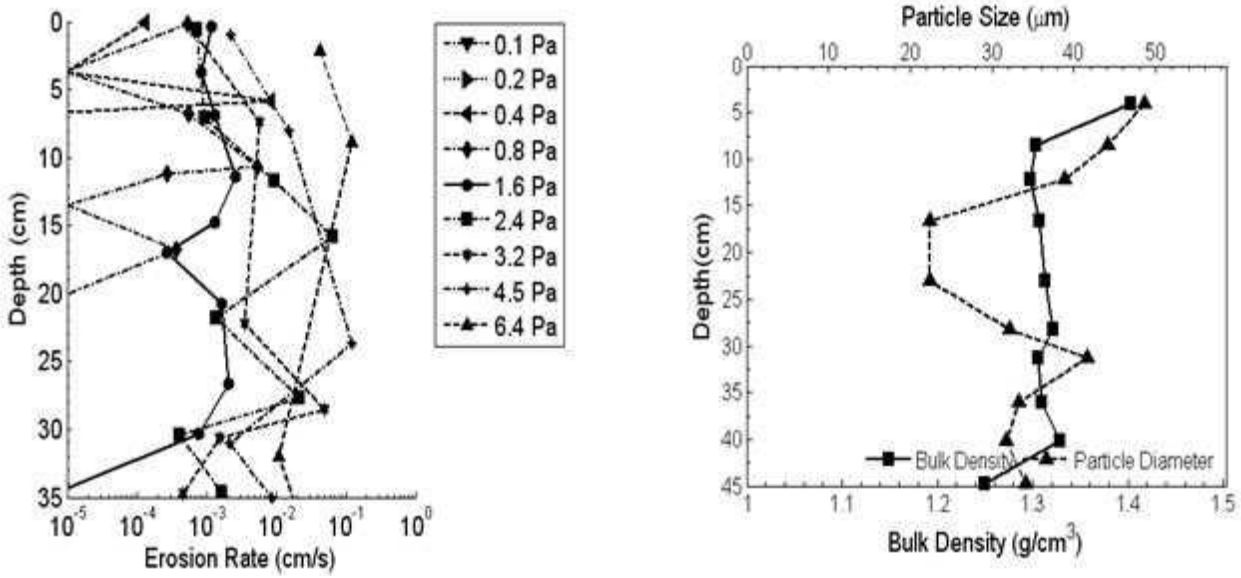

Measured erosion rates, particle size, and bulk density from P05A

Figure 3-31

Lower Eight Miles of the Lower Passaic River

2014

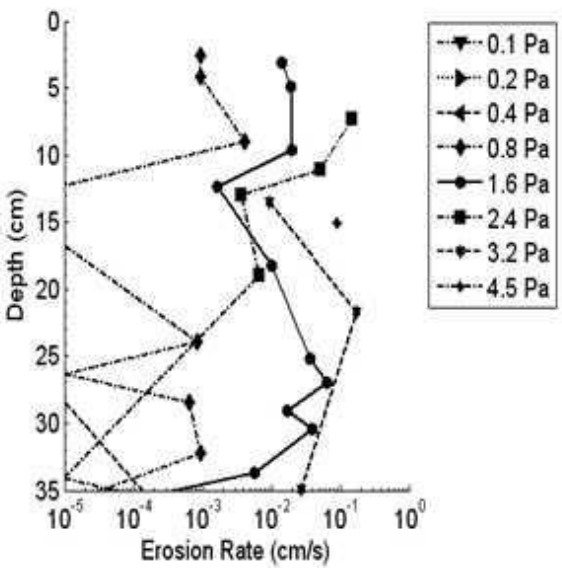

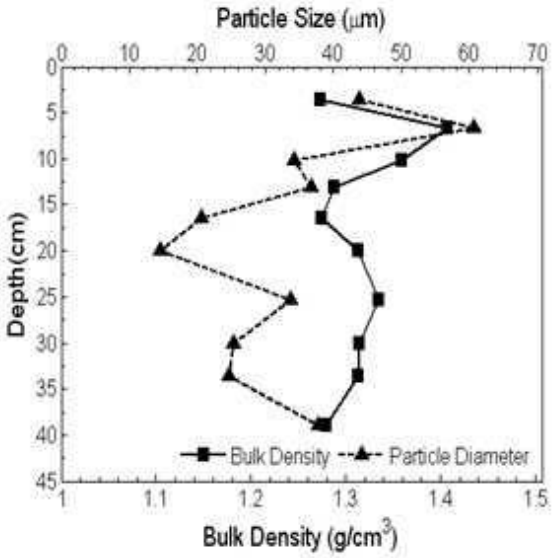

Measured erosion rates, particle size, and bulk density from P05B

Figure 3-32

Lower Eight Miles of the Lower Passaic River

2014

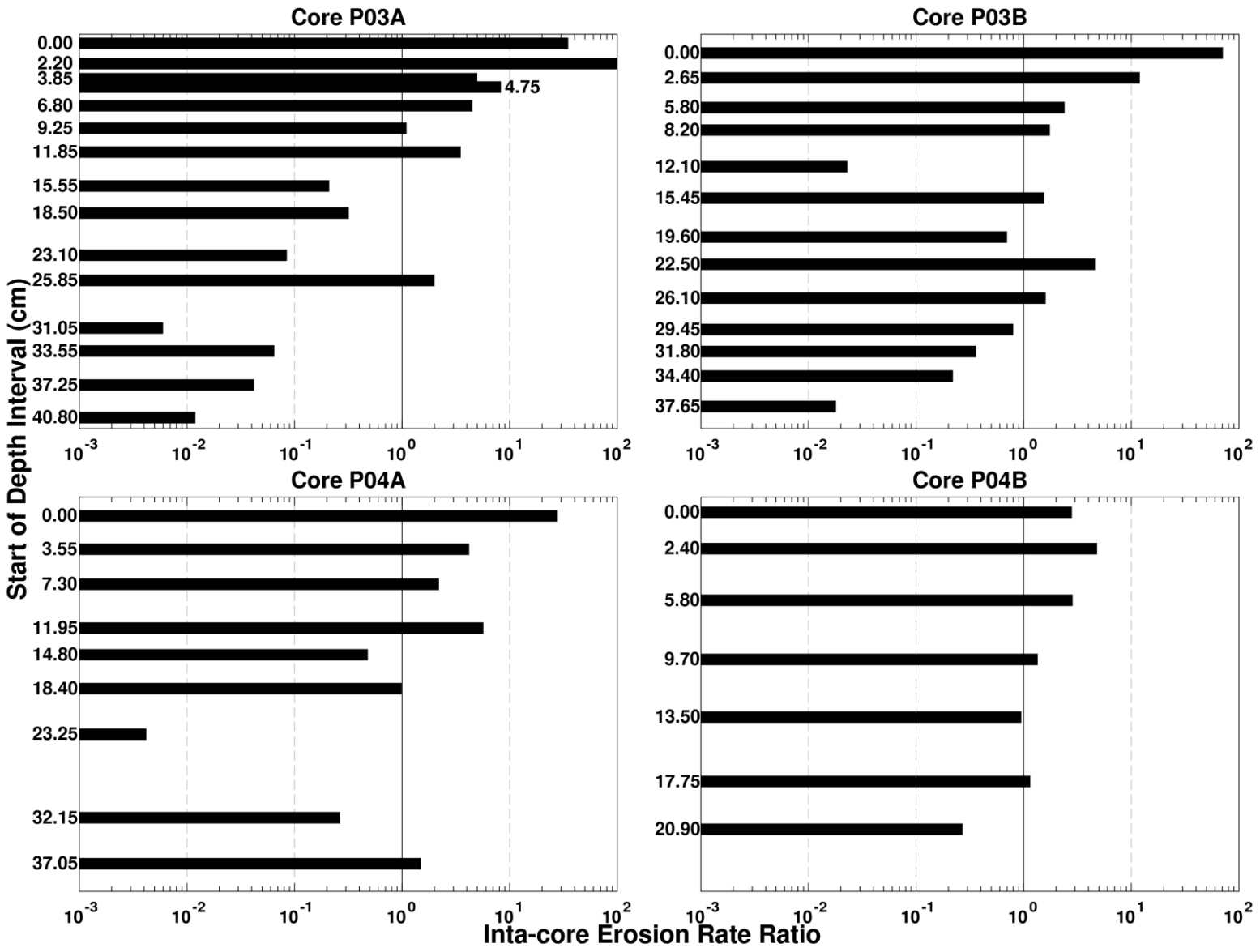

Intra-core Erosion rate ratio for cores from stations 3 and 4

Figure 3-33

Lower Eight Miles of the Lower Passaic River

2014

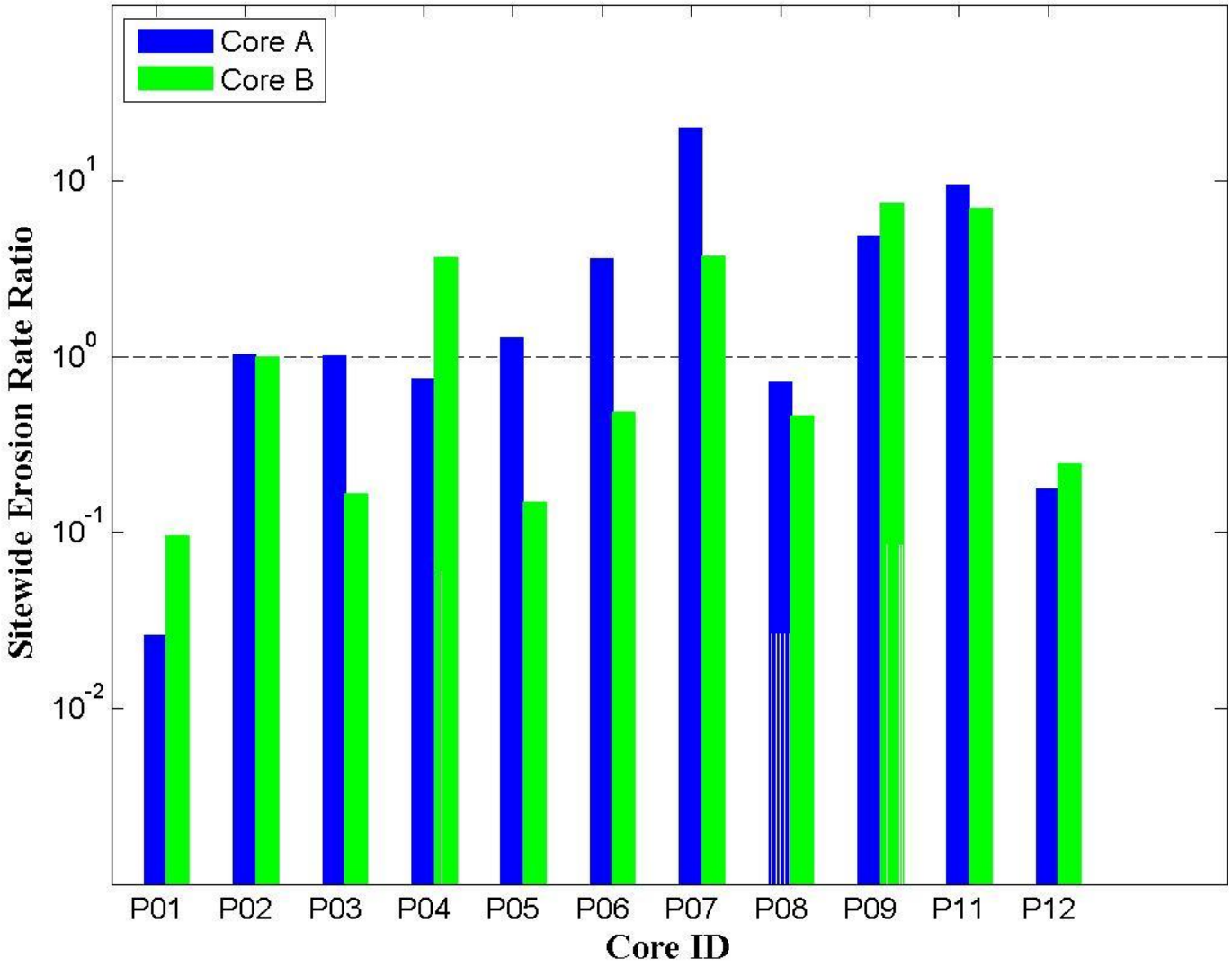

Comparison of erosion properties for cohesive cores

Lower Eight Miles of the Lower Passaic River

Figure 3-34

2014

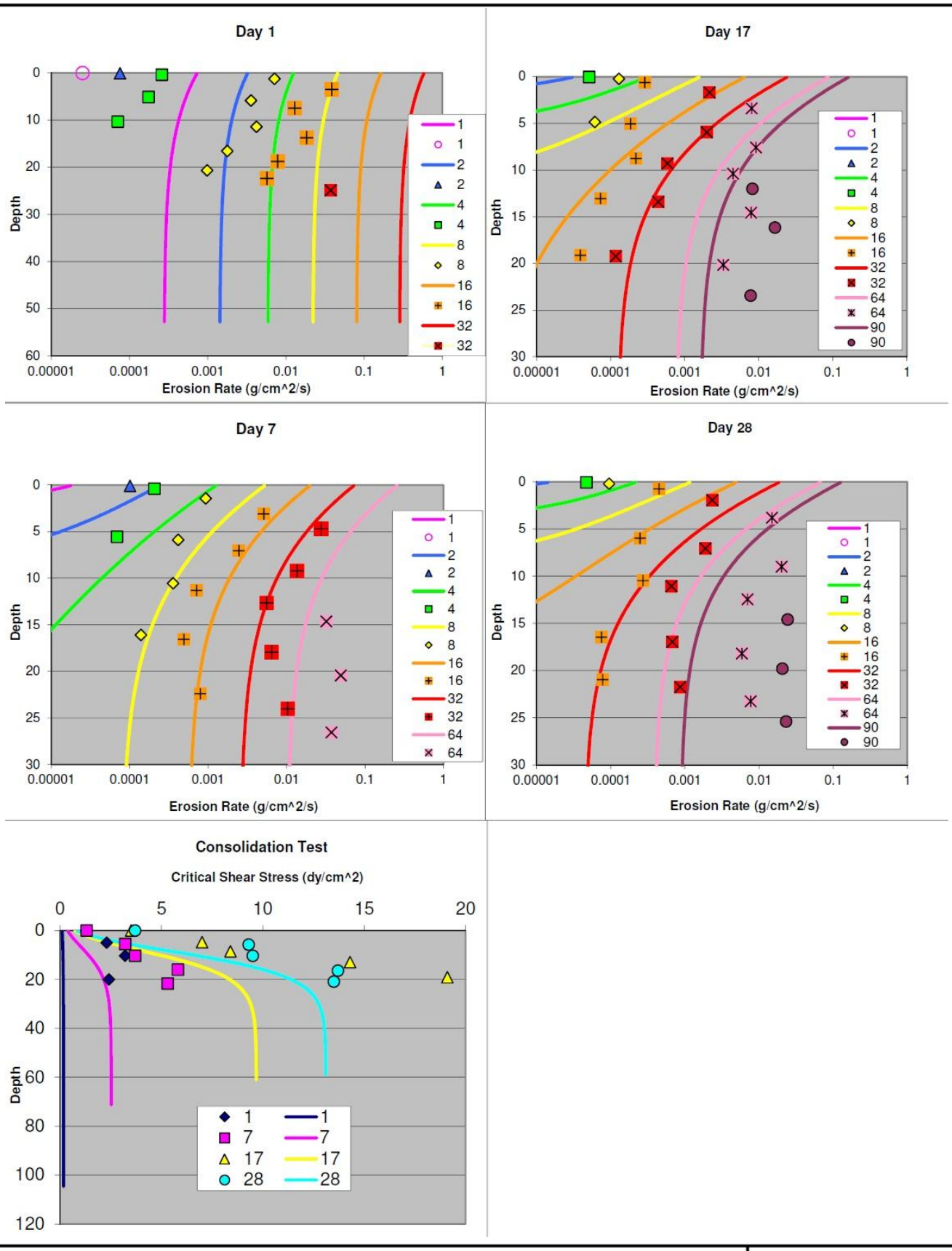

Consolidation Experiment Data and Model Fit

Figure 3-35

Lower Eight Miles of the Lower Passaic River

2014

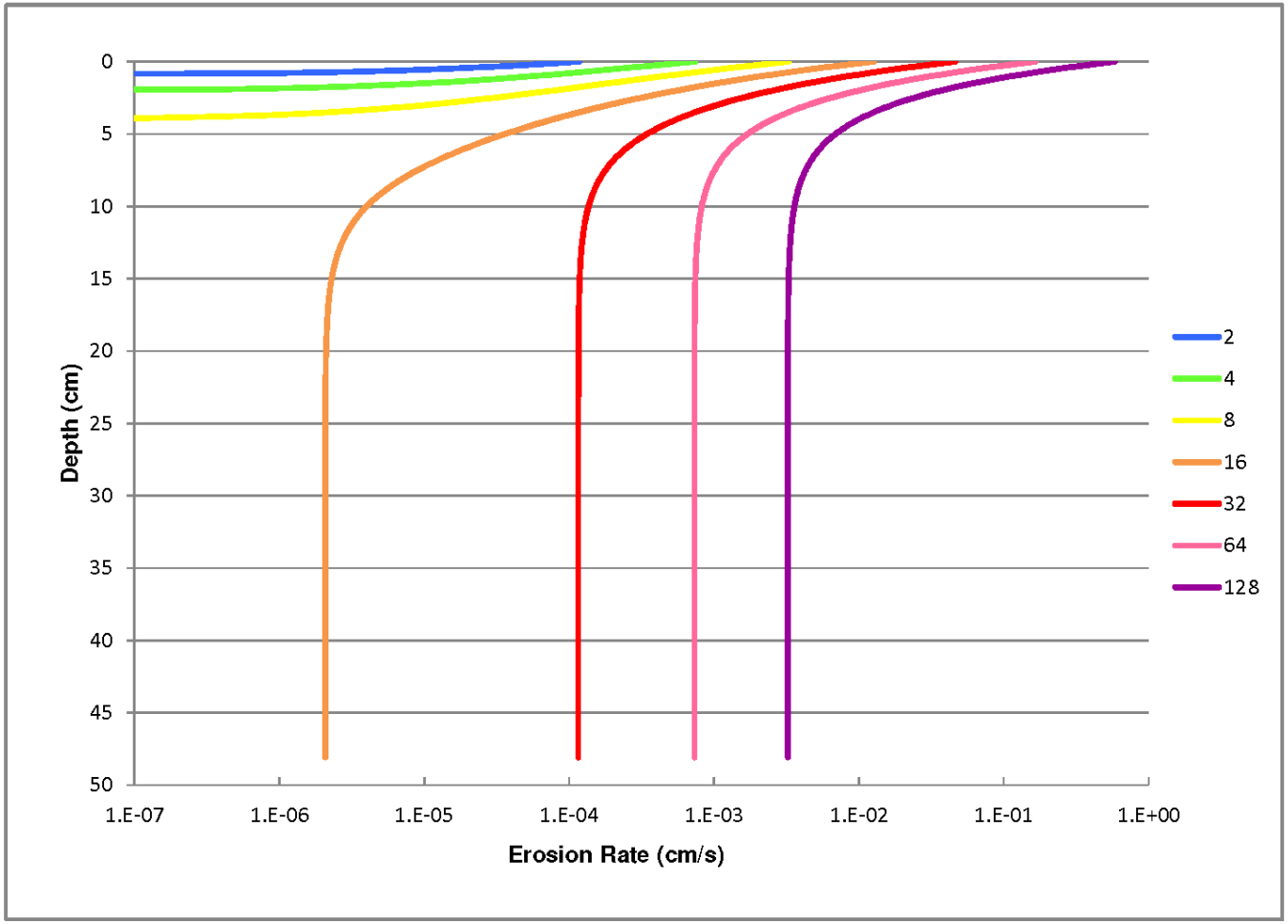

Cohesive Core Parent Bed Erosion Rates

Lower Eight Miles of the Lower Passaic River

Figure 3-36

2014

Core Distribution

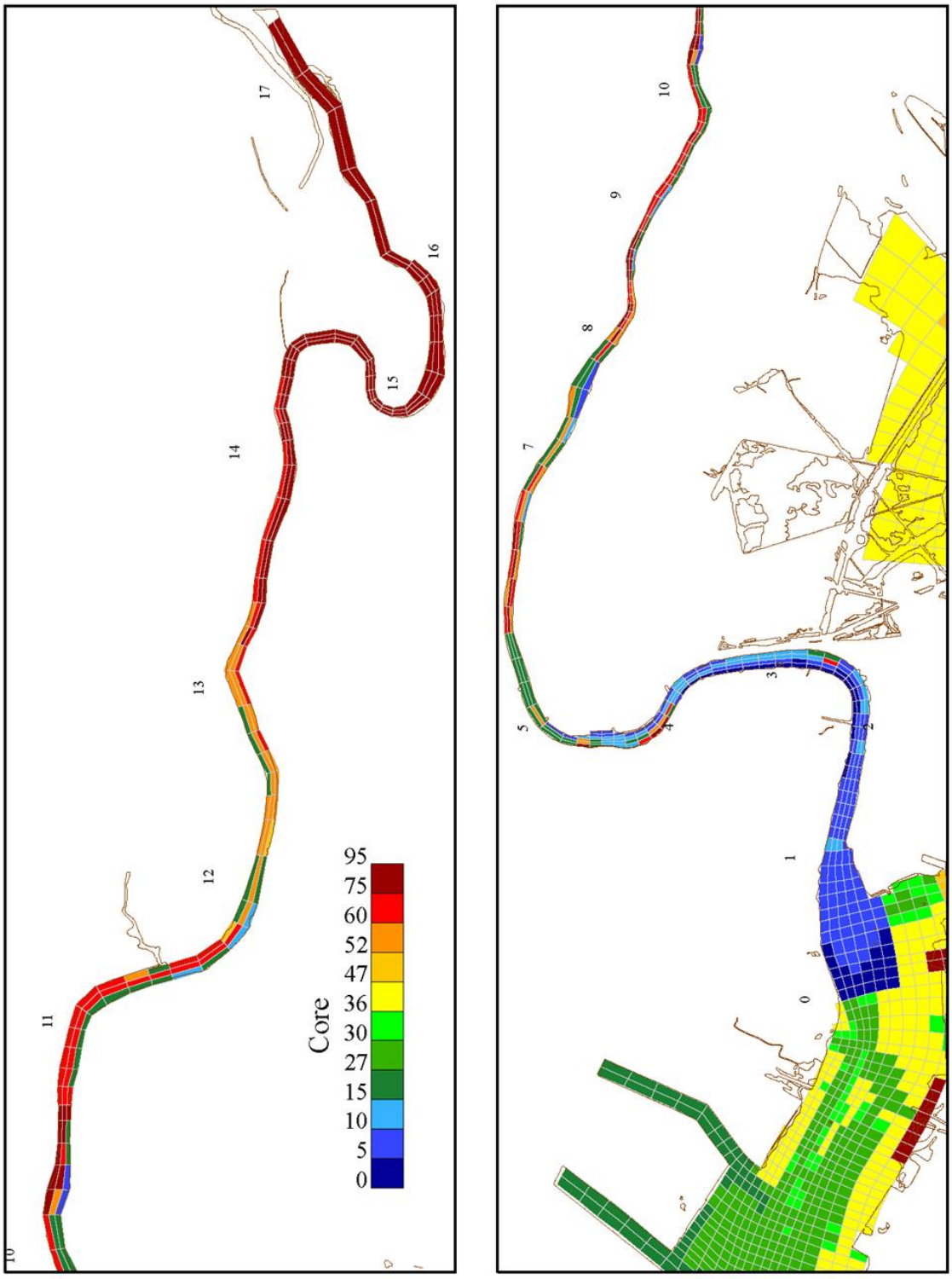

Core distribution	Figure 3-37
Lower Eight Miles of the Lower Passaic River	2014

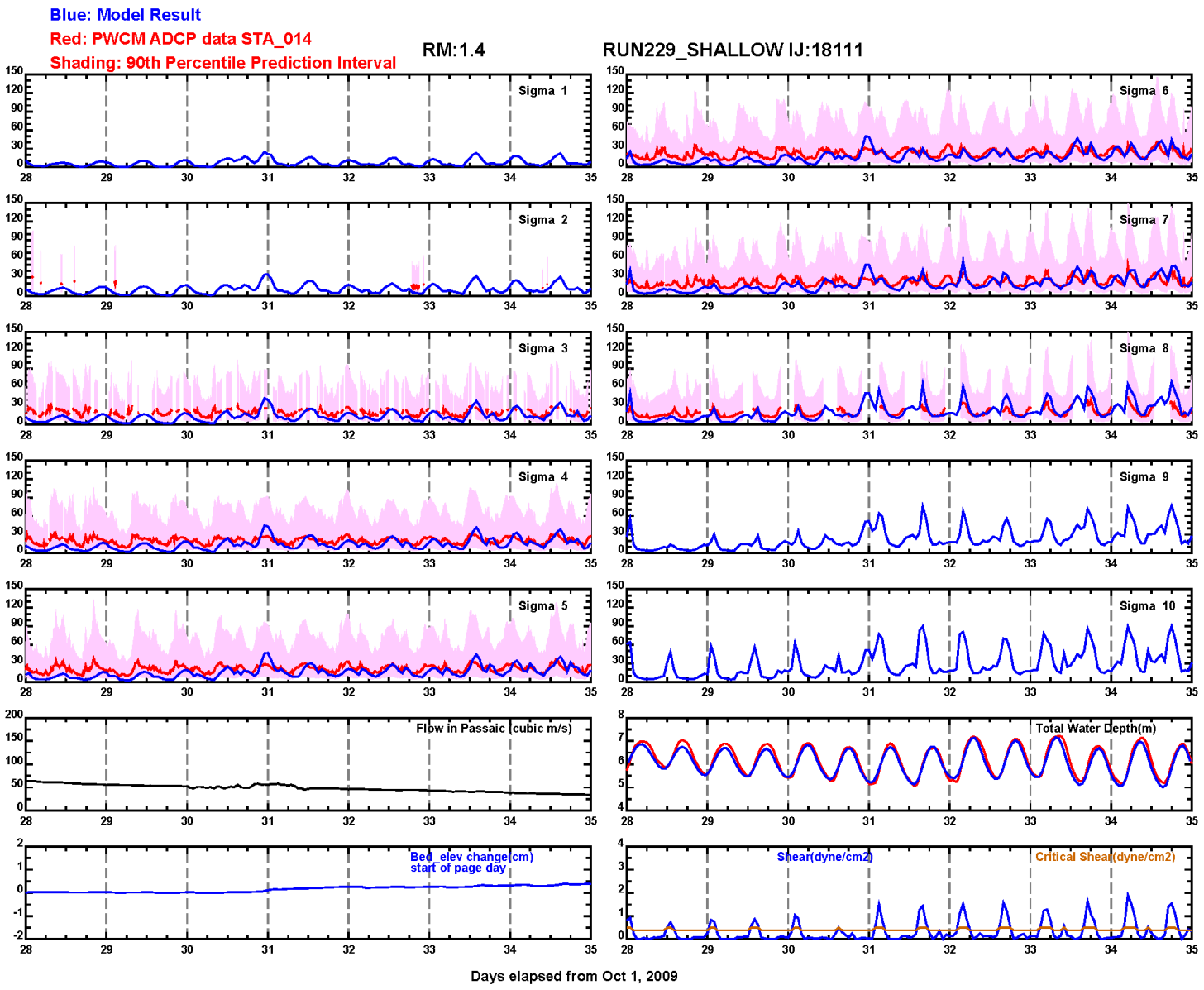

PWCM Fall TSS data (mg/L) versus model results for Station at 1.4 - October 29 to November 4, 2009

Lower Eight Miles of the Lower Passaic River

Figure 4-1

2014

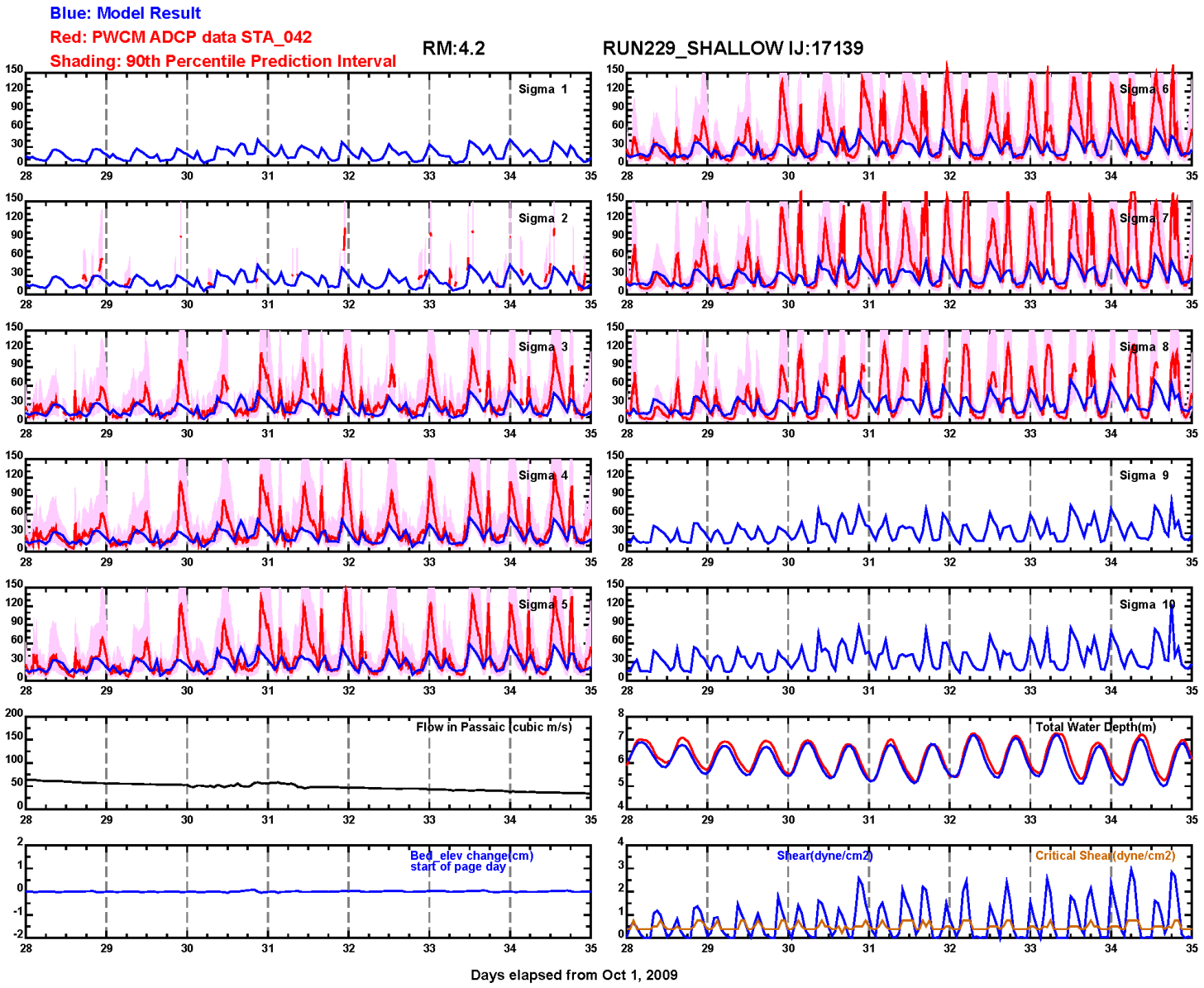

PWCM Fall TSS data (mg/L) versus model results for Station at 4.2 - October 29 to November 4, 2009

Lower Eight Miles of the Lower Passaic River

Figure 4-2

2014

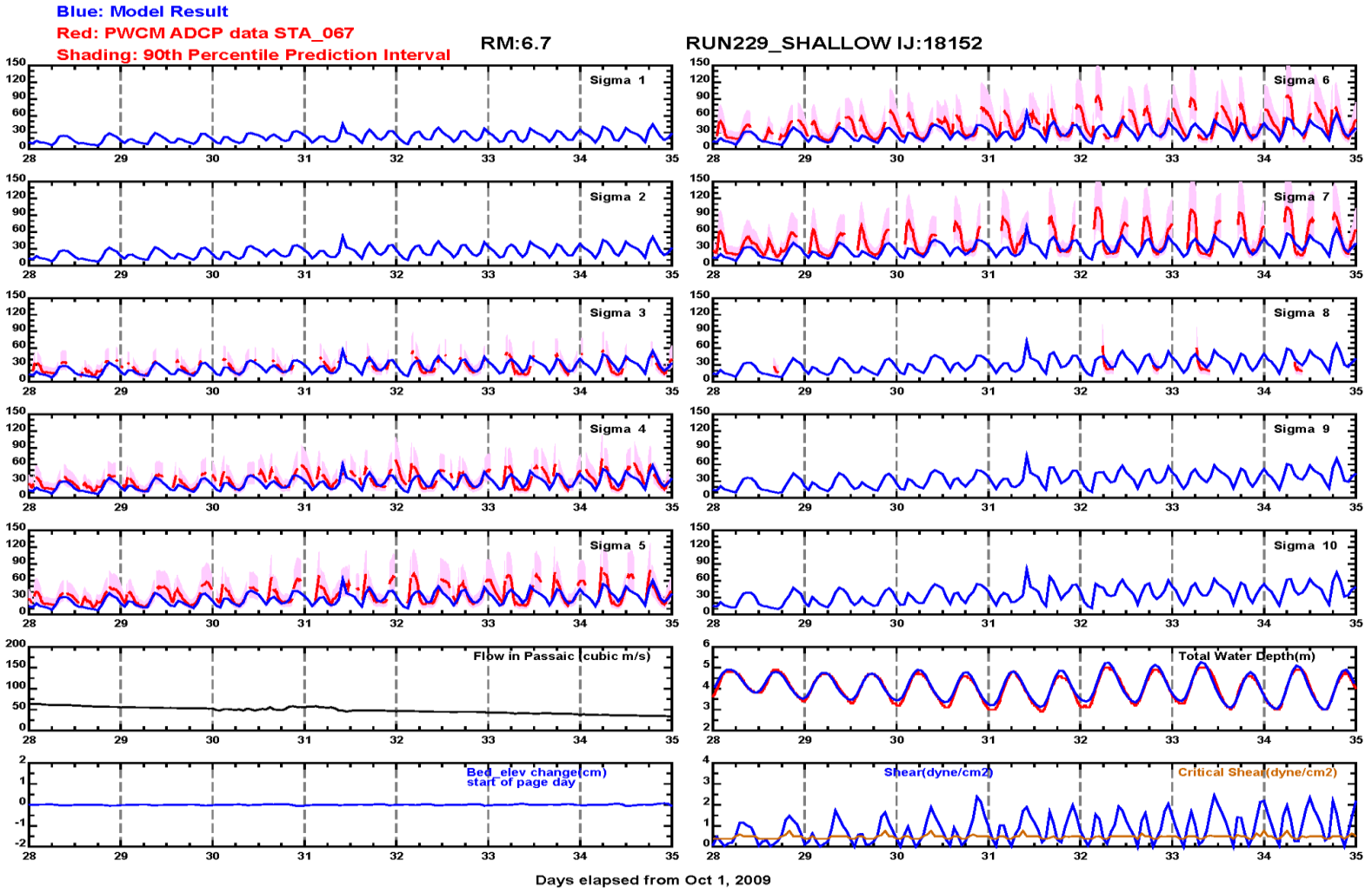

PWCM TSS data (mg/L) versus model results for Station at 6.7 - October 29 to November 4, 2009

Figure 4-3

Lower Eight Miles of the Lower Passaic River

2014

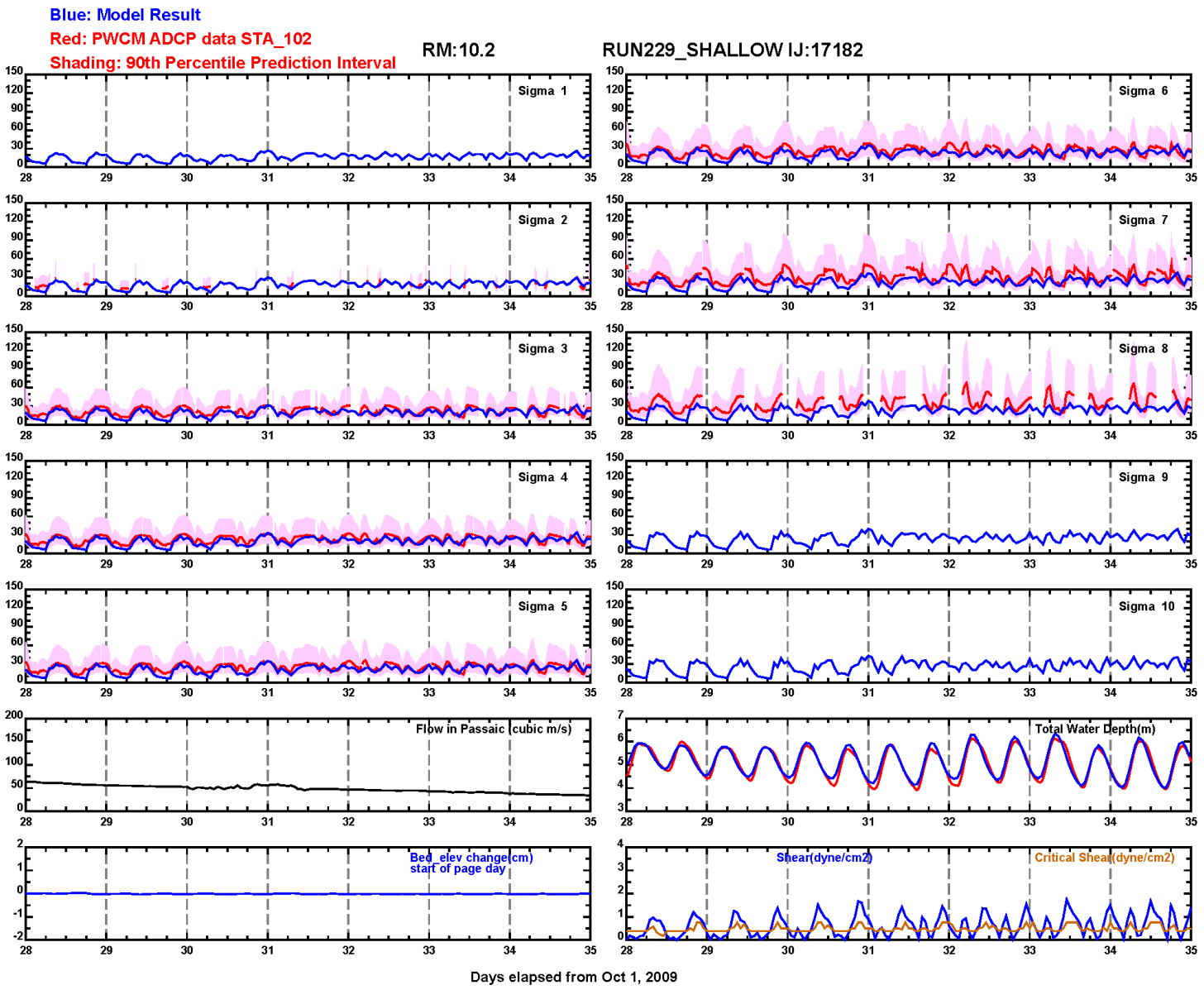

PWCM Fall TSS data (mg/L) versus model results for Station at 10.2 - October 29 to November 4, 2009

Lower Eight Miles of the Lower Passaic River

Figure 4-4

2014

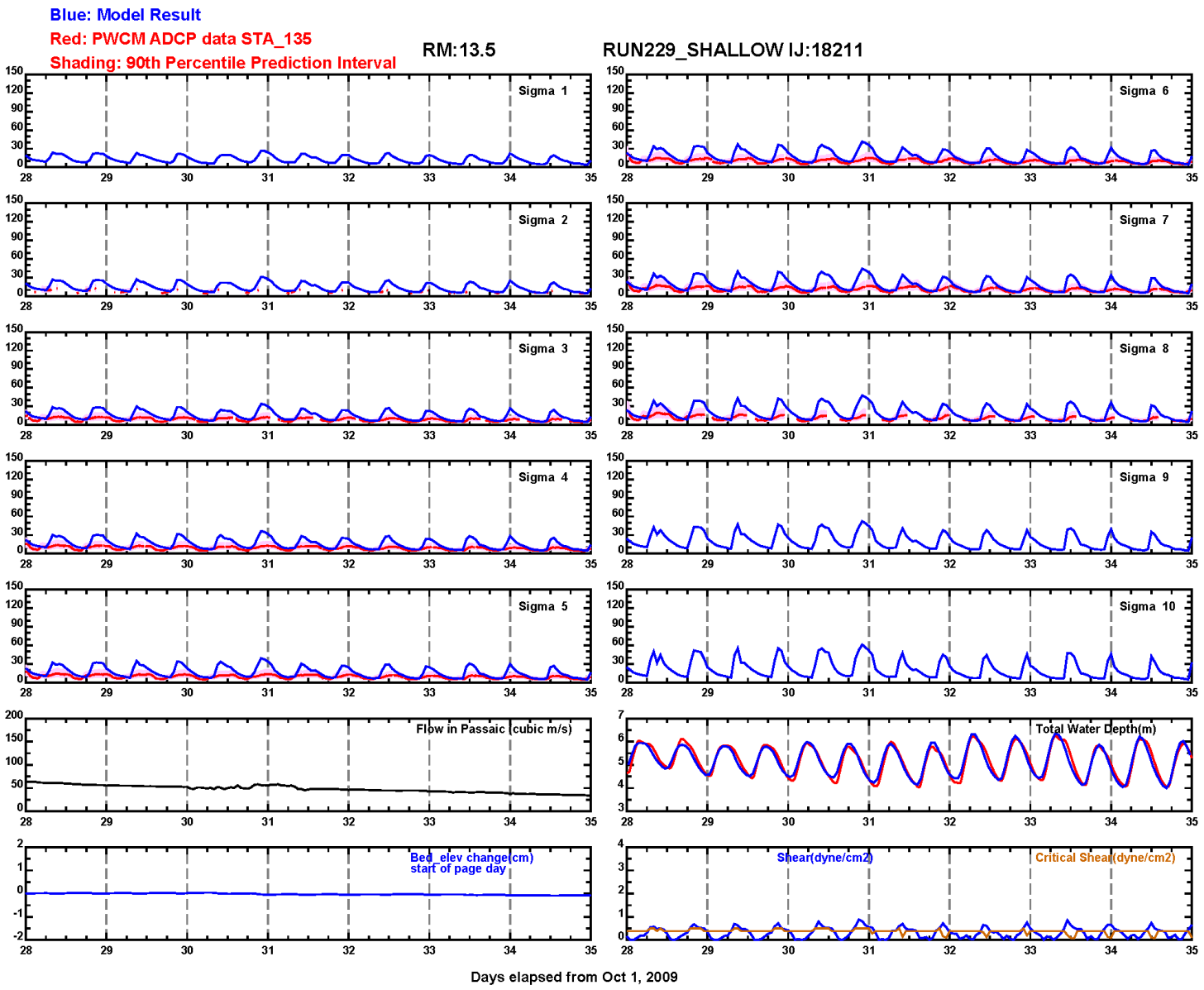

PWCM Fall TSS data (mg/L) versus model results for Station at 13.5 - October 29 to November 4, 2009

Lower Eight Miles of the Lower Passaic River

Figure 4-5

2014

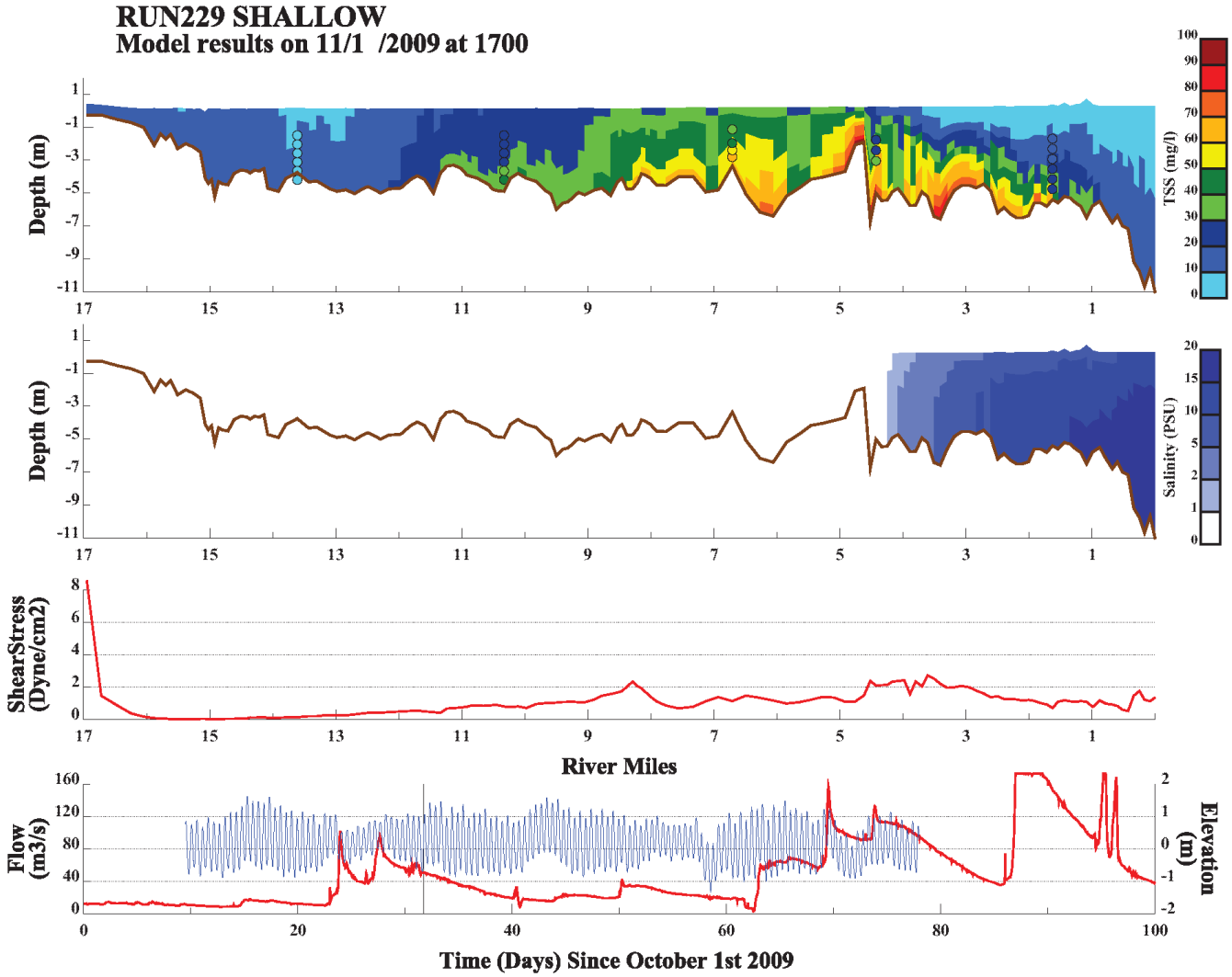

Axial slice of model TSS on 11/01/2009 at 17:00

Lower Eight Miles of the Lower Passaic River

Figure 4-6

2014

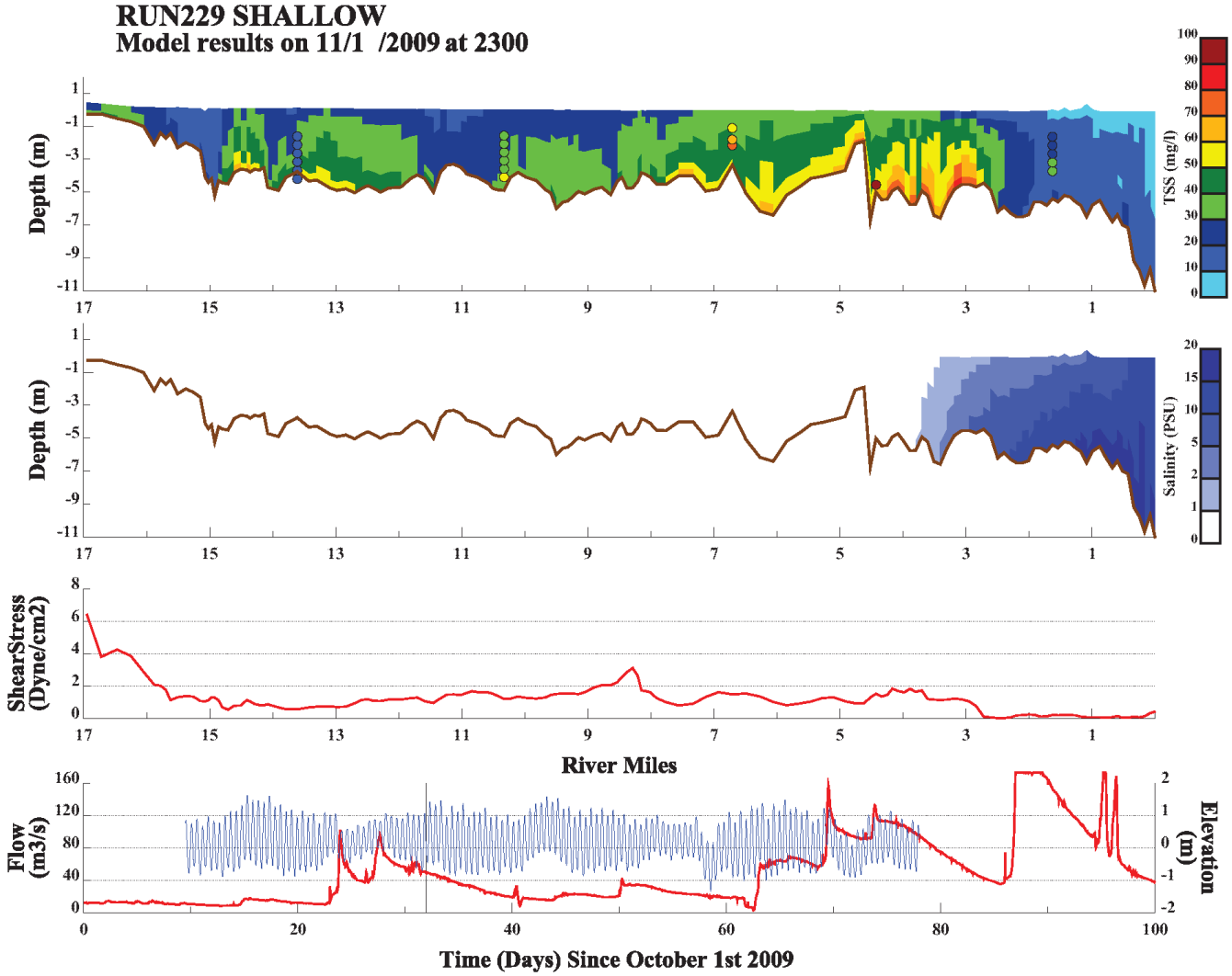

Axial slice of model TSS on 11/01/2009 at 23:00

Figure 4-7

Lower Eight Miles of the Lower Passaic River

2014

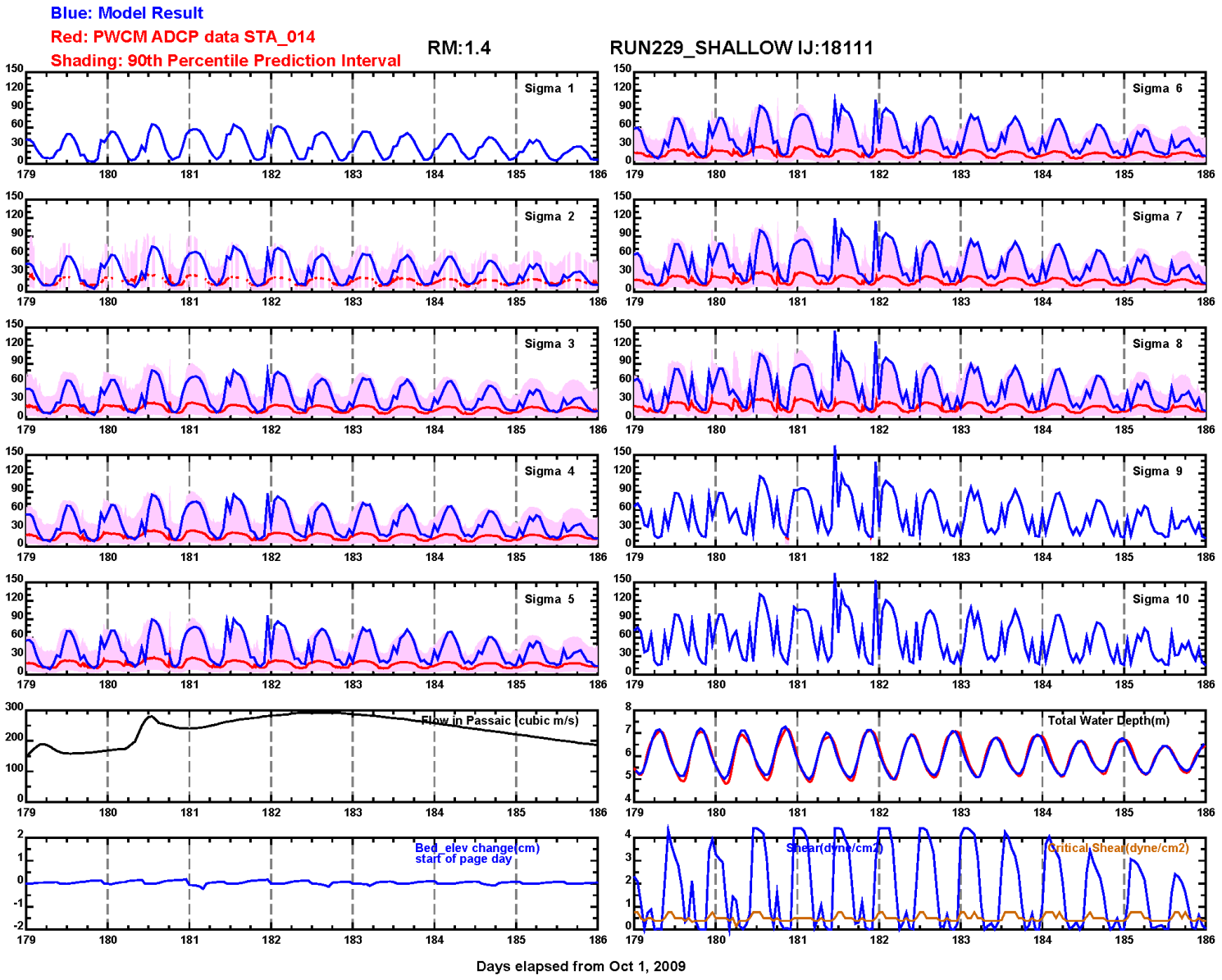

PWCM Spring TSS data (mg/L) versus model results for Station at 1.4 - March 29 to April 4, 2010

Figure 4-8

Lower Eight Miles of the Lower Passaic River

2014

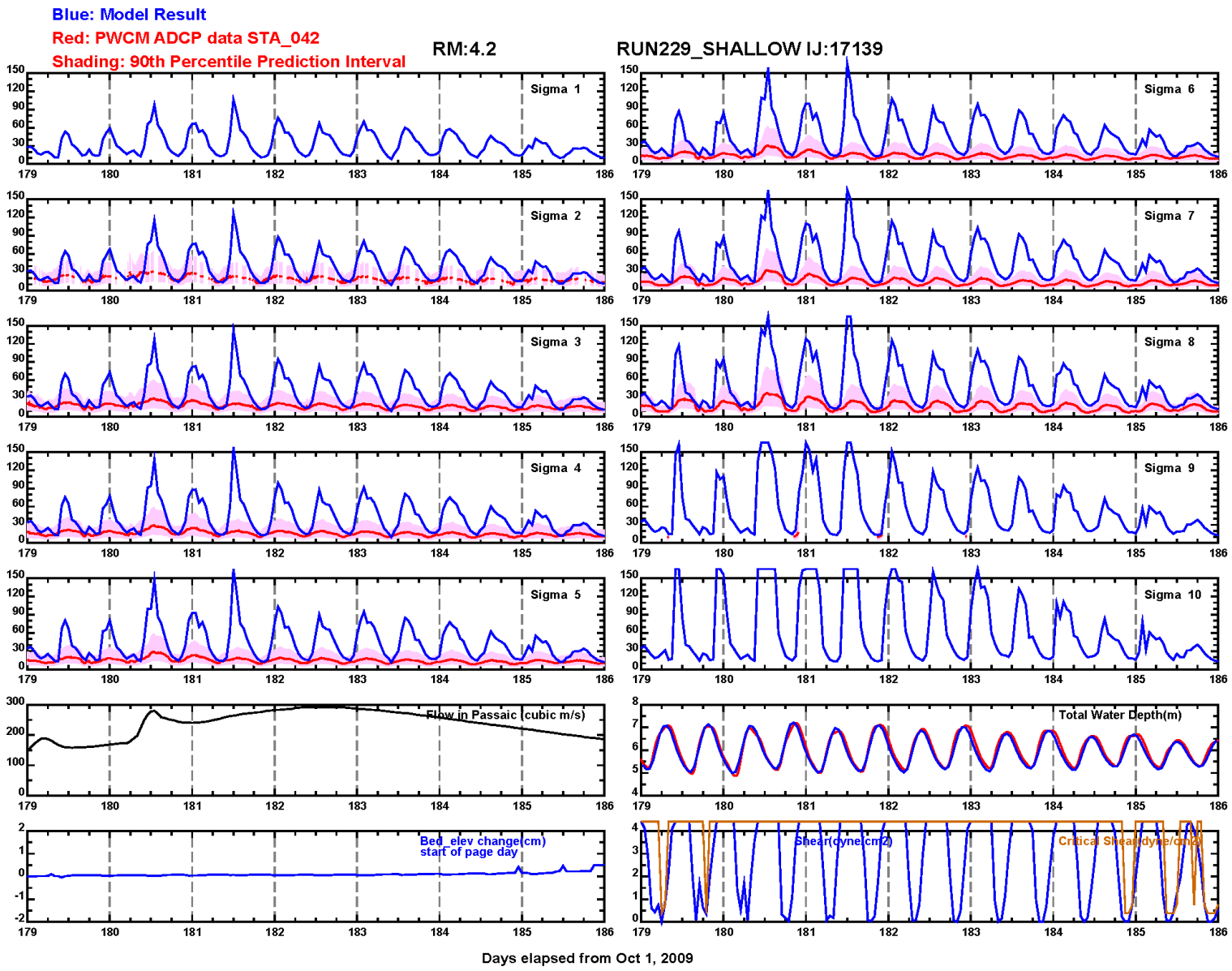

PWCM Spring TSS data (mg/L) versus model results for Station at 4.2 - March 29 to April 4, 2010

Figure 4-9

Lower Eight Miles of the Lower Passaic River

2014

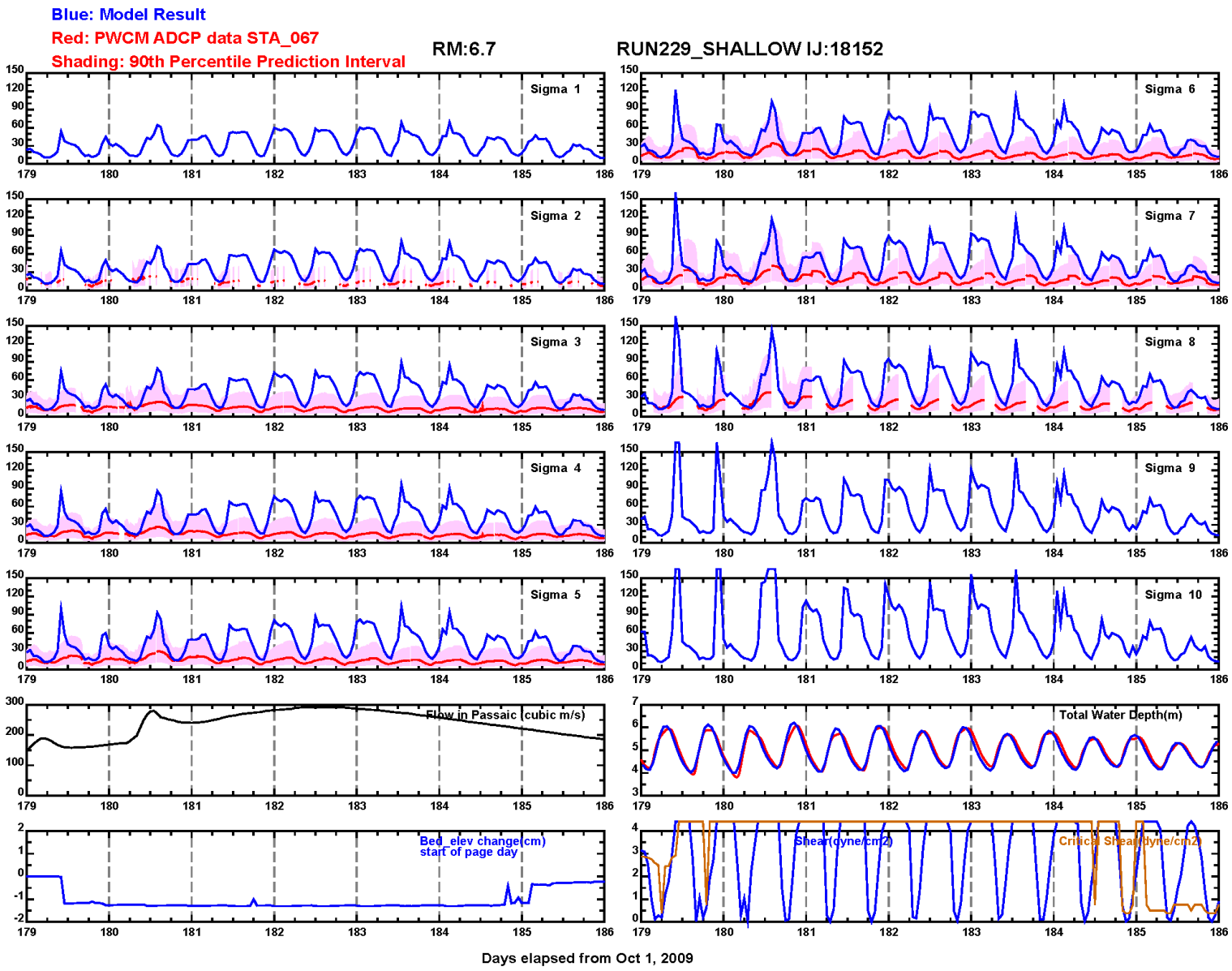

PWCM Spring TSS data (mg/L) versus model results for Station at 6.7 - March 29 to April 4, 2010

Figure 4-10

Lower Eight Miles of the Lower Passaic River

2014

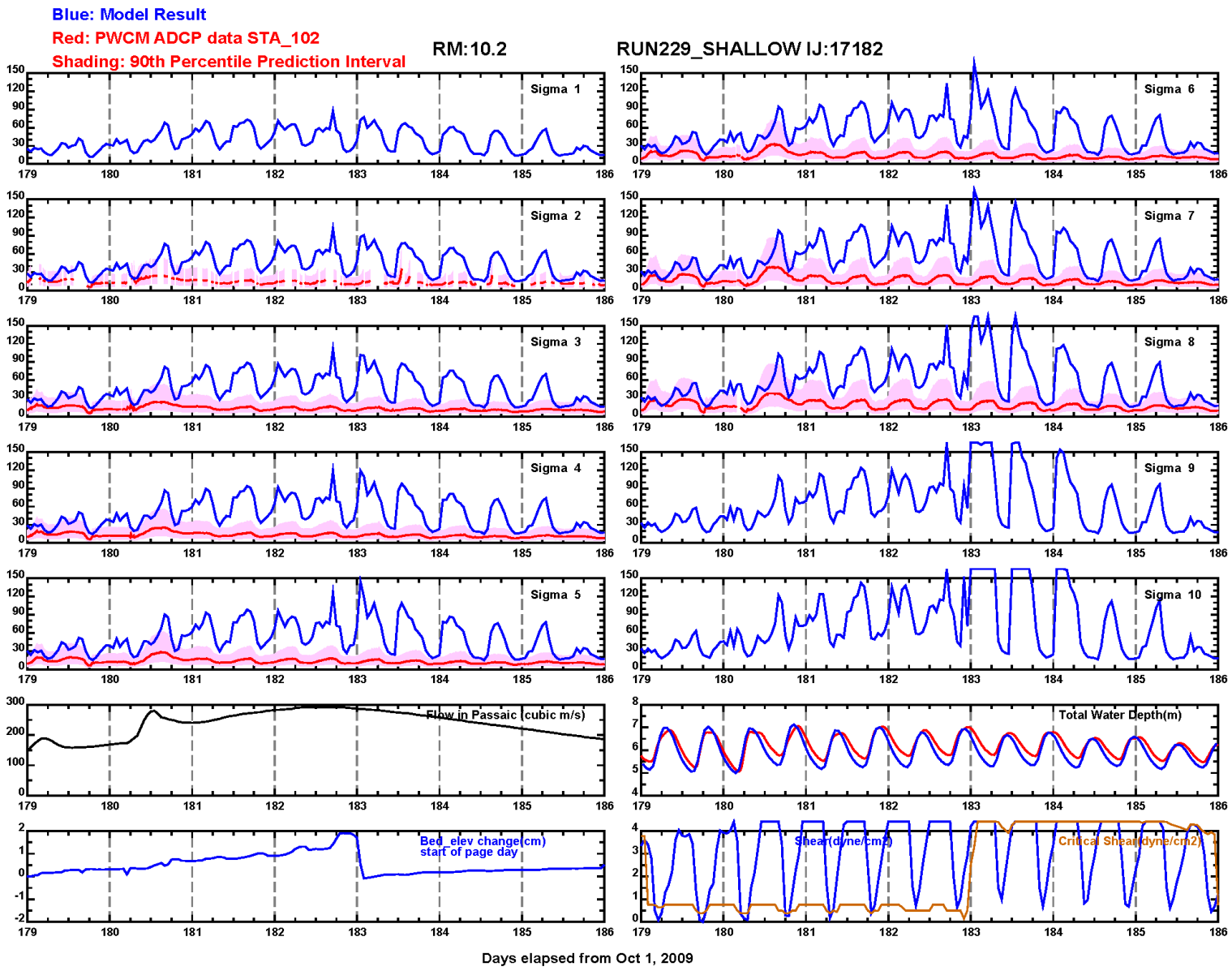

PWCM Spring TSS data (mg/L) versus model results for Station at 10.2 - March 29 to April 4, 2010

Figure 4-11

Lower Eight Miles of the Lower Passaic River

2014

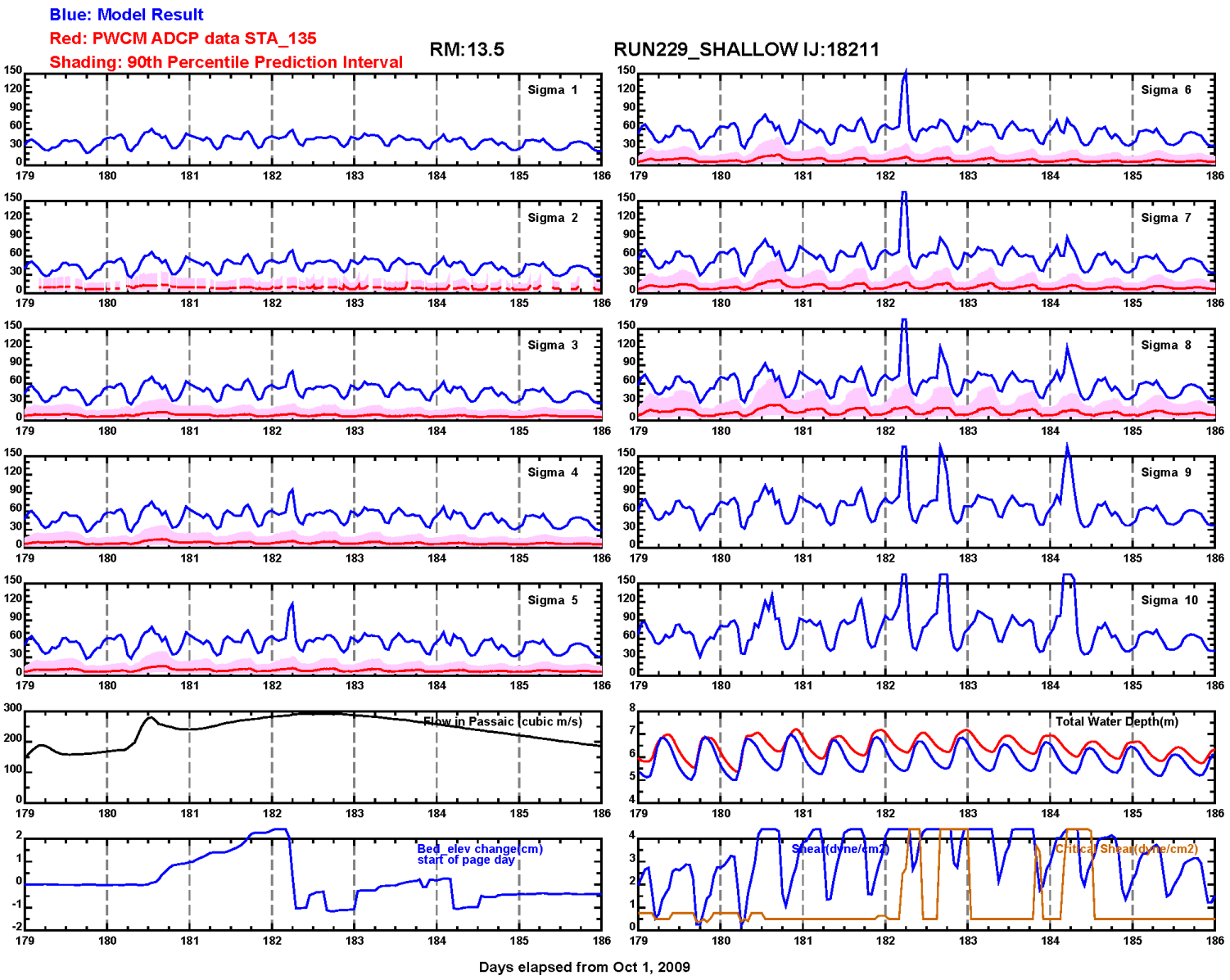

PWCM Spring TSS data (mg/L) versus model results for Station at 13.5 - March 29 to April 4, 2010

Figure 4-12

Lower Eight Miles of the Lower Passaic River

2014

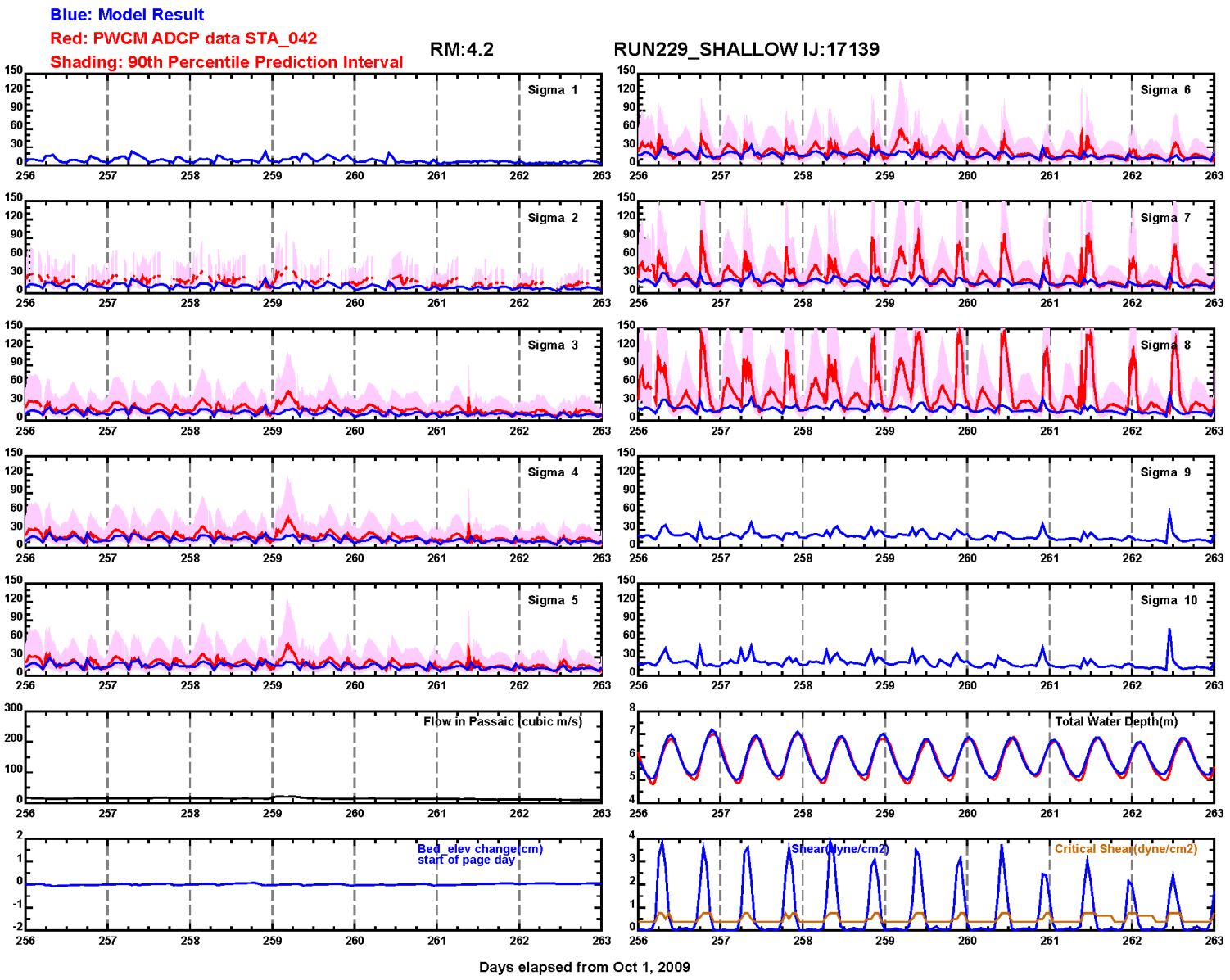

PWCM Spring TSS data (mg/L) versus model results for Station at 4.2 - June 14-21

Figure 4-13

Lower Eight Miles of the Lower Passaic River

2014

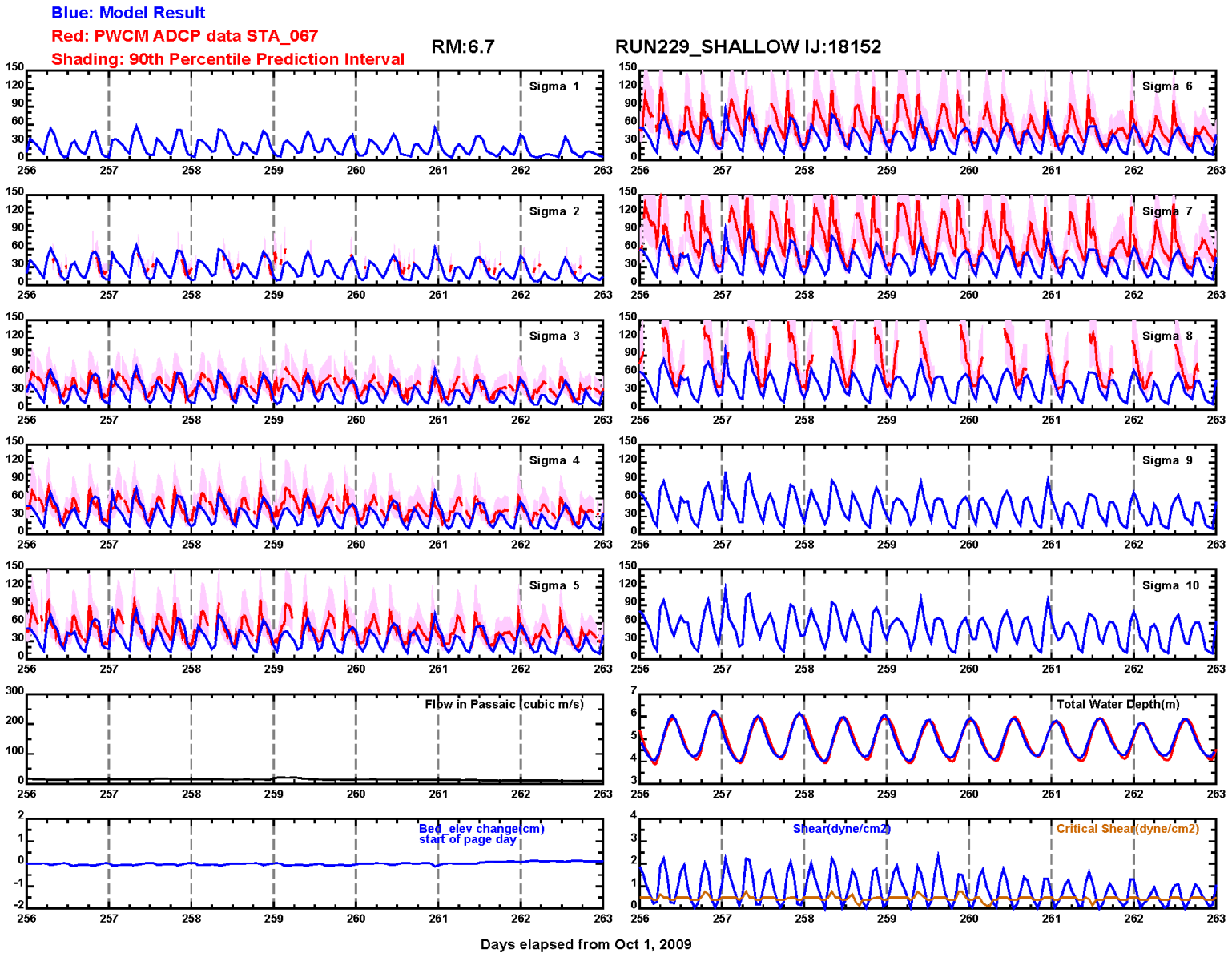

PWCM Spring TSS data (mg/L) versus model results for Station at 6.7 - June 14-21

Figure 4-14

Lower Eight Miles of the Lower Passaic River

2014

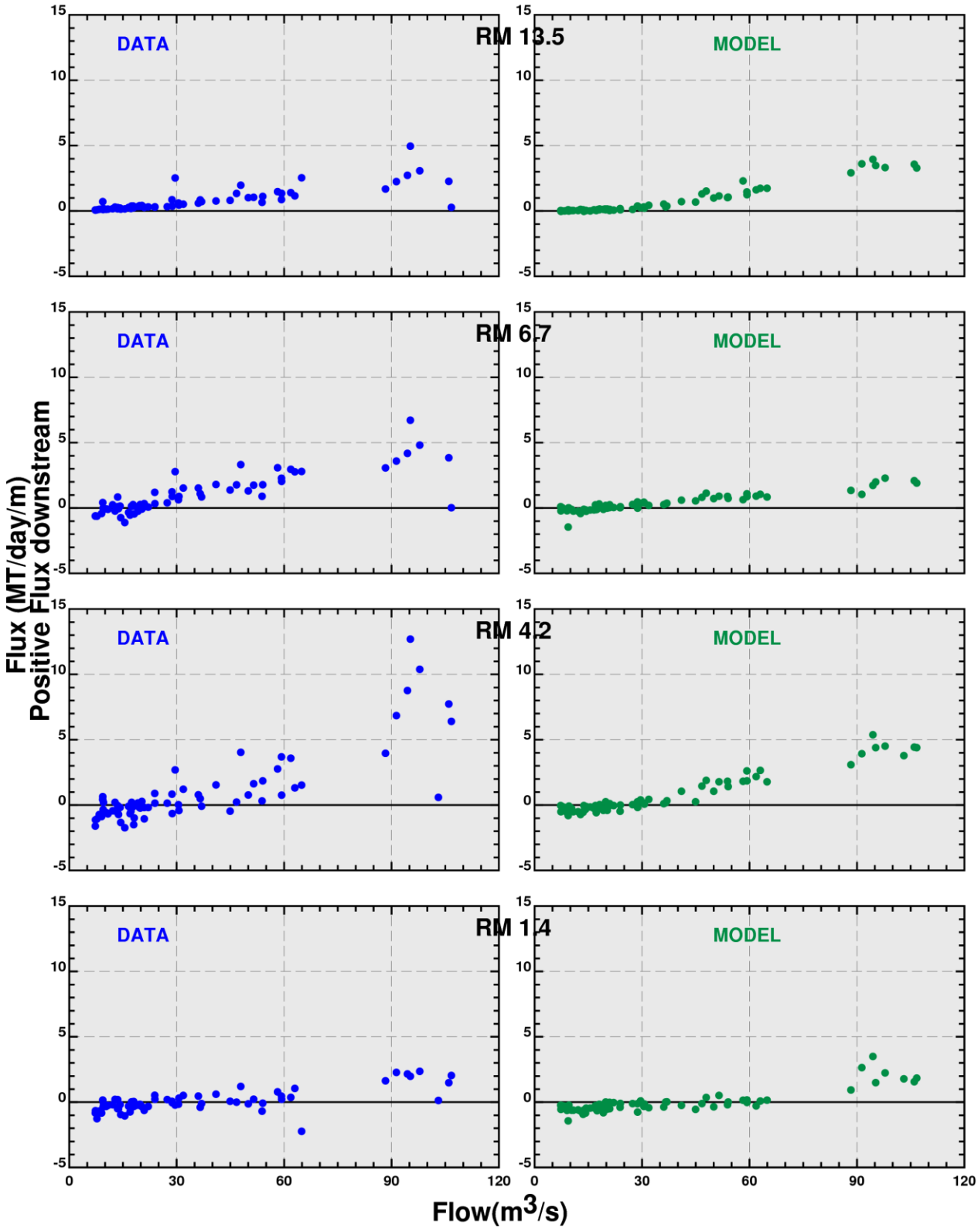

Data-based and model-simulated solids fluxes during PWCM period

Figure 4-15

2014

Lower Eight Miles of the Lower Passaic River

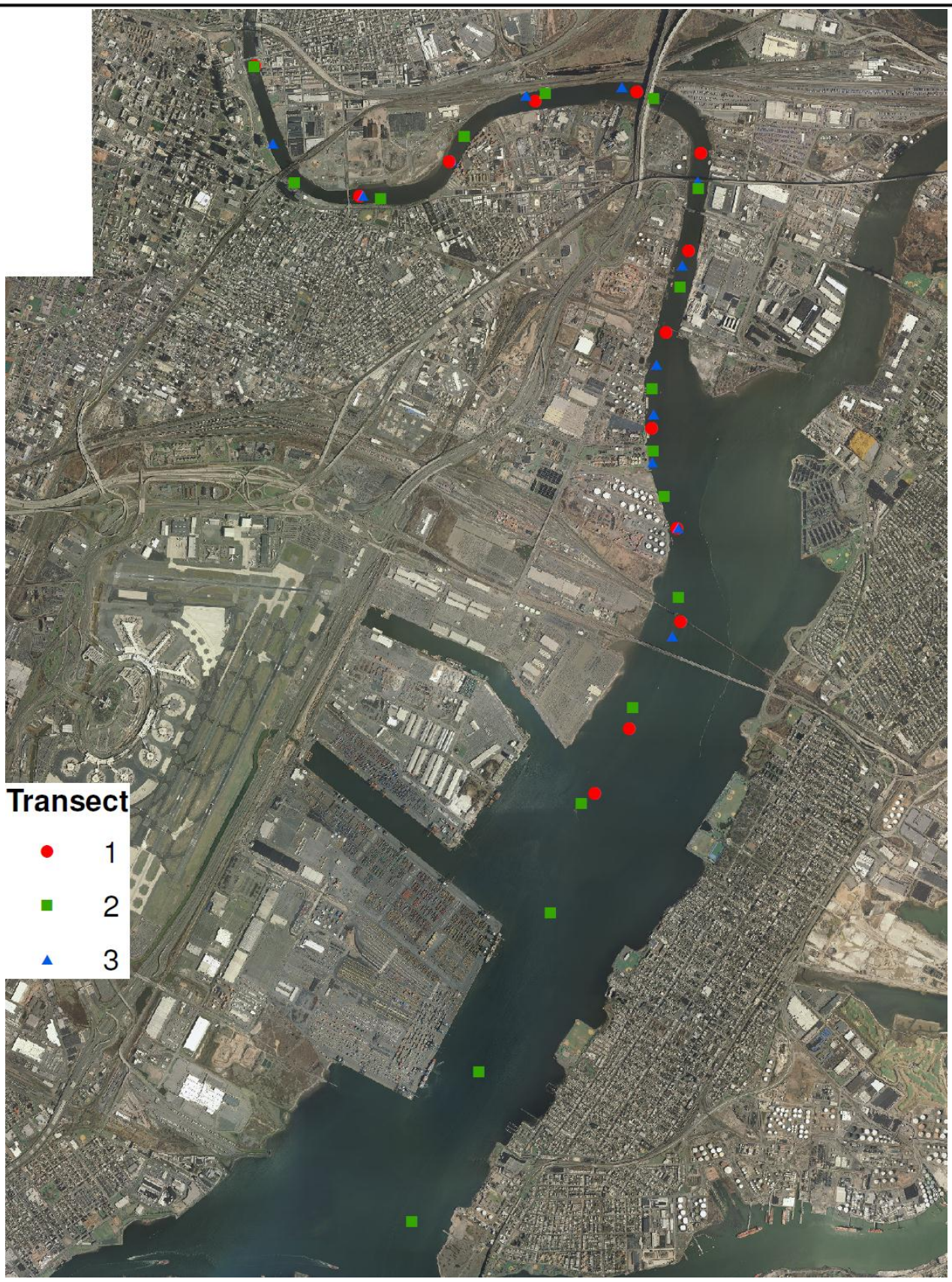

Mar 16, 2010 high flow transect locations

Figure 4-16

Lower Eight Miles of the Lower Passaic River

2014

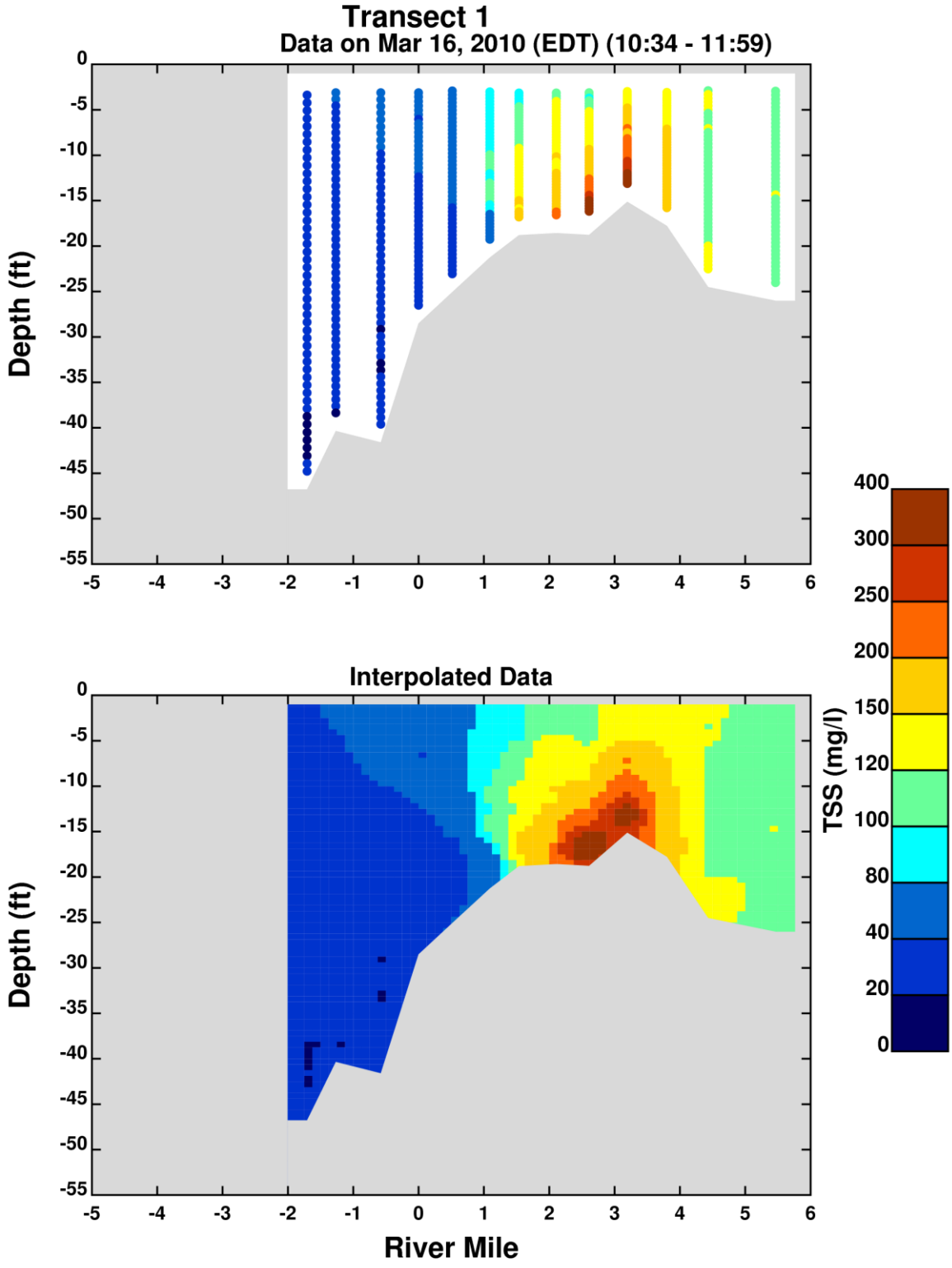

2010 TSS estimates for Transect 1

Figure 4-17

Lower Eight Miles of the Lower Passaic River

2014

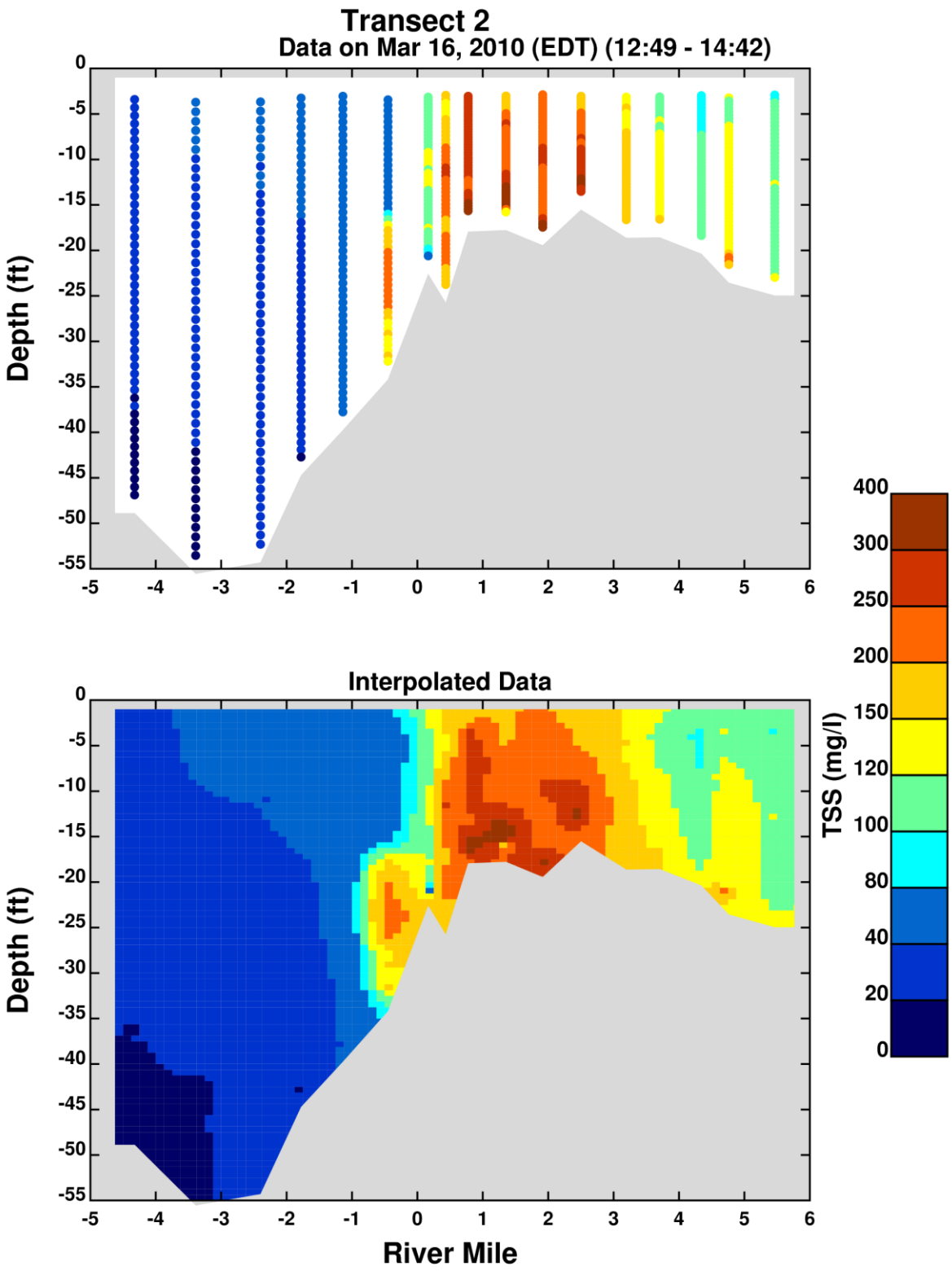

2010 TSS estimates for Transect 2

Figure 4-18

Lower Eight Miles of the Lower Passaic River

2014

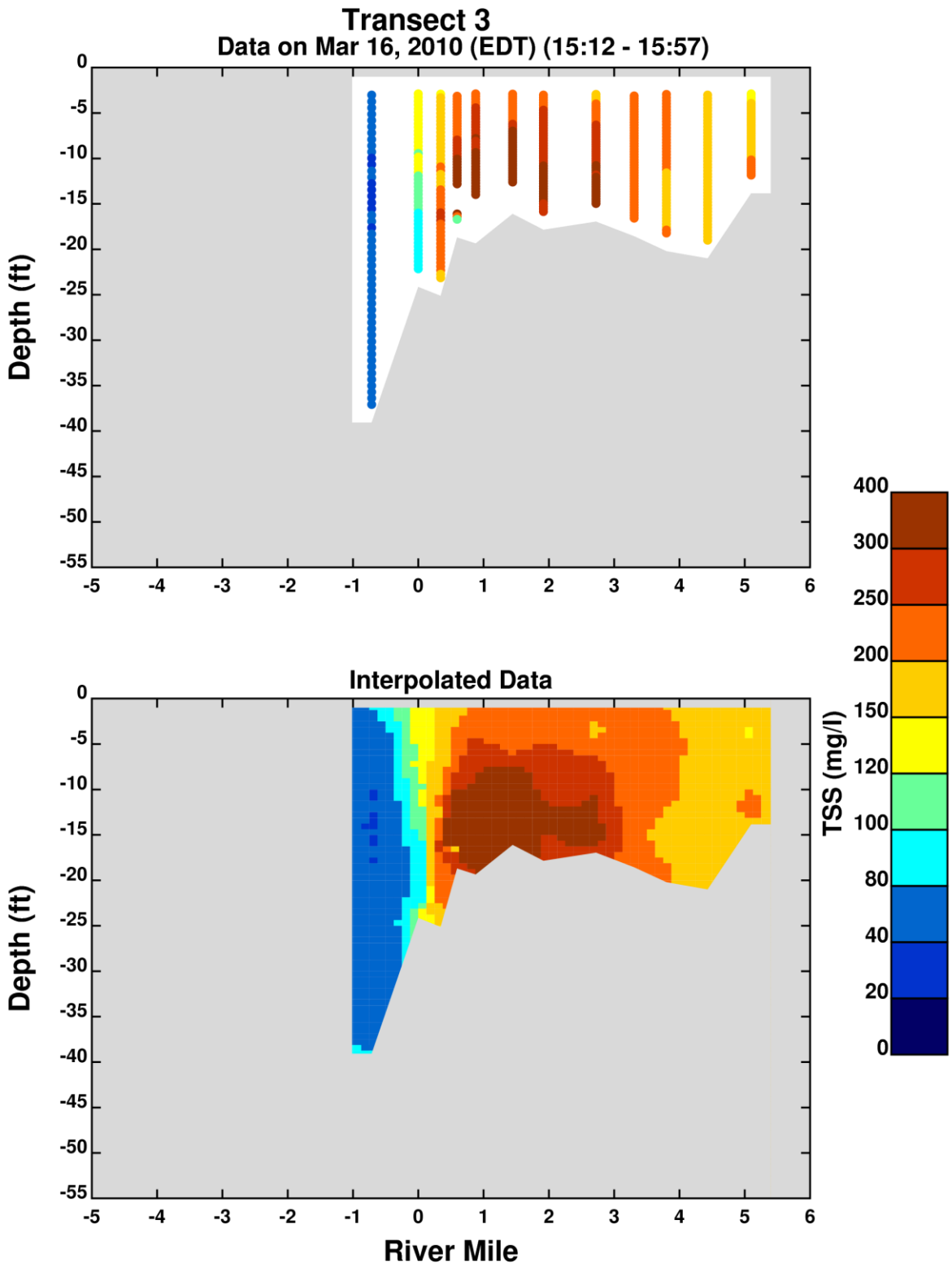

2010 TSS estimates for Transect 3

Figure 4-19

Lower Eight Miles of the Lower Passaic River

2014

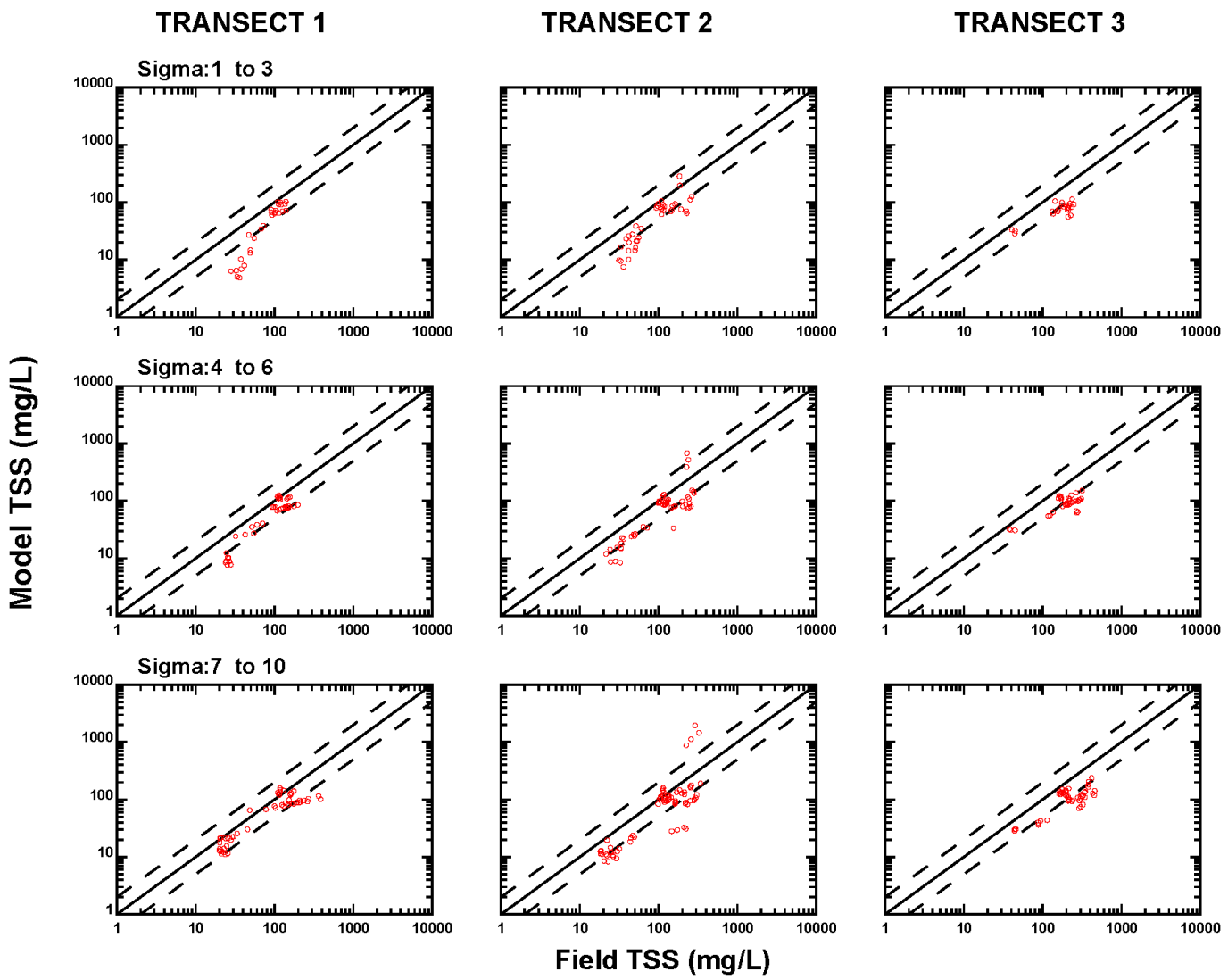

Scatter Plot for Model Data Comparison

Lower Eight Miles of the Lower Passaic River

Figure 4-20

2014

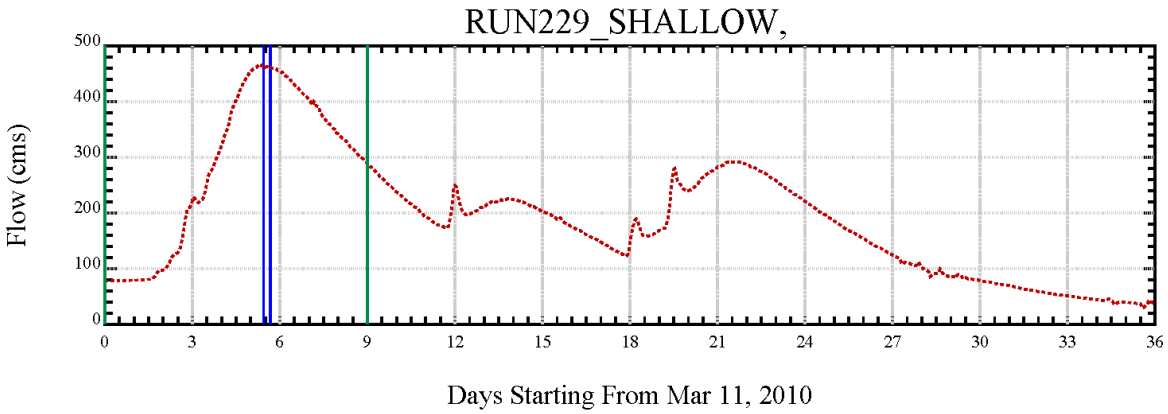

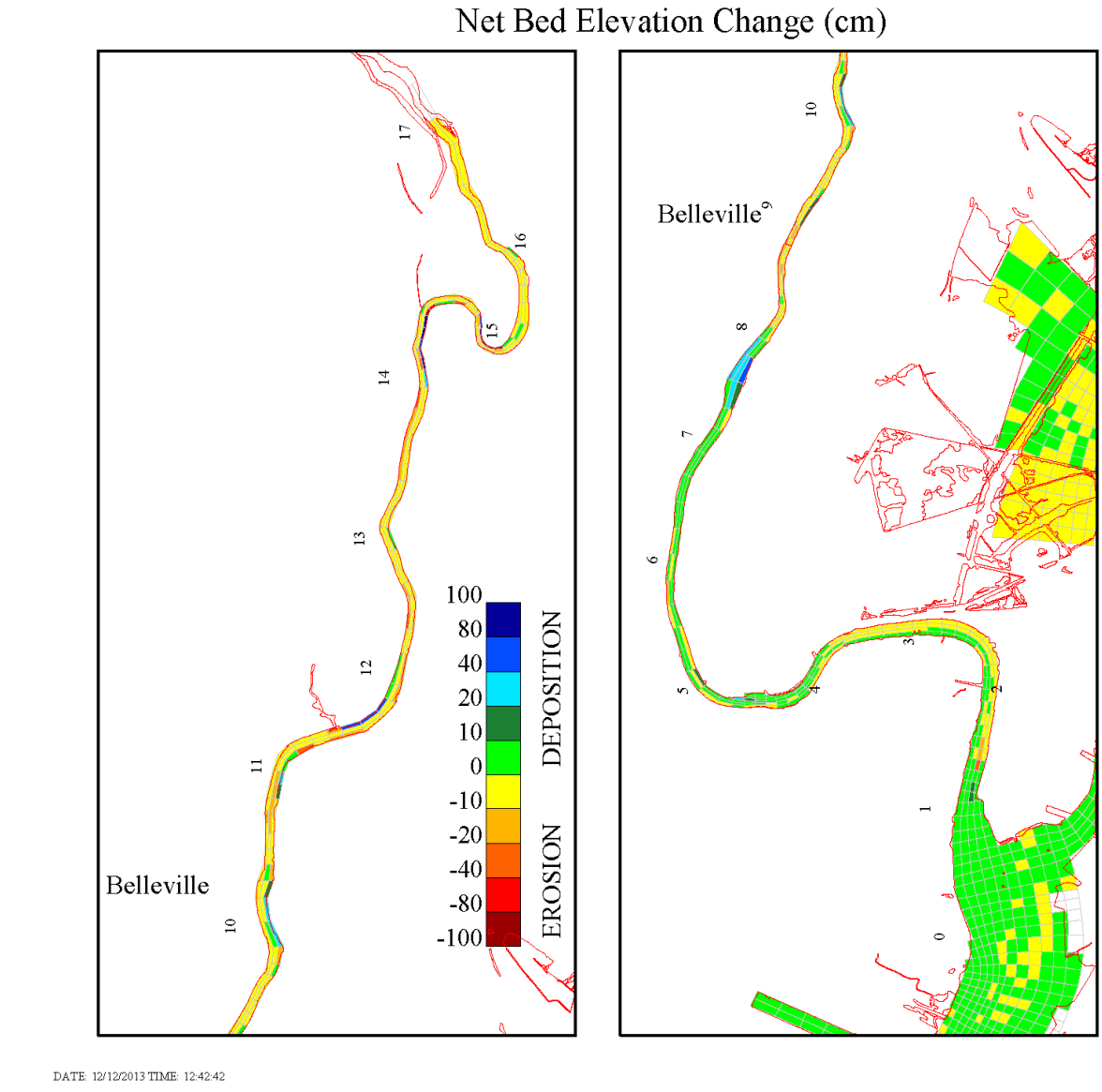

Simulated Net Bed Elevation during March 2010 Event

Figure 4-21

Lower Eight Miles of the Lower Passaic River

2014

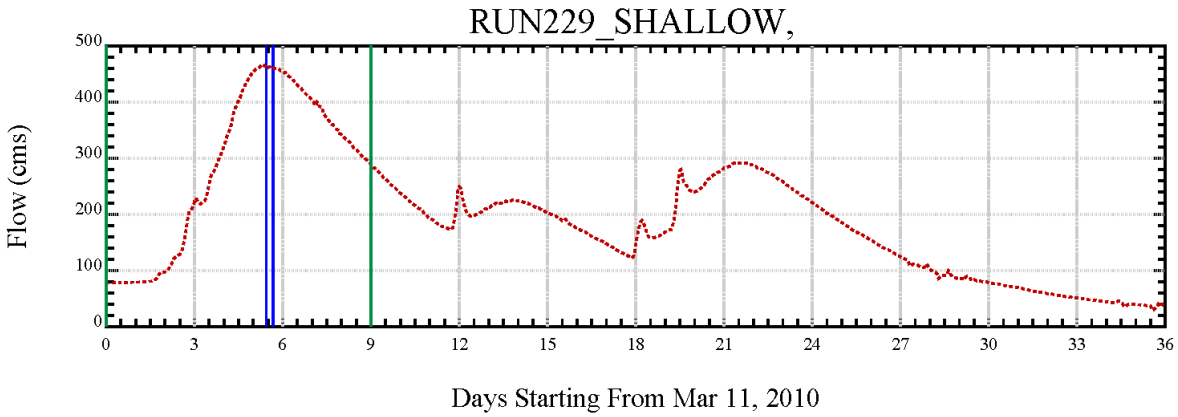

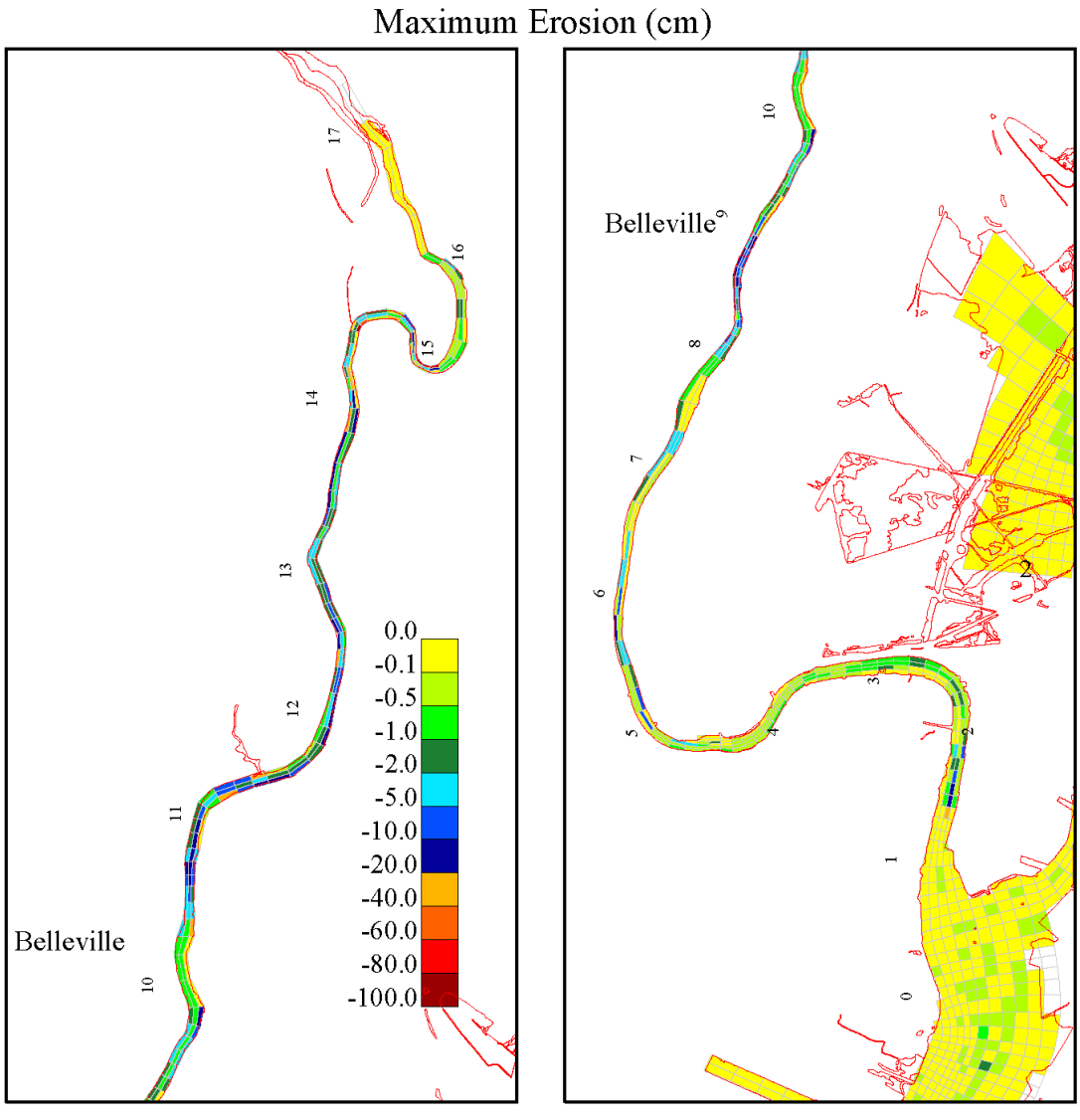

Simulated Maximum Bed Erosion Depth during March 2010 Event

Figure 4-22

Lower Eight Miles of the Lower Passaic River

2014

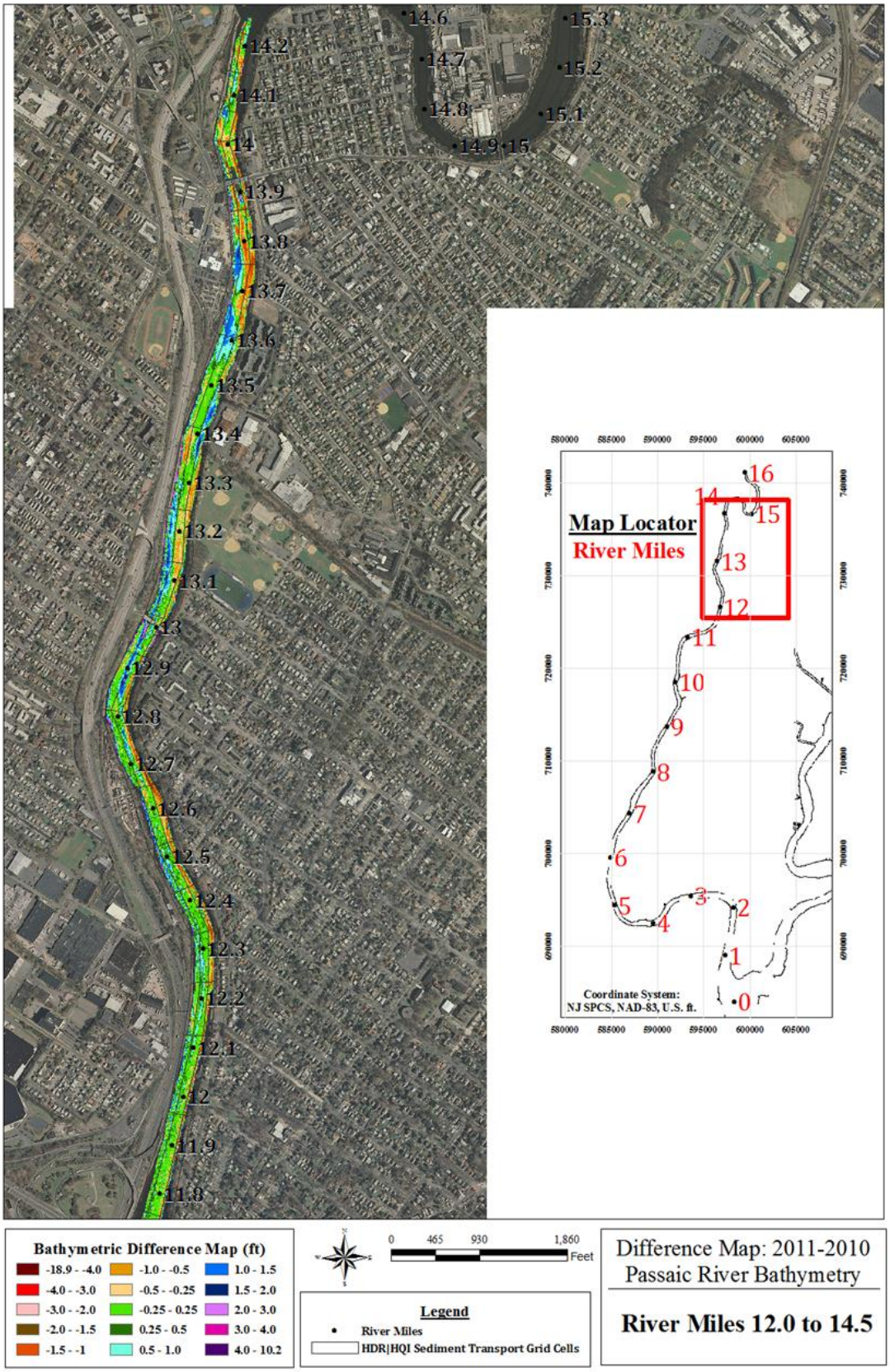

Change in bed elevation from 2010-2011 multibeam surveys (RM12-14.5)

Lower Eight Miles of the Lower Passaic River

Figure 4-23

2014

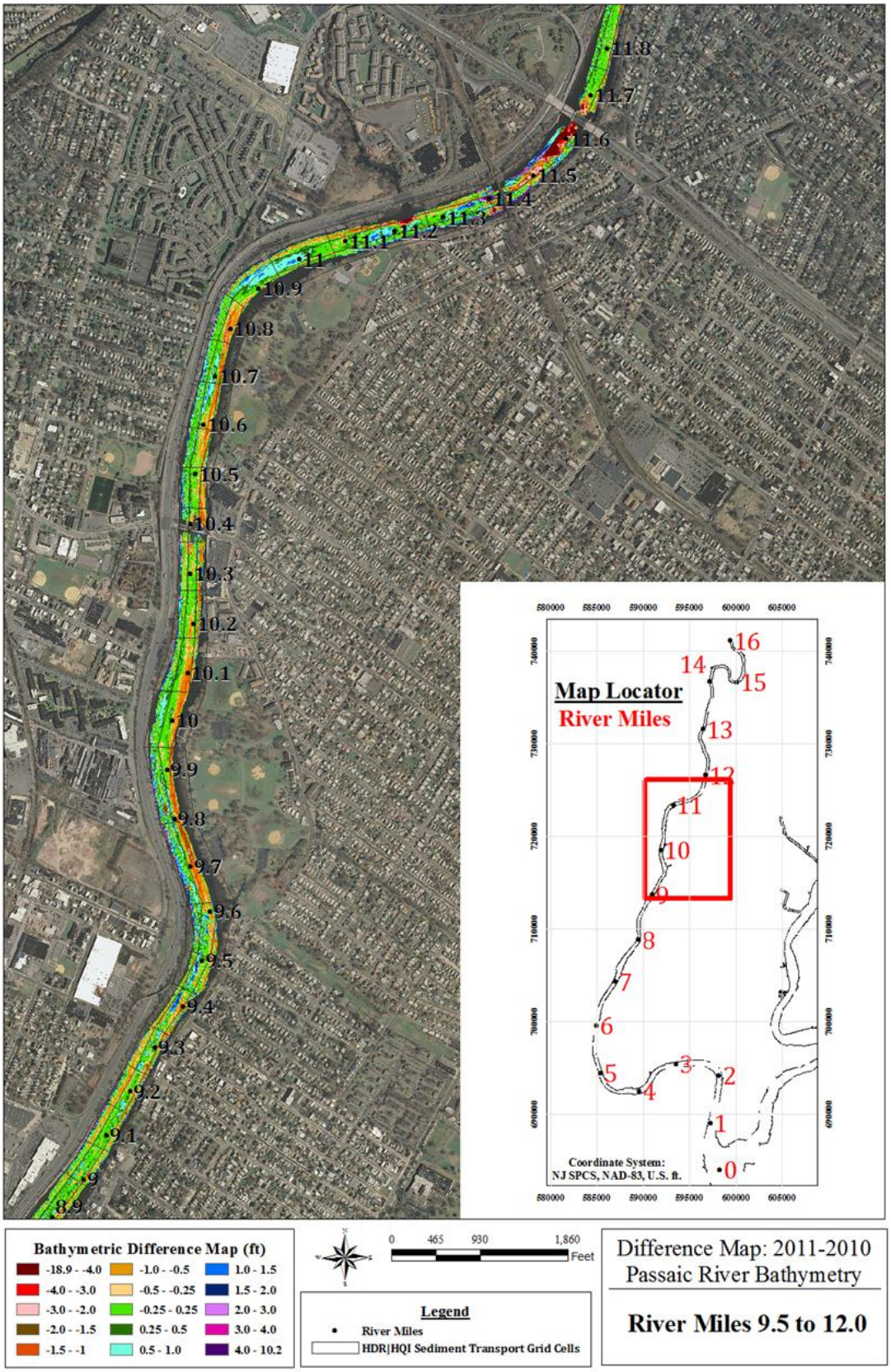

Change in bed elevation from 2010-2011 multibeam surveys (RM9.5-12.0)

Lower Eight Miles of the Lower Passaic River

Figure 4-24

2014

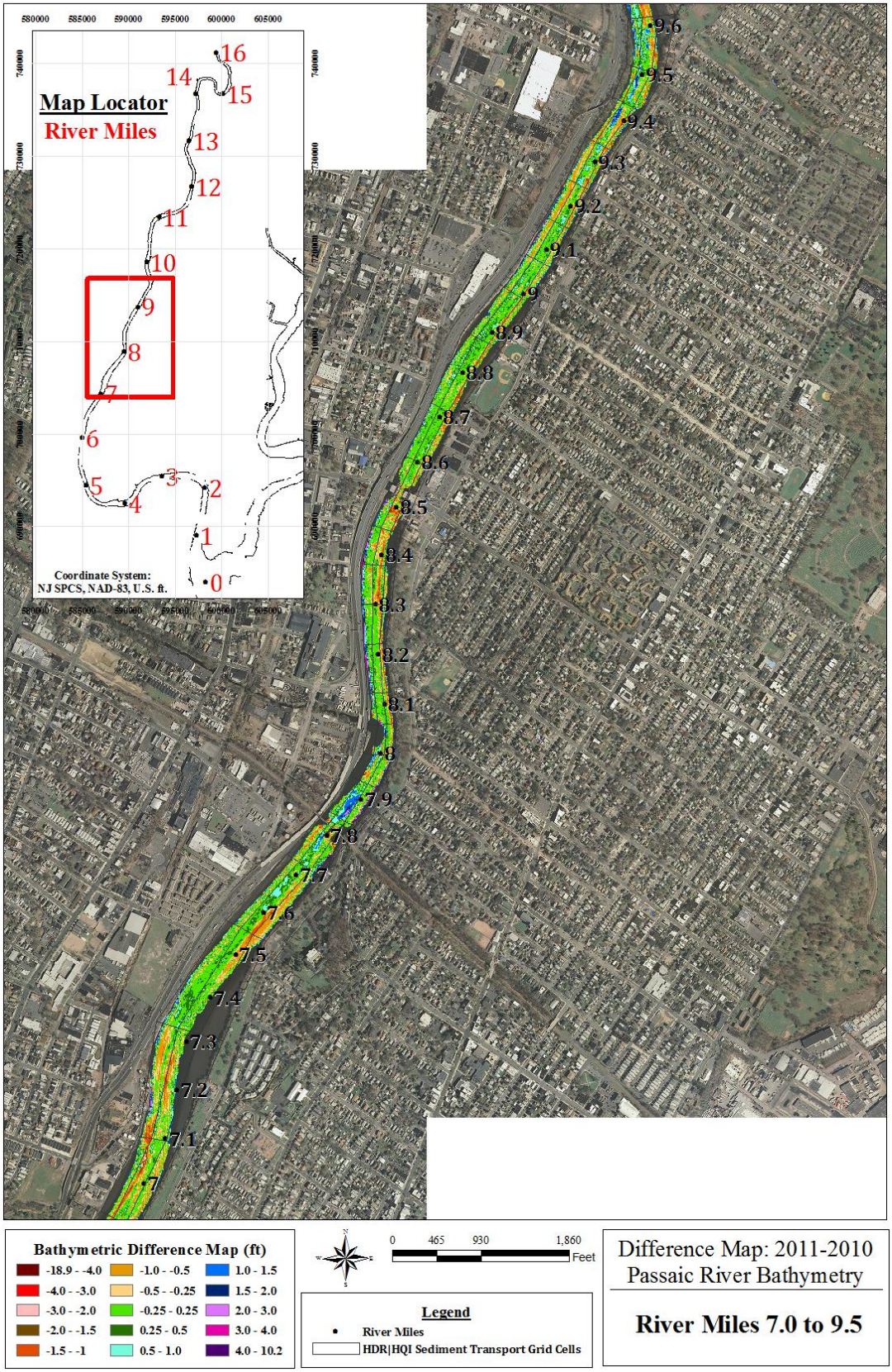

Change in bed elevation from 2010-2011 multibeam surveys (RM7.0-9.5)

Lower Eight Miles of the Lower Passaic River

Figure 4-25

2014

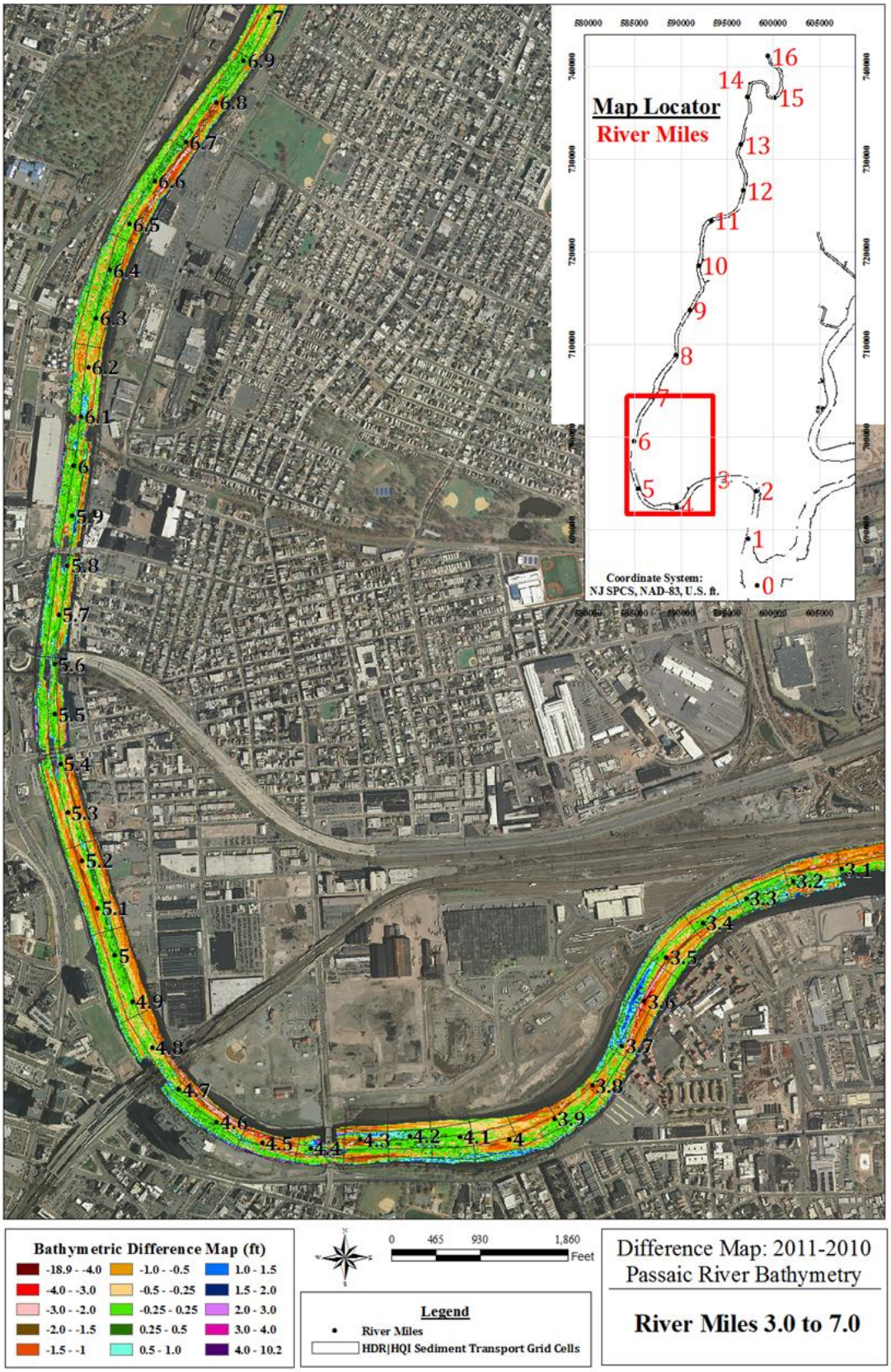

Change in bed elevation from 2010-2011 multibeam surveys (RM3.0-7.0)

Lower Eight Miles of the Lower Passaic River

Figure 4-26

2014

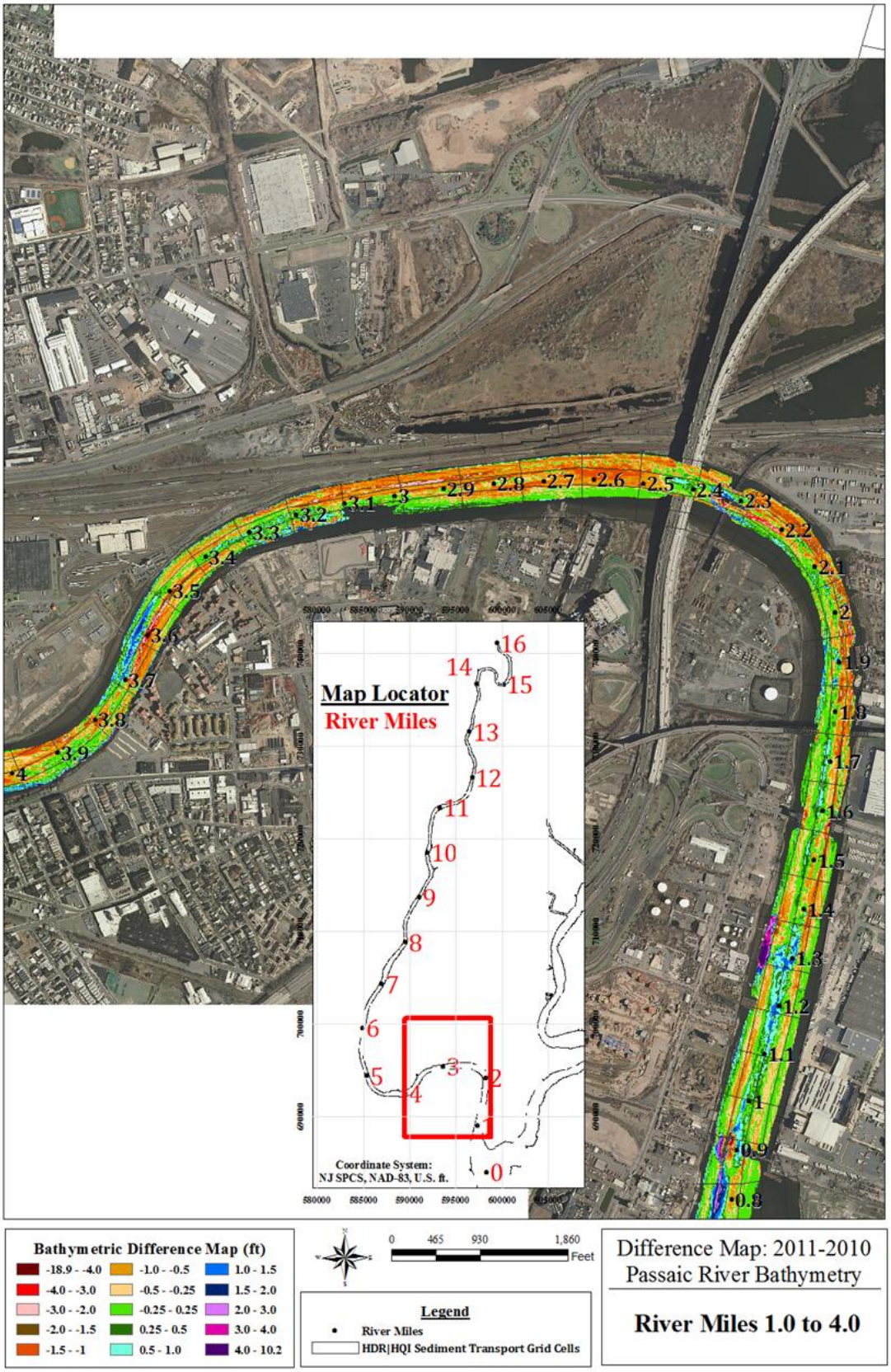

Change in bed elevation from 2010-2011 multibeam surveys (RM1.0-4.0)

Lower Eight Miles of the Lower Passaic River

Figure 4-27

2014

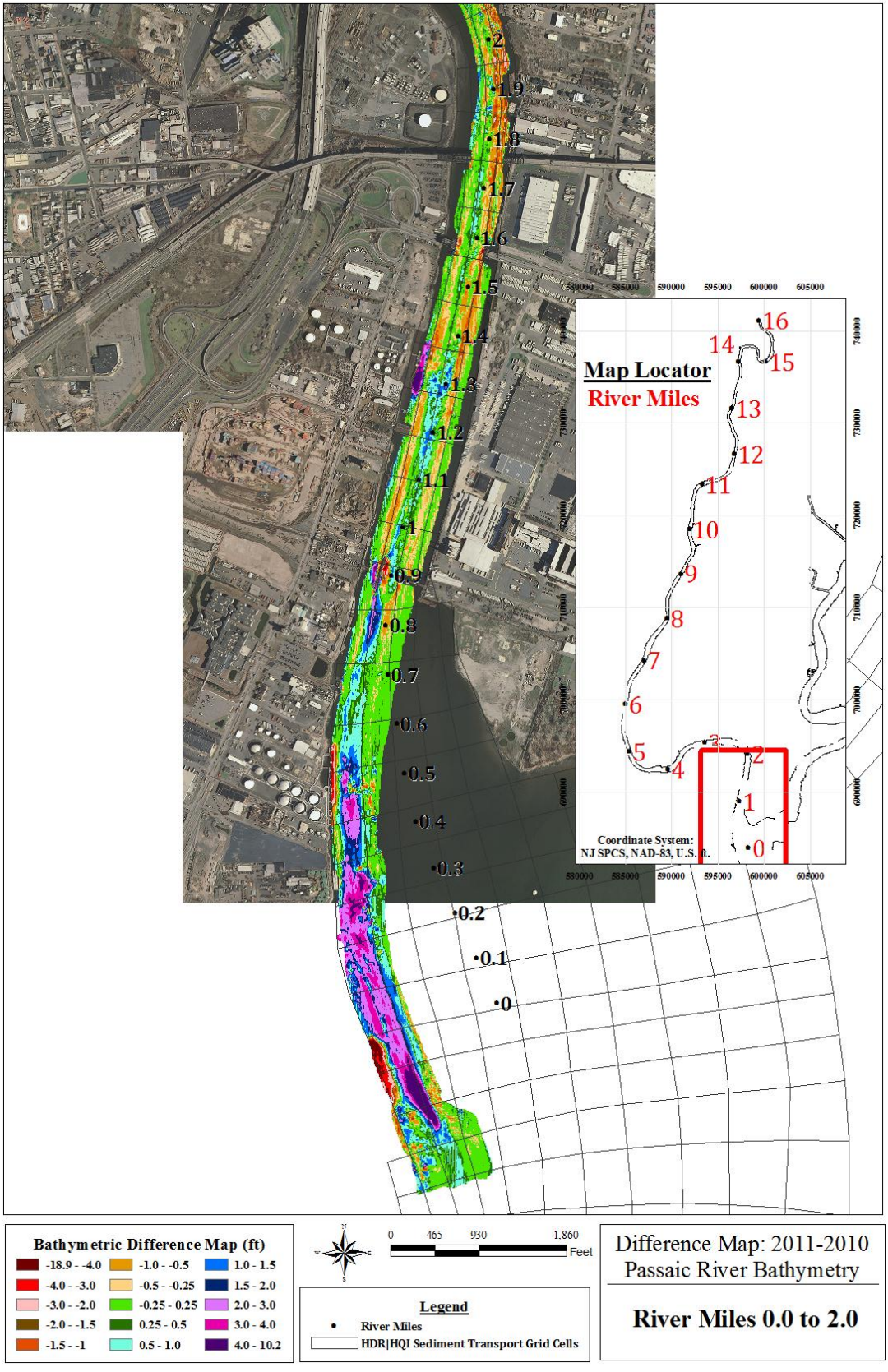

Change in bed elevation from 2010-2011 multibeam surveys (RM0.0-2.0)

Lower Eight Miles of the Lower Passaic River

Figure 4-28

2014

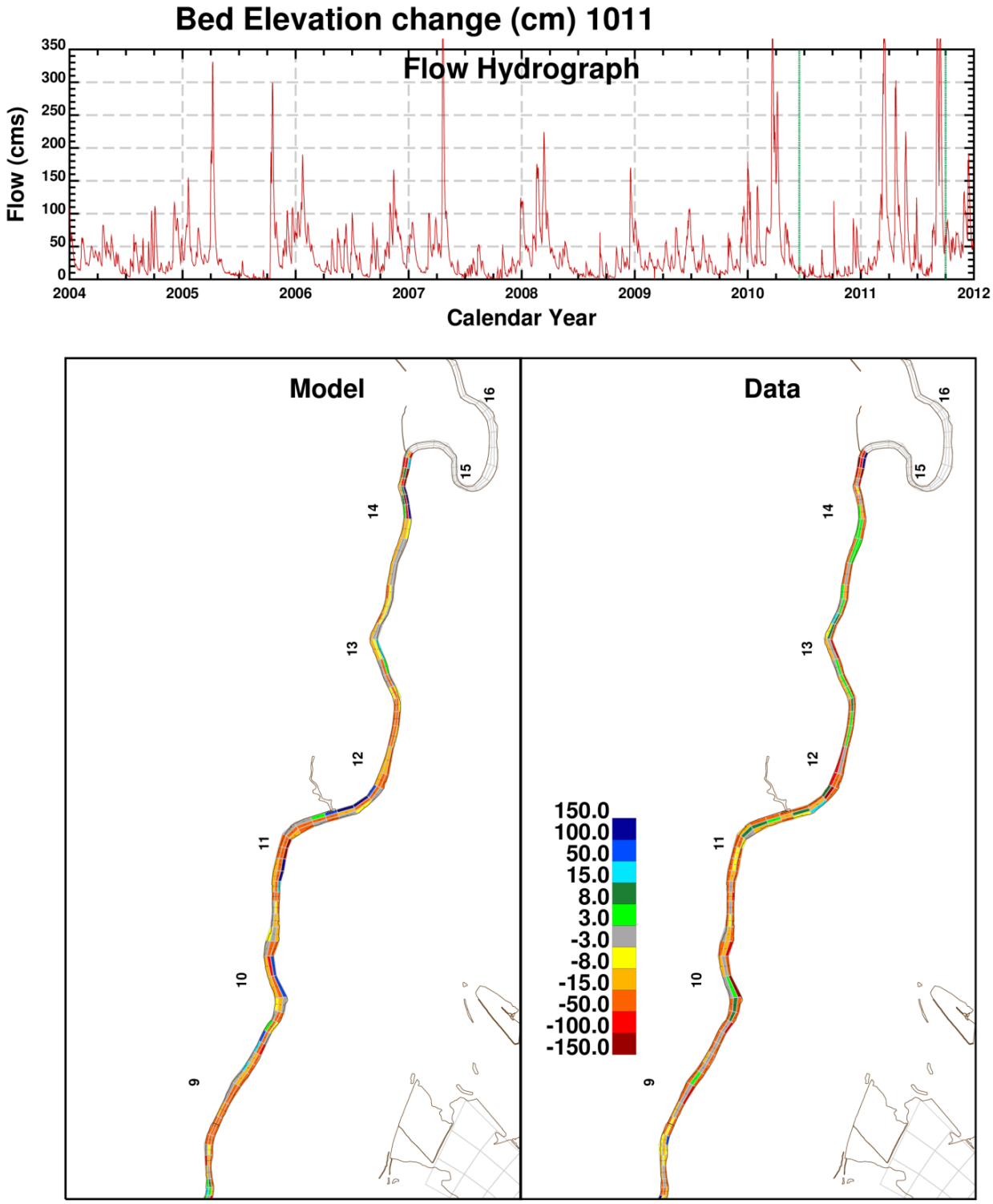

Comparison of simulated bed elevation changes to 2010-2011 multi-beam bathymetry data (RM8.3-14)

Lower Eight Miles of the Lower Passaic River

Figure 4-29

2014

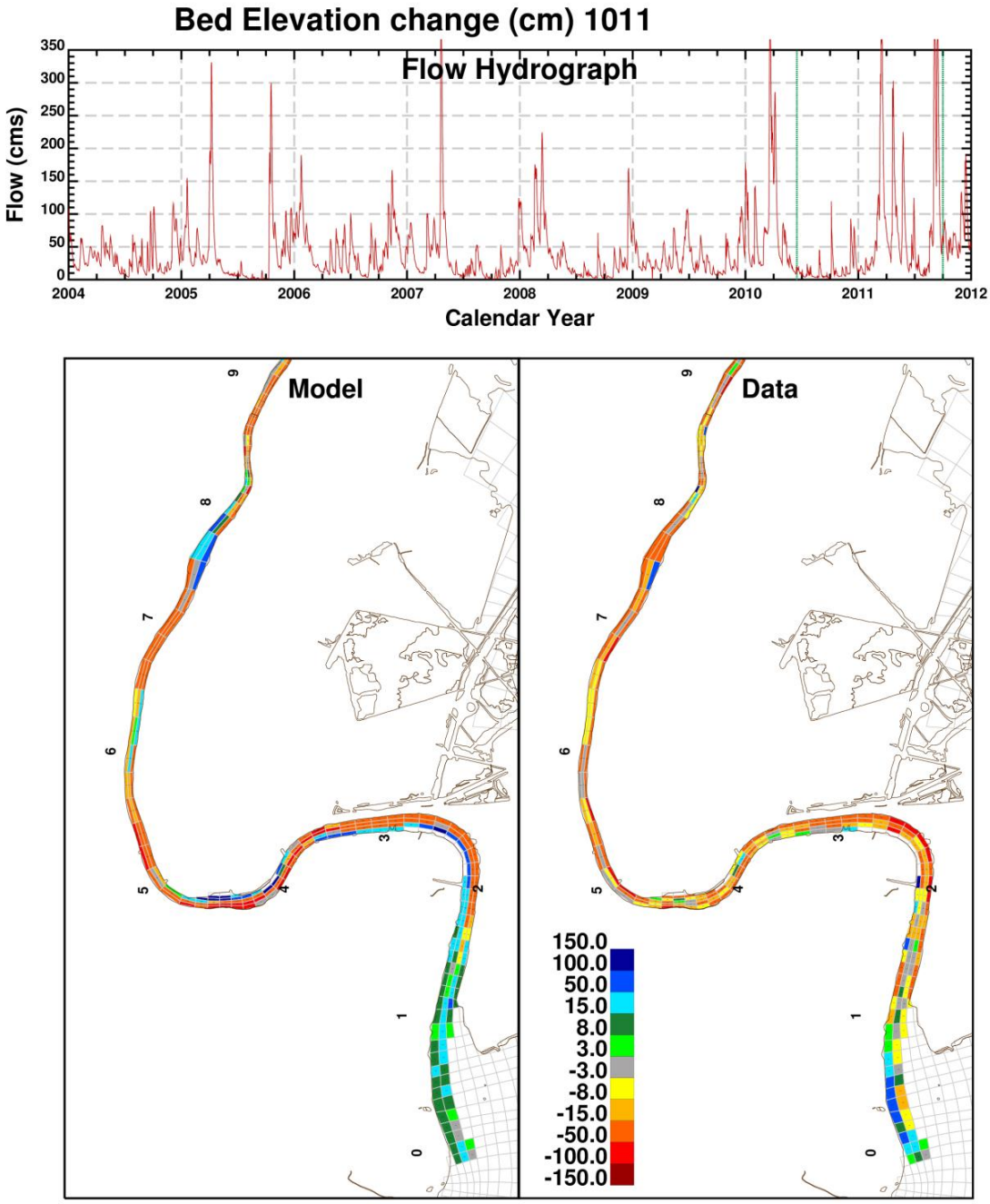

Comparison of simulated bed elevation changes to 2010-2011 multi-beam bathymetry data (RM0-8.3)

Lower Eight Miles of the Lower Passaic River

Figure 4-30

2014

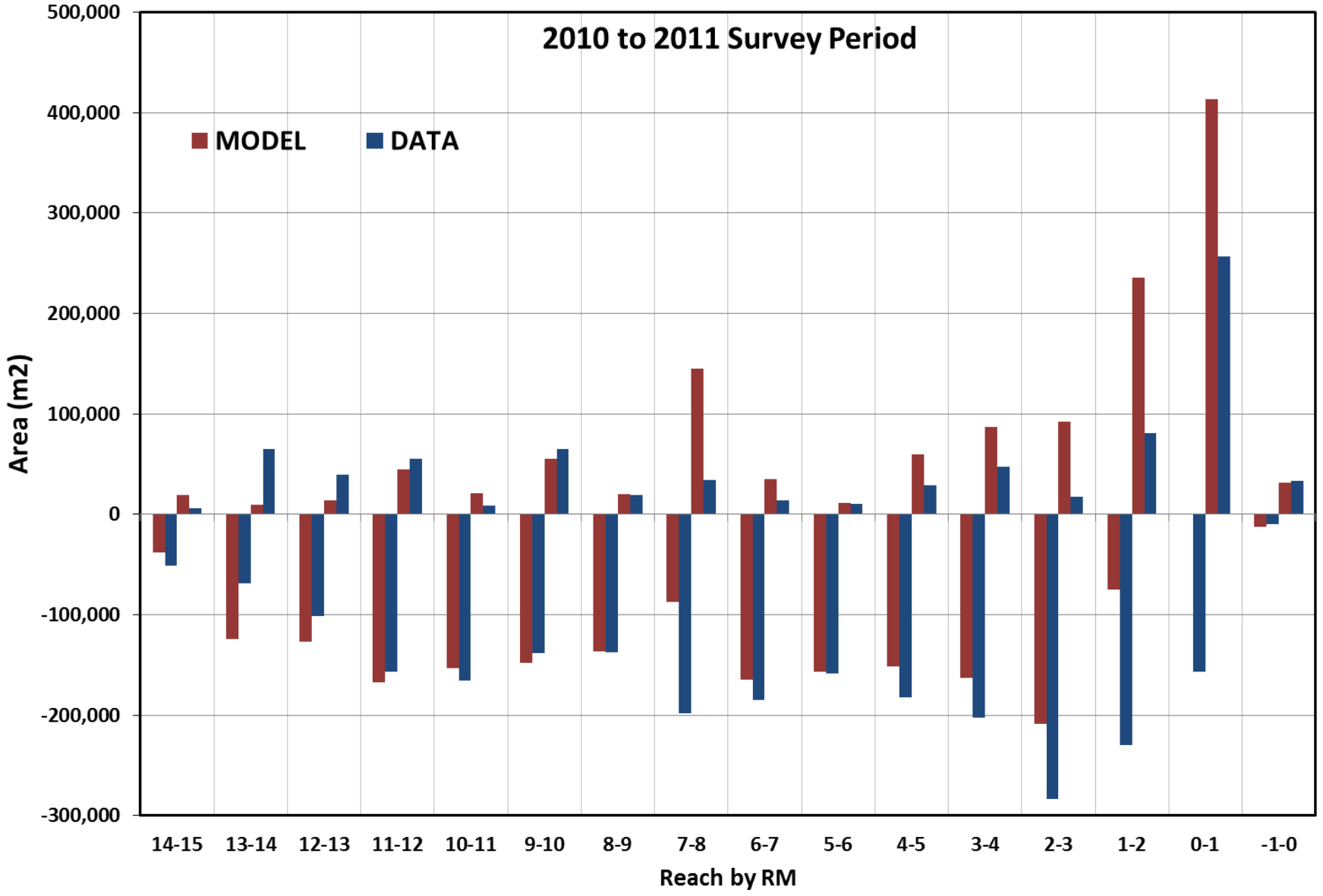

Area of Net Erosion and Net Deposition by Rivermile between the 2010 and 2011 Multibeam Bathymetric Surveys

Lower Eight Miles of the Lower Passaic River

Figure 4-31

2014

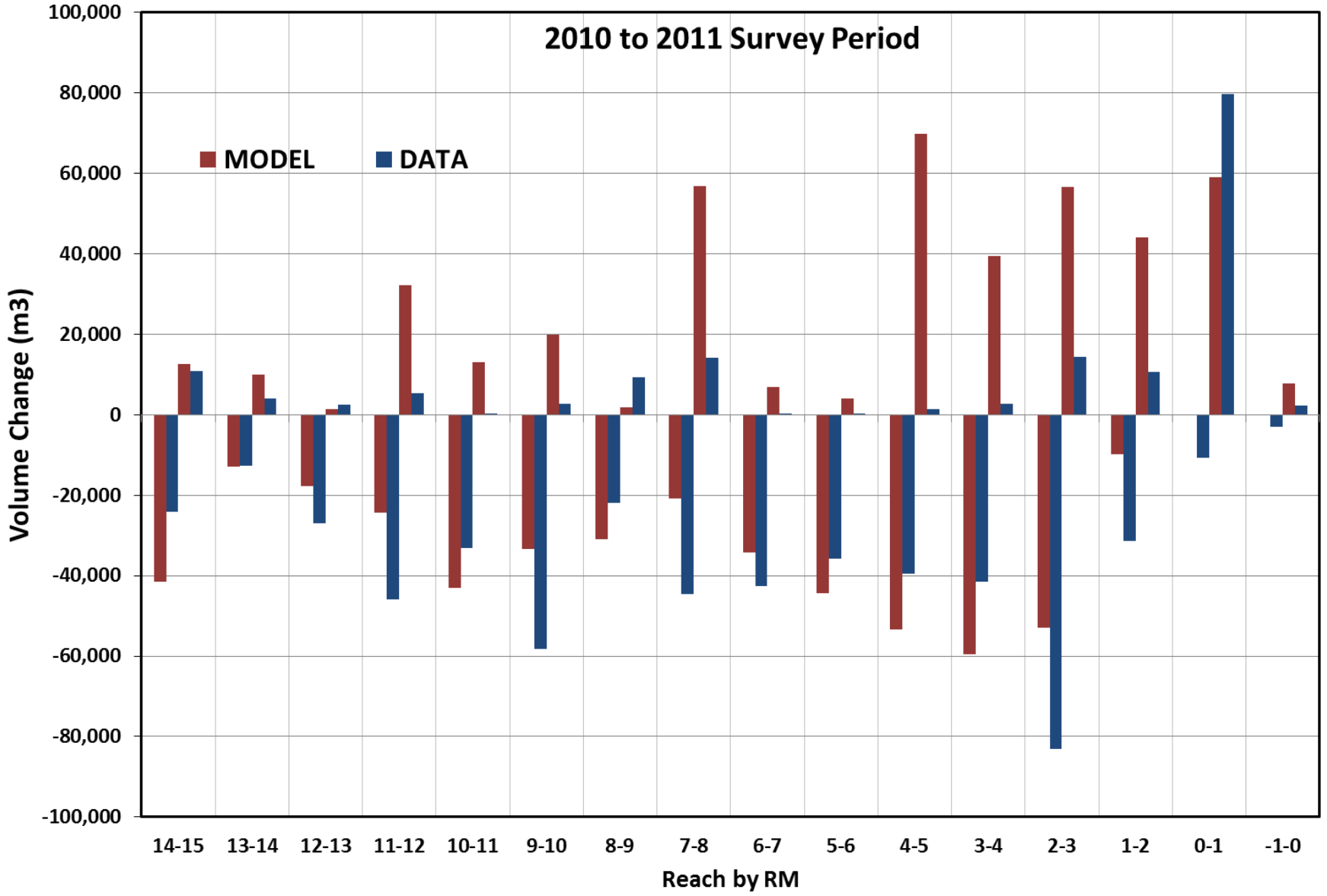

Volume of Net Erosion and Net Deposition by Rivermile between the 2010 and 2011 Multibeam Bathymetric Surveys

Lower Eight Miles of the Lower Passaic River

Figure 4-32

2014

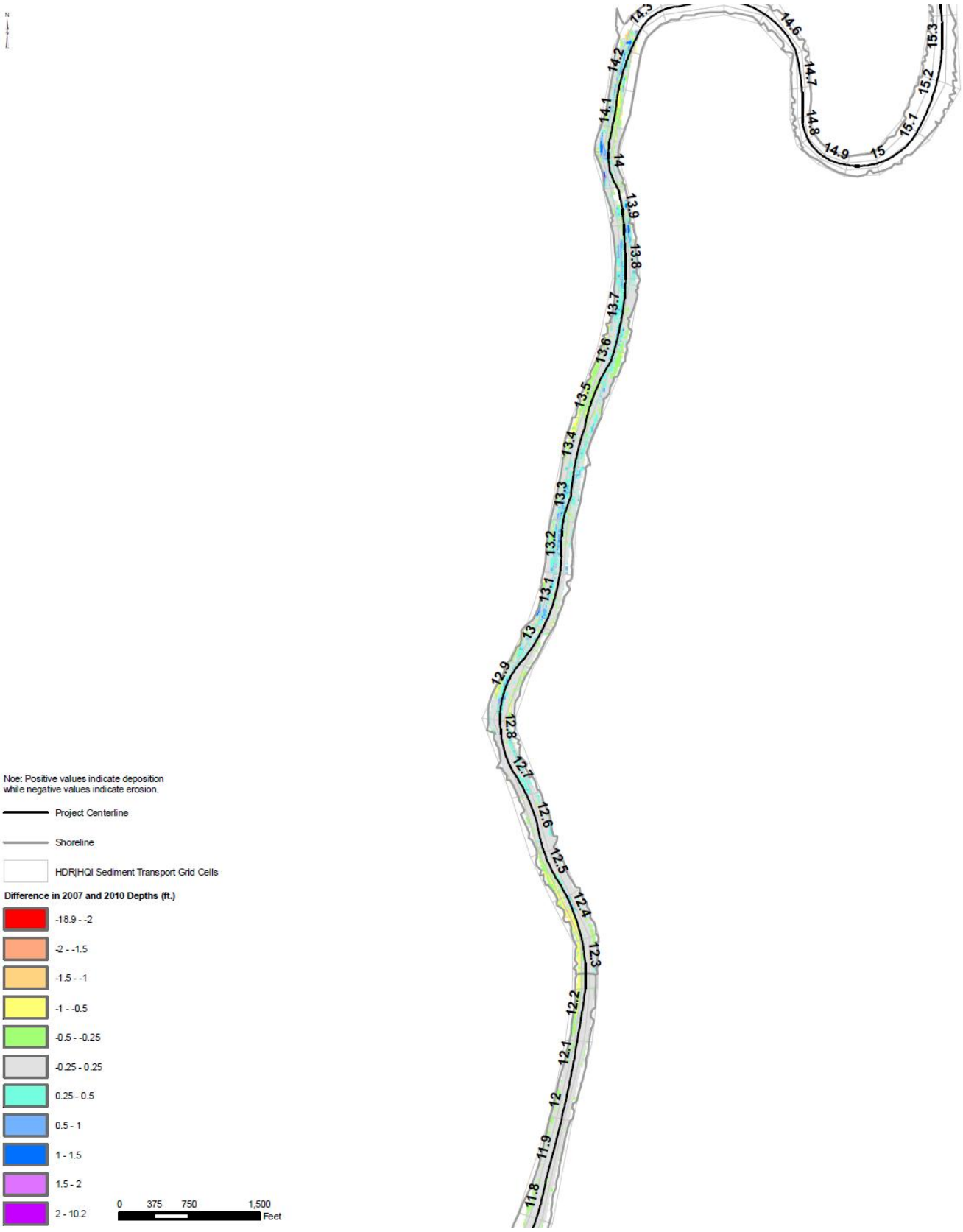

Change in bed elevation from 2007 to 2010 multibeam surveys (RM11.8-14.3)

Lower Eight Miles of the Lower Passaic River

Figure 4-33

2014

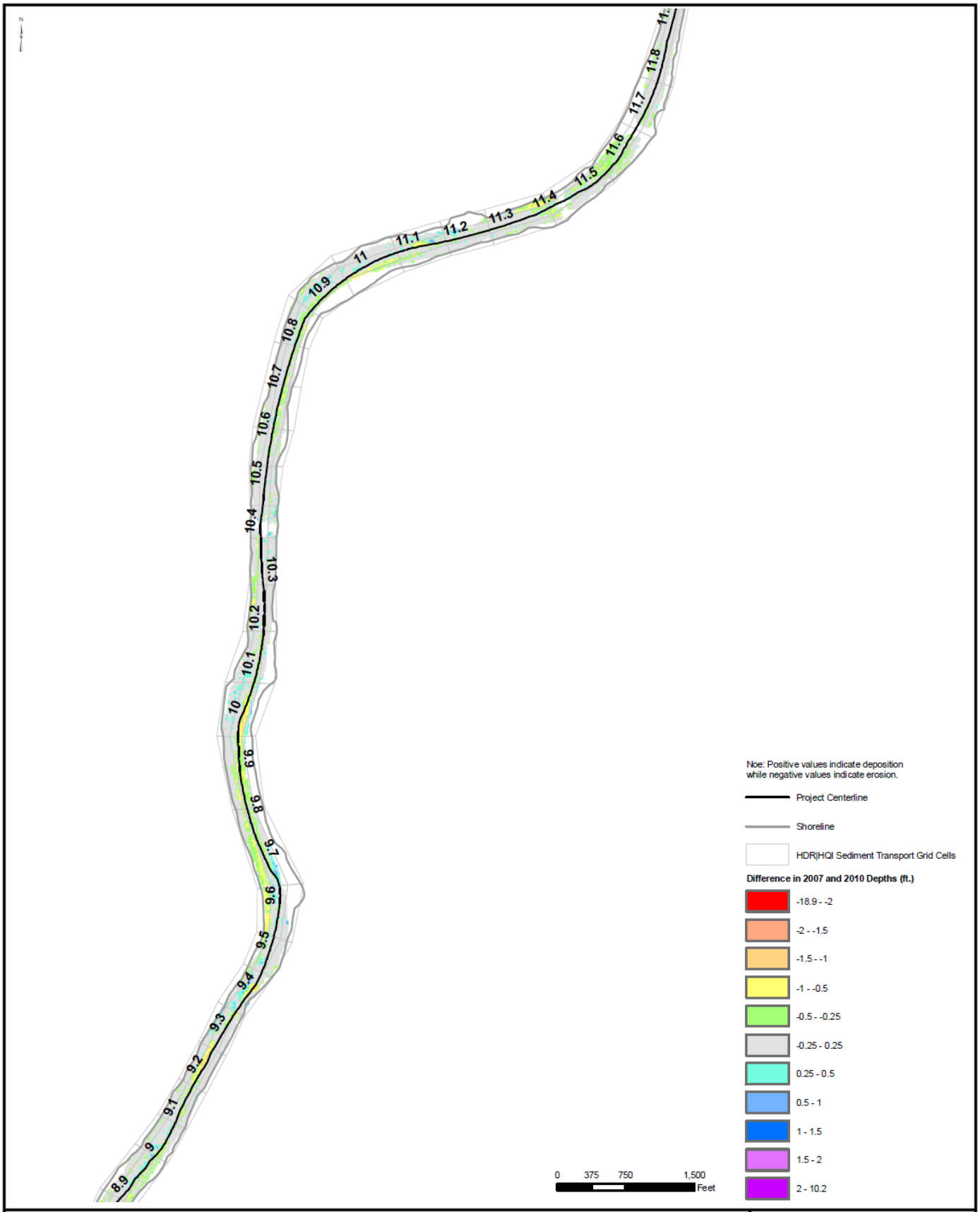

Change in bed elevation from 2007 to 2010 multibeam surveys (RM8.9-11.8)

Lower Eight Miles of the Lower Passaic River

Figure 4-34

2014

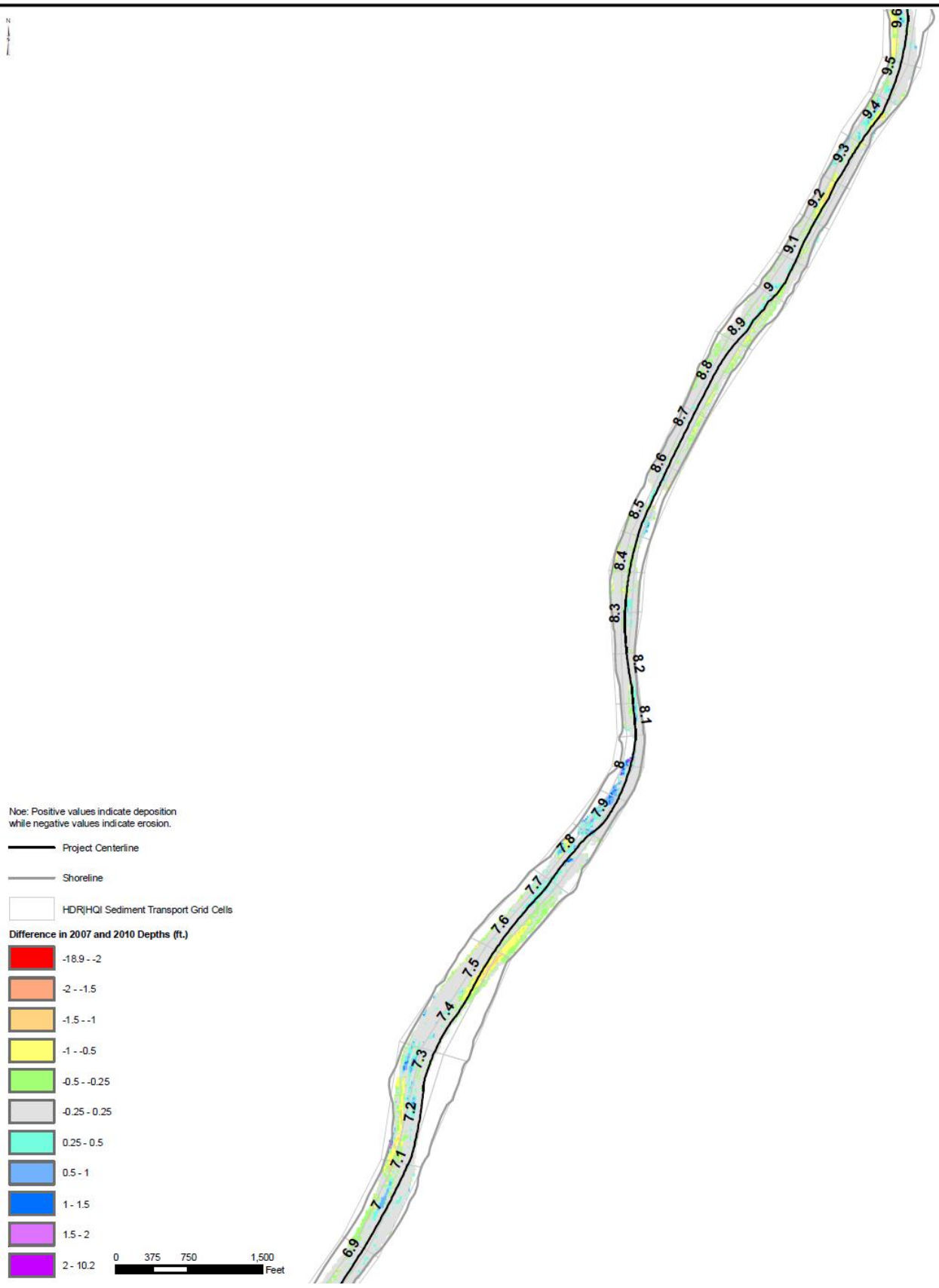

Change in bed elevation from 2007 to 2010 multibeam surveys (RM6.9-9.6)

Lower Eight Miles of the Lower Passaic River

Figure 4-35

2014

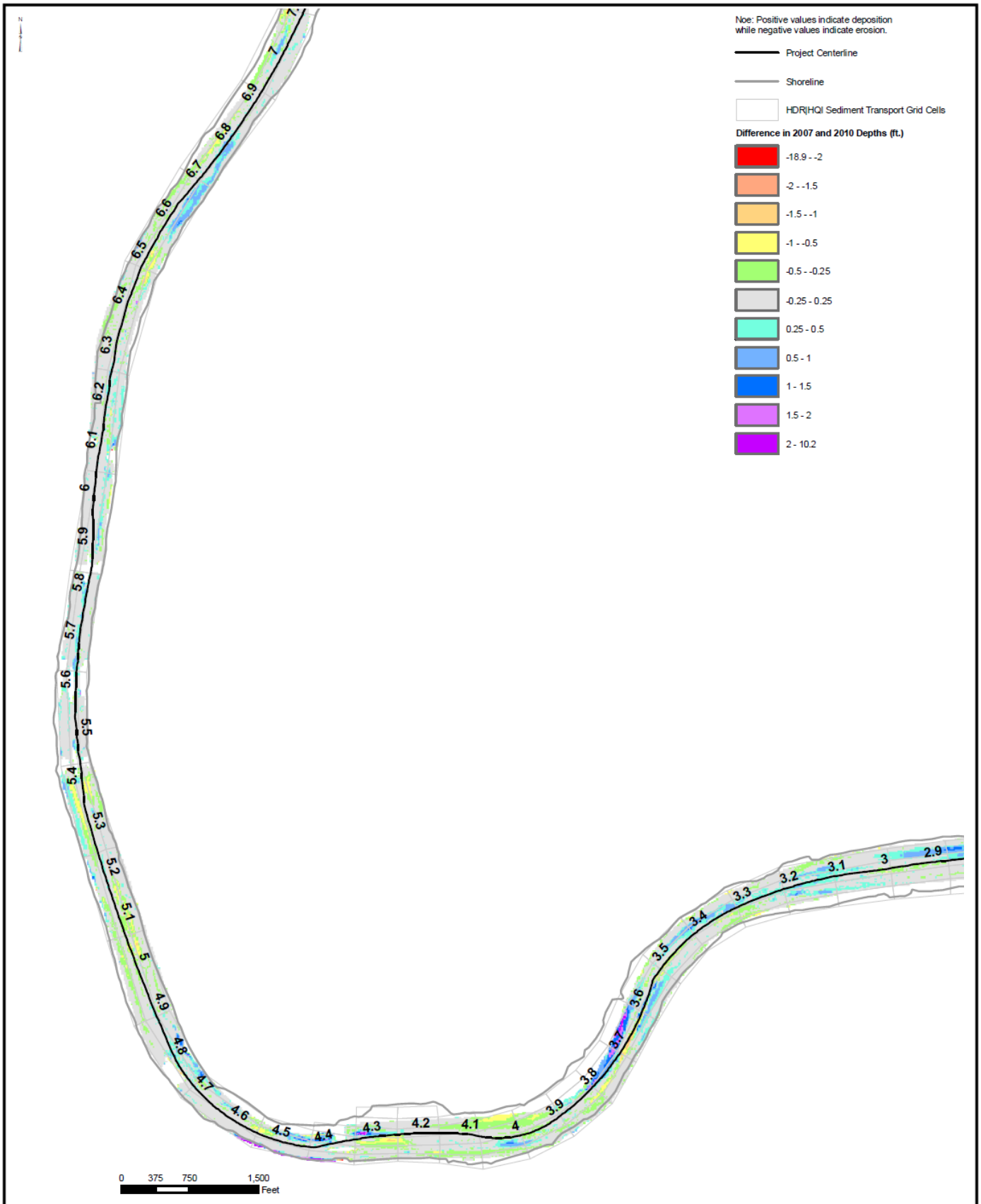

Change in bed elevation from 2007-2010 multibeam surveys (RM3-7)

Figure 4-36

Lower Eight Miles of the Lower Passaic River

2014

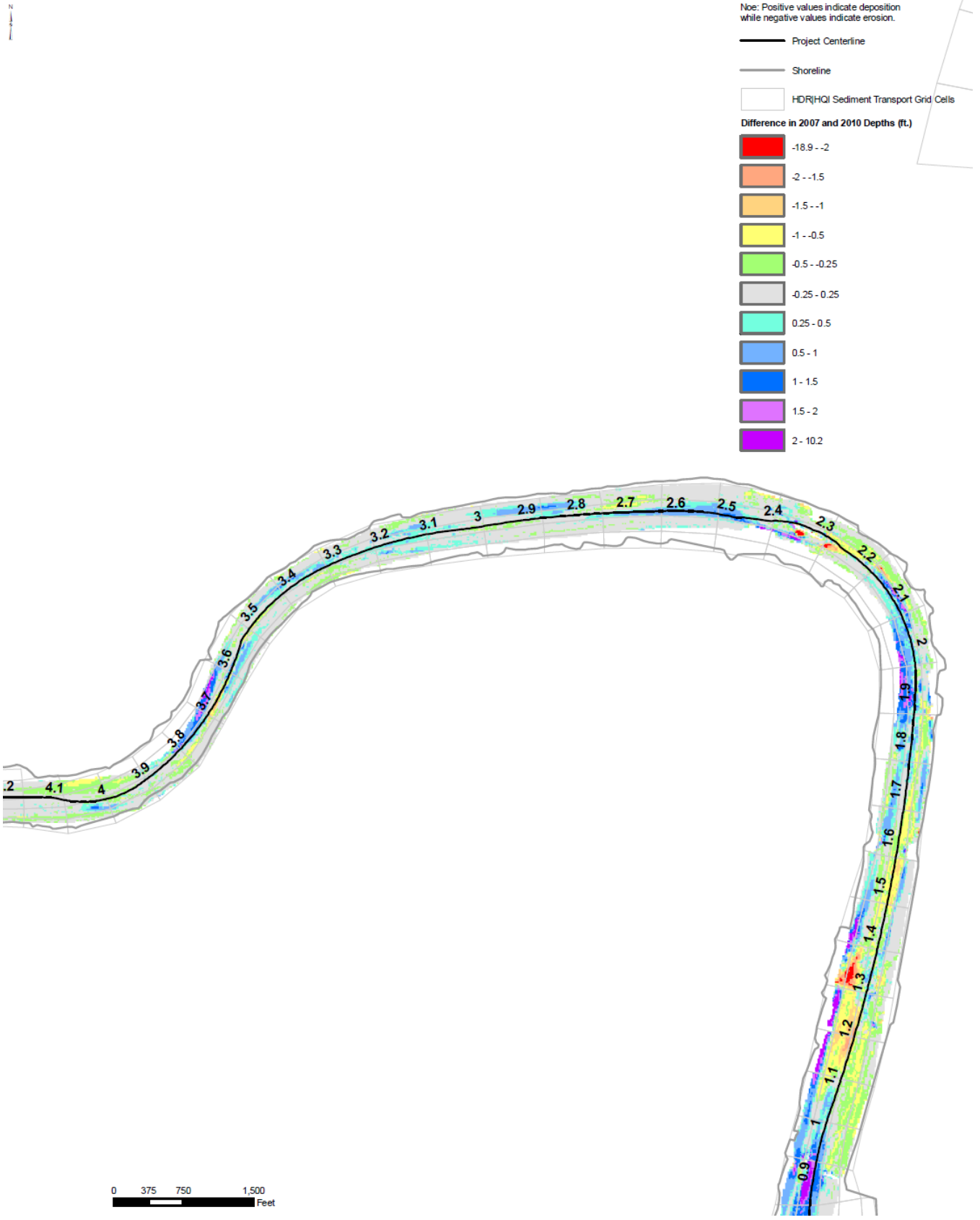

Change in bed elevation from 2007-2010 multibeam surveys (RM0.9-4.1)

Lower Eight Miles of the Lower Passaic River

Figure 4-37

2014

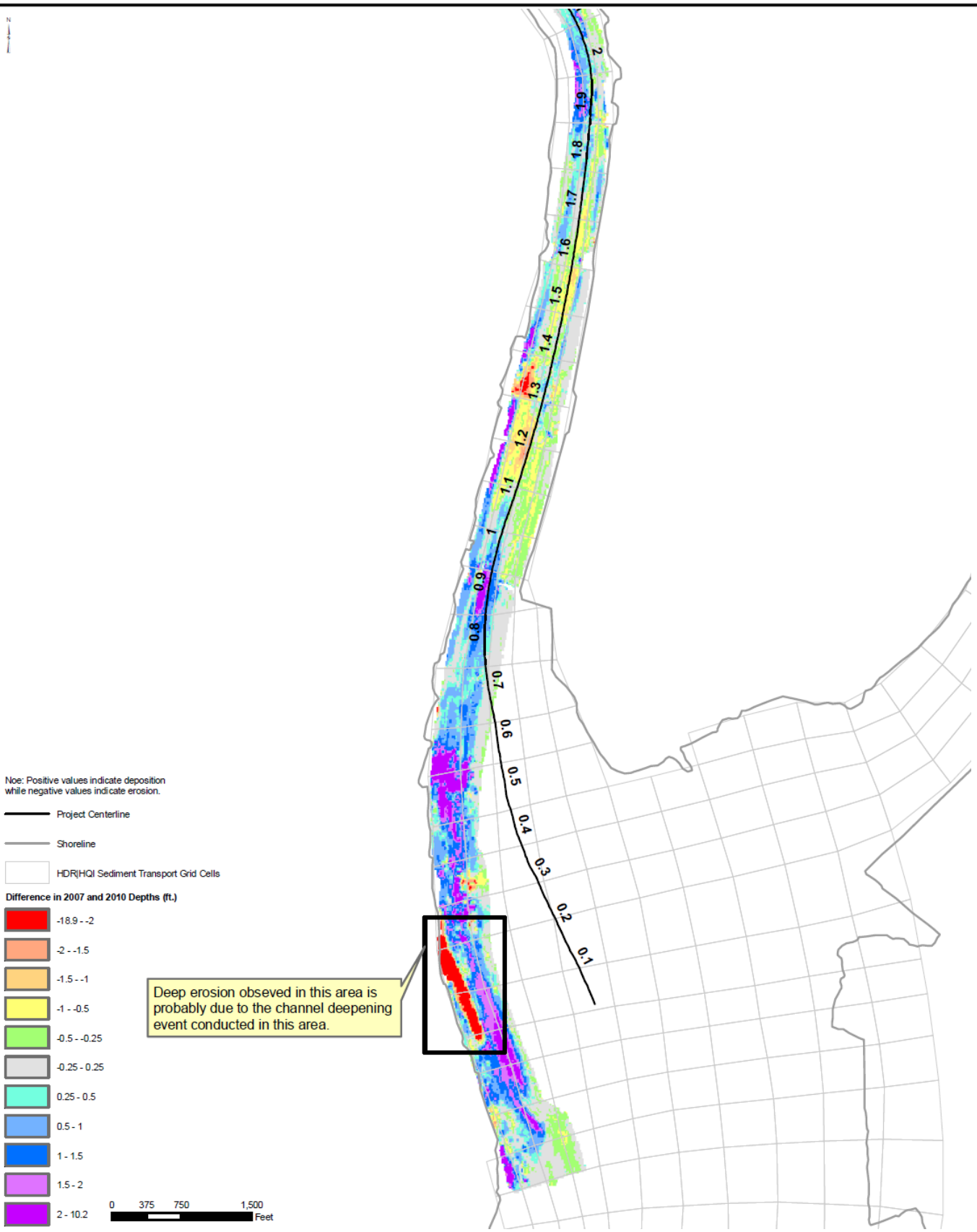

Change in bed elevation from 2007-2010 multibeam surveys (RM0-2)

Figure 4-38

Lower Eight Miles of the Lower Passaic River

2014

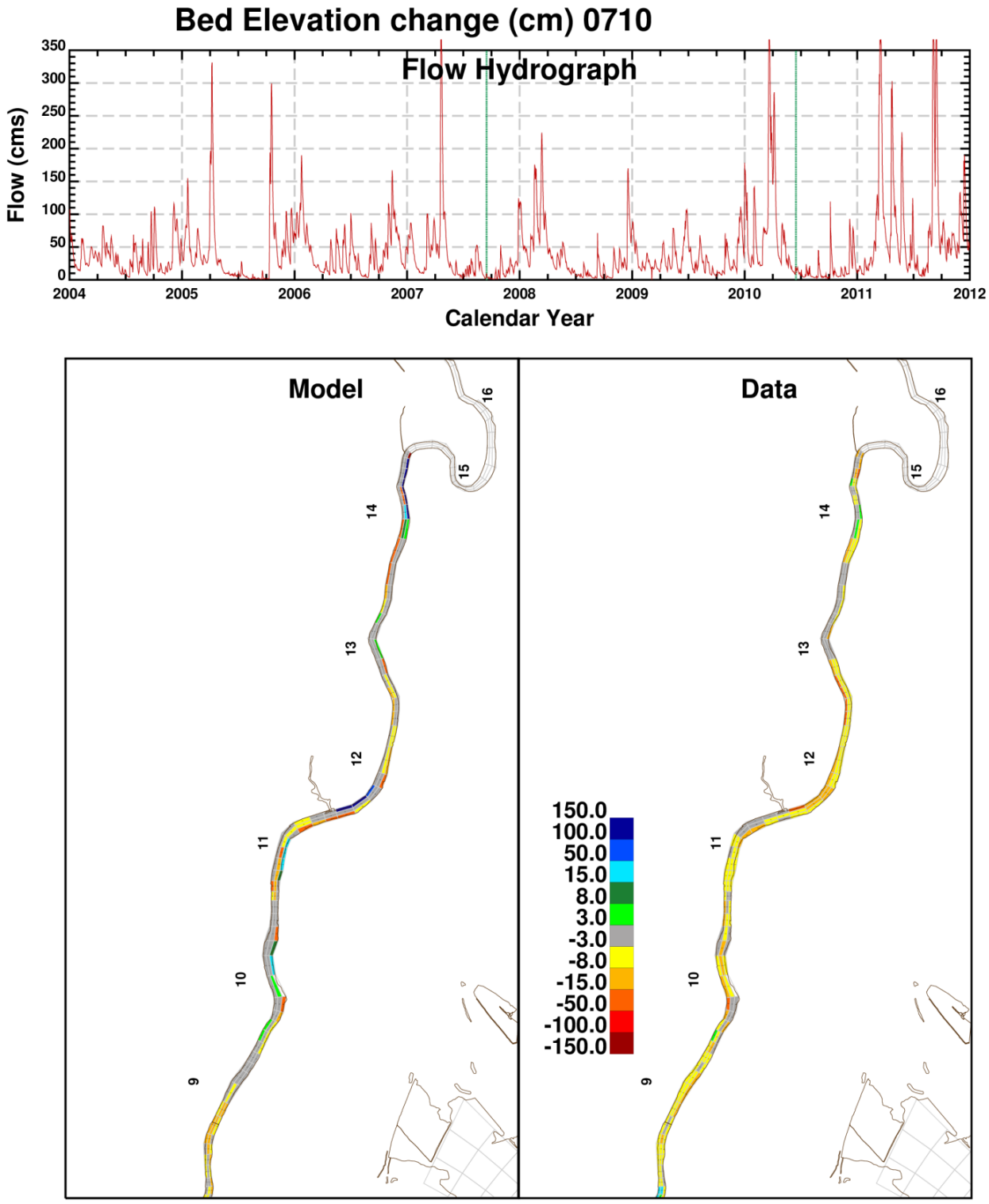

Comparison of simulated bed elevation changes to 2007-1010 multi-beam bathymetry data (RM8.3-14)

Lower Eight Miles of the Lower Passaic River

Figure 4-39

2014

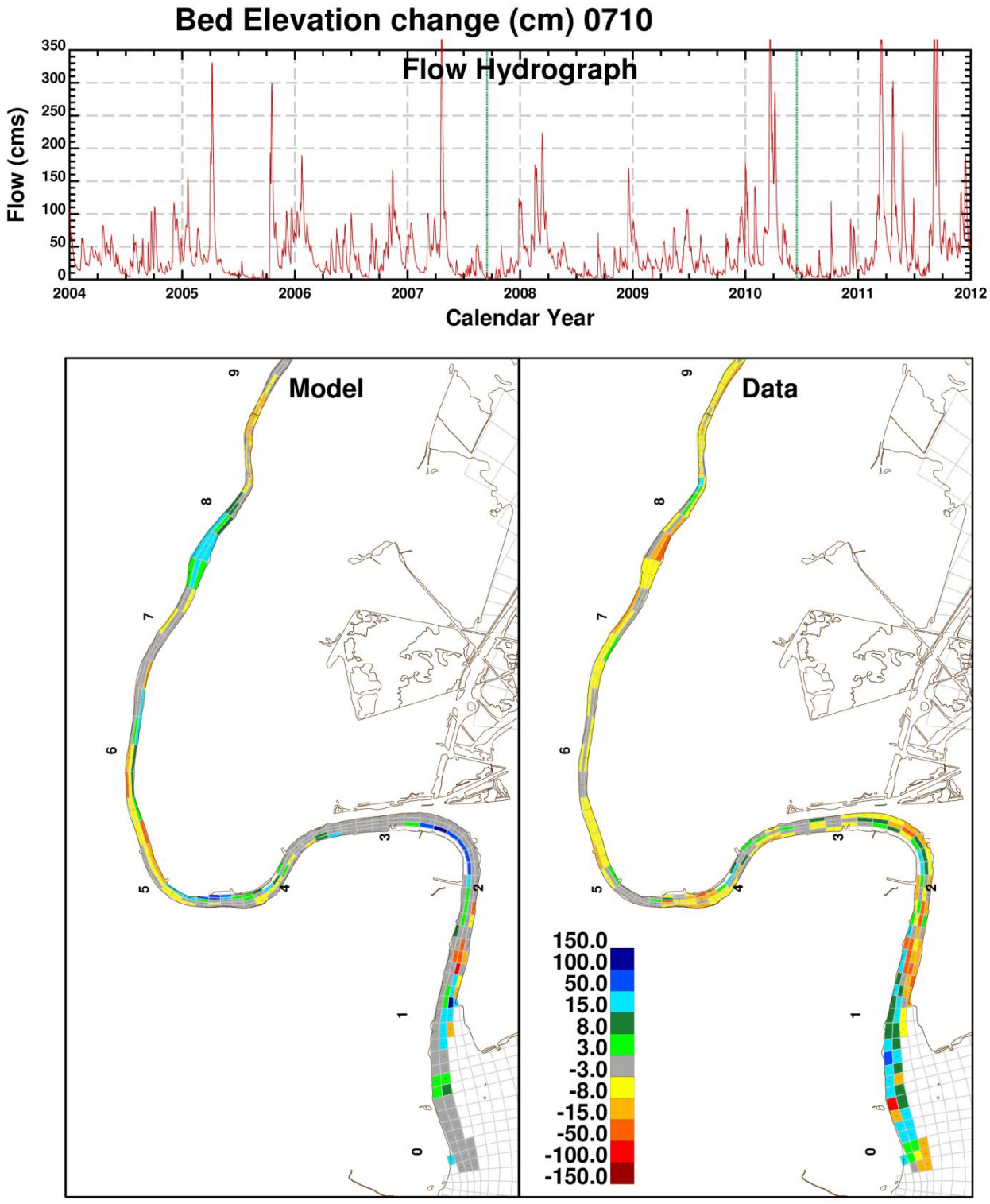

Comparison of simulated bed elevation changes to 2007-1010 multi-beam bathymetry data (RM0-8.3)

Lower Eight Miles of the Lower Passaic River

Figure 4-40

2014

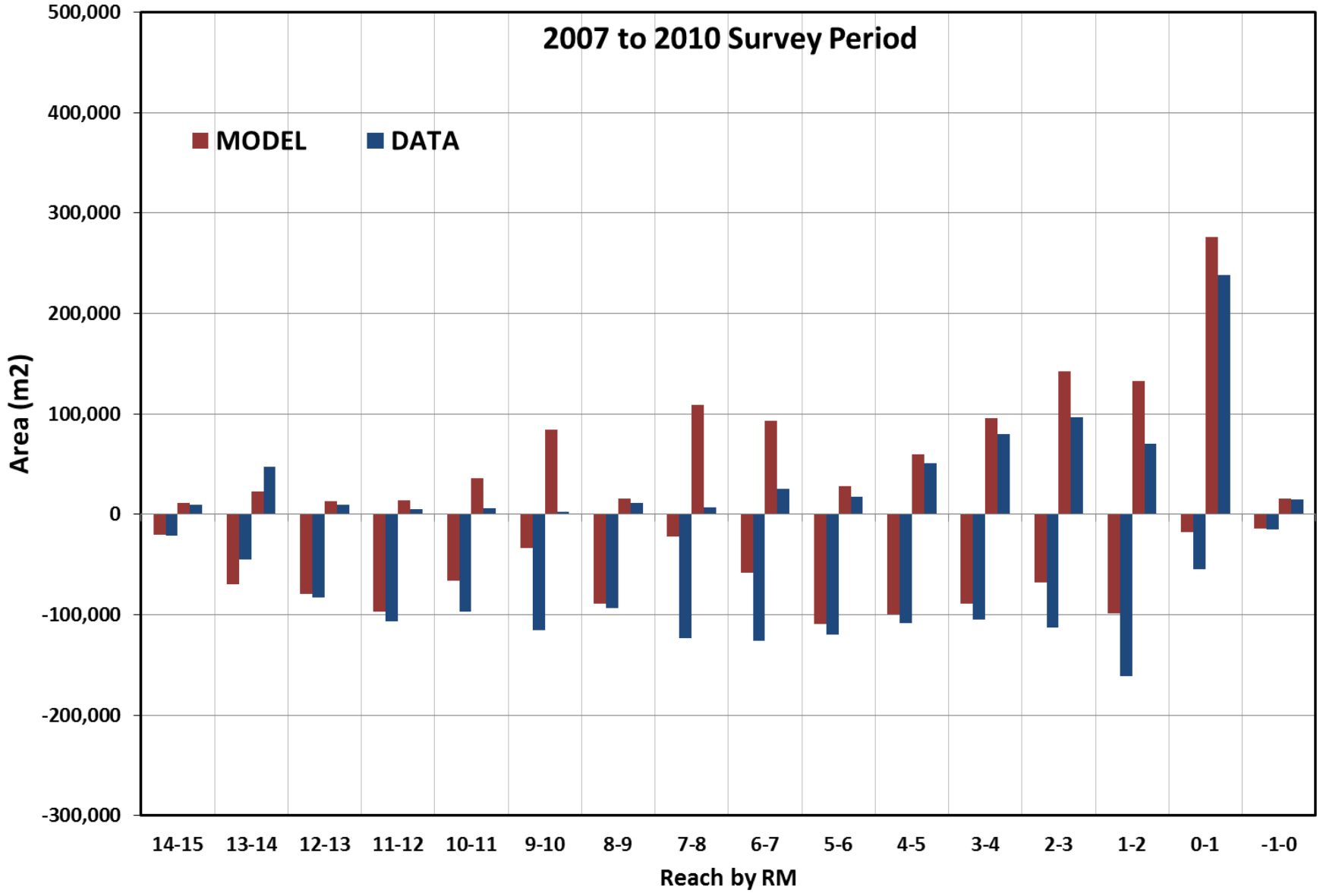

Area of Net Erosion and Net Deposition by Rivermile between the 2007 and 2010 Multibeam Bathymetric Surveys

Lower Eight Miles of the Lower Passaic River

Figure 4-41

2014

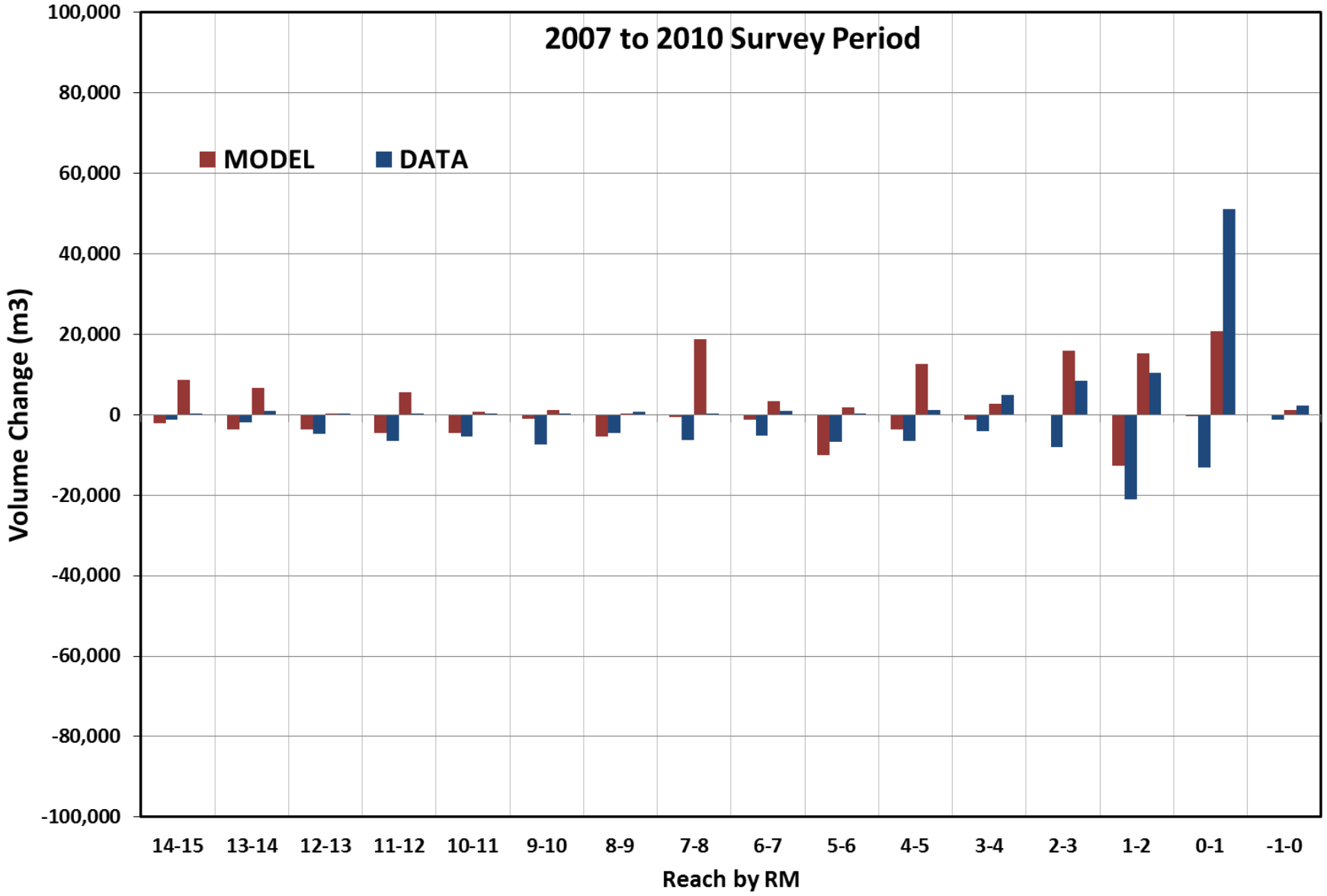

Volume of Net Erosion and Net Deposition by Rivermile between the 2007 and 2010 Multibeam Bathymetric Surveys

Lower Eight Miles of the Lower Passaic River

Figure 4-42

2014

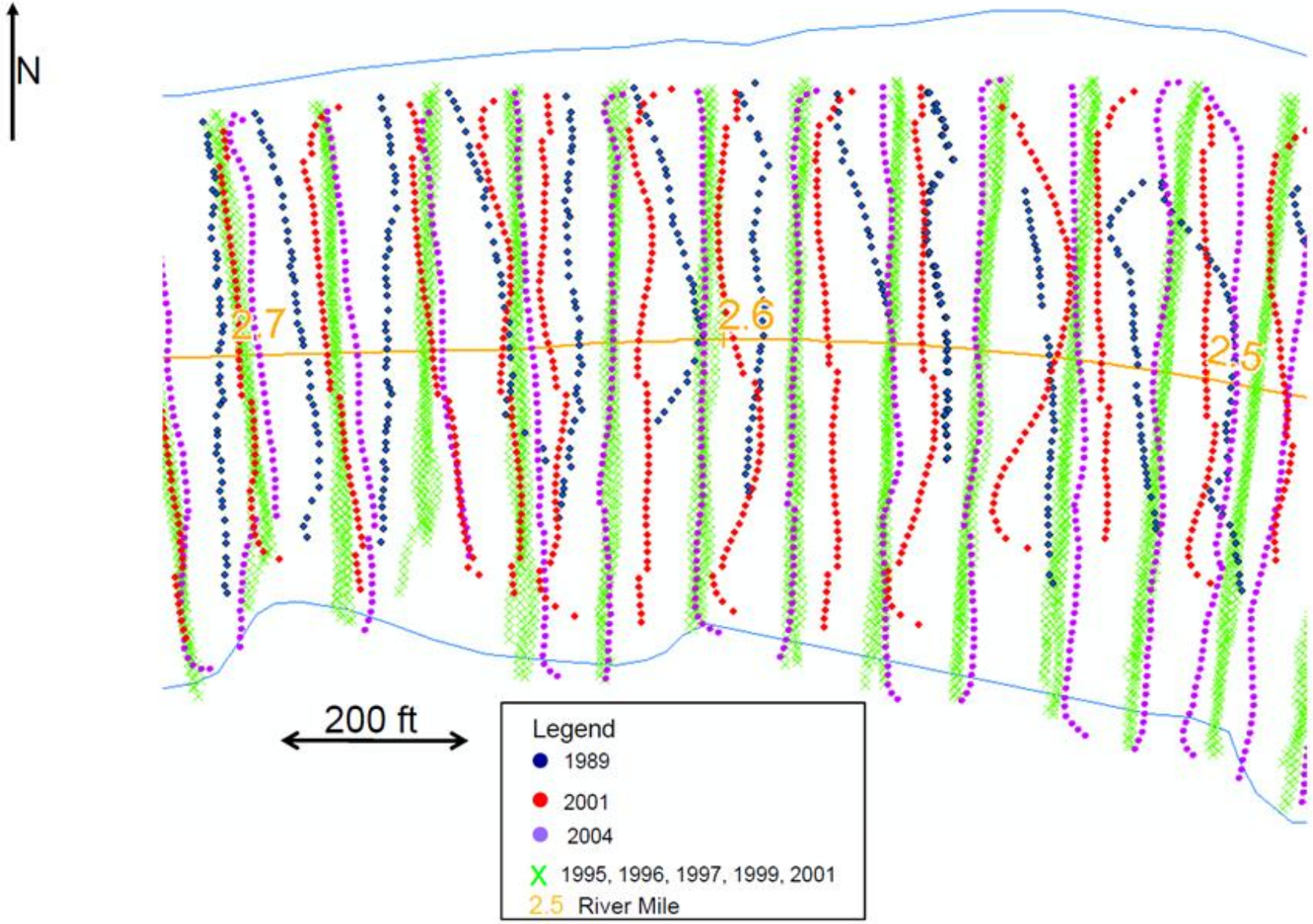

Alignment of Single beam bathymetry transects from 1989-2004 surveys

Lower Eight Miles of the Lower Passaic River

Figure 4-43

2014

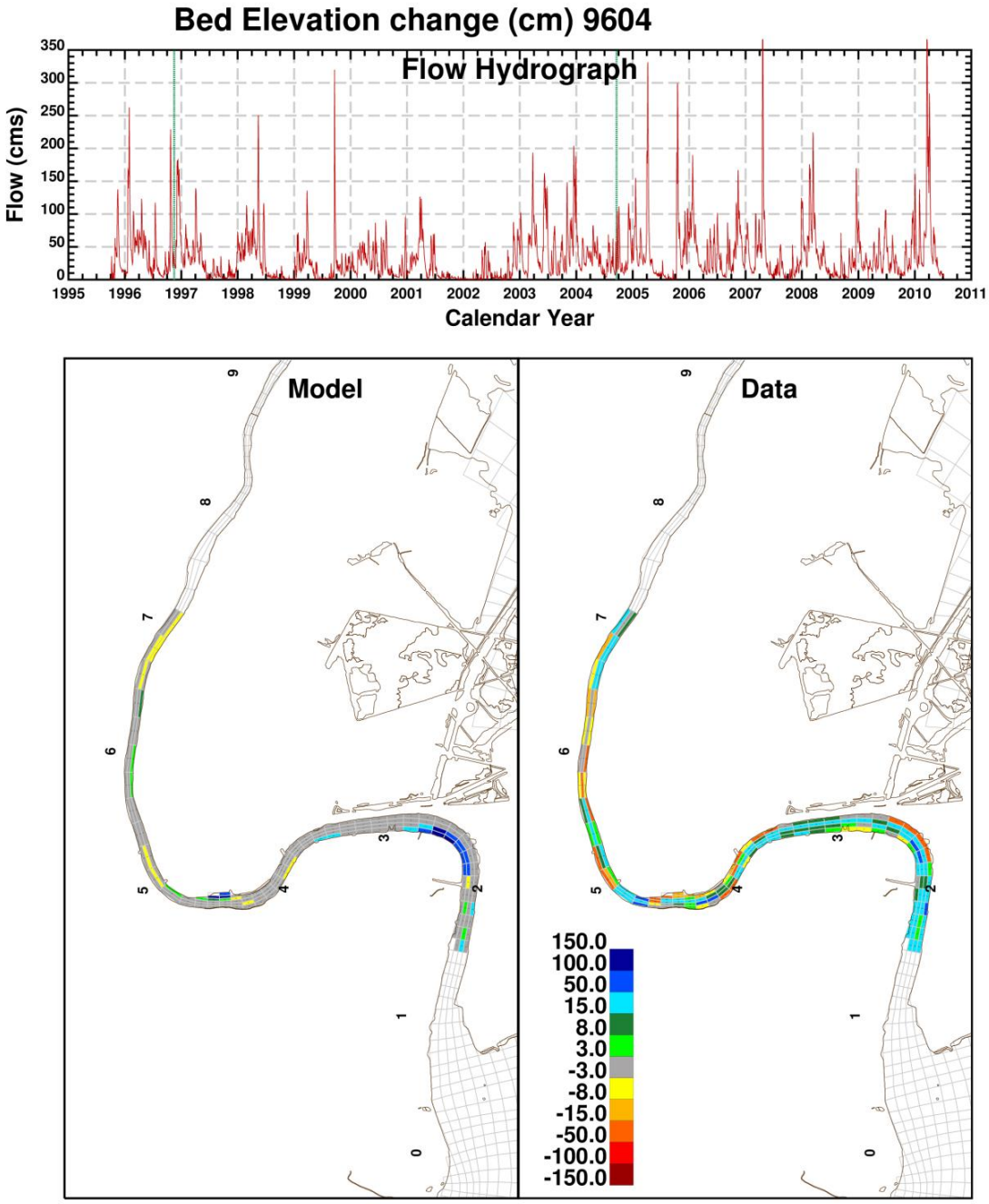

Comparison of simulated bed elevation changes to 1996-2004 single beam bathymetry data

Lower Eight Miles of the Lower Passaic River

Figure 4-44

2014

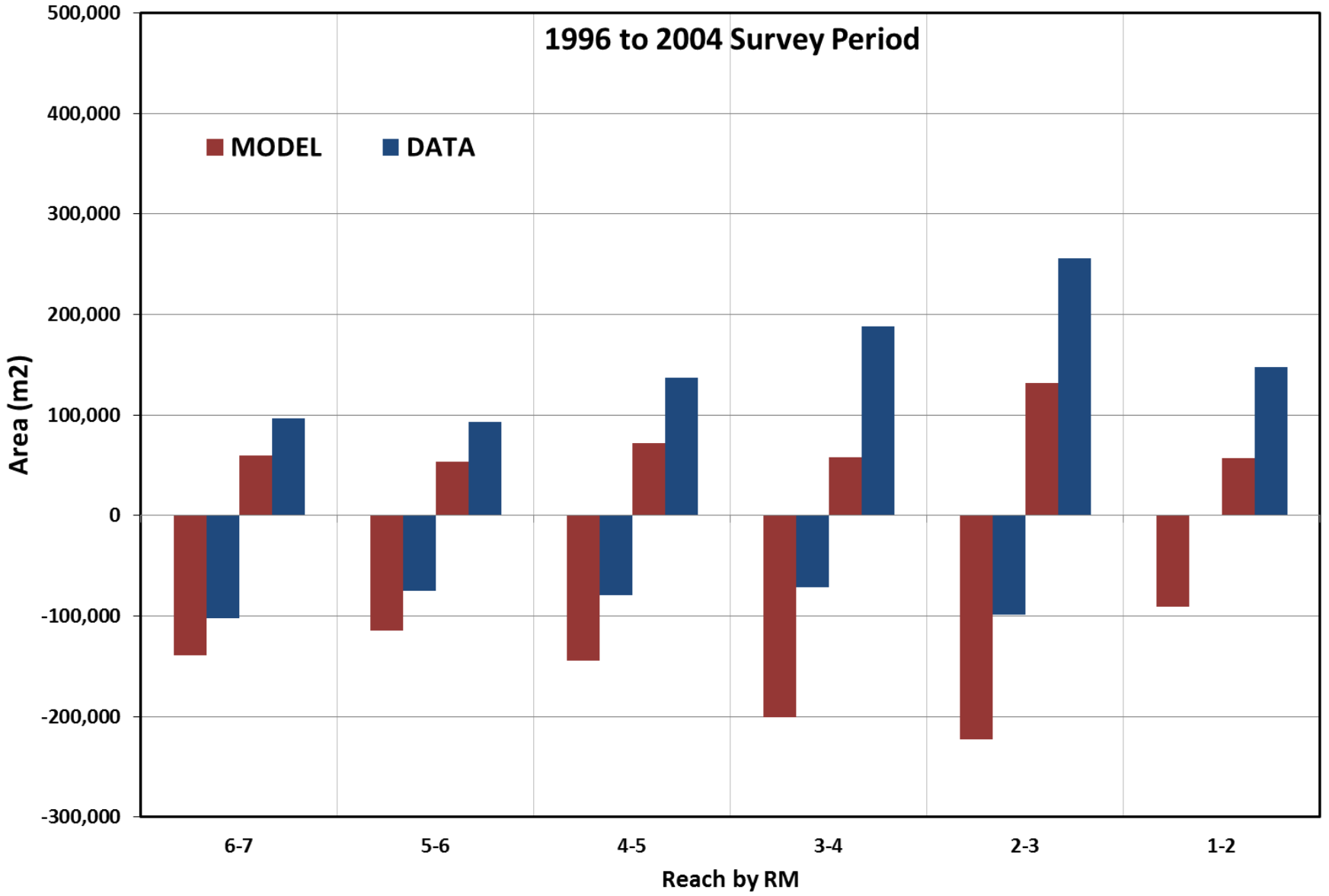

Area of Net Erosion and Net Deposition by Rivermile between the 1996 and 2004 Single Beam Bathymetric Surveys

Lower Eight Miles of the Lower Passaic River

Figure 4-45

2014

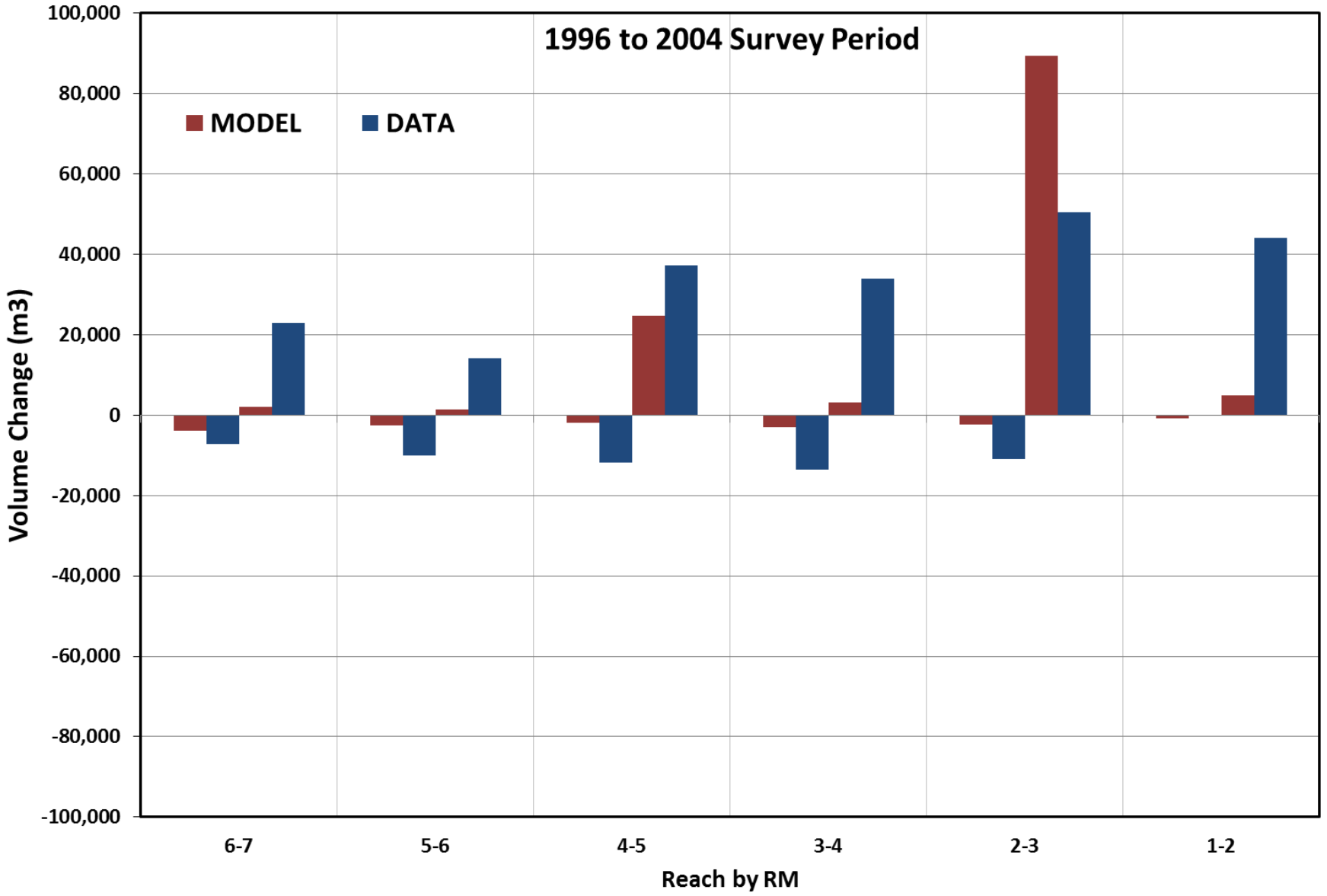

Volume of Net Erosion and Net Deposition by Rivermile between the 1996 and 2004 Single Beam Bathymetric Surveys

Lower Eight Miles of the Lower Passaic River

Figure 4-46

2014

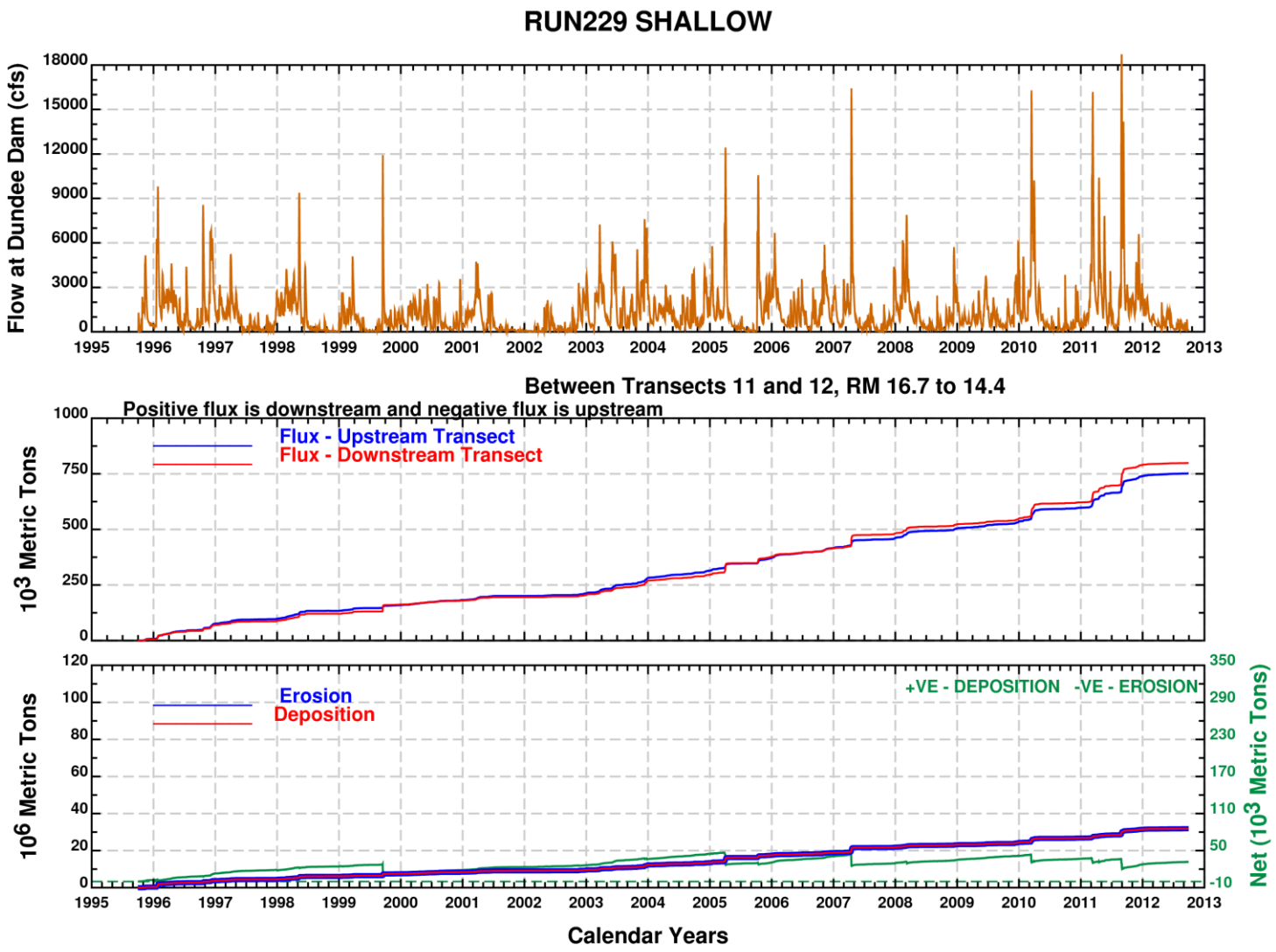

Water Column Solids Transport and Erosion and Deposition Fluxes – RM16.7 – 14.4

Lower Eight Miles of the Lower Passaic River

Figure 4-47

2014

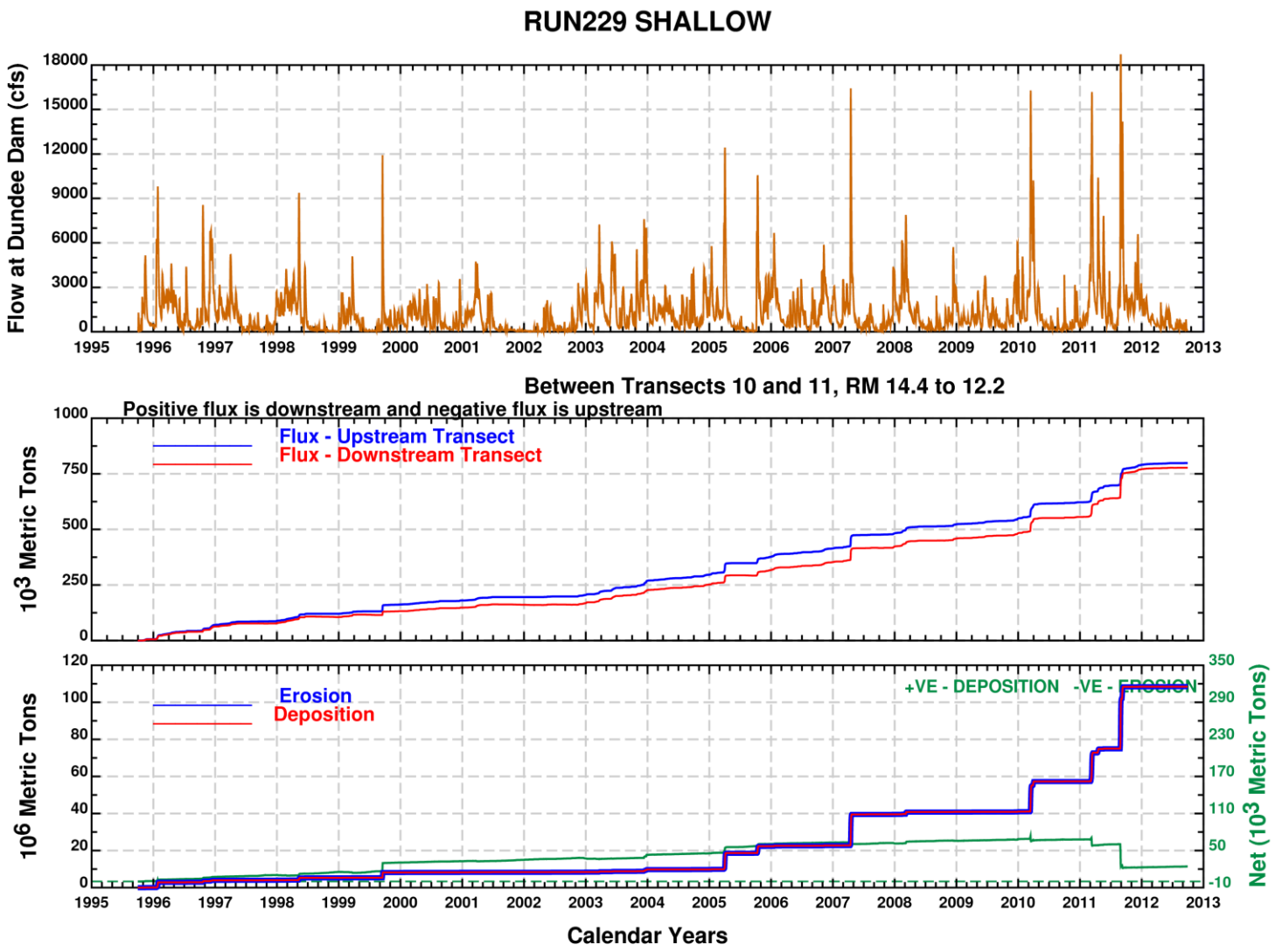

Water Column Solids Transport and Erosion and Deposition Fluxes – RM14-4 – 12.2

Lower Eight Miles of the Lower Passaic River

Figure 4-48

2014

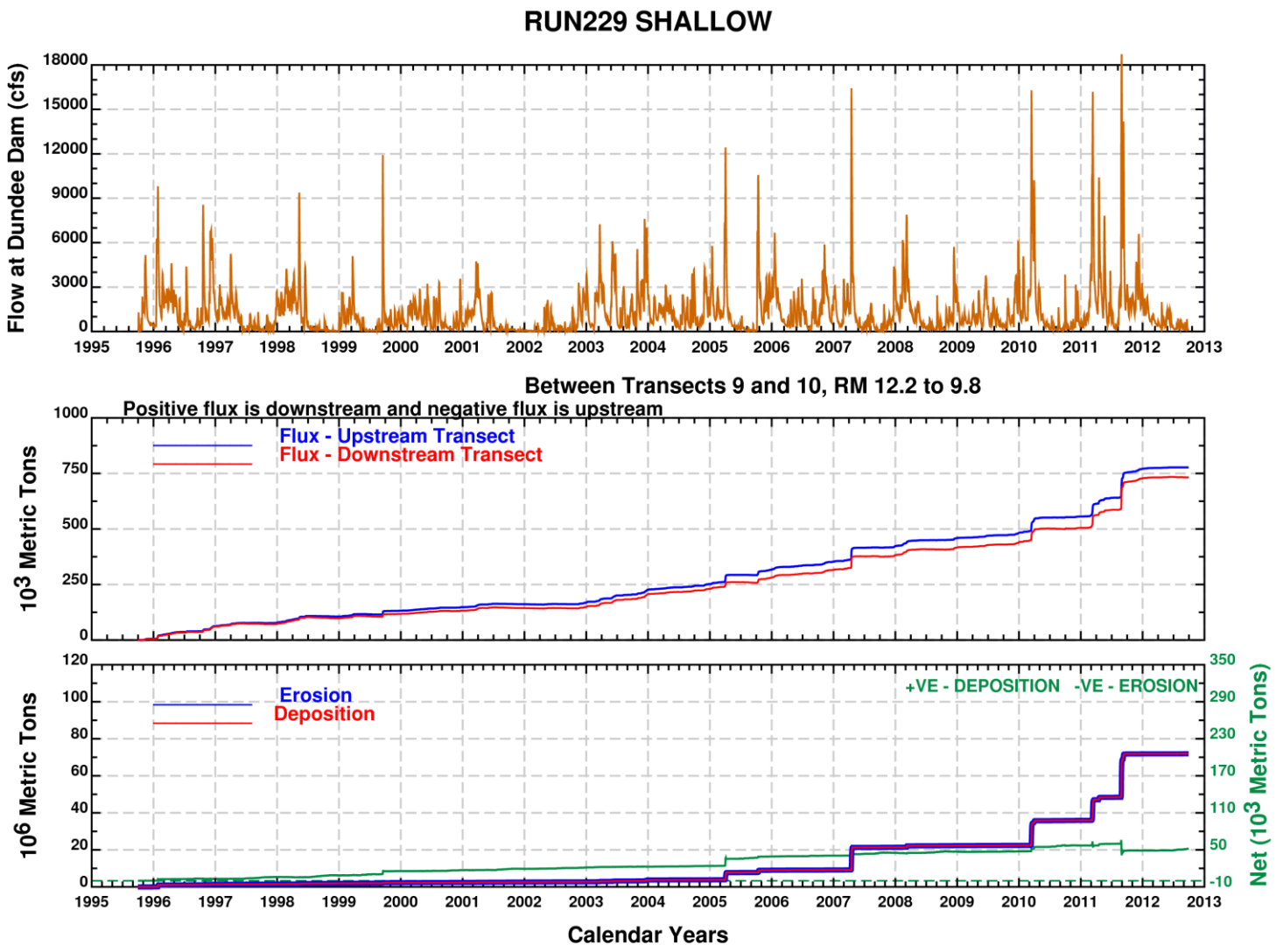

Water Column Solids Transport and Erosion and Deposition Fluxes – RM12.2 – 9.8

Lower Eight Miles of the Lower Passaic River

Figure 4-49

2014

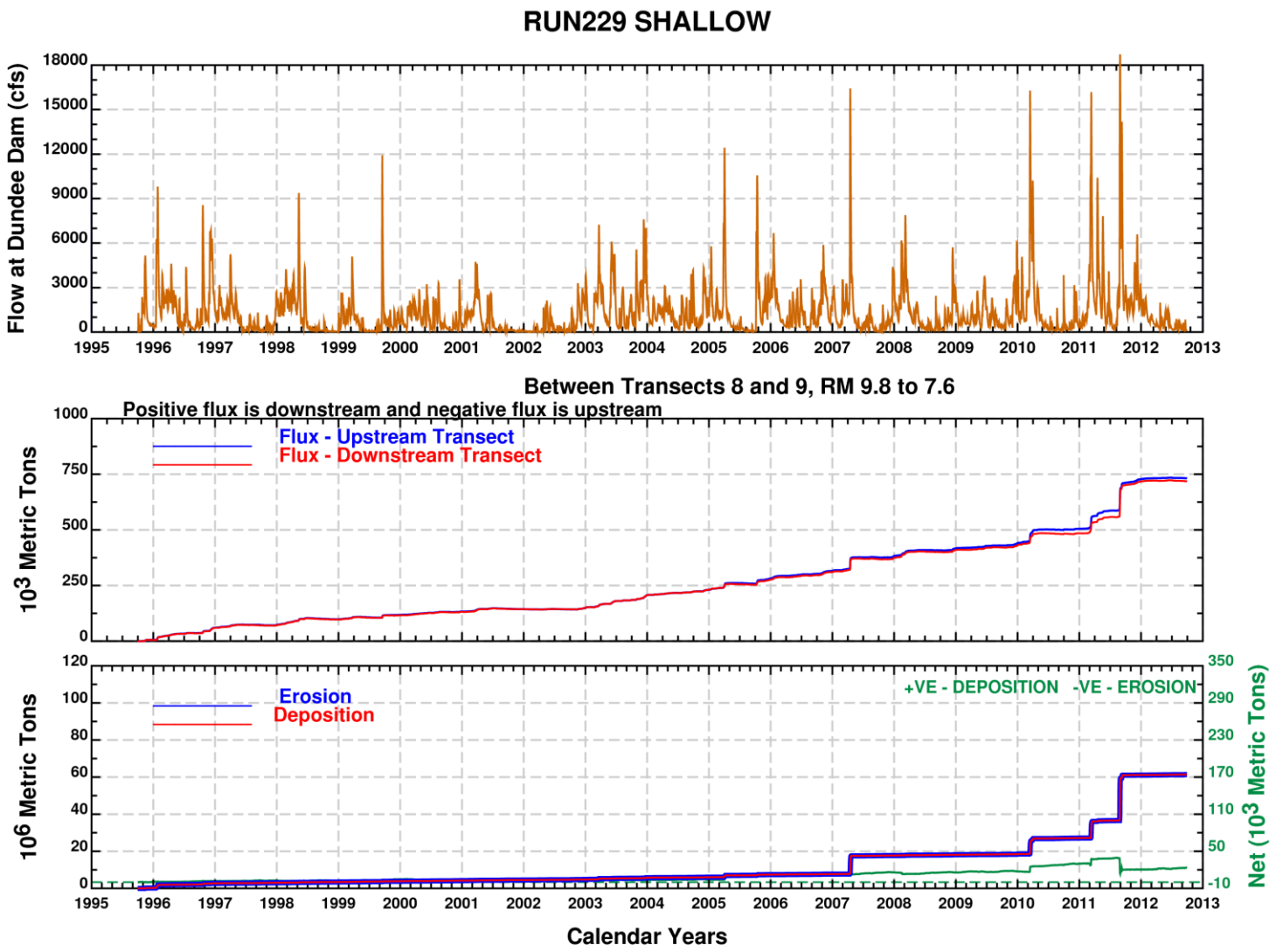

Water Column Solids Transport and Erosion and Deposition Fluxes – RM9.8 – 7.6

Lower Eight Miles of the Lower Passaic River

Figure 4-50

2014

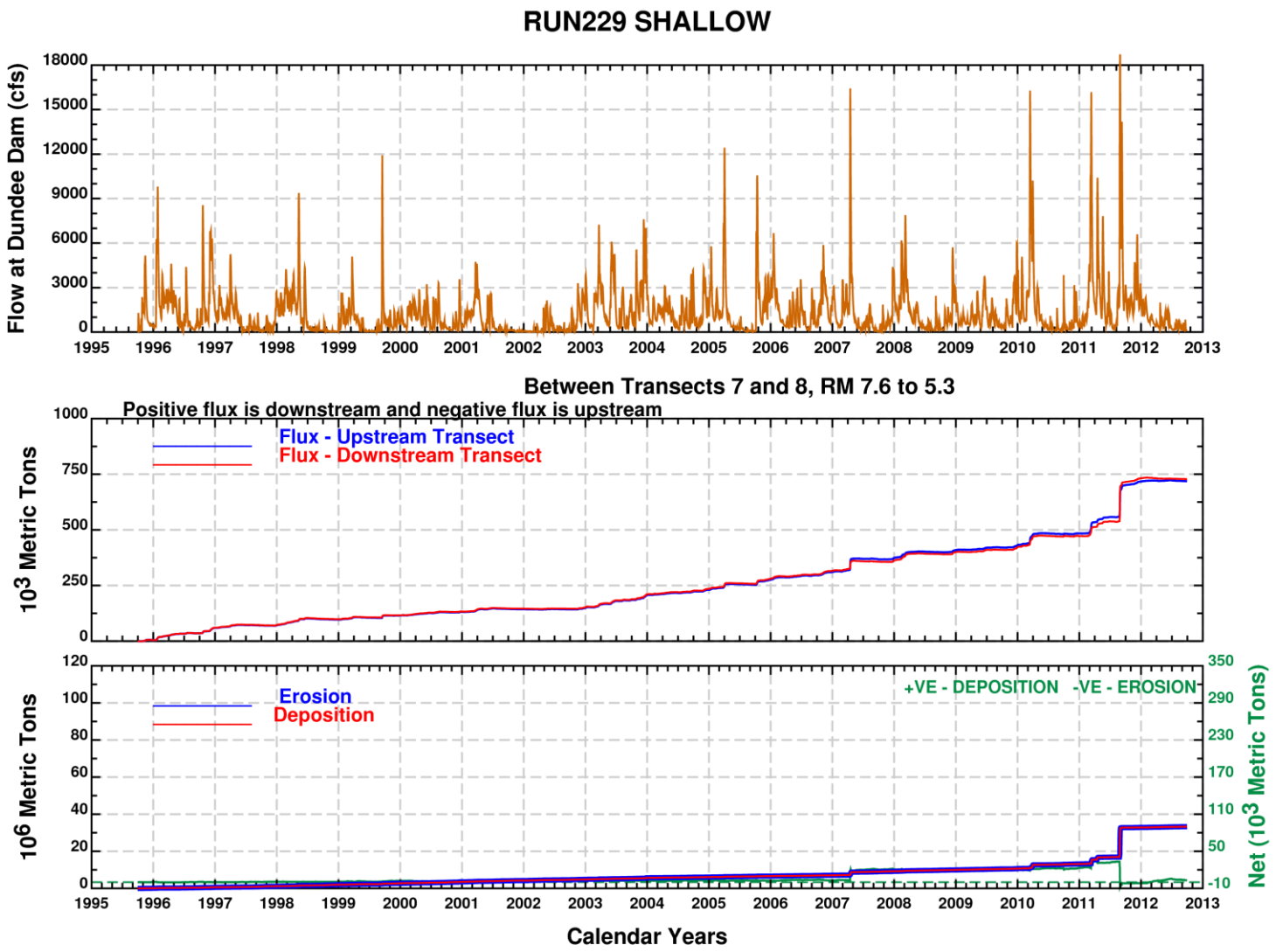

Water Column Solids Transport and Erosion and Deposition Fluxes – RM7.6 – 5.3

Lower Eight Miles of the Lower Passaic River

Figure 4-51

2014

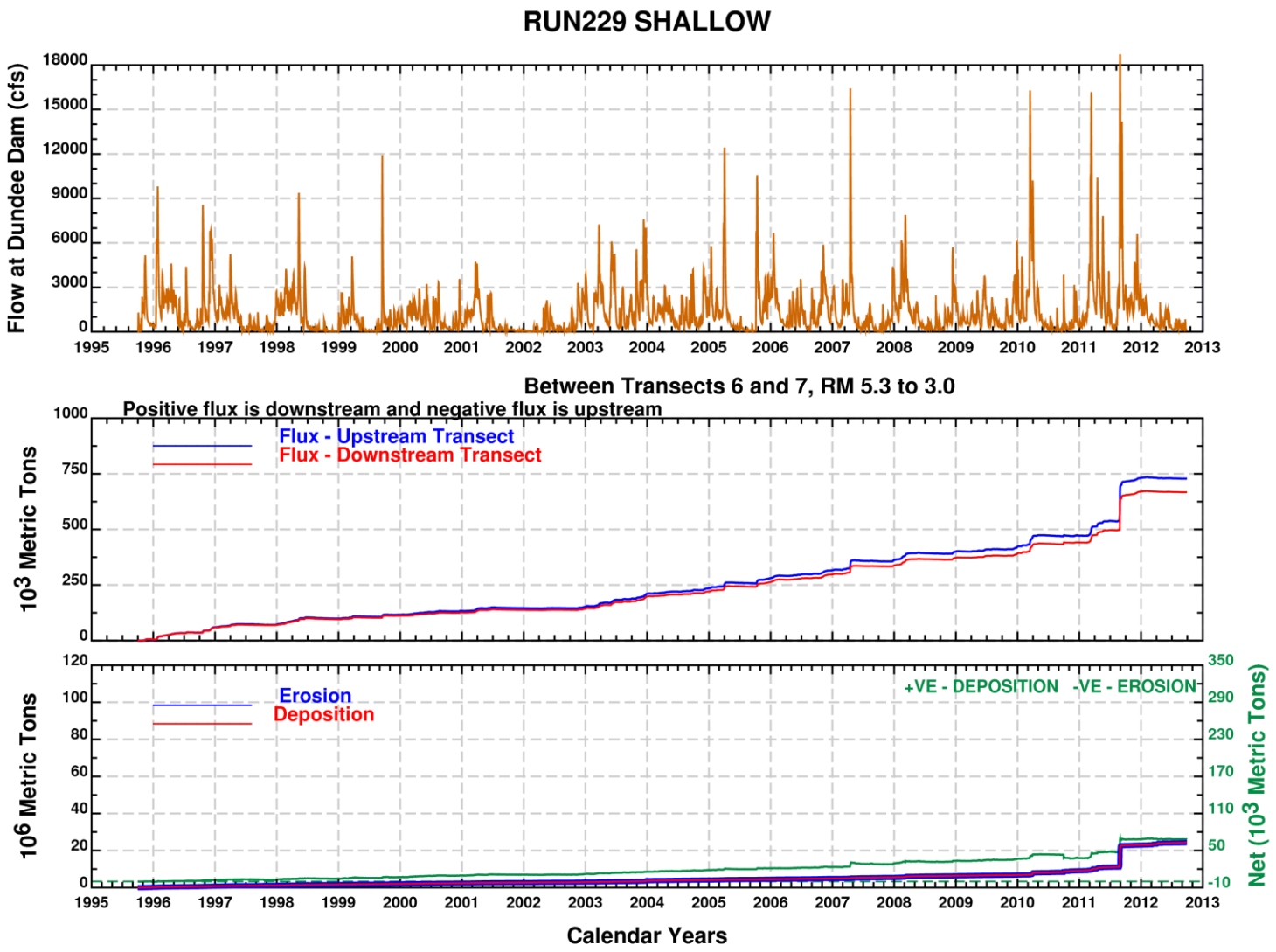

Water Column Solids Transport and Erosion and Deposition Fluxes – RM5.3 – 3.0

Lower Eight Miles of the Lower Passaic River

Figure 4-52

2014

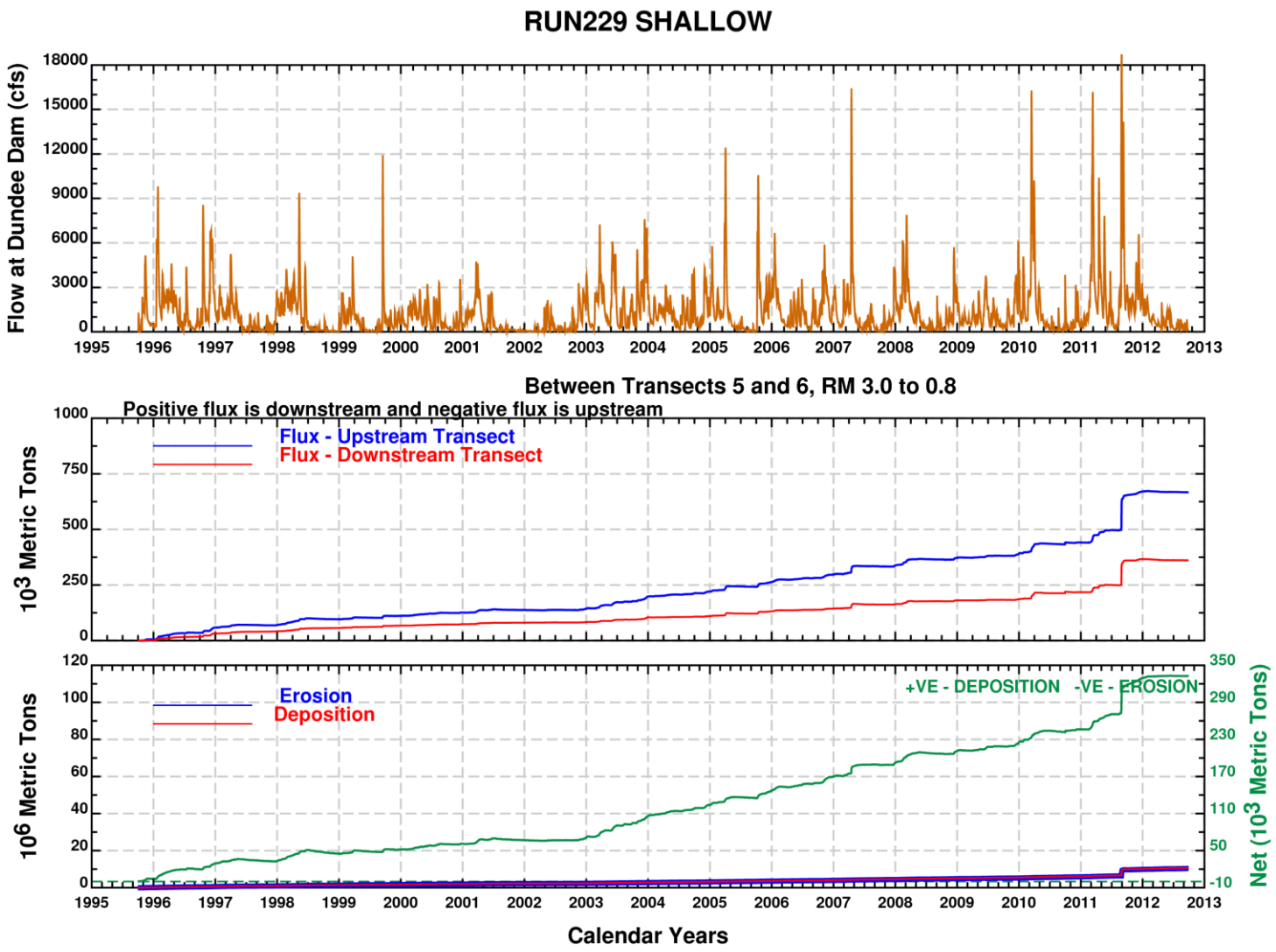

Water Column Solids Transport and Erosion and Deposition Fluxes – RM3.0 – 0.8

Lower Eight Miles of the Lower Passaic River

Figure 4-53

2014

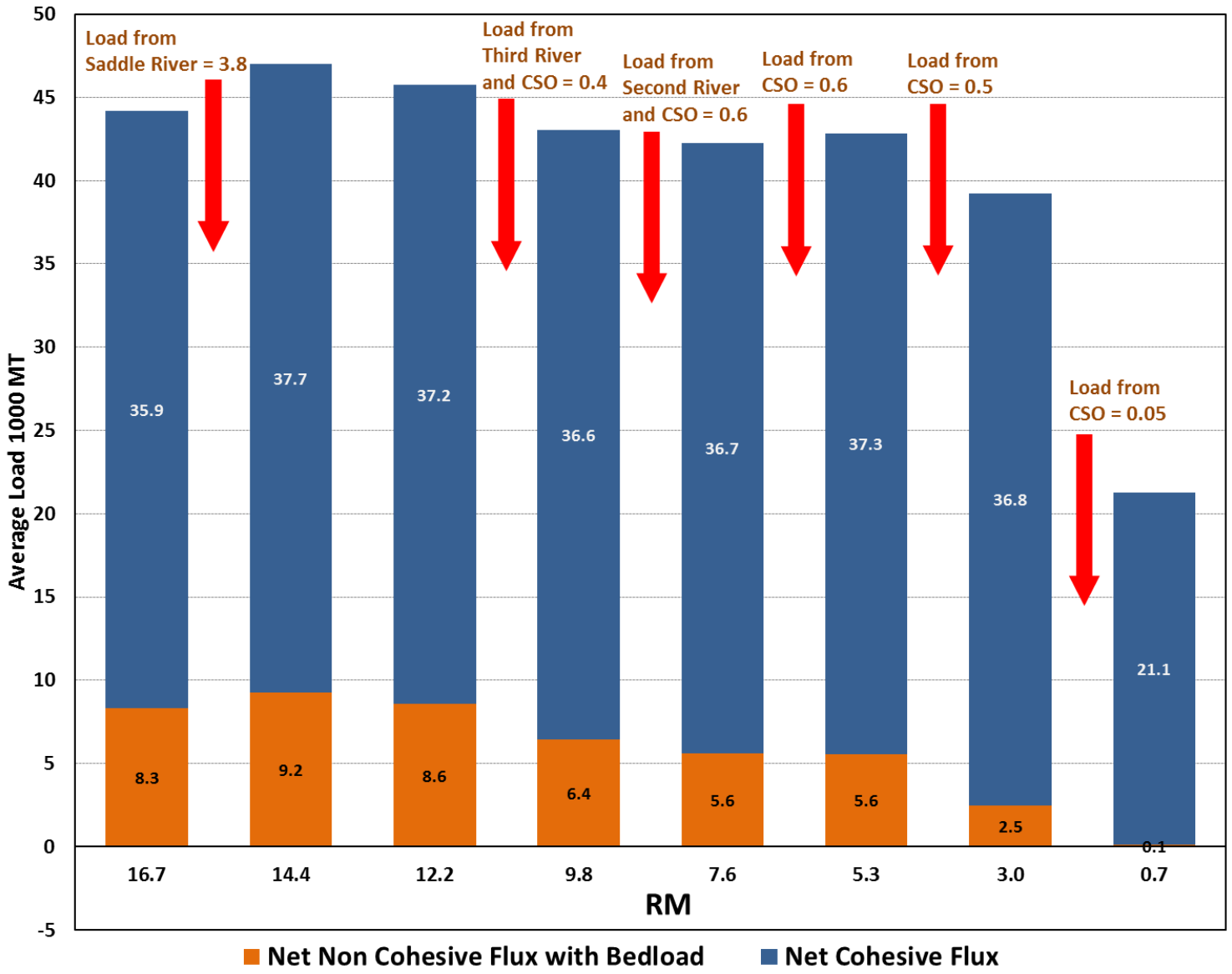

Water year 1995-2010 average cohesive and non-cohesive solids loading through the Lower Passaic River

Lower Eight Miles of the Lower Passaic River

Figure 4-54

2014

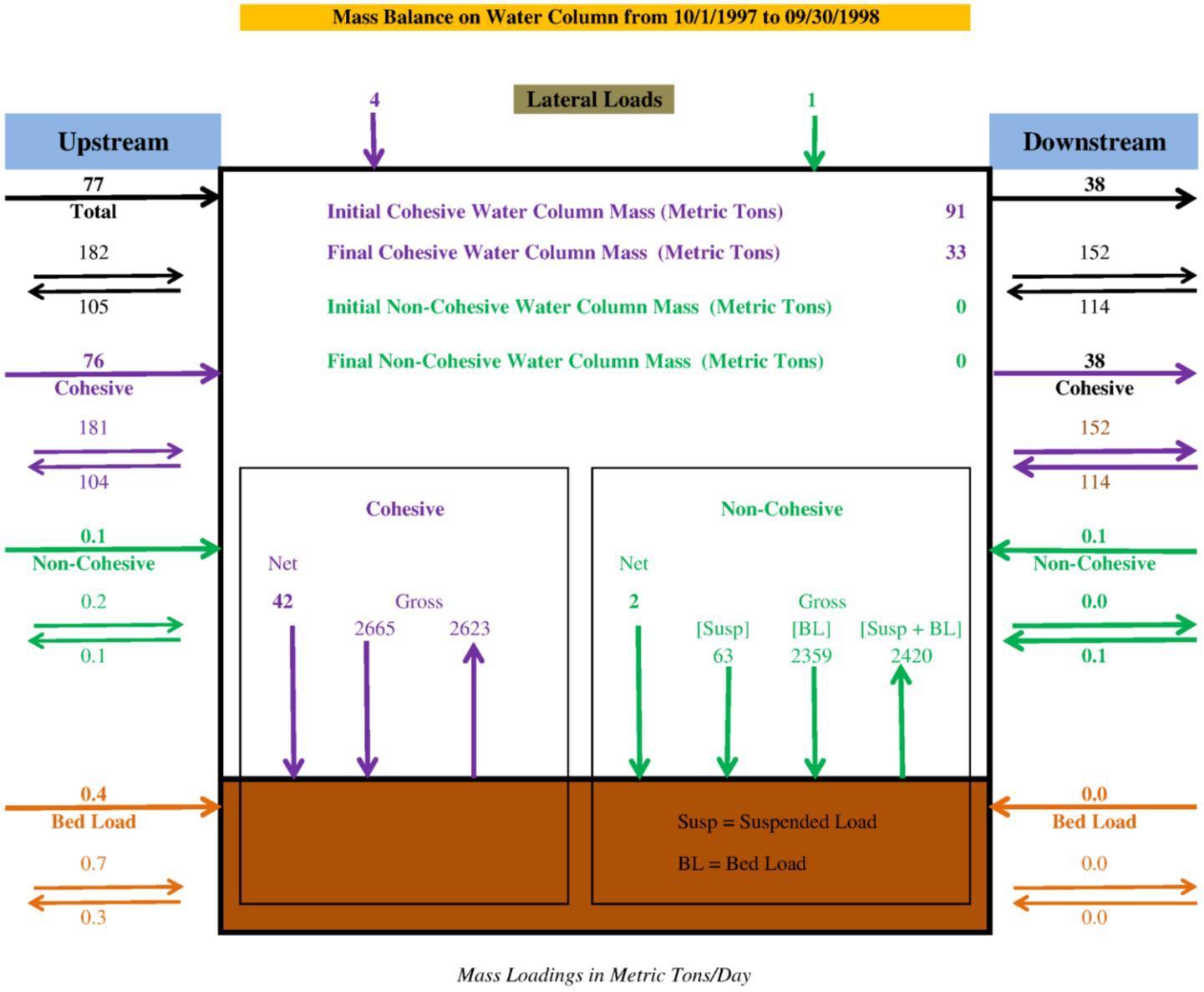

Mass Loadings in Metric Tons/Day

Solids Transport Summary for RM8.3 - RM0.8 - Full Water year 1998

Lower Eight Miles of the Lower Passaic River

Figure 4-55

2014

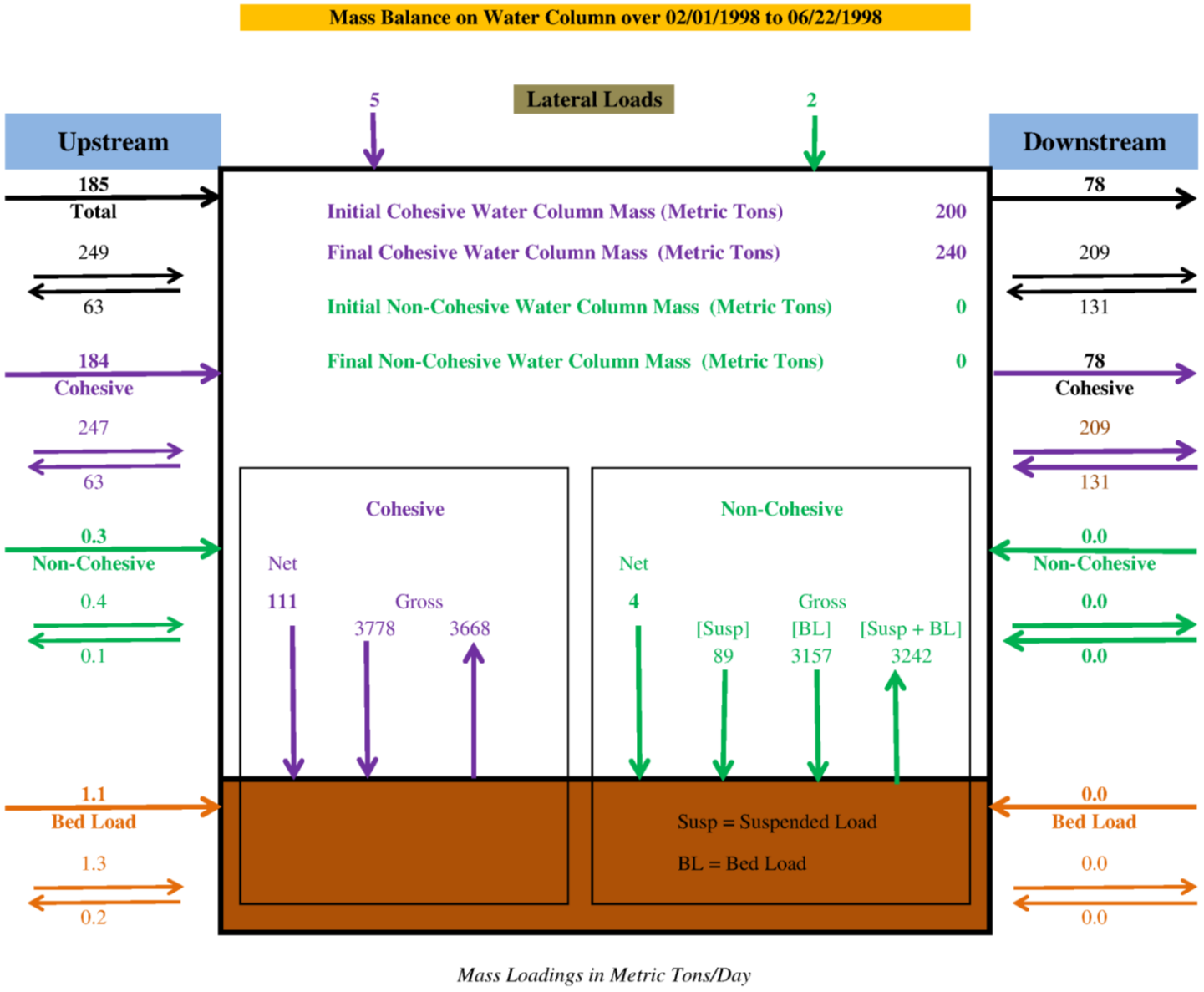

Solids Transport Summary for RM8.3 - RM0.8 - Water year 1998 - High-Flow Period (February 1st to June 22nd)

Lower Eight Miles of the Lower Passaic River

Figure 4-56

2014

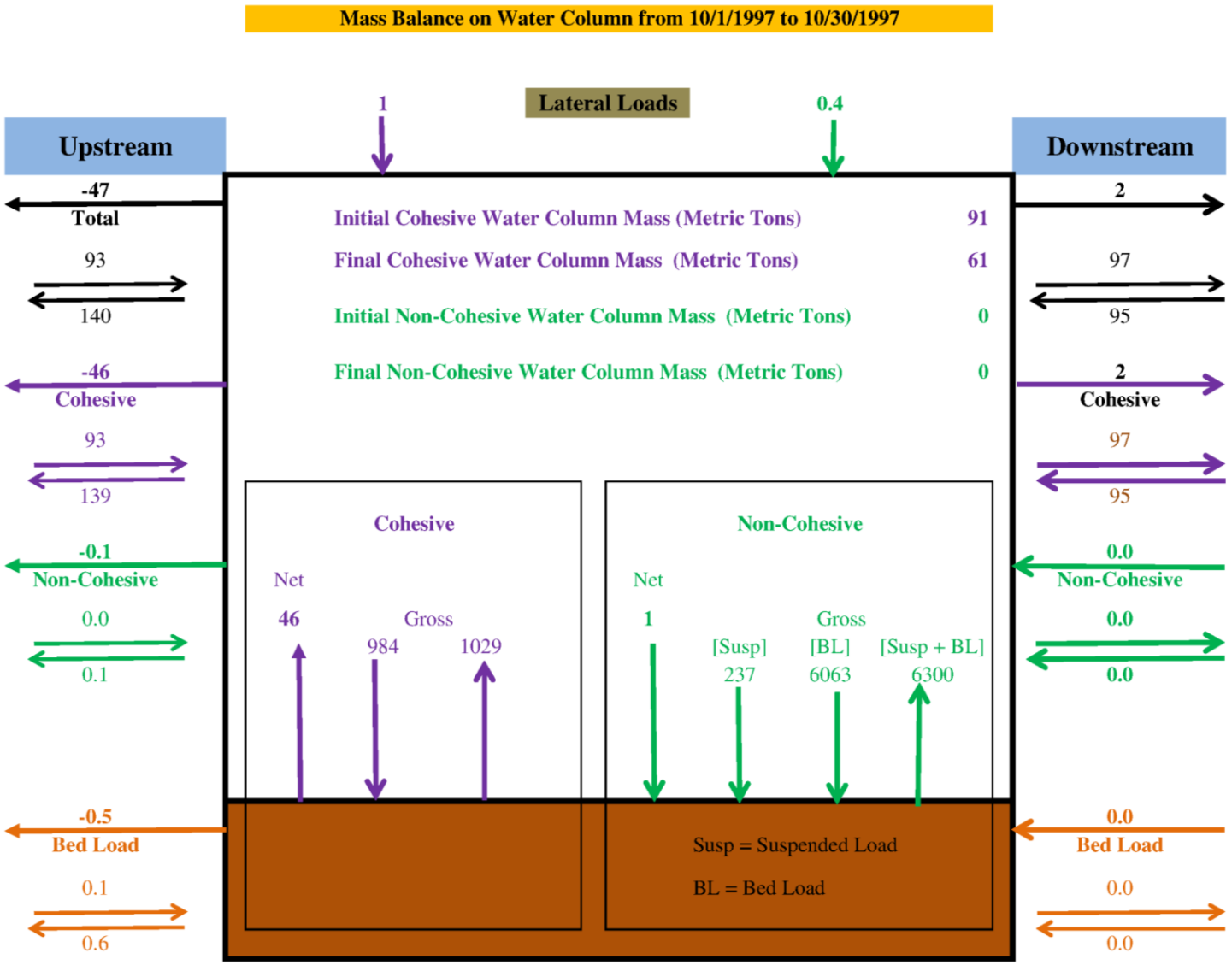

Mass Loadings in Metric Tons/Day

Solids Transport Summary for RM8.3 - RM0.8 - Water year 1998 - Low-Flow Period (October 1st to October 30th)

Lower Eight Miles of the Lower Passaic River

Figure 4-57

2014

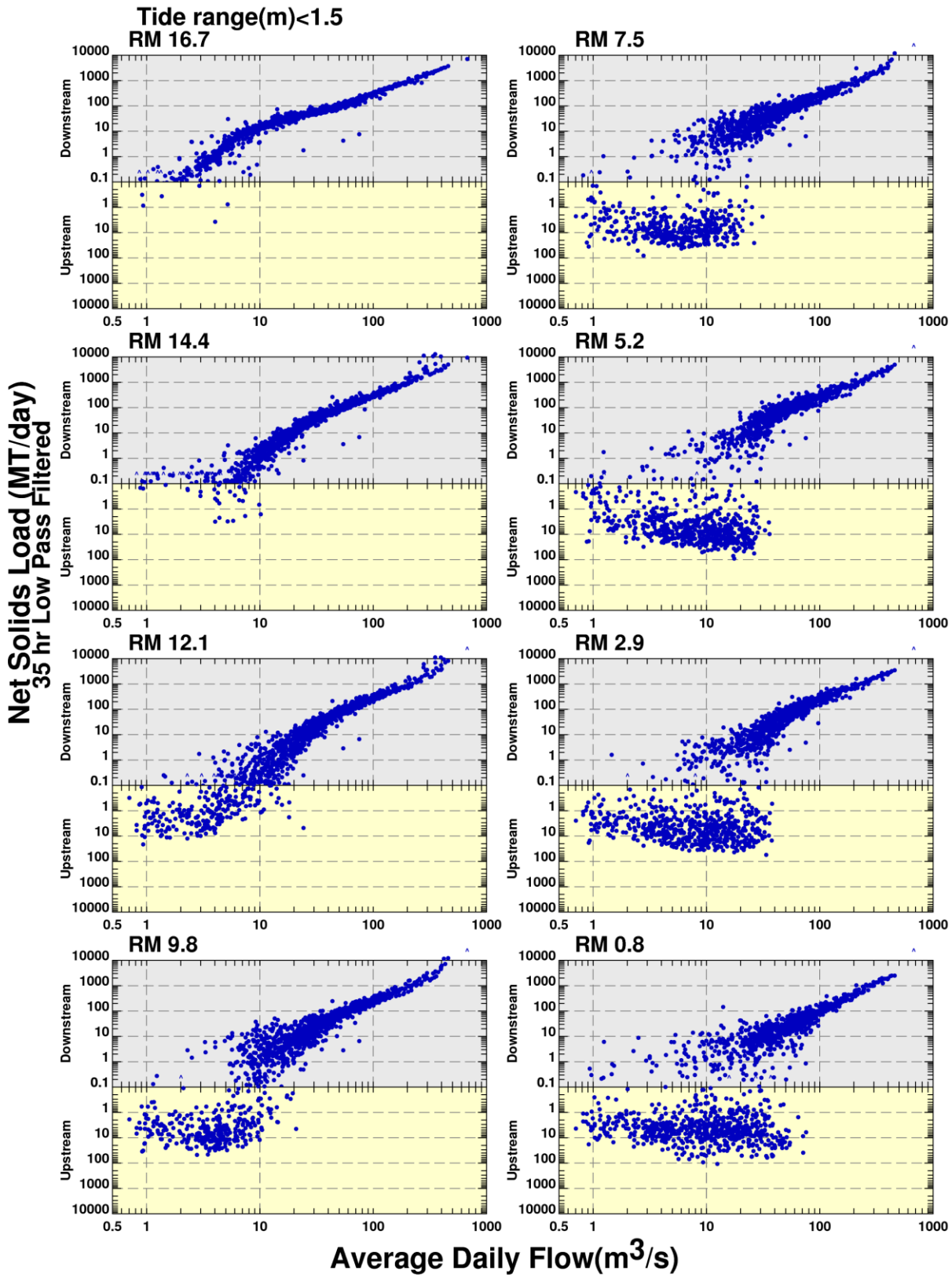

Water year 1995-2010 daily solids loading vs. flow at eight cross-channel transects for Tidal range <1.5 m

Lower Eight Miles of the Lower Passaic River

Figure 4-58

2014

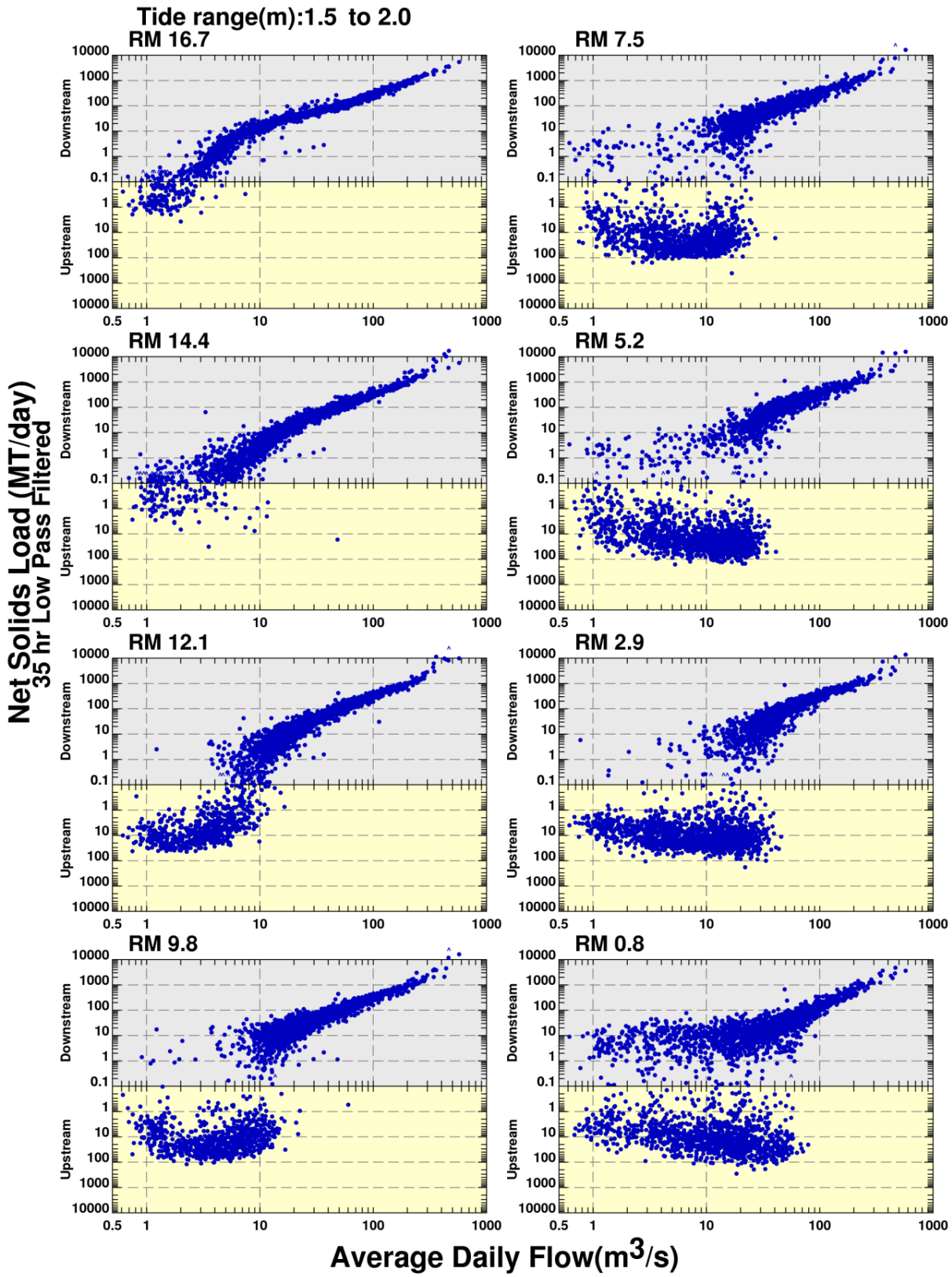

Water year 1995-2010 daily solids loading vs. flow at eight cross-channel transects for Tidal range 1.5 to 2.0 m

Lower Eight Miles of the Lower Passaic River

Figure 4-59

2014

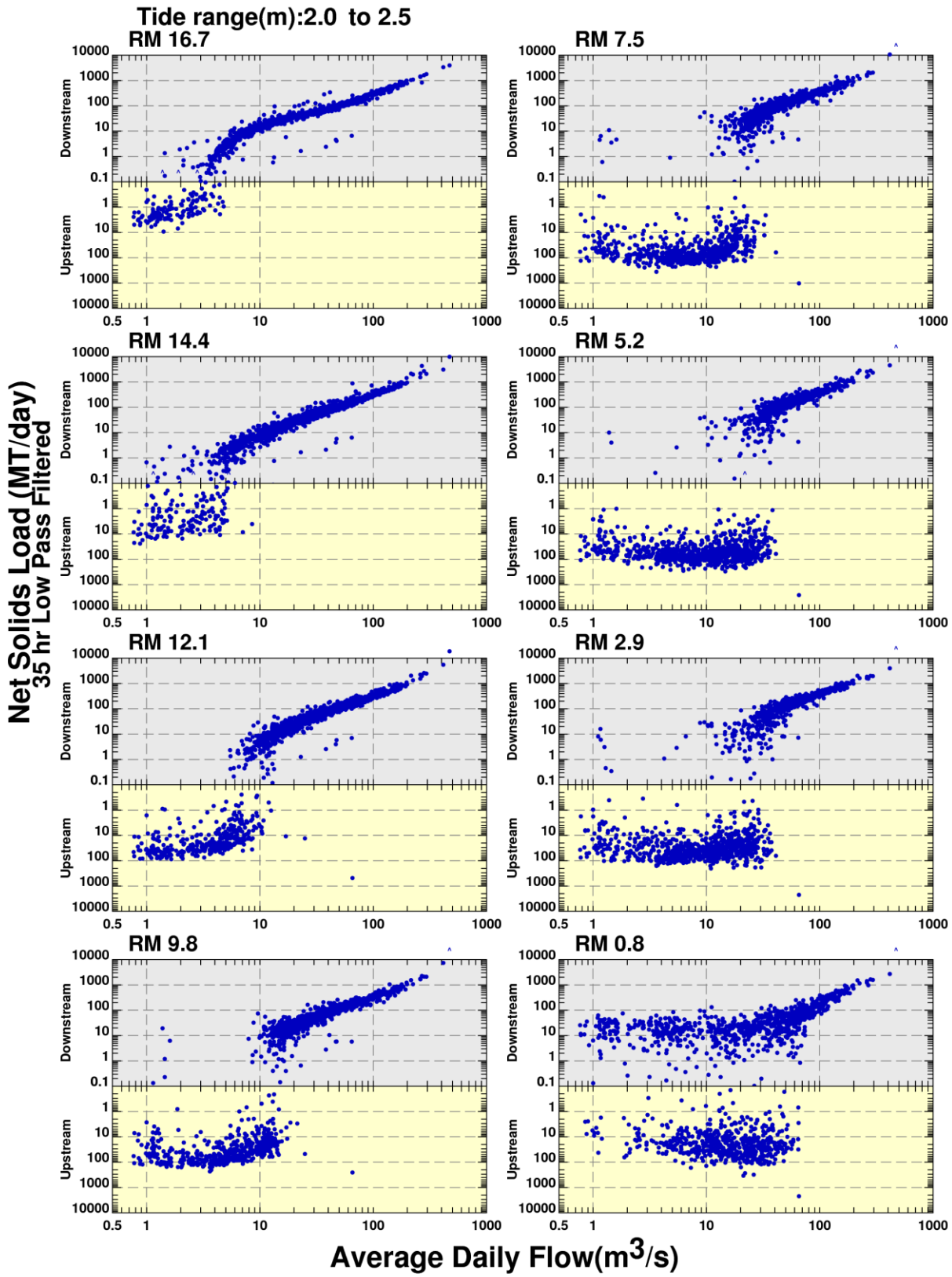

Water year 1995-2010 daily solids loading vs. flow at eight cross-channel transects for Tidal range 2.0 to 2.5 m

Lower Eight Miles of the Lower Passaic River

Figure 4-60

2014

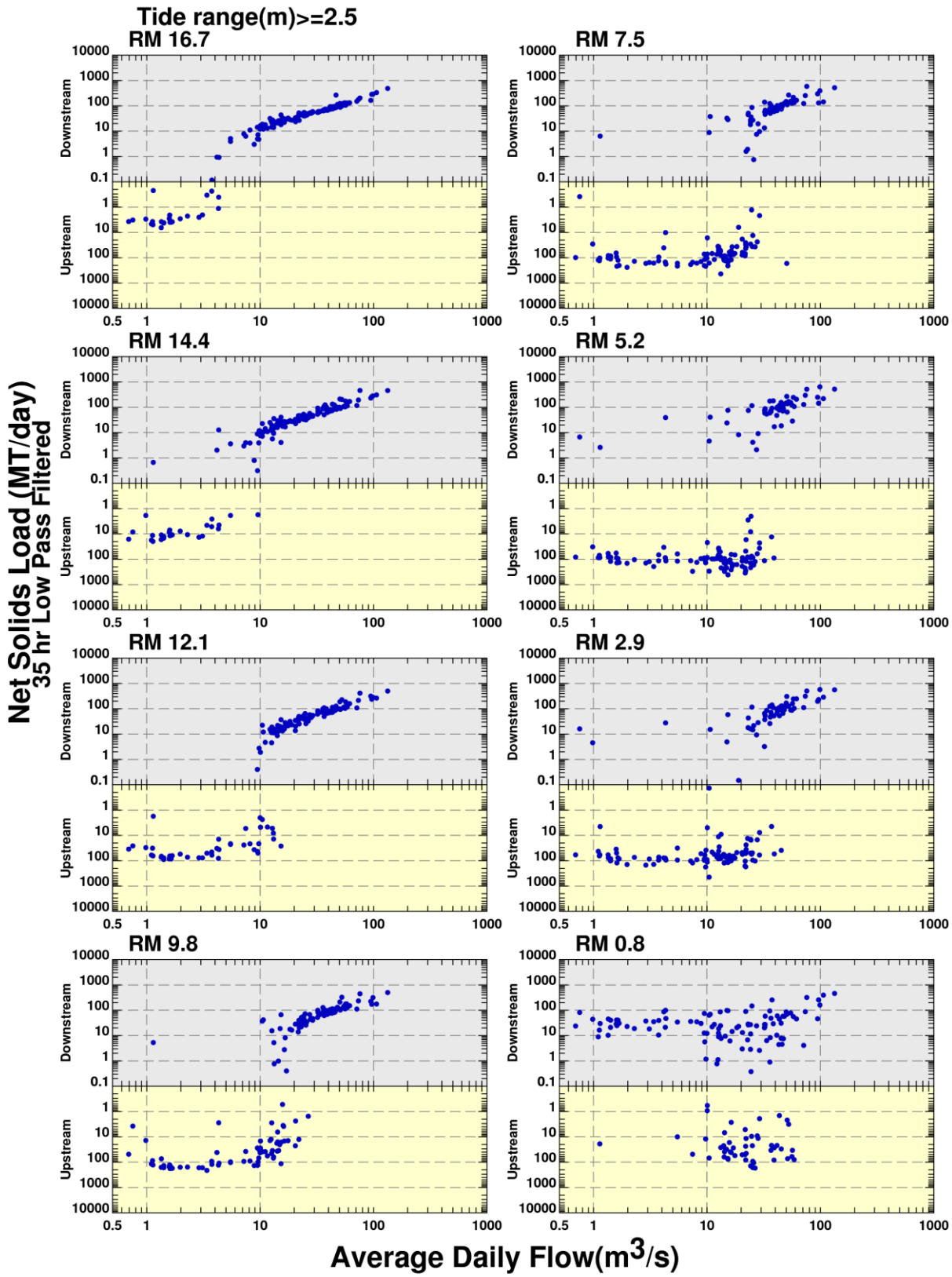

Water year 1995-2010 daily solids loading vs. flow at eight cross-channel transects for Tidal range >2.5 m

Lower Eight Miles of the Lower Passaic River

Figure 4-61

2014

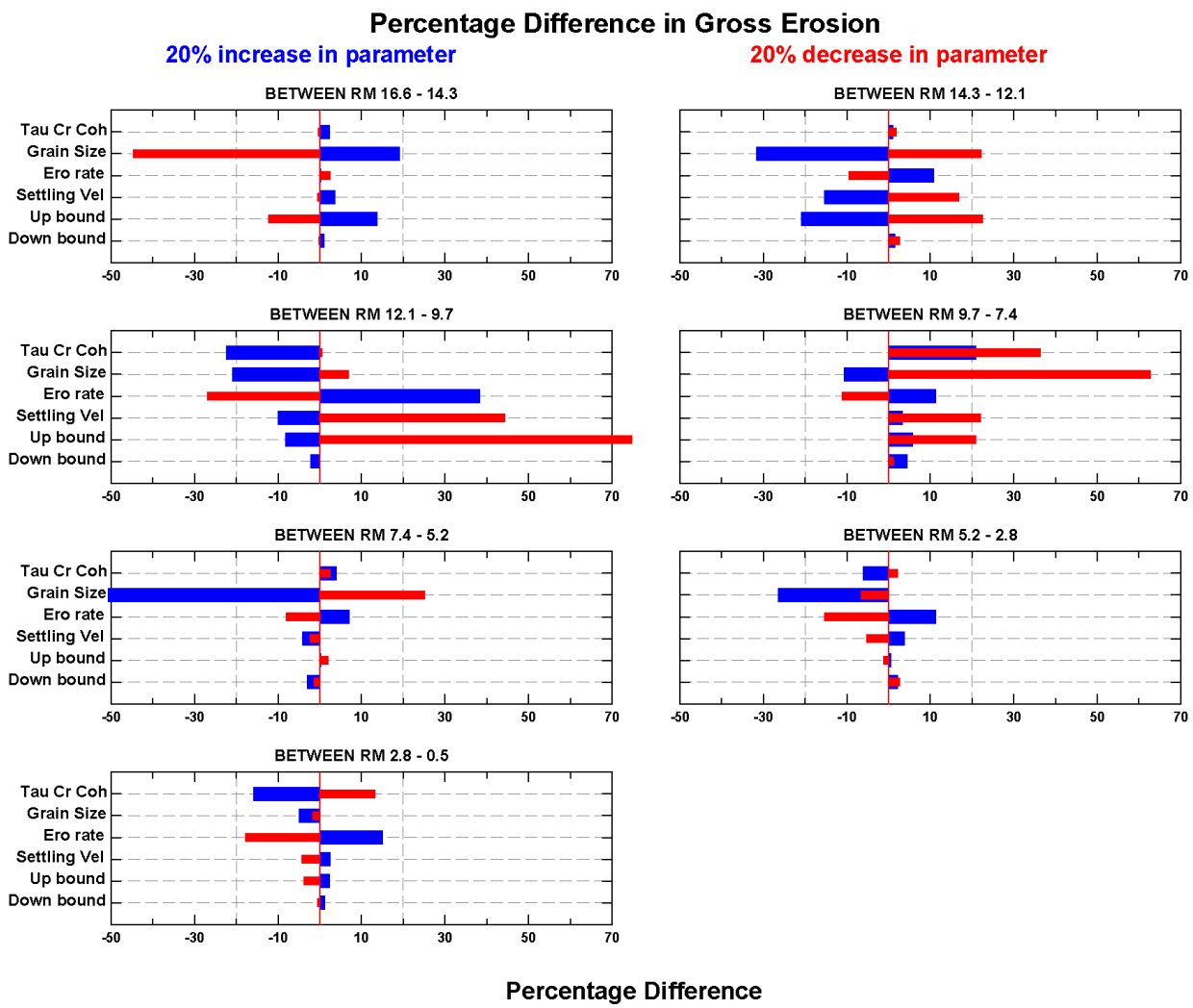

Sensitivity of Gross Erosion to Parameter Changes

Lower Eight Miles of the Lower Passaic River

Figure 5-1

2014

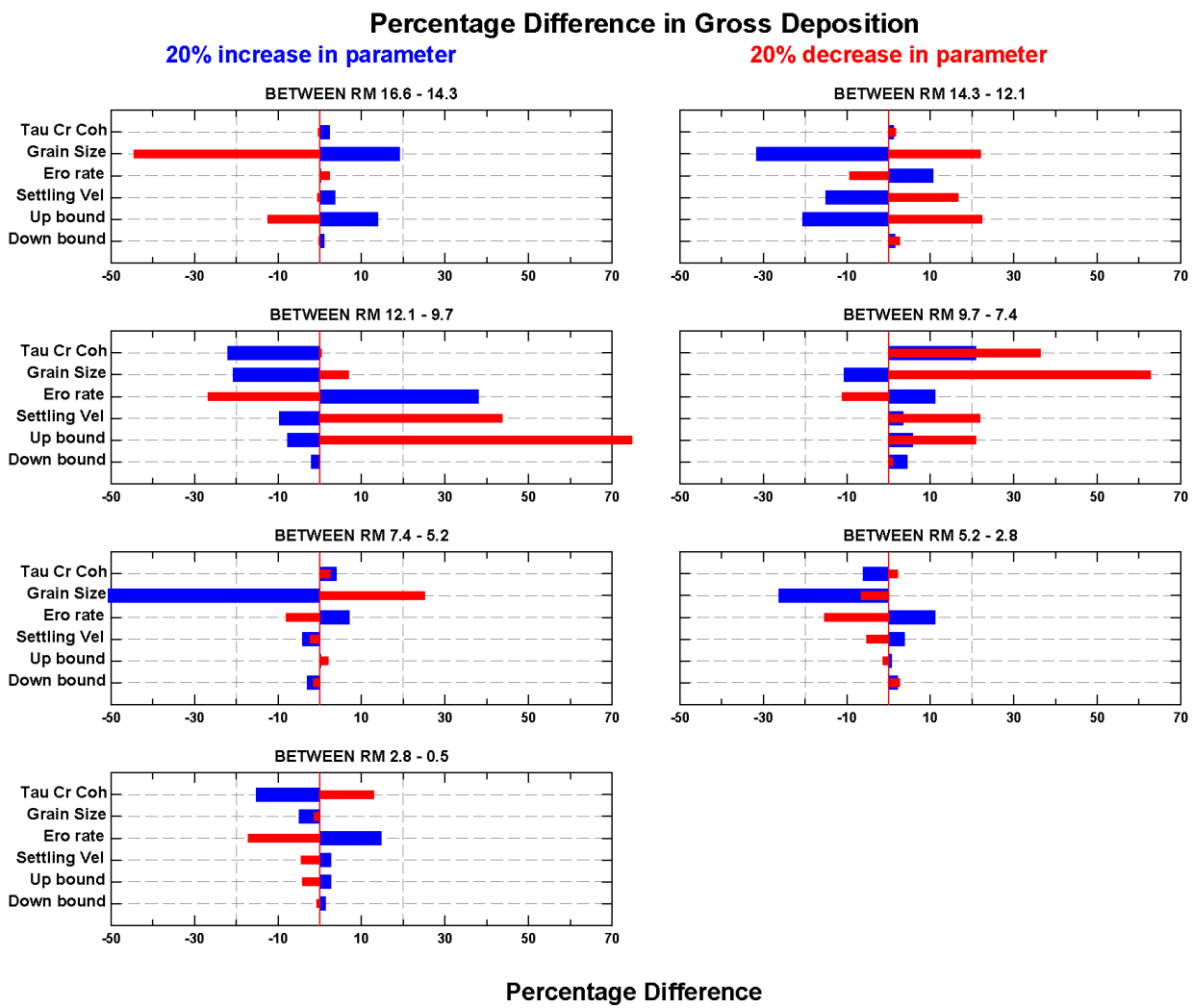

Sensitivity of Gross Deposition to Parameter Changes

Lower Eight Miles of the Lower Passaic River

Figure 5-2

2014

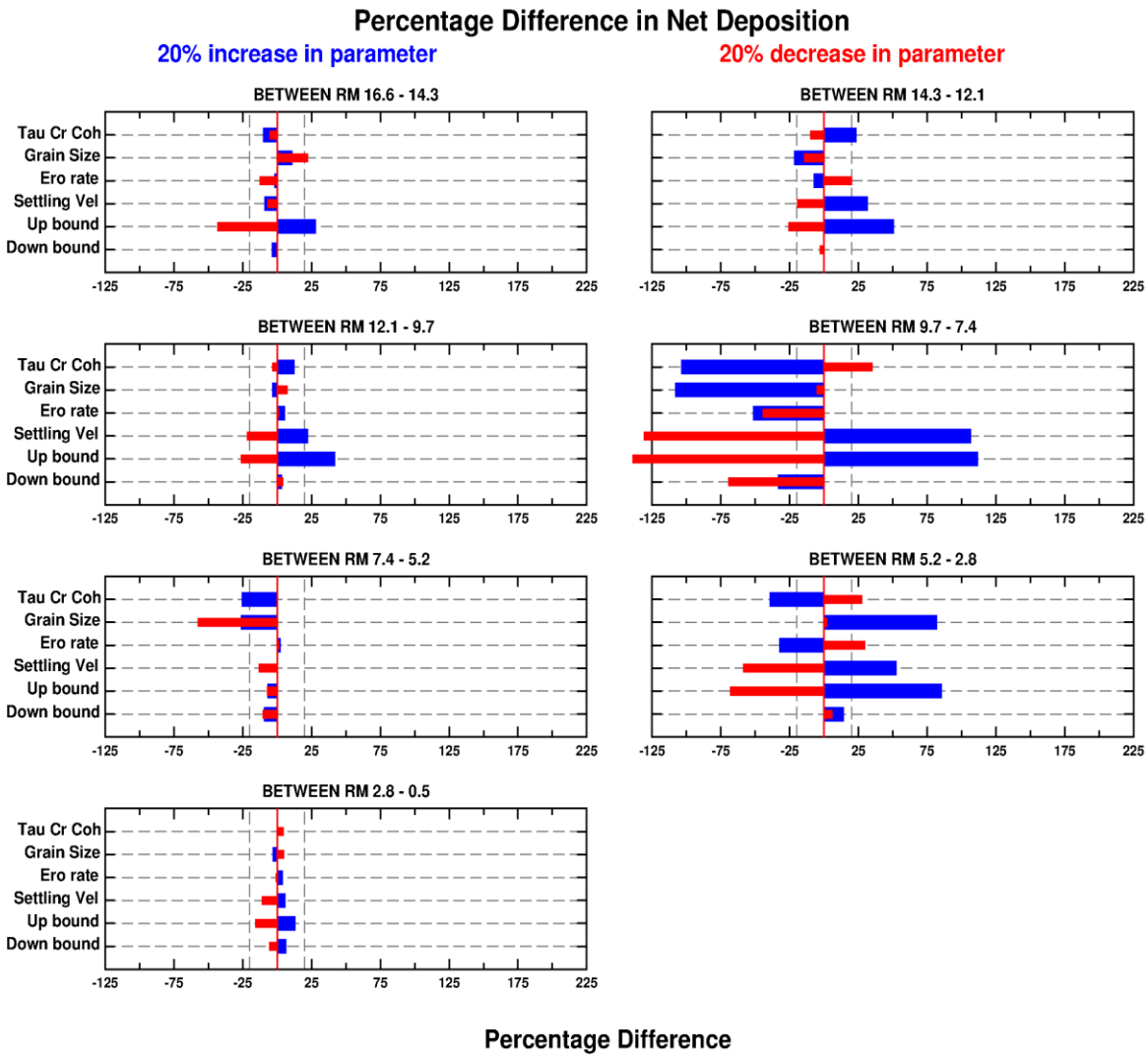

Sensitivity of Net Deposition to Parameter Changes

Lower Eight Miles of the Lower Passaic River

Figure 5-3

2014

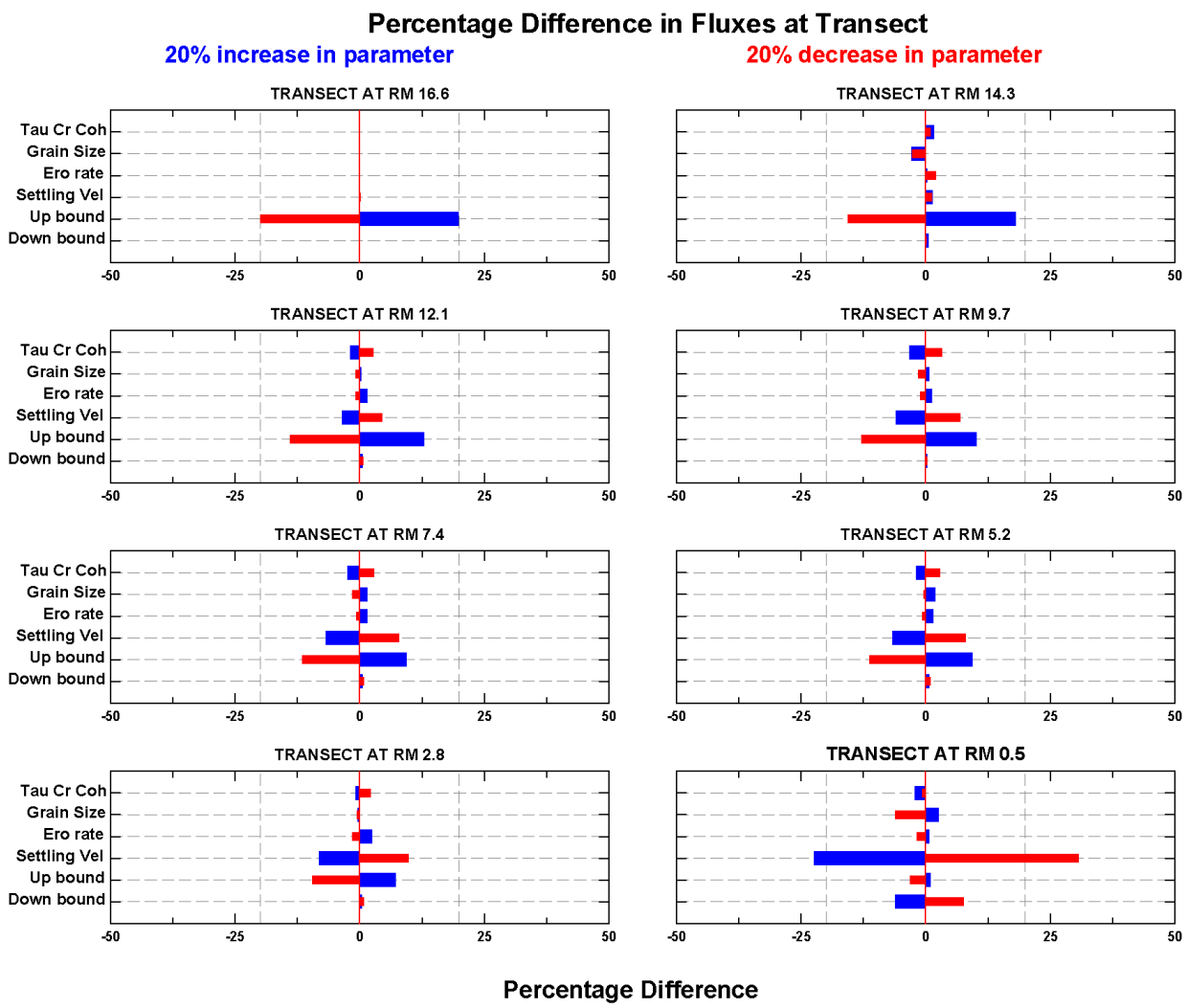

Sensitivity of Water Column Fluxes to Parameter Changes

Lower Eight Miles of the Lower Passaic River

Figure 5-4

2014

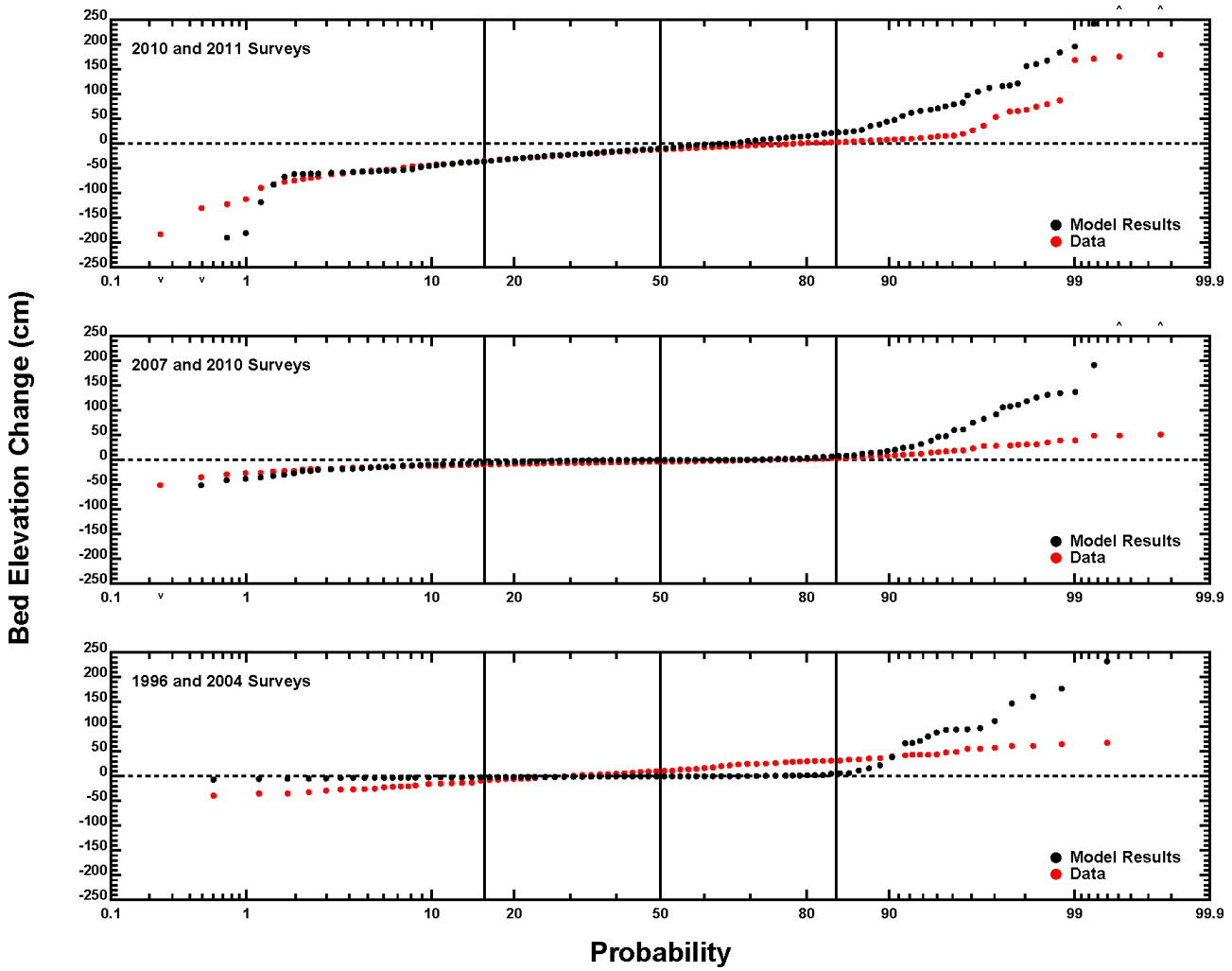

Cumulative Frequency Distribution of Simulated and Measured Bed Elevation Changes

Lower Eight Miles of the Lower Passaic River

Figure 5-5

2014

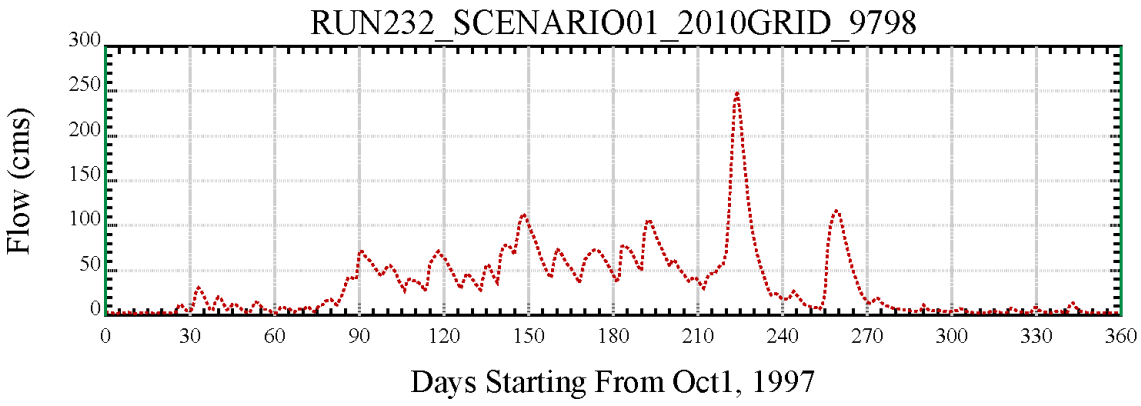

Fraction for Dundee Dam Silt

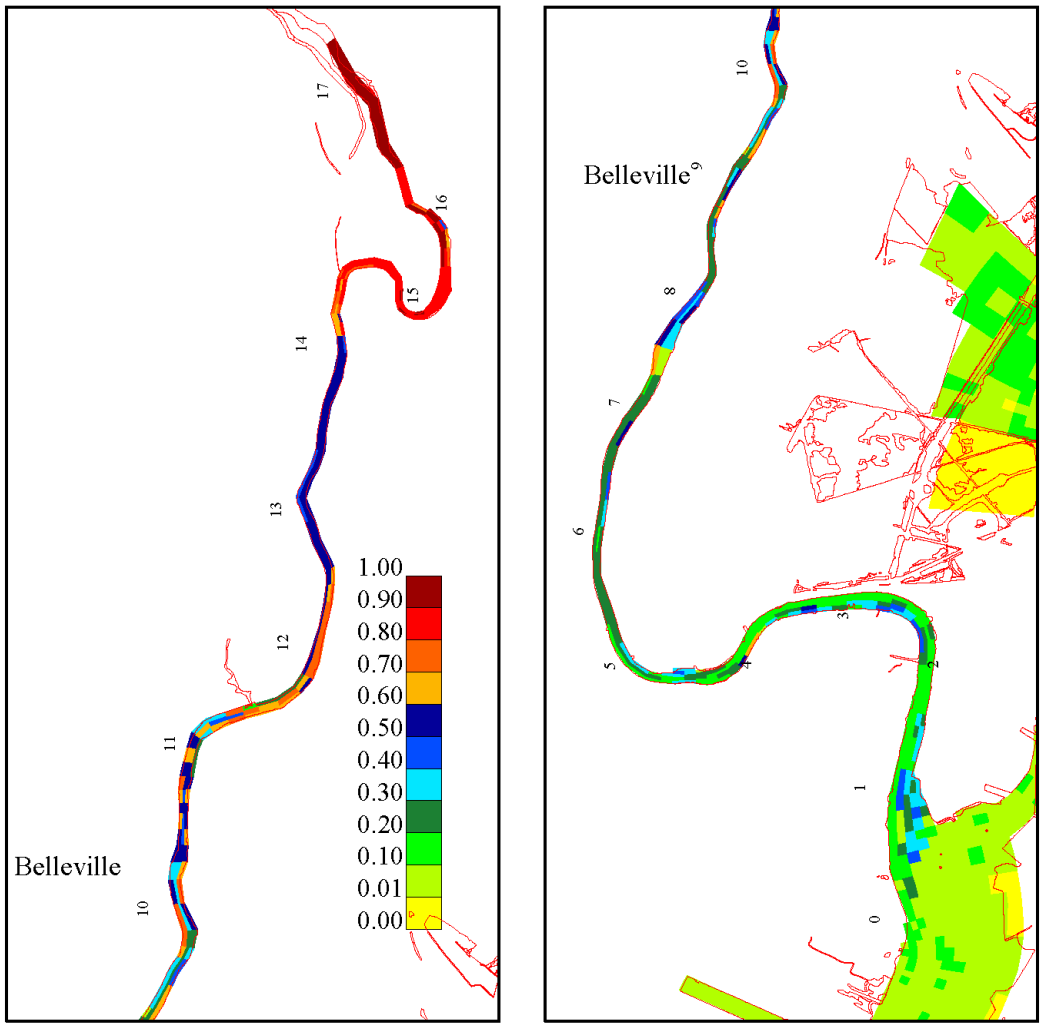

Solids Tracer Simulation Results for Solids Passing Over Dundee Dam	Figure 6-1
Lower Eight Miles of the Lower Passaic River	2014

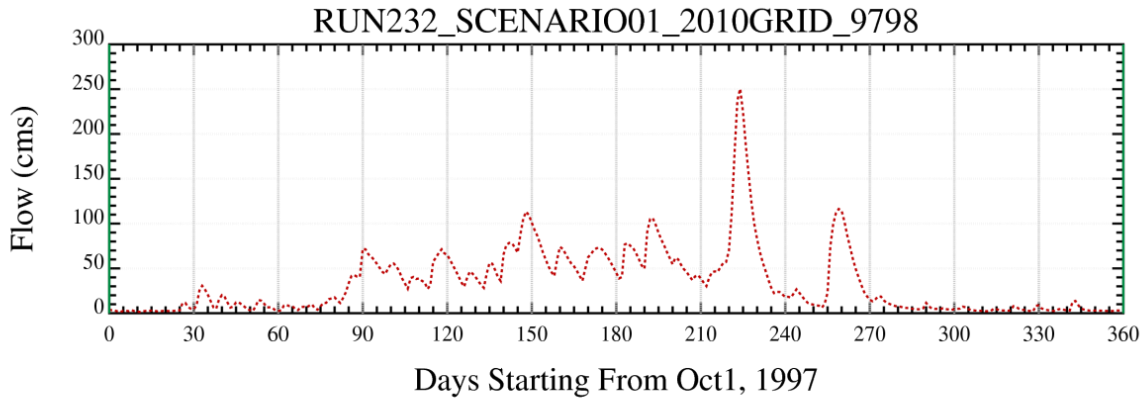

Fraction for Resuspended Passaic Silt

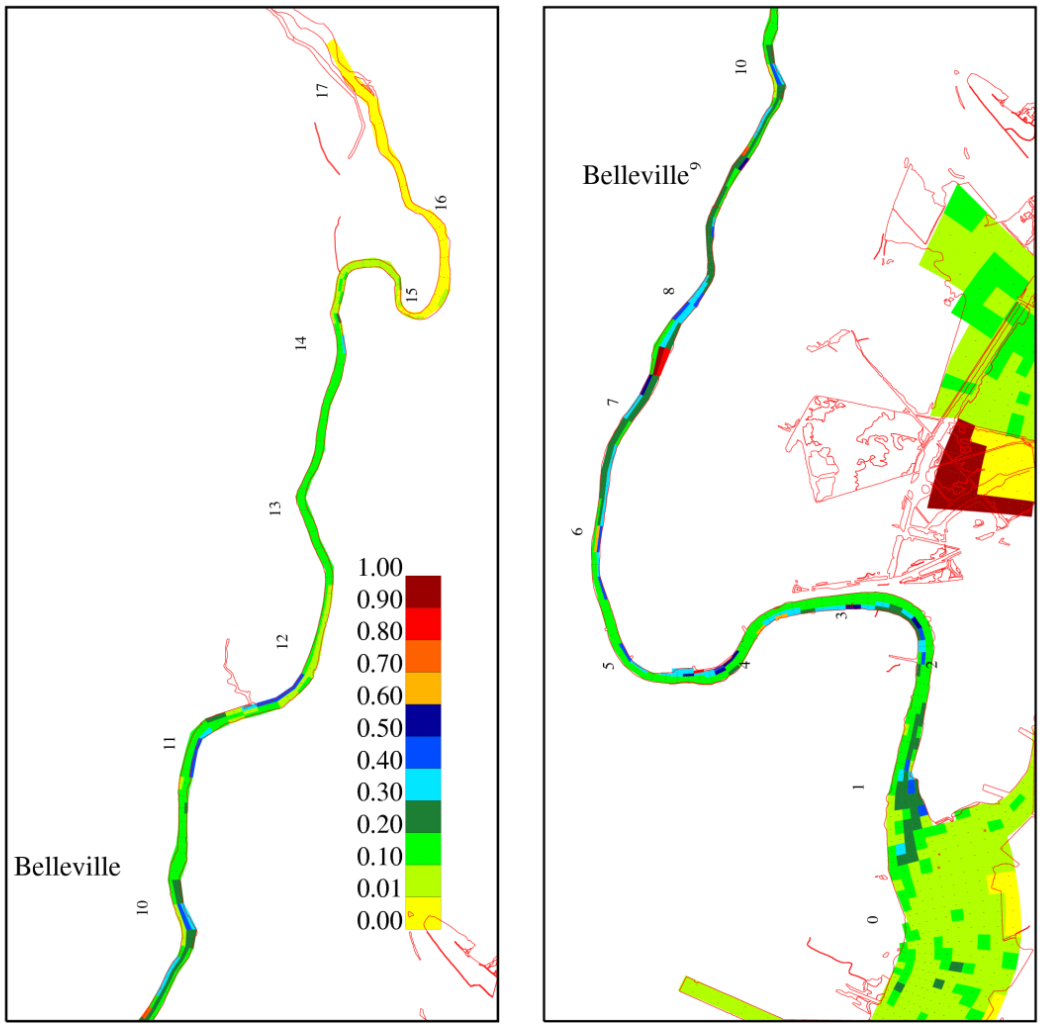

Solids Tracer Simulation Results for Solids from Resuspended LPR Sediment

Lower Eight Miles of the Lower Passaic River

Figure 6-2

2014

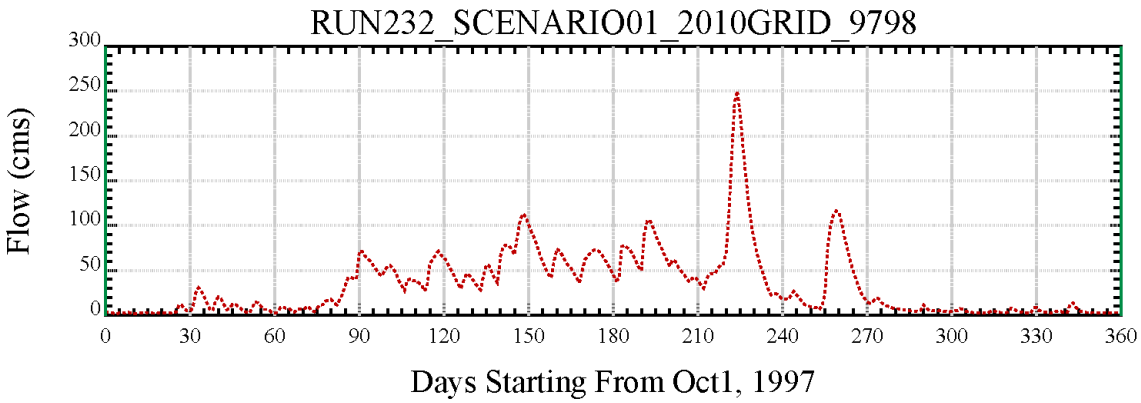

Fraction for Open Boundary Silt

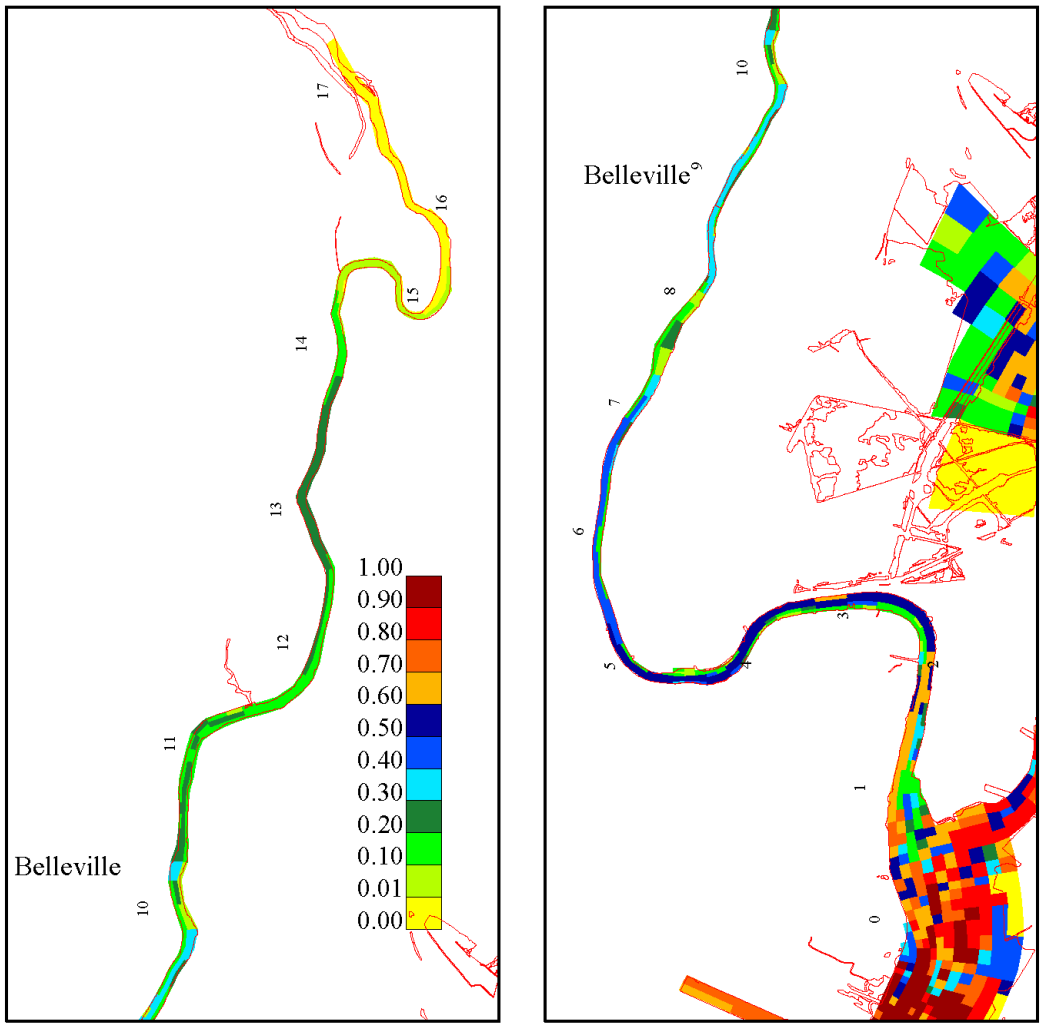

Solids Tracer Simulation Results for Open Boundary Solids Input	Figure 6-3
Lower Eight Miles of the Lower Passaic River	2014

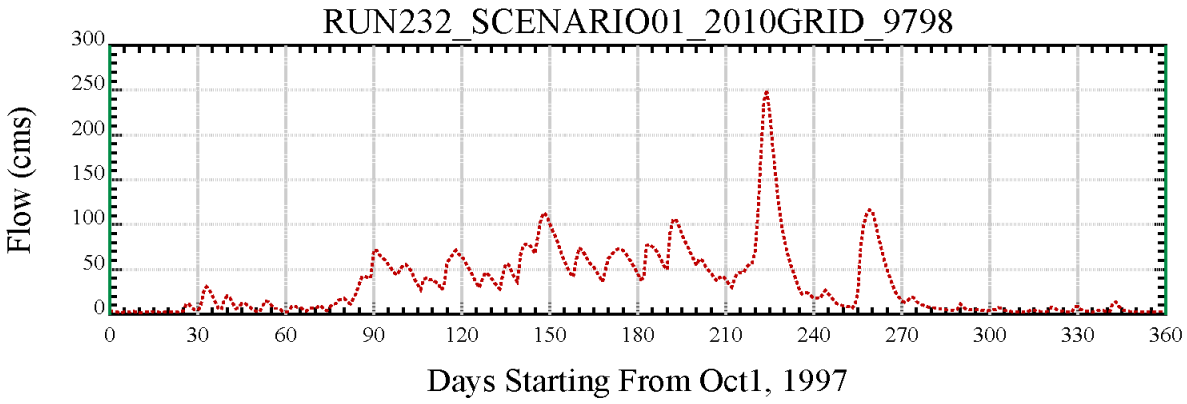

Fraction for Newark Bay Silt

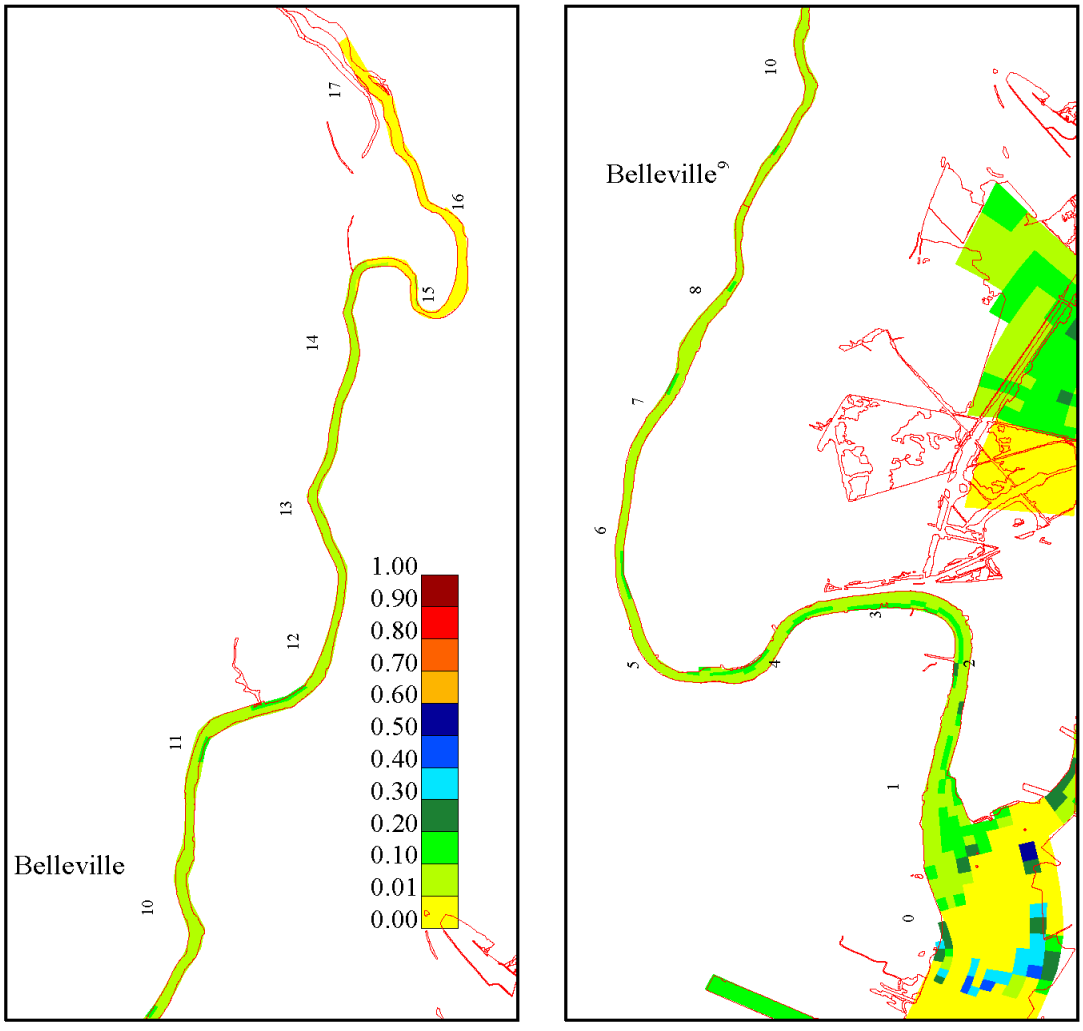

Solids Tracer Simulation Results for Solids from Newark Bay	Figure 6-4
Lower Eight Miles of the Lower Passaic River	2014

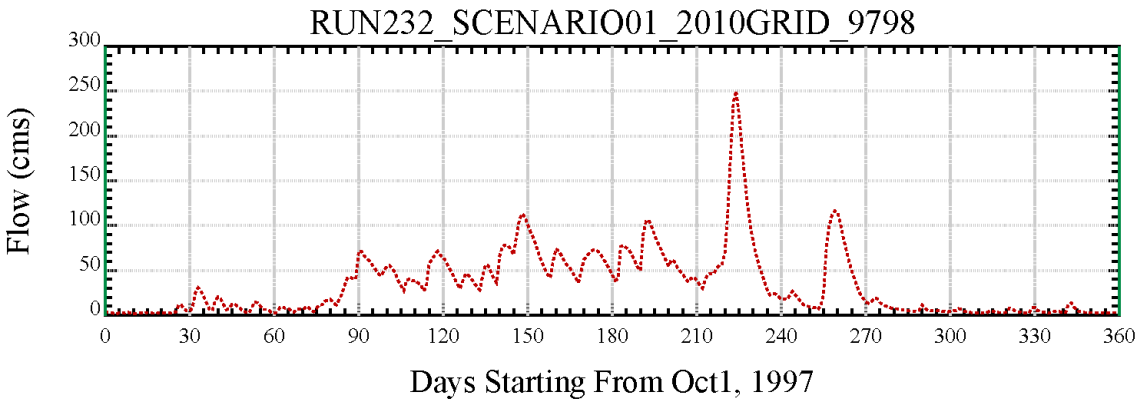

Fraction for Hackensack Silt

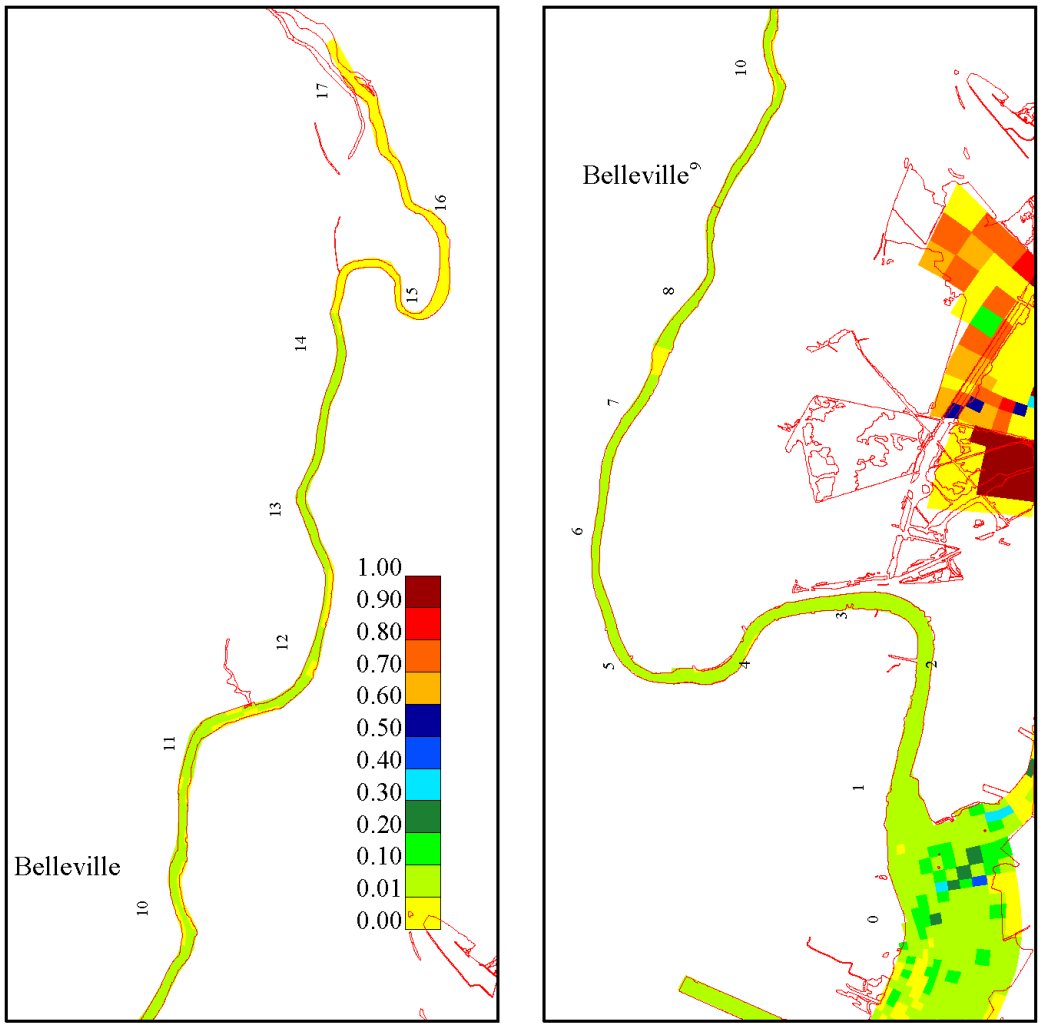

Solids Tracer Simulation Results for Solids from the Hackensack River	Figure 6-5
Lower Eight Miles of the Lower Passaic River	2014

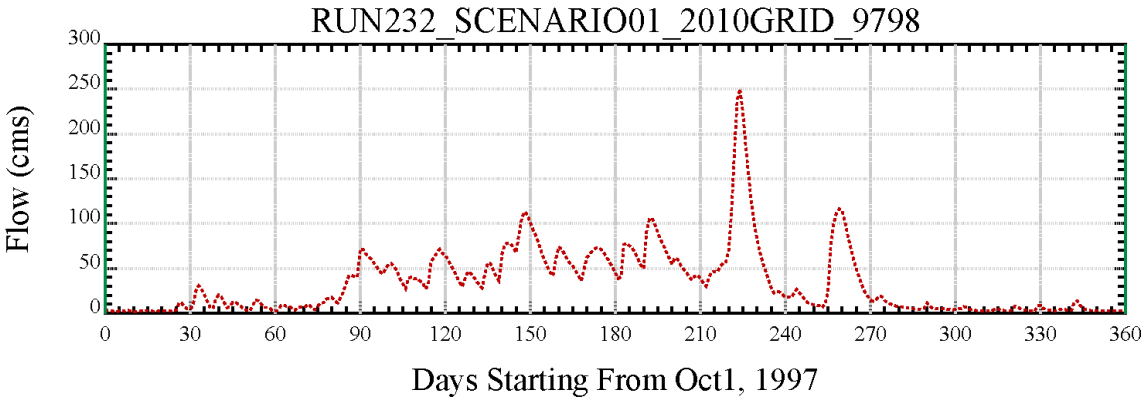

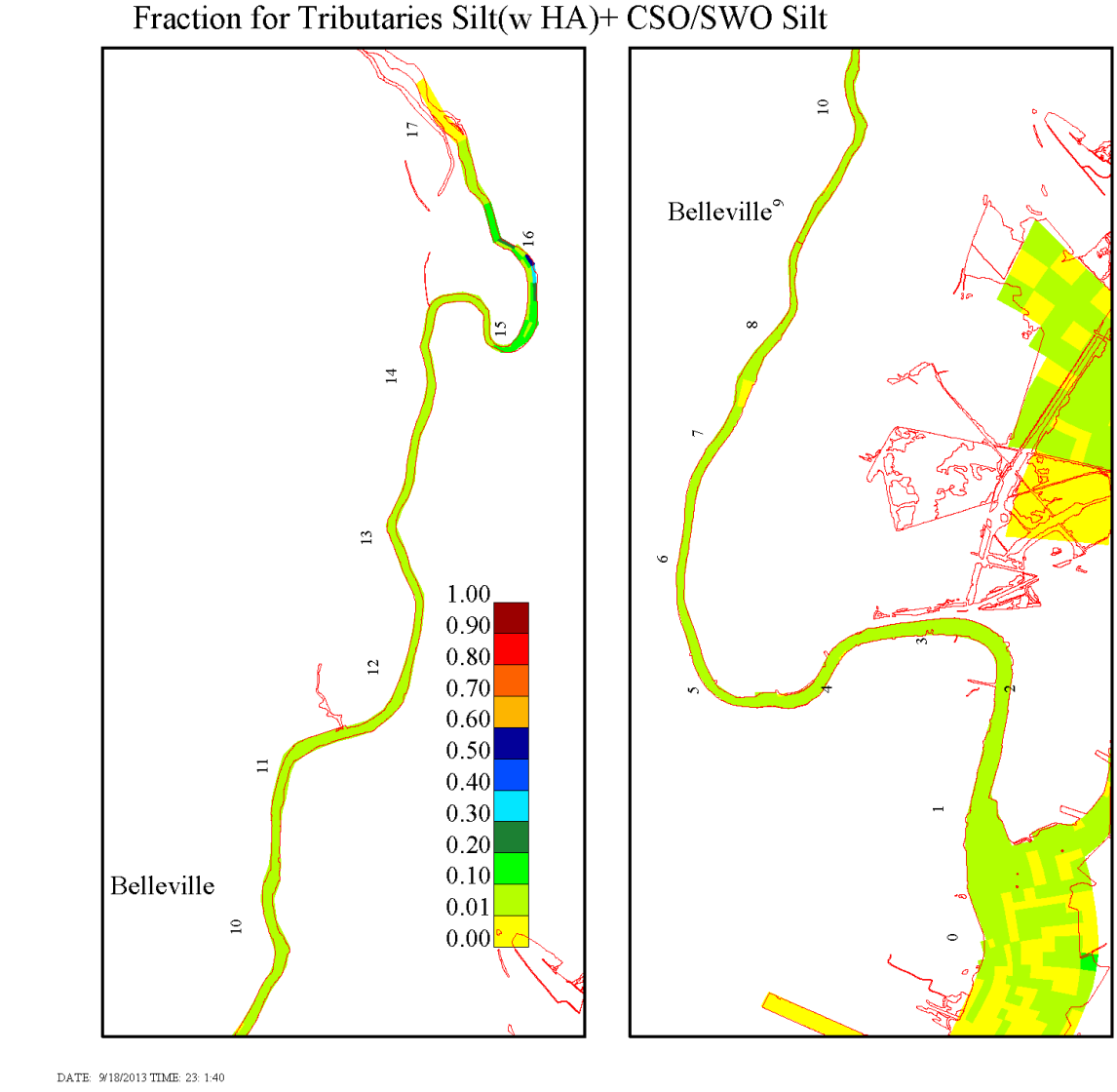

Solids Tracer Simulation Results for Solids Tributaries and CSO/Stormwater Inputs *Lower Eight Miles of the Lower Passaic River*	Figure 6-6 2014

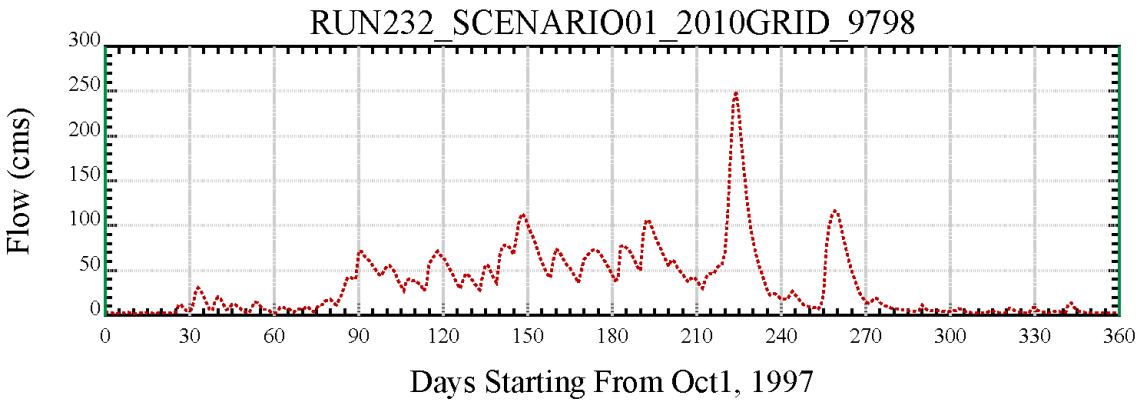

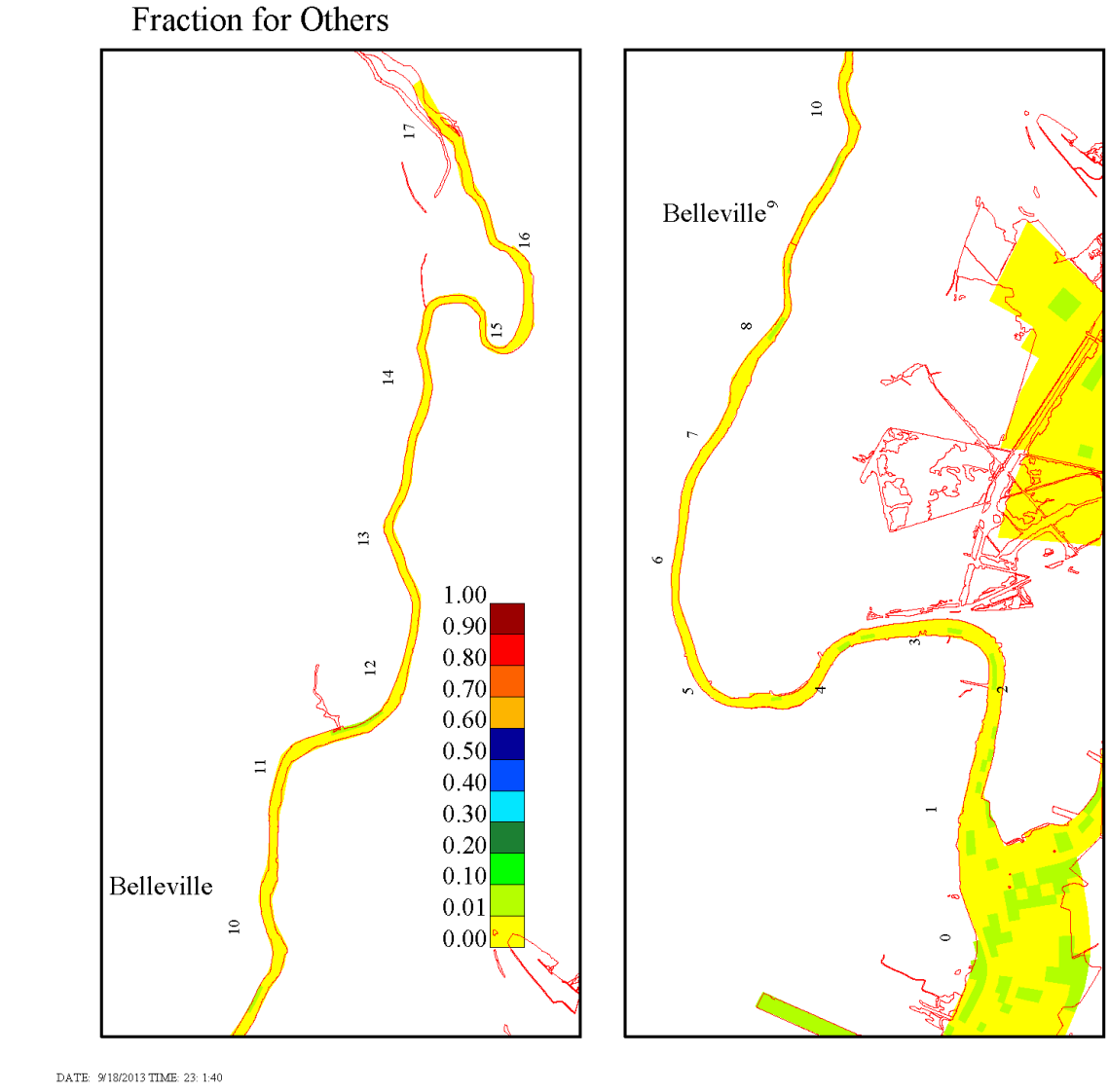

Solids Tracer Simulation Results for Solids from Other Sources (in-place sediments in the Kills)

Lower Eight Miles of the Lower Passaic River

Figure 6-7

2014

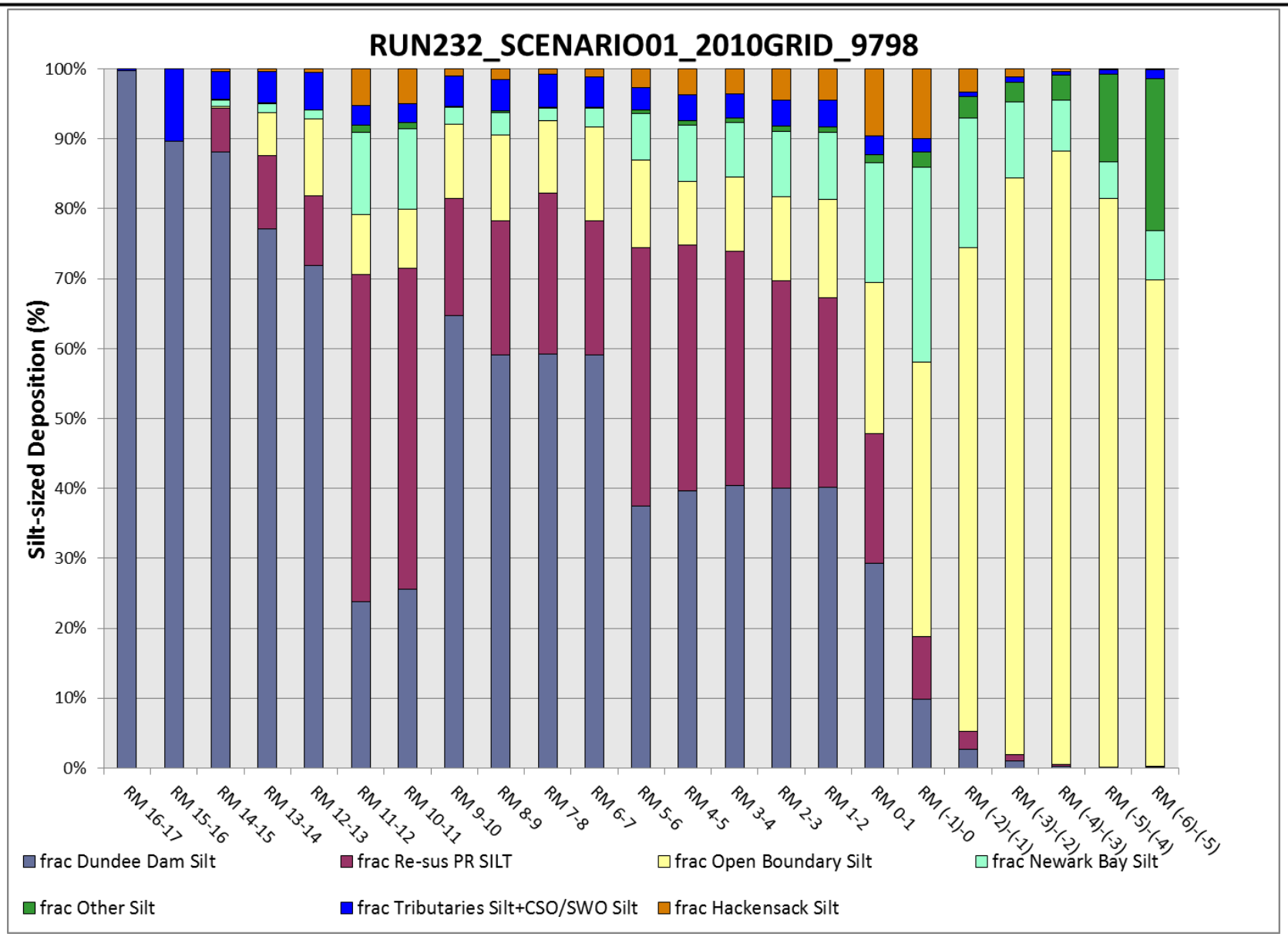

Solids Tracer Simulation Results Averaged Over One-mile Reaches

Lower Eight Miles of the Lower Passaic River

Figure 6-8

2014

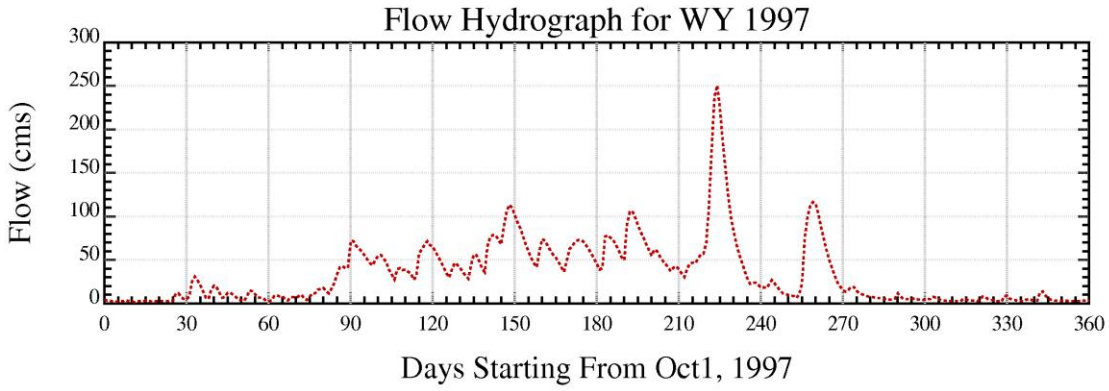

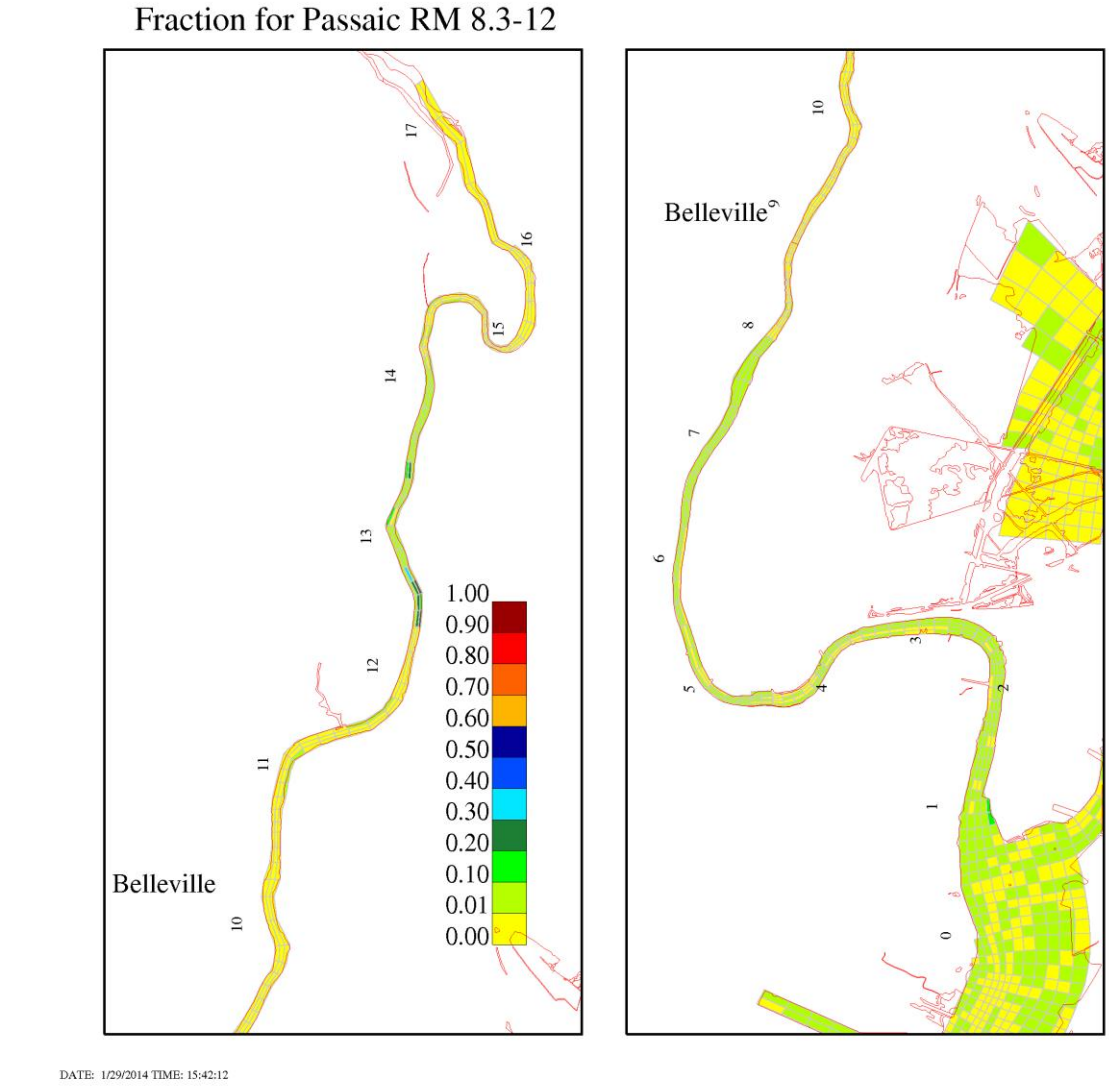

Eight-mile capping Simulation - Solids Tracer Results for Solids from River mile 8.3-12 LPR Sediment

Lower Eight Miles of the Lower Passaic River

Figure 6-9

2014

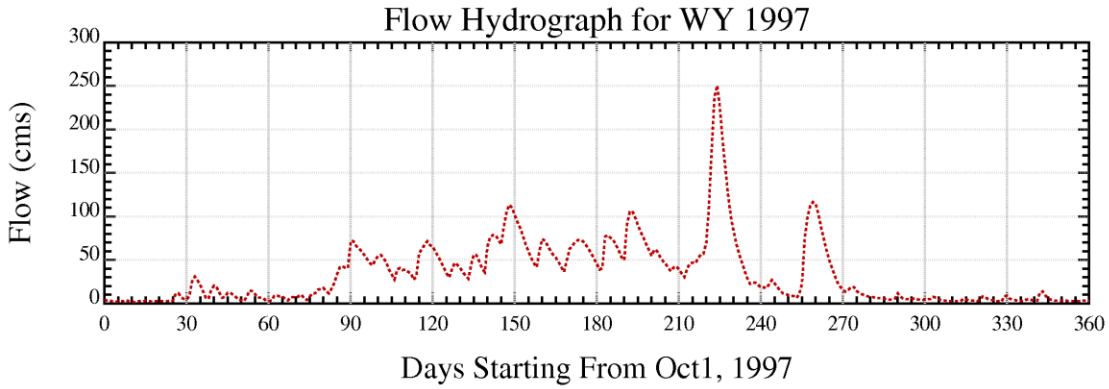

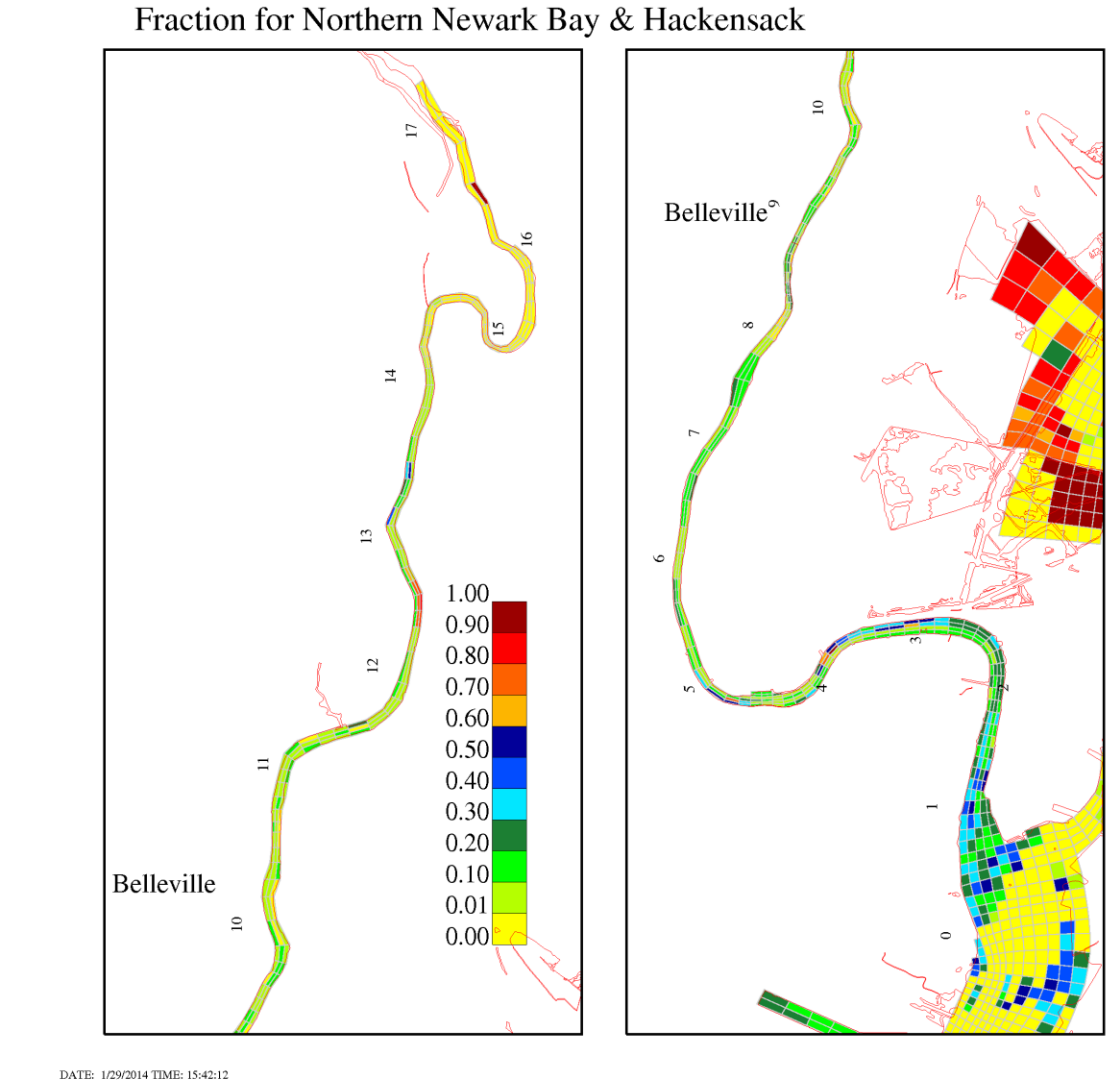

Eight-mile capping Simulation - Solids Tracer Results for Solids from Northern Newark Bay and Hackensack River Sediment

Lower Eight Miles of the Lower Passaic River

Figure 6-10

2014

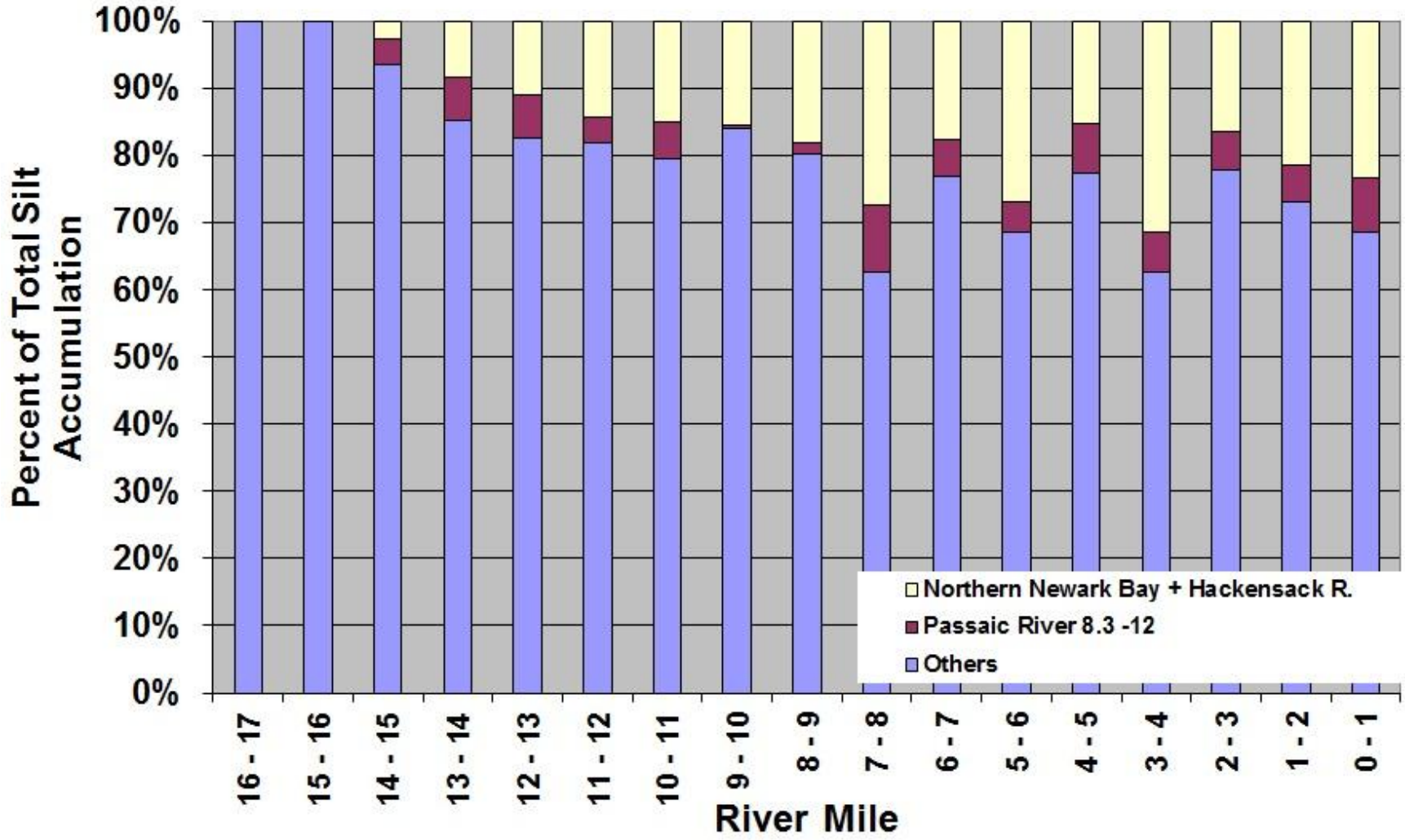

Eight-mile Capping Simulation Results averaged over one-mile Reaches

Lower Eight Miles of the Lower Passaic River

Figure 6-11

2014

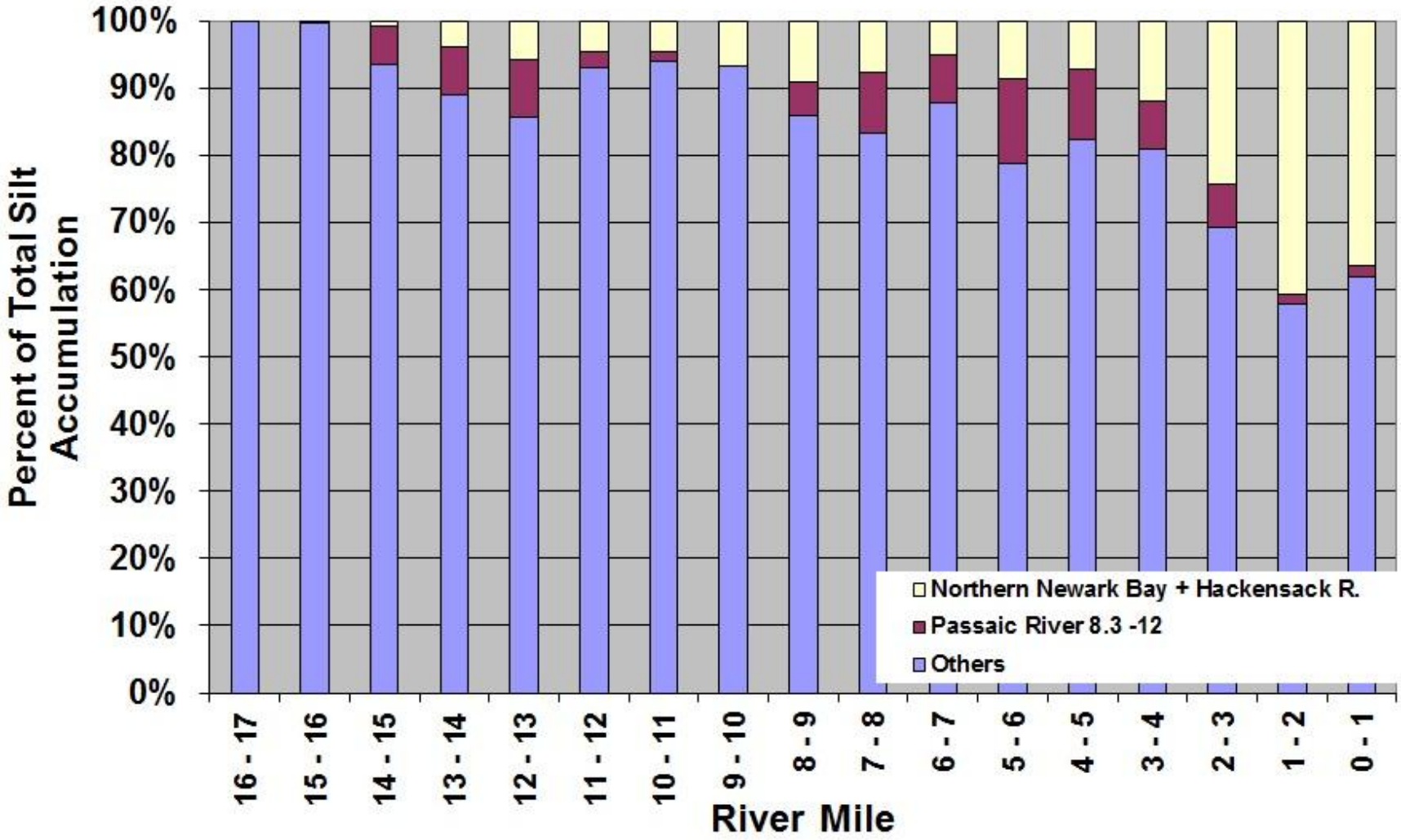

Deepened Bathymetry and Eight-mile Backfill Simulation Results averaged over one-mile Reaches

Lower Eight Miles of the Lower Passaic River

Figure 6-12

2014

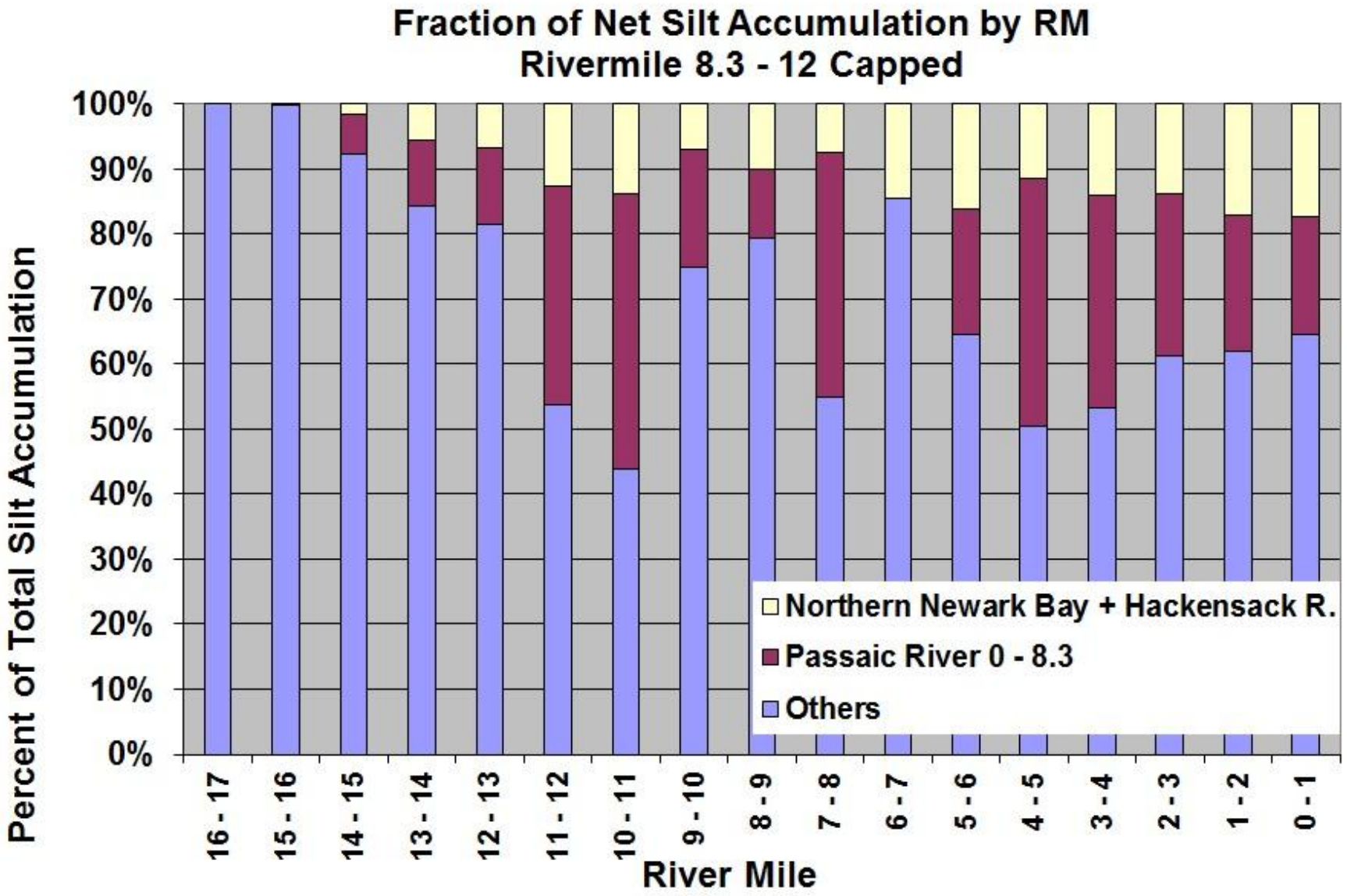

River Mile 8.3-12 Capping Simulation Results averaged over one-mile Reaches

Figure 6-13

Lower Eight Miles of the Lower Passaic River

2014

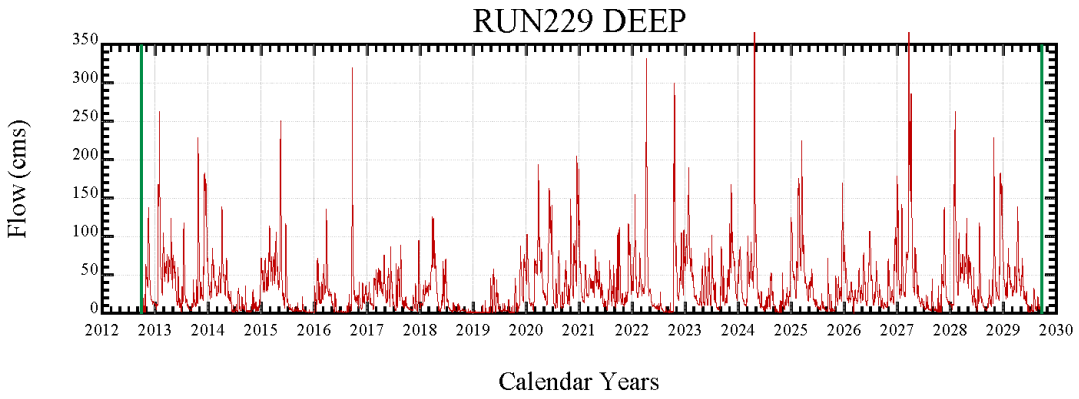

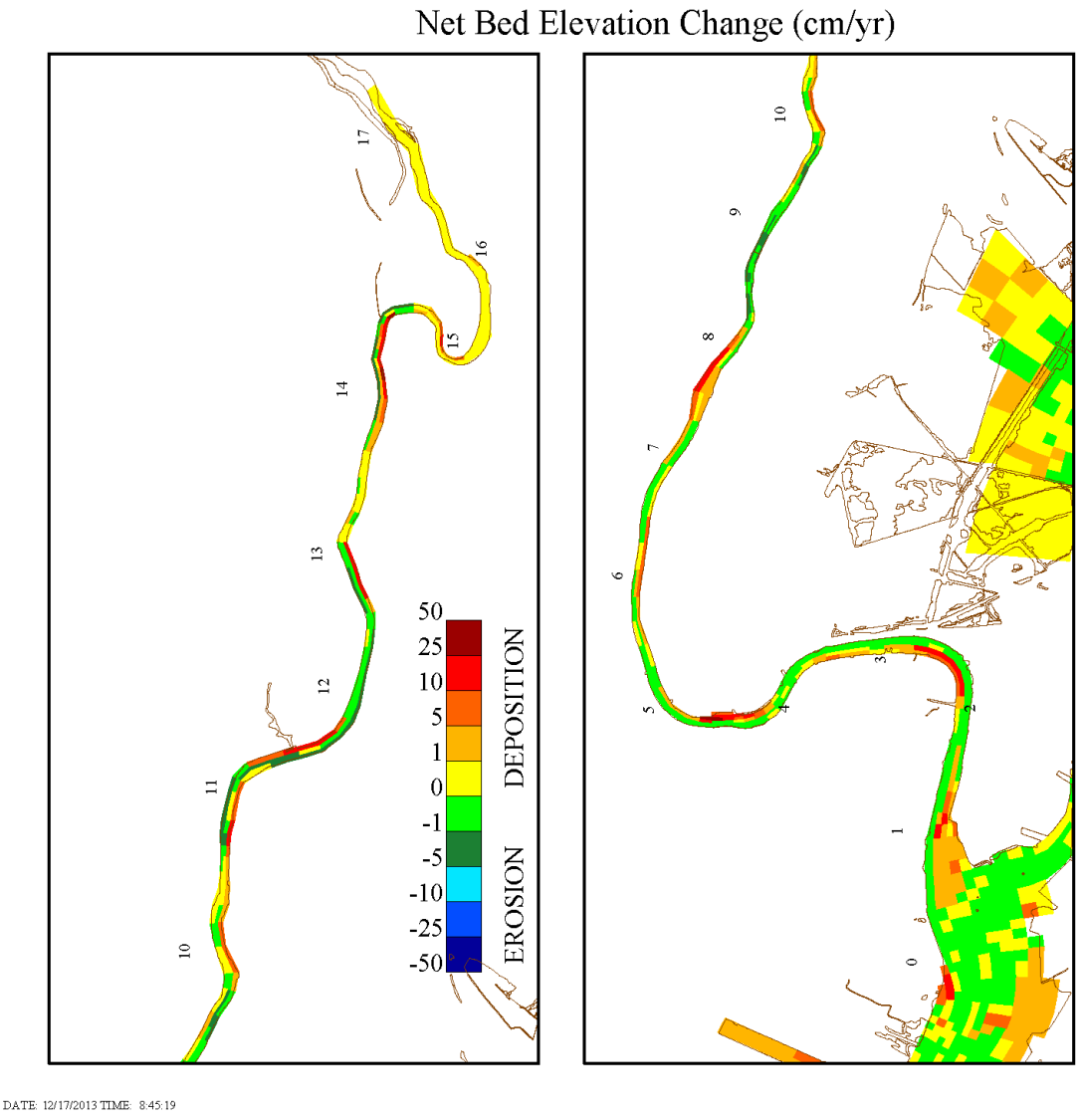

Spatial Distribution of Bed Elevation Changes During No Action Simulation (Alternative 1)

Lower Eight Miles of the Lower Passaic River

Figure 6-14

2014

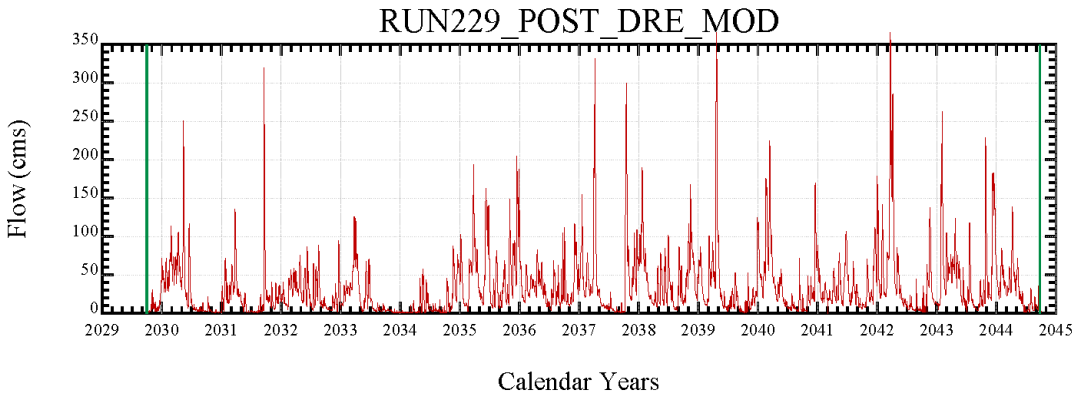

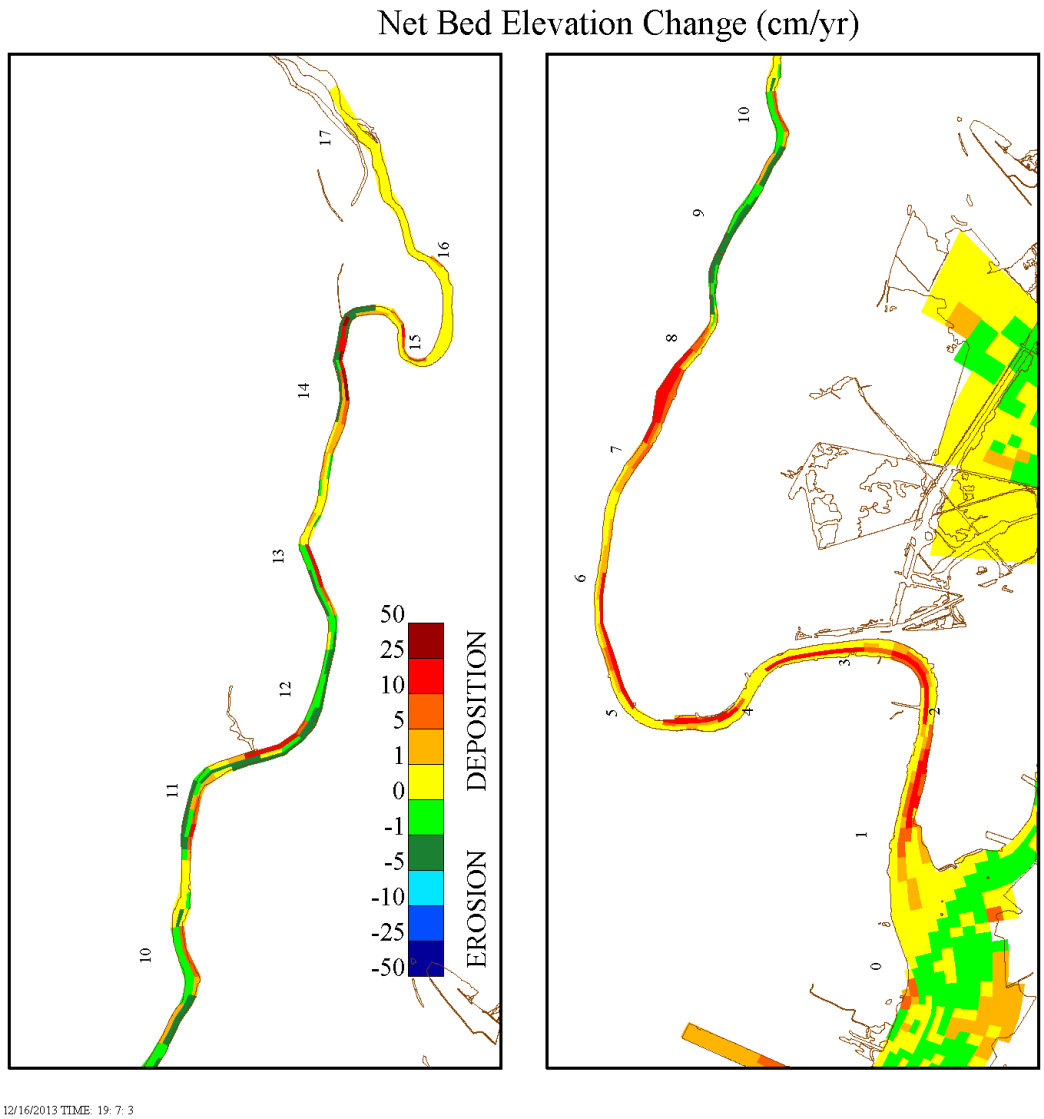

Spatial Distribution of Bed Elevation Changes During Deep Dredging Simulation (Alternative 2)

Lower Eight Miles of the Lower Passaic River

Figure 6-15

2014

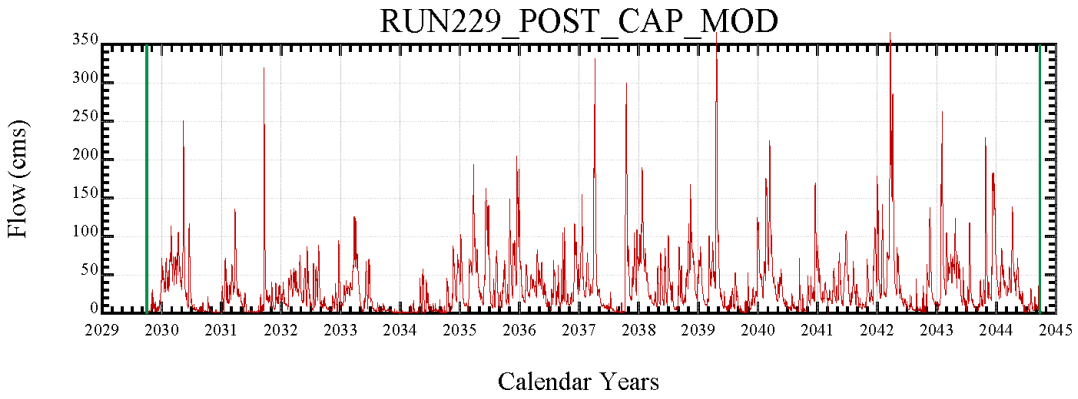

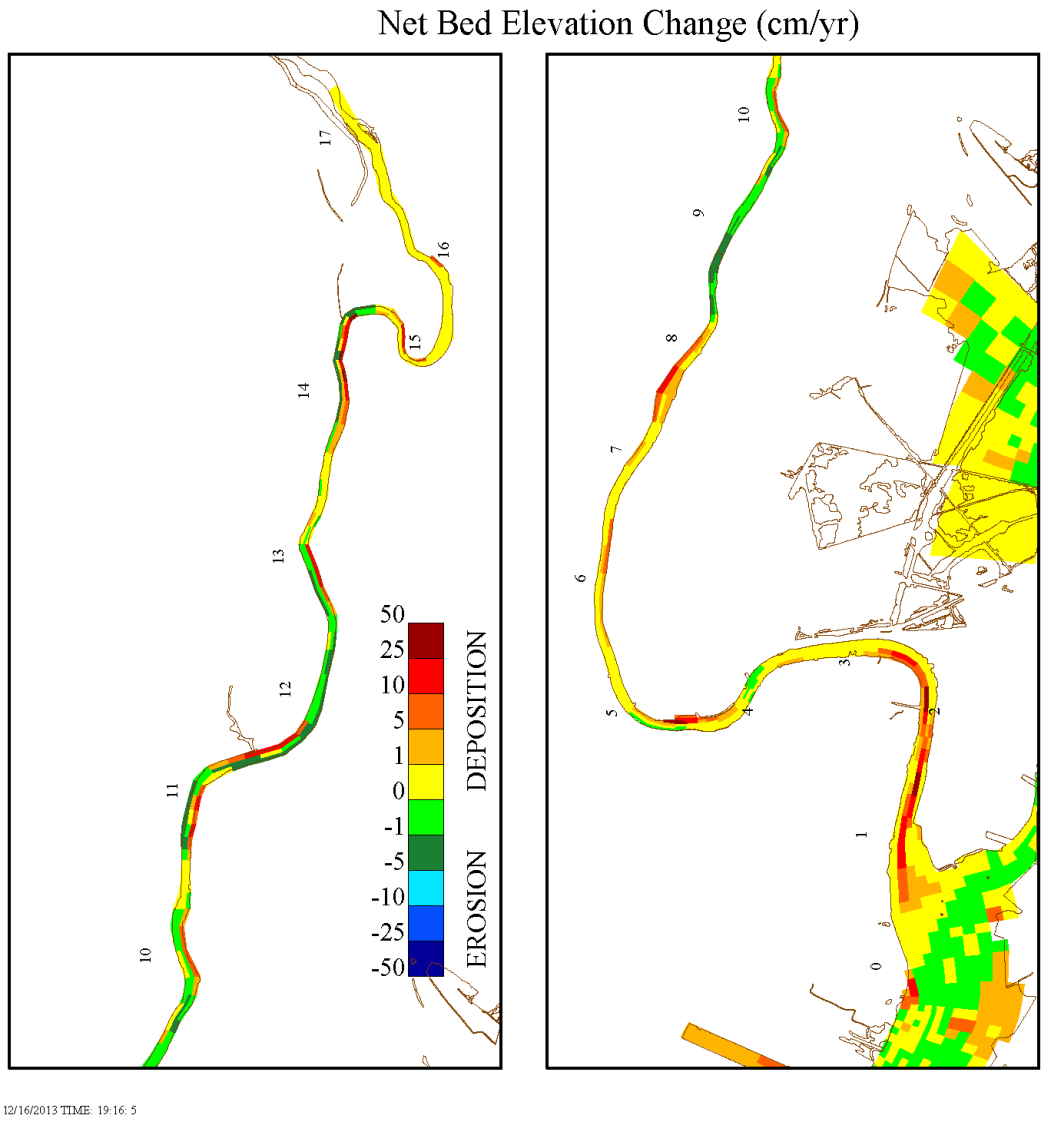

Spatial Distribution of Bed Elevation Changes During Full Capping Simulation (Alternative 3)

Lower Eight Miles of the Lower Passaic River

Figure 6-16

2014

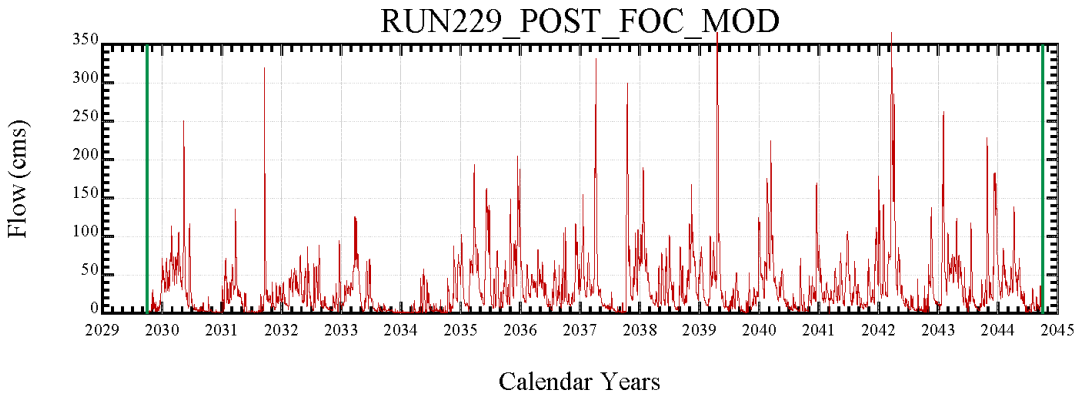

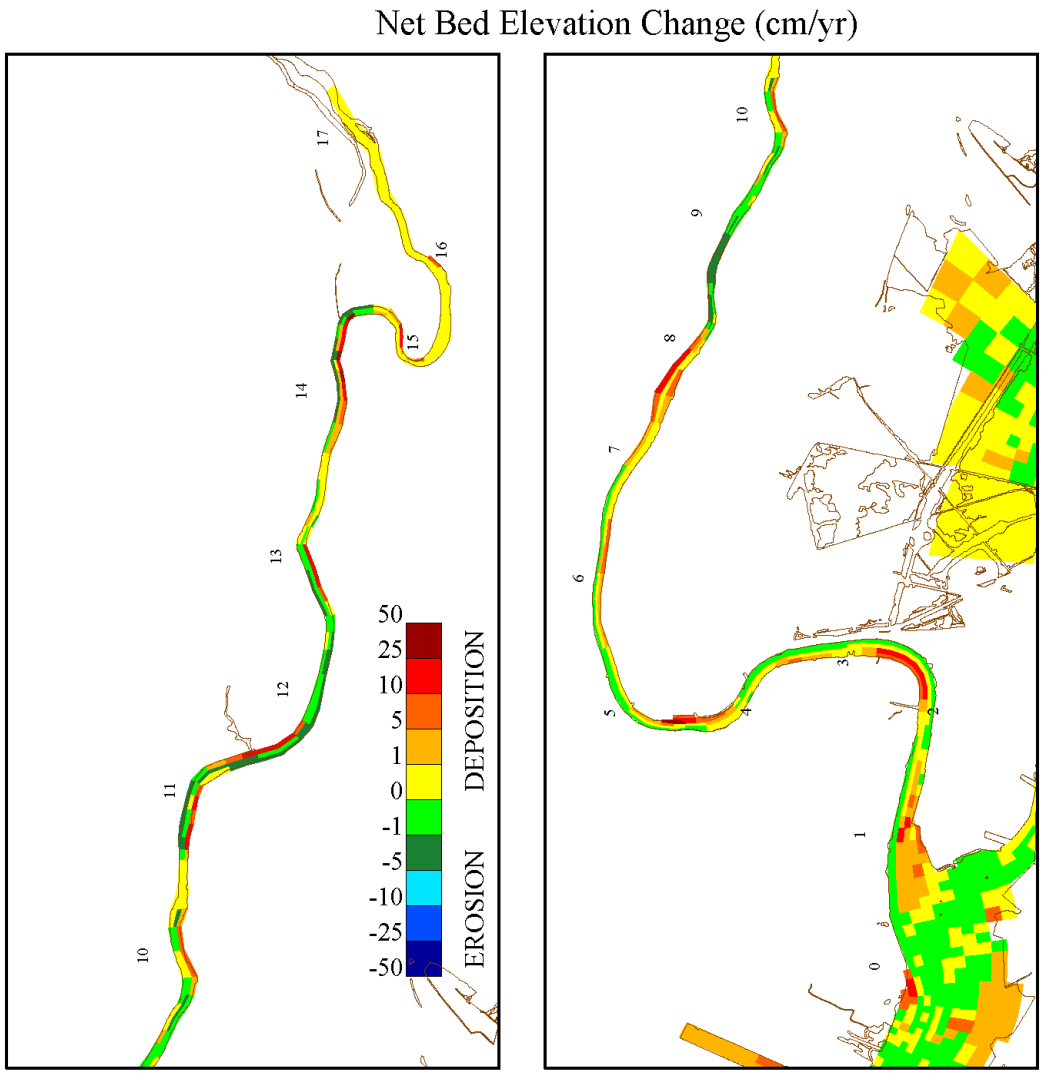

Spatial Distribution of Bed Elevation Changes During Focused Capping Simulation (Alternative 4) *Lower Eight Miles of the Lower Passaic River*	Figure 6-17 2014

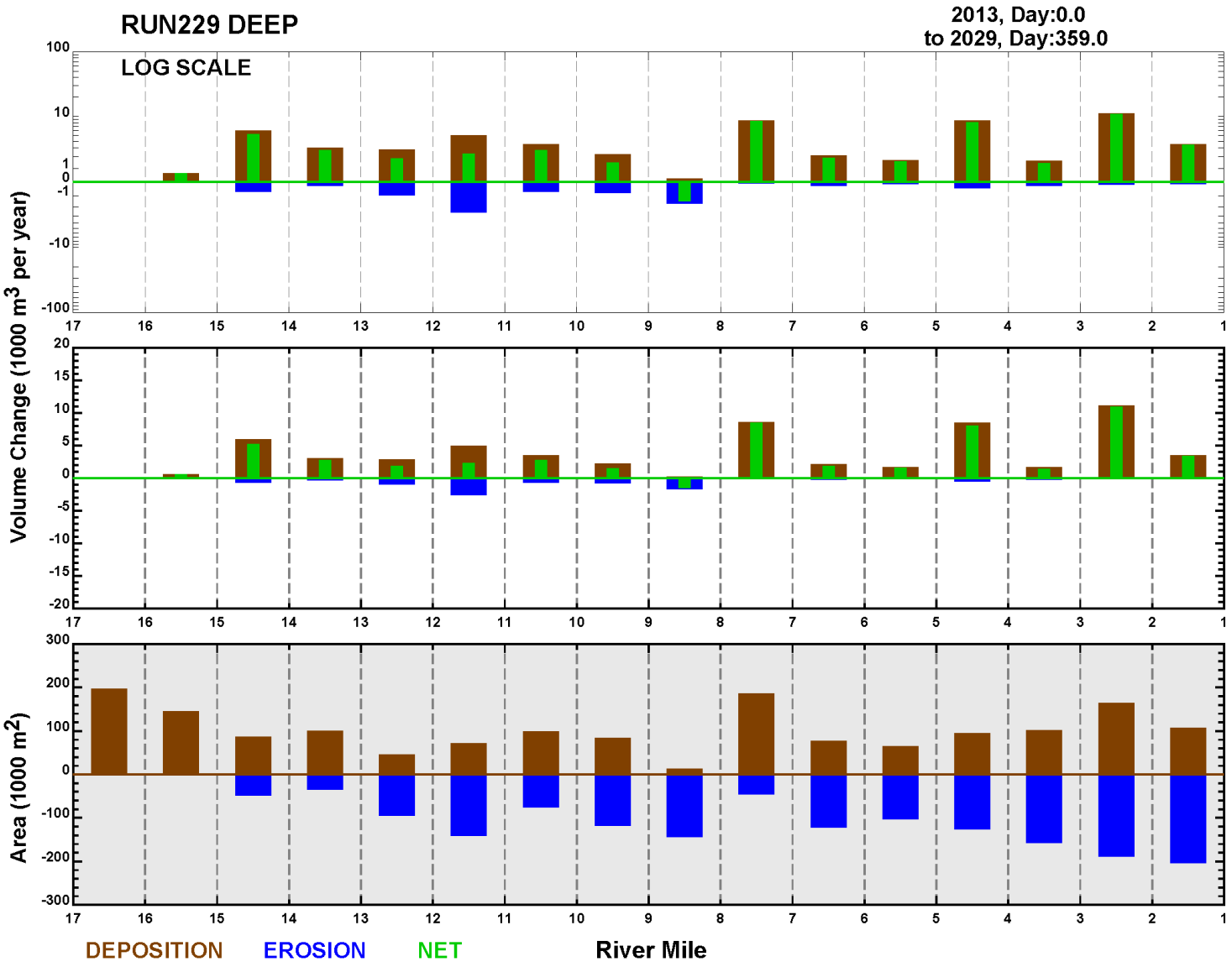

Summary of the Volume and Area of Deposition and Erosion by 1-mile Reaches During No Action Simulation (Alternative 1)

Lower Eight Miles of the Lower Passaic River

Figure 6-18

2014

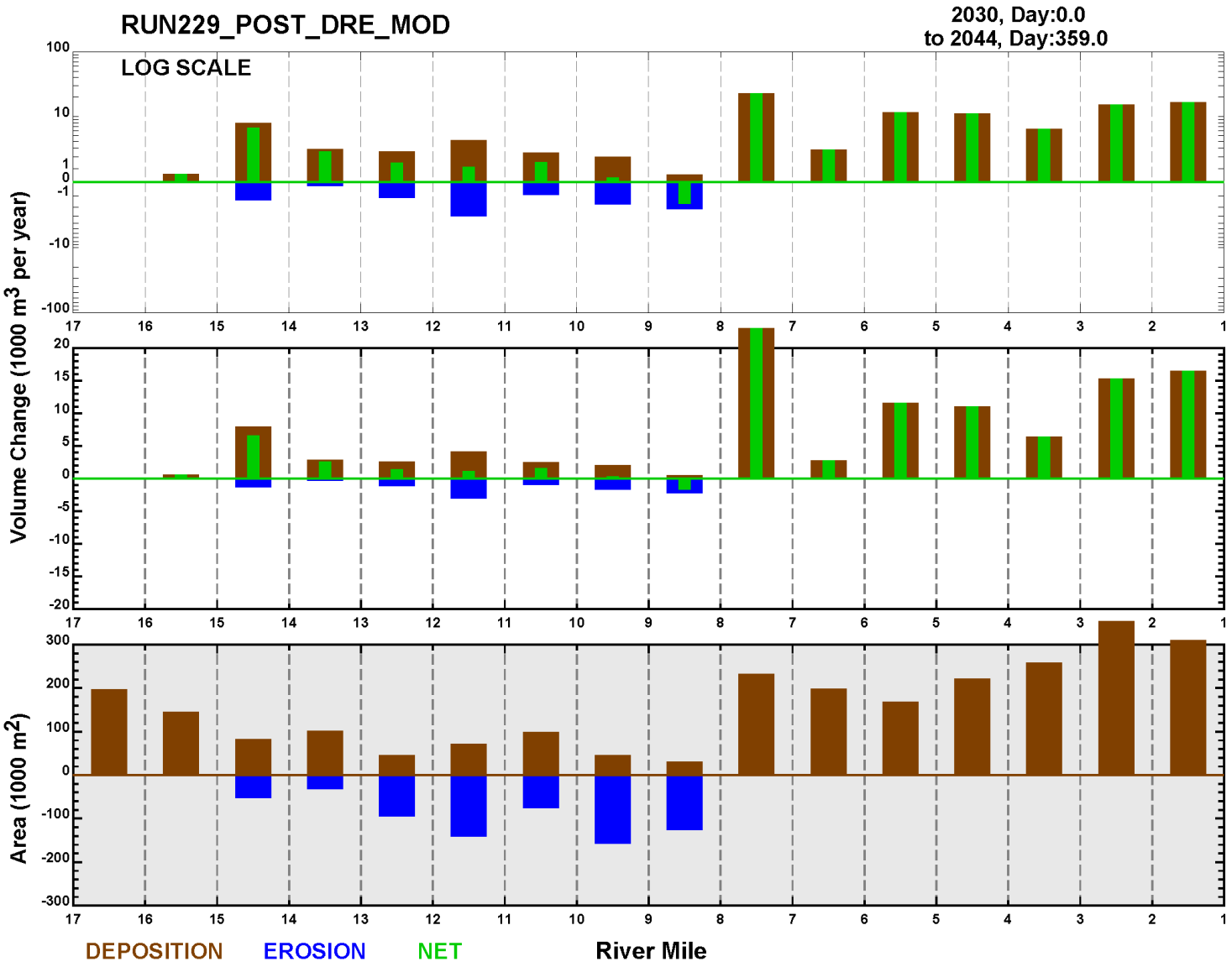

Summary of the Volume and Area of Deposition and Erosion by 1-mile Reaches During Deep Dredging Simulation (Alternative 2)

Lower Eight Miles of the Lower Passaic River

Figure 6-19

2014

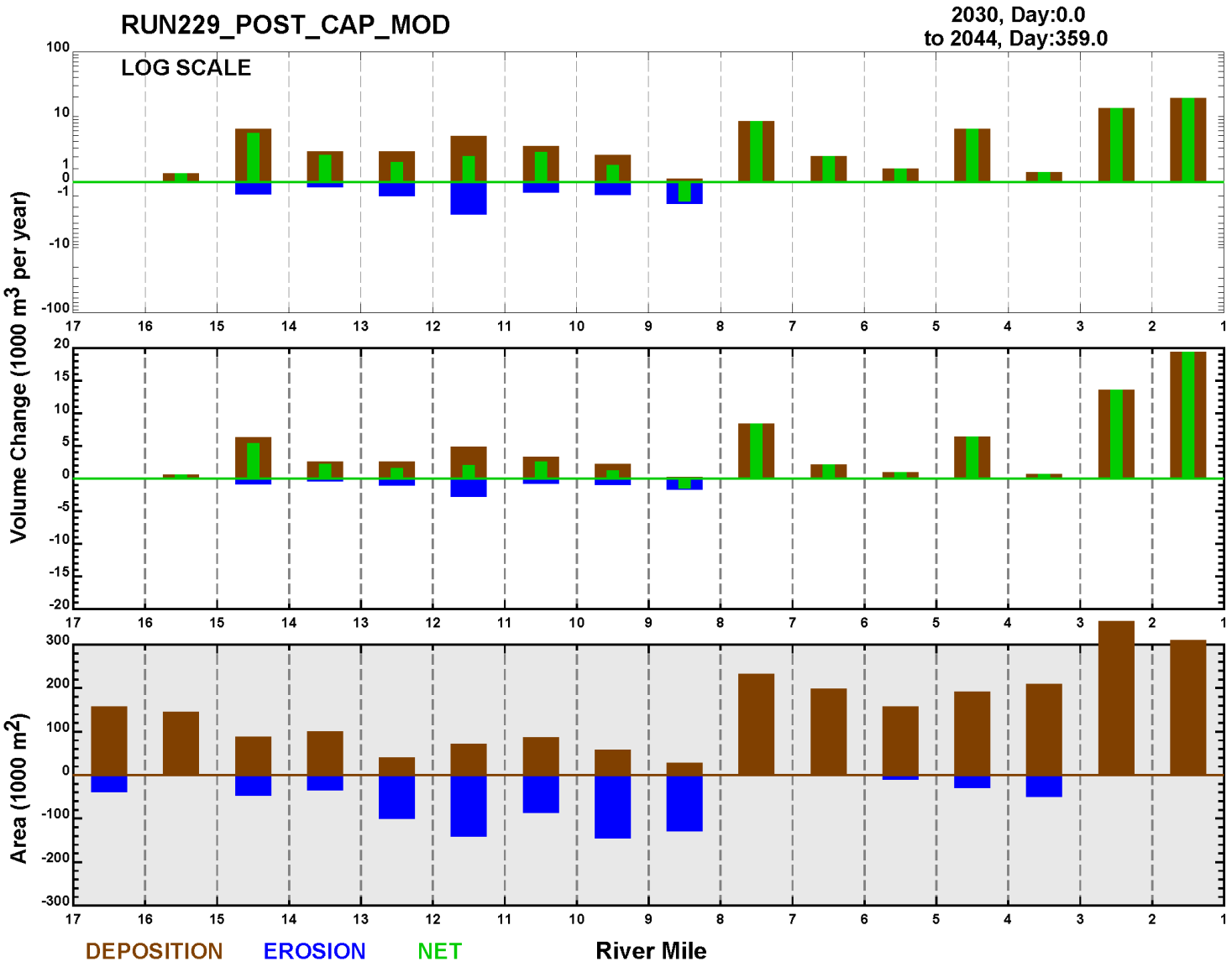

Summary of the Volume and Area of Deposition and Erosion by 1-mile Reaches During Full Capping Simulation (Alternative 3)

Lower Eight Miles of the Lower Passaic River

Figure 6-20

2014

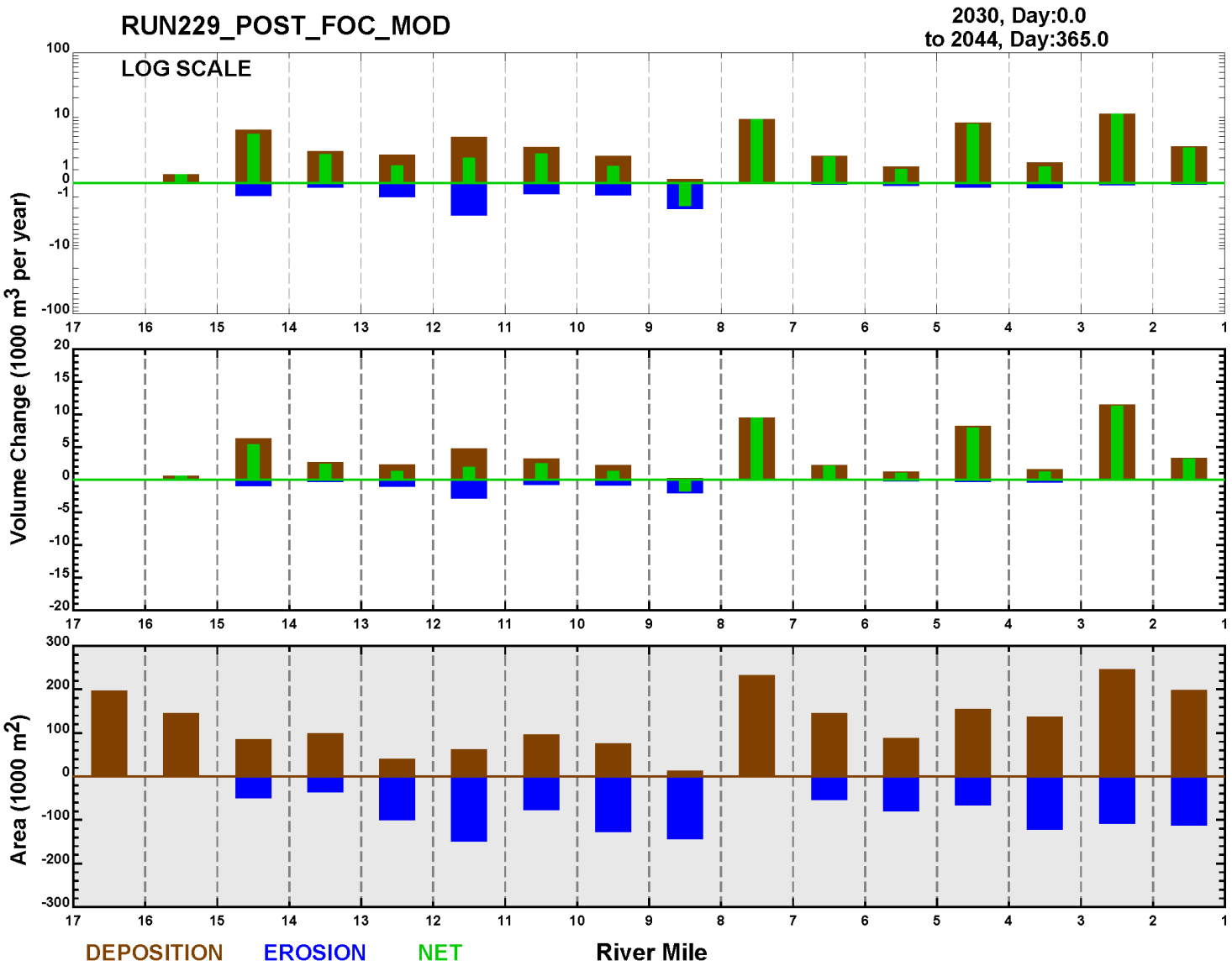

Summary of the Volume and Area of Deposition and Erosion by 1-mile Reaches During Focused Capping Simulation (Alternative 4)

Lower Eight Miles of the Lower Passaic River

Figure 6-21

2014